La diffusion moléculaire sur des surfaces des matériaux de carbone : Études spectroscopiques et théoriques

Emanuel Bahn

UNIVERSITÉ DE GRENOBLE

THÈSE

Pour obtenir le grade de

DOCTEUR DE L'UNIVERSITÉ DE GRENOBLE

Spécialité : **Physique de la Matière Condensèe et du Rayonnement**

Arrêté ministériel : 7 août 2006

Présentée par

Emanuel Bahn

Thèse dirigée par **Peter Fouquet**
et codirigée par **John Ellis**

préparée au sein de **l'Institut Laue-Langevin**
et de **l'Ecole Doctorale de Physique**

Molecular Diffusion on Surfaces of Carbon Materials

Spectroscopic and Theoretical Studies

Thèse soutenue publiquement le **14 décembre 2015**,
devant le jury composé de :

Mme Judith Peters
Professeur, Université Joseph Fourier, Présidente
Mme Franziska Traeger
Professeur, Westfälische Hochschule, Rapporteur
Mr Daniel Farías
Professeur, Universidad Autónoma de Madrid, Rapporteur
Mr Peter Fouquet
Staff Scientist, Institut Laue-Langevin, Directeur de thèse
Mr John Ellis
University Reader, University of Cambridge, Co-Directeur de thèse

To my parents and to Justine.

Résumé en Français

Cette thèse de doctorat porte sur ma recherche doctorale sur la diffusion moléculaire sur des surfaces de matériaux carbonés. Ces travaux de recherche ont été effectués sous forme d'études de spectroscopie neutronique et d'hélium. Des modèles théoriques ont été développés pour l'analyse et l'interprétation des données expérimentales. Dans une première partie, la méthode de croissance épitaxiale d'une couche de graphène sur une surface (111) d'un cristal de nickel est décrite. Basés sur des études de spectroscopie à écho de spin d'hélium, des modèles d'adsorption et de diffusion d'eau et de benzène sur la surface de graphène ont ensuite été élaborés. L'objectif est de décrire précisément la structure de l'adsorbât et la diffusion moléculaire sur la surface. Dans une deuxième partie des études portant sur la diffusion d'hydrogène moléculaire adsorbé dans un aérogel de carbone, dans un carbone poreux, et dans un graphite exfolié sont présentés. Les résultats expérimentaux de spectroscopie en temps-de-vol neutronique nous permettent d'établir le rapport entre la mobilité des molécules d'hydrogène et les propriétés spécifiques aux matériaux de carbone.

Abstract

This thesis presents my PhD work about molecular diffusion on surfaces of carbon materials. The main research has been undertaken in the form of neutron and helium spectroscopy studies and theoretical models have been developed for an interpretation of experimental data. In the first part, the growth procedure of an epitaxial graphene layer on the (111) surface of a nickel crystal is described and the adsorption and diffusion of water and of benzene on the graphene surface are discussed. Results from helium spin-echo spectroscopy studies are presented with the aspiration to obtain a detailed qualitative and quantitative description of the structure of the adsorbate and the molecular diffusion on the surface. In the following chapters, the diffusion of molecular hydrogen adsorbed in carbon aerogel, in a novel porous carbon D-96-7, and in exfoliated graphite is discussed, based on results from neutron time-of-flight spectroscopy. The aim is a detailed understanding of the connection between porosity, surface chemistry, and the molecular diffusion.

Contents

Acknowledgements

I would like to address a few words of acknowledgement to all those, who have helped and supported me throughout my three years of PhD work.

First I would like to thank my supervisor Peter Fouquet, who has helped me with infinite patience to formulate my ideas and to keep the right direction on the many occasions when the matter was confusing. I also want to thank John Ellis, my second supervisor, and Bill Allison, for the lengthy discussions and for their help and advice with the complex matter. My gratitude goes to my team mate in the Cavendish lab, Anton Tamtögl, who has helped me with endless commitment, from times where we ran experiments day and night, to his extensive corrections of my manuscript. I am also grateful to David Ward, Jianding Zhu, Peter Townsend and Fulden Eratam, for their warm welcome in the group.

I want to thank especially Irene Calvo-Almazan for enduring with me the hard times of the development of our model and, like an encyclopaedia of surface diffusion, for assisting me with her knowledge and expertise. My gratitude goes to our collaborators for the fruitful scientific cooperation, especially Orsolya Czakkel and Krisztina László for the creation of the carbon aerogel and the successful experiments and to Leidy Hoyos for the creation of the porous carbon and the great scientific results.

I am also indebted to the instrument scientists and technicians, Mark Telling, Franz Demmel and Mark Kibble from OSIRIS, Mohamed Zbiri and Marek Koza from IN6 and Dimitri Renzy from IN11, for their extensive help with the experimental procedures, Anne Martel for the spontaneous allocation of SANS beam-time, Adam Brewer and Stewart Clarke for their advice on structural refinement and the courtesy of their software, David Weatherup for his advice on the graphene growth procedure, David Hess for his help with the use of the chemistry labs and especially Simon Baudoin for his constant help on so many occasions.

I also want to express my gratitude towards the jury members of my thesis defence, Judith Peters, Franziska Traeger and Daniel Farías, for their participation despite the

long distances that some had to travel, for their attentive and in-depth reading of the thesis manuscript and for the fruitful discussion and the various helpful hints.

My dear friends Jennifer, Patrick and Maxime, thank you so much for your help!

Finally and most of all, I want to thank those who give me their love and support every day, Erika, Wolf, Max, Maria and Justine. Without you I would not have had the power to finish this work.

Publications Related to this Thesis

1. Bahn, E., Hedgeland, H., Jardine, A., Henry, P., Hansen, T. and Fouquet, P., The structure of deuterated benzene films adsorbed on the graphite (0001) basal plane: what happens below and above the monolayer coverage? Physical Chemistry Chemical Physics **16**, pp. 22116–22121 (2014)

2. Bahn, E., Czakkel, O., Nagy, B., László, K., Demmel, F., Telling, M. and Fouquet, P., Dynamics of molecular hydrogen in carbon aerogel. Carbon **98**, pp. 572–581 (2016)

3. Calvo-Almazán, I., Bahn, E., Koza, M., Zbiri, M., Maccarini, M., Telling, M., Miret-Artés, S. and Fouquet, P., Benzene diffusion on graphite described by a rough hard disk model. Carbon **79**, pp. 183–191 (2014)

4. Tamtögl, A., Bahn, E., Zhu, J., Fouquet, P., Ellis, J. and Allison, W., Graphene on Ni(111): Electronic Corrugation and Dynamics from Helium Atom Scattering. J. Phys. Chem. C **119**, pp 25983–25990 (2015)

Acronyms

BET	Brunauer-Emmett-Teller
BJH	Barrett-Joyner-Halenda
BS	neutron backscattering
CE	Chudley-Elliott
CG	carbon aerogel
CoM	centre of mass
DFT	density functional theory
DSF	dynamic structure factor
eV	electronvolt
FFT	fast Fourier transform
HAS	helium atom scattering
HeSE	helium spin-echo
HOPG	highly ordered pyrolytic graphite
HWHM	half width at half maximum
ILL	Institut Laue-Langevin
ISF	intermediate scattering function
LEED	low-energy electron diffraction
MD	molecular dynamics
meV	milli-electron volt
ML	monolayer

NMR	nuclear magnetic resonance
NSE	neutron spin-echo
PA	polarisation analysis
PES	potential energy surface
QENS	quasi-elastic neutron scattering
QHAS	quasi-elastic helium atom scattering
RHD	rough hard disk
SANS	small-angle neutron scattering
SE	spin-echo
TDS	thermal desorption spectroscopy
TOF	time-of-flight
UHV	ultra high vacuum
VCF	Van Hove correlation function
vdW	van der Waals

1 Introduction en Francais

L'adsorption physique des molécules de carbone joue un rôle prépondérant dans différents domaines technologiques, par exemple le développement des piles à combustible, le stockage d'énergie et le dopage moléculaire de graphène. D'un point de vue plus fondamental, l'étude de diffusion moléculaire sur une surface de carbone est primordiale pour la compréhension détaillée du frottement à la surface et de la lubrification [1, 2, 3, 4].

L'adsorption d'hydrogène dans des matériaux poreux en carbone a été étudiée avec grand intérêt durant la dernière décennie, puisque le carbone est vu de plus en plus comme un matériau prometteur pour le stockage d'hydrogène, en particulier à bord de véhicules légers [5]. La possibilité de créer des structures de grande porosité et de surface spécifique très élevée, combinée avec un faible poids spécifique, a mené à la création d'un grand nombre de matériaux poreux en carbone, dont le but est d'adsorber des grandes quantités d'hydrogène [2, 6, 7]. La majorité des études expérimentales sur ces systèmes ont pour objectif de définir des capacités d'adsorption. Bien que l'adsorption et les propriétés chimiques sont profondément reliées au taux de diffusion, il existe relativement peu d'études sur la diffusion d'hydrogène adsorbé.

Le graphène a attiré un grand intérêt durant les dernières années et beaucoup d'applications potentielles sont en discussion. Suite à études théoriques depuis les années 1940, des progrès significatifs ont été réalisés pendant la dernière décennie en ce qui concerne l'isolation et la croissance de graphène [8]. Le dopage de graphène avec des molécules adsorbées a été montré et il ouvre des perspectives pour des applications potentielles [9, 10]. Un dopage non intentionnel à cause d'eau adsorbée a mené à la première observation [11] et depuis, l'effet a été montré sur différentes molécules de gaz [10, 12]. Dans ce contexte, la diffusion moléculaire sur la surface de graphène devient très intéressante, en particulier en raison de la possibilité de déterminer avec une très bonne précision les forces d'interaction à partir des taux de diffusion [13].

L'objectif de cette recherche doctorale est l'investigation des propriétés d'adsorption, de structure et de dynamique d'une série de molécules adsorbées sur des surfaces de matériaux carbonés. Les molécules étudiées sont l'hydrogène moléculaire, l'eau, et le benzène. Les substrats de carbone sont: une couche de graphène sur la surface (111) de nickel, un graphite exfolié, un aérogel de carbone et un carbone poreux. Dans ce but, une série d'expériences de spectroscopie neutronique et d'hélium a été effectuée et des modèles théoriques ont été développés afin d'expliquer les données expérimentales avec le plus de détails possibles.

Plan du manuscrit

Dans le chapitre 3, le lecteur est introduit aux concepts généraux de la diffusion neutronique et d'hélium. Un résumé des théories respectives de diffusion est donné et les méthodes de spectroscopie en temps-de-vol neutronique, de spectroscopie à écho de spin neutronique (NSE), et de spectroscopie à écho de spin d'hélium (HeSE) sont expliquées. Le but est de présenter le cadre théorique et conceptuel, qui est nécessaire pour apprécier l'analyse de données, ainsi que les modèles théoriques, qui sont appliqués dans les chapitres suivants.

Dans le chapitre 4, la croissance d'une couche de graphène épitaxiale à la surface (111) d'un cristal de nickel par dépôt chimique en phase vapeur est expliquée. Le chapitre développe ensuite des études structurales de diffusion d'hélium (HAS), lesquelles confirment une concordance entre le réseau hexagonal de graphène et le réseau fcc de nickel. Une haute réflectivité et une inertie chimique sont observées, ainsi qu'une très faible ondulation de densité électronique. Finalement, des spectres de phonons dans le régime de basse énergie, obtenus par spectroscopie HeSE, sont présentés. Ils montrent les mêmes modes qu'à la surface vierge de nickel, notamment le mode Rayleigh et la résonance longitudinale.

Le chapitre 5 a pour sujet l'adsorption d'eau à la surface de graphène/Ni(111). Des études HAS d'adsorption et de désorption sont présentées, où il est montré que la formation d'îlots domine l'adsorption à basse température, tandis que de la désorption se produit à haute température à partir des surfaces d'îlots. Des valeurs précises pour la section efficace de diffusion d'hélium de la molécule d'eau et pour l'énergie de désorption sont dérivées. Les résultats d'une étude structurale HAS montrent l'existence de glace amorphe à basse température, ainsi qu'un dé-mouillage de la

surface de graphène sous réchauffement. La partie principale du chapitre est focalisée sur la diffusion des molécules de H_2O à la surface de graphène. A partir des résultats d'expériences HeSE, nous proposons un procès de diffusion par sauts entre des sites d'adsorption situés au-dessus du centre de l'hexagone de graphène. Des valeurs pour le taux et la barrière de potentiel pour la diffusion sont calculés à partir des données expérimentales. Des phonons Rayleigh du graphène et de glace sont également observés, ainsi qu'un processus rapide, auquel nous attribuons une diffusion rotationelle des molécules à la surface du graphène.

Dans le chapitre 6, des études structurales du benzène adsorbé à la surface de base (0001) de graphite sont présentées incluant des mesures de diffraction neutronique sur un substrat de graphite exfolié. Dans le régime sous-monocouche, l'existence d'une structure proportionnelle $(\sqrt{7} \times \sqrt{7})\mathbf{R}19°$ est confirmée. Des mesures à couverture plus grande révèlent la formation d'îlots 3D au lieu d'une deuxième couche. Les îlots multicouches présentent la structure du benzène cristallin.

Dans le chapitre 7, des investigations structurales et dynamiques de benzène adsorbé à la surface de graphène/Ni(111) sont présentées. Dans une première partie, des études d'adsorption sont illustrées, lesquelles montrent la formation de couche jusqu'à la couverture complète par une monocouche. Des études de désorption thermique et isothermique montrent la désorption en un seul pic, ce qui nous permet de déduire une valeur pour l'énergie de désorption. Dans une deuxième partie, des résultats des mesures HAS structurales sont présentés, qui confirment l'existence d'une structure proportionnelle $(\sqrt{7} \times \sqrt{7})\mathbf{R}19°$. La partie principale du chapitre présente ensuite des résultats d'une série d'expériences HeSE, lesquels montrent la coexistence d'une diffusion lente et d'une diffusion rapide. La diffusion rapide est constituée en partie d'une diffusion de type Brownien et en partie de diffusion balistique. La dernière montre une asymétrie directionnelle, que l'on attribue à la géométrie de la surface d'énergie potentielle. La diffusion lente porte la signature d'une diffusion par sauts, son origine reste encore inexpliquée.

Dans le chapitre 8, les résultats des mesures de spectroscopie neutronique en temps-de-vol (TOF) d'hydrogène moléculaire adsorbé dans un carbone poreux D-96-7 et dans du graphite exfolié sont présentés. Une caractérisation de D-96-7 est donnée, à partir d'études d'adsorption isothermique et de diffusion aux petits angles. Des études structurales de diffusion neutronique pour les deux matériaux sont ensuite exposées. La partie principale du chapitre se concentre sur des études de diffusion neutronique quasi-élastique (QENS), où la coexistence de deux types

de diffusion a été observée, une diffusion par sauts et une diffusion Brownienne. L'application d'un modèle de disques durs rugueux (RHD) permet le calcul des contributions de frottement cinétique et de frottement de surface. Finalement, les résultats sont comparés avec ceux des études préalables des systèmes de carbone.

Dans le chapitre 9, nous présentons des études d'hydrogène moléculaire adsorbé dans un aérogel de carbone. Dans une première partie, une caractérisation du matériel est donnée à partir de mesures d'adsorption isothermique et de diffusion aux petits angles. Dans la partie principale, nous discutons l'analyse des données et les résultats d'une mesure neutronique TOF. Nous avons observé que l'aérogel de carbone est un catalyseur fort de conversion d'états de spin de la molécule d'hydrogène. Nous proposons un lien entre la conversion incomplète et un confinement rotationnel des molécules dans des ultra-micropores. Finalement, nous présentons des résultats d'études QENS, avec lesquels nous montrons une diffusion activée des molécules d'hydrogène, puis nous comparons les résultats avec des études préalables sur d'autres systèmes de carbone.

2 Introduction

The pvhysical adsorption of molecules on carbon surfaces plays an important role in very different aspects of our everyday life. From fuel cell and energy storage technologies, over molecular doping of graphene, to a basic understanding of surface friction and lubrication: understanding the way how a molecule adsorbs and diffuses on a carbon surface is of fundamental interest [1, 2, 3, 4].

Hydrogen adsorption in porous carbon materials has been studied with great interest during the last decade since carbon is increasingly seen as a promising candidate for hydrogen storage, especially on-board light vehicles [5]. The possibility to create highly porous structures with very large specific surface areas together with a low specific weight has led to the creation of a large number of highly porous carbon materials, where the hope is to adsorb high quantities of hydrogen in a reversible process [2, 6, 7]. The majority of experimental studies on these systems aims at defining adsorption capacities; even though adsorption and chemical properties are deeply connected with surface diffusion rates, relatively few experimental studies on the diffusion of adsorbed hydrogen exist.

Graphene, a pure carbon material that consists of a single sheet of hexagonal carbon, has received an enormous attention in the last years, with many potential applications being discussed. While it has been studied theoretically since the 1940s, large progress in its production by isolation or growth has been achieved in the last decade [8]. Doping of graphene by single molecules has been proven to work and opens perspectives for potential applications [9, 10]. Its first observation was unintentional, when accidental doping was caused by adsorbed water molecules [11] and since then, the effect has been shown on different gases and aromatic molecules [10, 12]. In this context, the diffusion of water and benzene on the graphene surface becomes highly interesting, especially because of the ability to precisely determine interaction strengths from diffusion rates [13].

The goal of this PhD work is to investigate the adsorptive, structural, and dynamical properties at an atomic length scale of water, benzene, and hydrogen on the surface of carbon materials, such as epitaxially grown graphene on a Ni(111) surface, exfoliated graphite, a novel highly porous carbon D96, and carbon aerogel. For that purpose, a series of neutron and helium spectroscopy experiments have been undertaken and theoretical models have been developed that aim at explaining the experimental data to the greatest possible extend.

Outline of the manuscript

In chapter 3, the reader is introduced to the general concepts of neutron and helium scattering. An outline of the respective scattering theories is given and the experimental methods of neutron time-of-flight (TOF) spectroscopy, neutron spin-echo (NSE) spectroscopy, and helium spin-echo (HeSE) spectroscopy are explained with a focus on the relevance to this PhD work. The goal is to supply the reader with the theoretical and conceptual framework, which is necessary to fully appreciate the data analysis and the validity of the theoretical models that are applied in the following chapters.

In chapter 4, the growth of an epitaxial graphene layer on a Nickel (111) surface by chemical vapour deposition is described and structural helium atom scattering (HAS) studies are discussed, which confirm a matching of the hexagonal graphene lattice with the Nickel fcc lattice. A high reflectivity and inertness are observed, as well as a very small electron density corrugation. Finally, phonon spectra in the low energy region obtained by HeSE studies are presented, which show the same modes as on the pristine Ni surface, namely the Rayleigh mode and the longitudinal resonance.

In chapter 5, we discuss the structural and dynamical properties of water adsorbed on the graphene/Ni(111) surface. HAS adsorption and desorption studies are presented, where it is shown that island formation governs low temperature adsorption, while desorption at higher temperatures happens from ice islands. Accurate values for the helium scattering cross section of the H_2O molecule and for the desorption energy are derived. The results from a structural HAS study then show the existence of amorphous ice at low temperature with a de-wetting of the graphene surface upon heating. The main part of the chapter focusses on the diffusion of H_2O molecules on the graphene surface. Based on HeSE measurements, we suggest a jump diffusion

process between adsorption sites that are located above the centre of a graphene hexagon and derive values for the rates and the potential barrier of diffusion. A second, fast diffusion is observed, which we attribute to a uni-axial rotational diffusion of single water molecules on the graphene surface. Furthermore, the persistence of the graphene phonon modes is discussed.

In chapter 6, structural studies of benzene adsorbed on the (0001) basal plane of graphite are presented, based on neutron diffraction measurements with a substrate of exfoliated graphite. In the sub-monolayer regime, the existence of a commensurate $(\sqrt{7} \times \sqrt{7})\mathbf{R}19°$ over-structure is confirmed and a melting at high temperature is observed. Measurements at higher coverage reveal formation of 3D islands instead of a second layer, which exhibit the structure of solid, crystalline benzene.

In chapter 7, structure and dynamics investigations of benzene adsorbed on the surface of graphene/Ni(111) are presented. In a first part, adsorption studies are discussed that reveal a layer formation up to the monolayer. Thermal and isothermal desorption studies exhibit a single peak that enables us to deduce a value for the desorption energy. In a second part, the results of structural HAS measurements that confirm the existence of a commensurate $(\sqrt{7} \times \sqrt{7})\mathbf{R}19°$ over-structure, are presented. The main part of the chapter then presents a series of HeSE measurements, which reveal the coexistence of a fast and slow diffusion. The fast diffusion consists partly of Brownian-type diffusion and partly of ballistic diffusion. The suggestion is made that the ballistic motion occurs along a preferential direction, which we link to the structure of the potential energy surface (PES). The slow diffusion exhibits the signature of activated jump diffusion, the exact nature and origin of which is unclear up to this point.

In chapter 8, neutron TOF studies of molecular hydrogen adsorbed in exfoliated graphite and in a novel highly porous carbon are presented. A characterisation of D-96-7, based on isothermal adsorption measurements, is given and structural neutron scattering investigations on both materials are discussed. The main part of the chapter focusses on quasi-elastic neutron scattering (QENS) studies of adsorbed hydrogen in the two materials, where a coexistence of two diffusion processes has been observed: jump diffusion and Brownian-type diffusion. Applying the rough hard disk (RHD) model allowed us to calculate the contributions from collisional and from surface friction, respectively. Finally, the results are compared to results on other carbon systems.

In chapter 9, we present studies of molecular hydrogen adsorbed in a carbon aerogel. In a first part, a characterisation of the carbon aerogel is given and results from isotherm adsorption measurements and their implications on an expected pore size distribution are discussed. In a second part, large scale as well as atomic length scale structures of the carbon aerogel are presented. In the main part, we discuss the analysis and results of experimental data obtained from a neutron backscattering measurement. In the first part of the analysis of the neutron scattering data we focus on the conversion of the spin states in the hydrogen molecule and on our observations of the carbon aerogel being a strong conversion catalyst. We discuss the suggestion that an incompleteness of the conversion is linked to rotational confinement of molecules in ultra-micropores. Finally, we present results from QENS studies where we show that a two-dimensional jump diffusion process governs the hydrogen dynamics and we compare the observed activation energy for diffusion and the diffusion constant to existing results on other carbon systems.

3 Methods

3.1 Adsorption and Desorption

The aim of this section is to give a brief overview over the main concepts of adsorption on surfaces. Adsorption is the association of an atom or a molecule to a surface. The surface is here referred to as the adsorbent, while the impinging particle is given the name adsorbate or adparticle, or, depending on its exact nature, adatom or admolecule. Adsorption can is commonly classified by two different regimes, chemisorption and physisorption. In a **chemisorption** process, a covalent bond is formed between the adsorbent and the surface, giving rise to an adsorption energy in the order of an electronvolt (eV). **Physisorption**, on the other hand, refers to a pro-

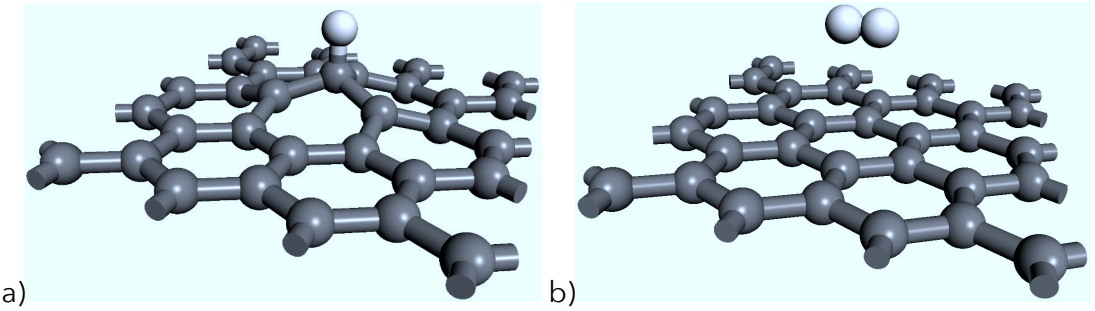

Figure 3.1: Illustration of the possible adsorption processes of hydrogen with a graphene surface. a) Chemisorption of a hydrogen atom to the surface by chemical bonding. The large interaction energy distorts the surface structure. b) Physisorption of a hydrogen molecule to the surface via van der Waals interaction.

cess where the adsorbate is bound by the weak van der Waals (vdW) interaction, with adsorption energies in the range of tens to hundreds of milli-electron volt (meV). This interaction results from permanent, spontaneous or induced electric dipoles or multipoles. In the case of two molecules, the electric dipole moment of each molecule scales with r^{-3}, therefore the strength of the vdW interaction scales with r^{-6}. The

potential energy of the system is often described by the Lennard-Jones potential, which consists of a r^{-12} term for the strong repulsive interaction stemming from the orthogonality of the electron wave functions and a r^{-6} term for the attractive vdW interaction. In the case of physisorption, this term scales with r^{-3} due to the large two-dimensional extension of the surface (Fig. 3.2).

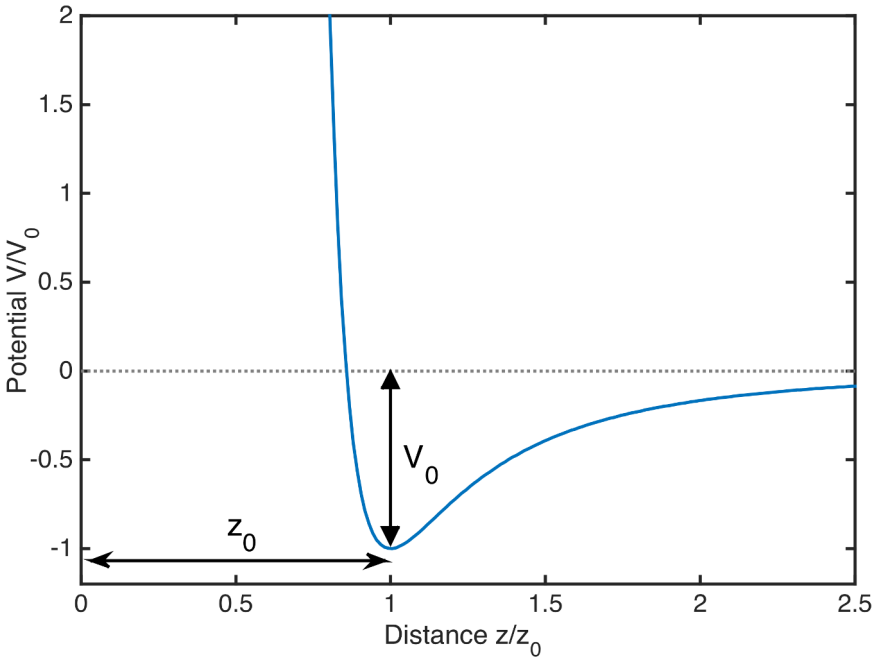

Figure 3.2: Illustration of the Lennard-Jones potential for the description of a physisorption process. V_0 denotes the potential minimum, z_0 denotes the distance of the adsorbate to the surface at minimum interaction potential.

3.1.1 Kinetics of Phisysorption on a Surface

The surface exposure E is defined as the impinging flux of adsorbate molecules on the surface integrated over the time of exposure. Its unit is the Langmuir, defined as 1 L = 1 torr $\cdot\mu$s = 1.33 mbar $\cdot\mu$s. The Langmuir model allows us to relate the surface coverage θ with the exposure through the kinetic theory of gases [14]:

$$\theta = \frac{E}{\sqrt{2\pi m k_B T_{gas}}} = \frac{\int p\,\mathrm{d}t}{\sqrt{2\pi m k_B T_{gas}}}, \tag{3.1}$$

with the gas temperature T_{gas}, the Boltzmann constant k_B, the mass of the adparticle m, and the pressure p. This rather simple model does not take into account desorption or multilayer adsorption and assumes a sticking coefficient of unity.

In a more detailed picture, the adsorbate can undergo different processes after adsorption on the surface, such as subsequent desorption, formation of flat or 3D islands, or ordering due to long range repulsive interaction between adparticles. Especially in the physisorption regime, adparticles are highly mobile. Depending on the inter-particle and the adparticle-surface interaction, the adsorbate can form three-dimensional islands or gradually cover the surface, forming a monolayer (the adsorbate wets the surface).

Isothermal Desorption

The reverse process of the adsorption is desorption, in which an adparticle leaves the surface. This is generally an activated process, where the desorption constant k_d follows an Arrhenius-type law:

$$k_d = A \exp\left(-\frac{E_d}{k_B T}\right), \tag{3.2}$$

where A is a pre-exponential factor and E_d is the desorption energy [14, 15]. The desorption rate $r = \mathrm{d}\theta/\mathrm{d}t$ is given by;

$$r = \frac{\mathrm{d}\theta}{\mathrm{d}t} = -k_d \theta^m, \tag{3.3}$$

where m is the order of desorption. A direct desorption of single molecules from the surface would correspond to a first order desorption process ($m = 1$), while recombinative desorption of e.g. two atoms into a dimer yields a second order process ($m = 2$). The case where the desorption rate is limited (e.g. multilayer desorption), coverage-independent zeroth-order desorption is observed ($m = 0$). For isothermal desorption (i.e. at constant temperature) and in the case of first order desorption, the surface coverage decays exponentially with time (at high enough temperatures). By measuring the decay rate at different temperatures, the activation energy of desorption E_d of a system can be established (see e.g. Sec. 5.2.2).

Thermal Desorption Spectroscopy

A common technique to establish binding energies is the thermal desorption spectroscopy (TDS). Hereby, the adsorbate covered surface is heated at a constant rate β while the flux of desorbed adparticles is monitored via the signal of a mass spectrometer or indirectly by observing the specular helium reflectivity (see Sec. 3.3). The desorption rate r depends on $\beta = \frac{\mathrm{d}T}{\mathrm{d}t}$ by $\frac{\mathrm{d}r}{\mathrm{d}T} = -\frac{k_d}{\beta} r^m$. Combining this with Eq. 3.2 yields:

$$\frac{\mathrm{d}\theta}{\mathrm{d}T} = -\theta^m \frac{A}{\beta} \exp\left(-E_d/k_B T\right) \tag{3.4}$$

The temperature T_p, where the maximum of the desorption peak is situated, is related to E_d:

$$\frac{E_d}{k_B T_d^2} = \frac{A}{\beta} \exp\left(-E_d/k_B T_p\right) \tag{3.5}$$

The Redhead equation makes the assumption that the activation energy and the pre-exponential factor are coverage-independent and gives an approximative solution [16]:

$$E_d = k_B T_p \left[\ln\left(\frac{A T_p}{\beta}\right) - 3.64\right]. \tag{3.6}$$

The Redhead equation is commonly applied for first order kinetic processes but it can also be used for fractional or zero order kinetics if the initial coverage for which TD traces are analysed corresponds to one complete monolayer [15].

3.2 Neutron Scattering

Neutron scattering has been highly successful in condensed matter research, mainly due to the fact that neutrons penetrate matter and scatter within the sample, revealing information about the inner structure and dynamics of the sample. Since the neutron is one of the fundamental building blocks of matter, thermal and cold neutrons fulfil two important criteria at once, that is their wavelength and energy correspond to typical inter-atomic distances and vibrational energies, respectively. In

Source	Energy [meV]	Temperature [K]	Wavelength [Å]	Velocity [m/s]
cold	0.1–10	1–120	30–3	140–1400
thermal	5–100	60–1000	4–1	1000–4400
hot	100–500	1000–6000	1–0.4	4400–10000

Table 3.1: Approximate energy, temperature and wavelength ranges for the three main kinds of neutrons produced in a research reactor (from [17]).

order to produce a neutron beam with sufficient flux for a typical condensed matter experiment, either a nuclear reactor or a spallation neutron source are required. The neutron scattering experiments that have contributed to this thesis have been carried out in both types of sources. We have performed a number of measurements at the research reactor Institut Laue-Langevin (ILL) in Grenoble, France, whose reactor is designed in a way that aims at maximising the production of neutrons. A nuclear fuel element of highly enriched uranium produces a high flux of fast neutrons that are moderated by a surrounding pool of heavy water and by a vessel filled with liquid hydrogen. Neutron guides, evacuated tubes with walls coated with supermirrors that reflect neutrons, point out from the centre of the reactor to scientific instruments situated some tens of meters away from the reactor pool. At the ISIS neutron source in Didcot, UK, neutrons are created by spallation. Here, a synchrotron accelerates a proton beam to 160 kW and orders the protons into small bundles. The proton bundles collide with a tungsten target that is rotating to dissipate the large amount of heat. Because of the high energy impact, the tungsten nuclei become excited and emit high energy neutrons. As in a research reactor, neutron guides lead from the target to instruments in a nearby experimental hall. For most instruments, including the ones that we used for the measurements presented here, thermal and cold neutrons are needed. This requires a substantial slowing down of the fast neutrons, which is achieved in a reactor by moderation in the heavy water reactor pool, and in the case of a spallation source and for the production of cold neutrons in general, by further collisional cooling in a bath of liquid hydrogen or deuterium at 20 K. Tab. 3.1 gives a comparison of typical neutron energies and wavelengths at different temperatures.

Situated at the end of the neutron guides are a range of different research instruments. To study condensed matter, the existing instruments can be categorised into two main groups. The *diffractometers* exploit neutron diffraction phenomena that occur in the elastic scattering process of a neutron with the nuclei of a sample. Elastic coherent scattering from repeating structures gives rise to interference that

returns structural information of a sample. In this thesis, measurements from the high-intensity two-axis diffractometer D20 and from the small-angle neutron scattering (SANS) diffractometer D22, both situated at ILL will be discussed. Neutron *spectrometers* exploit the energy transfer of a neutron with the sample in the event of inelastic neutron scattering to gain information about ordered and chaotic dynamics. We will discuss in this thesis results from experiments at the TOF spectrometer IN6 at ILL, from the neutron backscattering (BS) spectrometer OSIRIS at ISIS and from the NSE spectrometer IN11 at ILL.

3.2.1 Neutron Scattering Theory

In this section, we will give a brief introduction into the basic neutron scattering theory that is necessary to understand the interpretation of the experimental results. The section follows closely H. Schober's introductory article [18] and to some degree the introductory books by G.L. Squire [17] and by M. Bée [19]. In our experiments, neutrons have been scattered from condensed matter in order to gain information about the system of interest by analysing the energy and directional momentum of the scattered neutrons. In the energy range used in these investigations, the neutrons move non-relativistically and their only internal degree of freedom is their spin. The neutron is uncharged and the scattering process with nuclei involves only nuclear forces. Quantum-mechanically, the neutron wave function can be described by its wave-vector k, and its spin S, $\phi = |k, S\rangle$. The neutron is a lepton, i.e. $S = \pm\frac{1}{2}$ [18]. For a neutron with mass m and velocity v, the de Broglie relation states that its momentum p is related to its wave-vector k via $p = mv = \hbar k$ and its angular frequency ω to its energy E via $\hbar\omega = E$, where $\hbar$ is the reduced Planck constant. This also relates E to the neutron wavelength λ:

$$E = \frac{m}{2}v^2 = \frac{\hbar^2 k^2}{2m} = \frac{h^2}{2m\lambda^2}, \tag{3.7}$$

where h is the Planck constant. A neutron temperature T can also be defined because of the fact the neutron beam follows a Maxwell–Boltzmann velocity distribution, with the Boltzmann constant k_B [17]:

$$E = \frac{3}{2}k_B T. \tag{3.8}$$

The Neutron Scattering Cross Section

The scattering of a particle is described by the transition of the particle from its initial into its final state. Before and after the scattering process, the particle is considered free, the transition is described mathematically by an operator. The projection of initial and final state of the particle onto the transition operator yields the scattering probability [18]:

$$S_{f,i} = \langle k_f, S_f | \, \mathrm{U}(t \to +\infty, t \to -\infty) \, | k_i, S_i \rangle \, . \tag{3.9}$$

In a measurement, detectors are placed at a certain distance and cover a certain solid angle. The number of neutrons counted in these detectors depends on the detector size and its distance to the sample, as well as on the incoming neutron flux. In order to correct for these external parameters, one expresses scattering in form of the differential scattering cross section:

$$\mathrm{d}\sigma = \frac{\text{flux scattered into solid angle } \mathrm{d}\Omega}{\text{incoming flux}} = r^2 \, \mathrm{d}\Omega \frac{J_f(r, \theta, \phi, t)}{J_i(t)}, \tag{3.10}$$

with the scattering angles θ and ϕ and the distance r. The wave function $u_k(r)$ describes a neutron with a momentum $\hbar k$ at a position r. Let us assume that it scatters from a static potential $V(r)$, then it has to obey the stationary Schrödinger equation:

$$\left[-\frac{\hbar^2}{2m} \Delta + V(r) \right] u_k(r) = E(k) u_k(r). \tag{3.11}$$

The general solution in the asymptotic regime ($r \to \infty$) is given by the linear combination of a plane wave and a radial wave, corresponding to the unperturbed and the scattered wave, respectively:

$$u_k(r) \longrightarrow \frac{1}{\sqrt{V_B}} \left(e^{\mathrm{i}k.r} + f_k(\theta, \phi) \frac{e^{\mathrm{i}k.r}}{r} \right), \quad r \to \infty, \tag{3.12}$$

with the scattering amplitude $f_k(\theta, \phi)$ and a normalisation by a volume V_B. The scattering cross section then reads:

$$\frac{\mathrm{d}\sigma}{\mathrm{d}\Omega} = r^2 \,\mathrm{d}\Omega \frac{J_f(r, \theta, \phi, t)}{J_i(t)} = |f_k(\theta, \phi)|^2, \tag{3.13}$$

with the flux of incoming neutrons $J_i(t)$ and the flux $J_f(r, \theta, \phi, t)$ of neutrons scattered into the radial coordinates r, θ, ϕ at a time t.

Partial Wave Expansion and the Scattering Length

The scattering amplitude expresses the angular dependency of the scattering probability. For an isotropic and static potential, it can be expanded into partial waves:

$$f_k(\theta) = \frac{1}{2\mathrm{i}k} \sum_{l=0}^{\infty} \sqrt{4\pi(2l+1)}(e^{2\mathrm{i}\delta_l} - 1) Y_l^0(\theta), \tag{3.14}$$

with the spherical harmonics $Y_{l0}(\theta)$ and a phase shift δ_l of the partial wave of lth order. Since a thermal neutron has a wavelength in the order of ångströms ($1\,\text{Å} = 10^{-10}\,\text{m}$) and scatters from a nucleus of a size of about $10^{-15}\,\text{m}$, the scattering basically occurs in form of **s-wave scattering**, which means that only the $l = 0$ term contributes. The limit $k \to 0$ of $f(\theta)$ is known as the scattering length b:

$$b = \lim_{k\to 0} f_k(\theta) = \lim_{k\to 0} \frac{e^{2\mathrm{i}\delta_0} - 1}{k} = -\lim_{k\to 0} \frac{\delta_0(k)}{k}. \tag{3.15}$$

The Born Approximation

In order to find a general solution to the Schrödinger equation (3.11) via a Green's function, a perturbation treatment yields several important results. This is accomplished by an integral representation of the Schrödinger equation:

$$u_k(r) = u_k^0(r) + \int \mathrm{d}^3 r G_0(r, r') V(r') u_k(r') \tag{3.16}$$

with the Green's function

$$G_0(r, r') = -\frac{1}{4\pi}\frac{2m}{\hbar^2}\int \mathrm{d}^3 r' \frac{\exp(\mathrm{i}k \cdot |r - r'|)}{|r - r'|}. \tag{3.17}$$

Replacing $u_k(r')$ by the unperturbed wave $u_k^0(r')$ in the integral is called the **Born approximation**, it means that only the linear term in the Born series is kept:

$$u_k(r) = u_k^0(r) - \frac{1}{4\pi}\frac{2m}{\hbar^2}\int \mathrm{d}^3 r \frac{\exp(\mathrm{i}k \cdot |r - r'|)}{|r - r'|} V(r') u_k^0(r'). \tag{3.18}$$

The Fermi Pseudo-Potential

Since nuclear scattering is extremely short range, the potential can be expressed as a point potential, the **Fermi pseudo-potential**:

$$V(r) = \frac{2\pi\hbar^2}{m} b\delta(r). \tag{3.19}$$

The form factor is the Fourier transformed potential:

$$V(Q) = \int \mathrm{d}^3 r V(r) e^{-\mathrm{i}Q.r} = \frac{2\pi\hbar^2}{m} b. \tag{3.20}$$

It is a constant that is proportional to b. Making use of Fermi's golden rule, the differential cross section can be expressed in a double differential form:

$$\frac{\mathrm{d}^2\sigma}{\mathrm{d}\Omega\,\mathrm{d}E} = m^2\frac{(2\pi)^4}{\hbar^4}\frac{k_f}{k_i}|\left\langle k_f, \lambda_f\right| V \left|k_i, \lambda_i\right\rangle|^2, \tag{3.21}$$

with the initial (i) and final (f) wave-vector k and wavelength λ of the neutron, and its mass m. By inserting the pseudo potential into the above equation, the cross section becomes a projection of the initial onto the final state:

$$\frac{\mathrm{d}^2\sigma}{\mathrm{d}\Omega\,\mathrm{d}E} = \frac{k_f}{k_i}\frac{1}{2\pi\hbar}\sum_{j,j'=1}^{N} b_j b_{j'}^* \int \mathrm{d}t \left\langle e^{-\mathrm{i}Q.R_{j'}(0)} e^{\mathrm{i}Q.R_j(t)}\right\rangle e^{-\mathrm{i}\omega t}, \tag{3.22}$$

where the sum is made over all combinations of scatterers j,j' at positions $R_{j'}(0)$ and $R_j(t)$, and the *momentum transfer* $Q = k_i - k_f$ has been defined. Energy conservation is expressed by an integral over the time t of $e^{-i\omega t}$, with the *energy transfer* $\hbar\omega = E_i - E_f$.

Scattering Functions and Correlations

The differential scattering cross section can be expressed in a simple form:

$$\frac{d^2\sigma_{k_i \to k_f}}{d\Omega\, dE_f} = \frac{k_f}{k_i} S(Q,\omega) \tag{3.23}$$

where the dynamic structure factor (DSF) $S(Q,\omega)$ has been defined:

$$S(Q,\omega) = \frac{1}{2\pi\hbar} \sum_{j,j'=1}^{N} b_j b_{j'}^* \int dt \, \langle e^{-iQ.R_{j'}(0)} e^{iQ.R_j(t)} \rangle \, e^{-i\omega t}. \tag{3.24}$$

Since scattering in an experiment is a statistical process that involves a large number of scattering events, ensemble averaging of all scattering events is necessary. This results in the distinction of two different types of scattering. In the case of *coherent scattering*, phase information of the neutron wave function is maintained during the scattering event, in the case of *incoherent scattering* this phase information is lost:

$$S_{coh}(Q,\omega) = \frac{1}{2\pi\hbar} \sum_{j,j'=1}^{N} \overline{b_j b_{j'}^*} \int dt \, \langle e^{-iQ.R_{j'}(0)} e^{iQ.R_j(t)} \rangle \, e^{-i\omega t} \tag{3.25}$$

$$S_{inc}(Q,\omega) = \frac{1}{2\pi\hbar} \sum_{j=1}^{N} (\overline{b_j^2} - \overline{b_j}^2) \int dt \, \langle e^{-iQ.R_j(0)} e^{iQ.R_j(t)} \rangle \, e^{-i\omega t} \tag{3.26}$$

where the coherent DSF is determined by averaging over the scattering lengths b_j, while the incoherent DSF corresponds to the statistical variance of the scattering lengths.

Correlation Functions in Nuclear Scattering

The DSF forms a Fourier pair with two functions. A Fourier transformation of (3.24) between time and energy space yields the intermediate scattering function (ISF):

$$I(Q,t) = \frac{1}{N}\sum_{jj'} \langle \exp\{-\mathrm{i}Q.R_{j'}(0)\} \exp\{\mathrm{i}Q.R_{j'}(t)\}\rangle \,. \tag{3.27}$$

A further Fourier transformation of the ISF between real and momentum space yields the Van Hove correlation function (VCF):

$$G(r,t) = \frac{1}{N}\sum_{jj'} \langle \exp\{-\mathrm{i}Q.R_{j'}(0)\} \exp\{\mathrm{i}Q.R_{j'}(t)\}\rangle \,. \tag{3.28}$$

It expresses time-dependent pair-correlations between scatters. The Fourier relations are depicted in Fig. 3.3. In analogy to the DSF, these functions are also constituted by a coherent and an incoherent part. Looking again at the Fourier relations and at the definition of the DSF (Eq. (3.24)), it becomes evident that dynamical neutron scattering measures the Fourier transform of the time evolution of pair-correlations, or in the case of incoherent scattering, of self-correlations of particles. This relation between the scattering cross section and the positional correlation over time is of paramount importance for studying molecular diffusion.

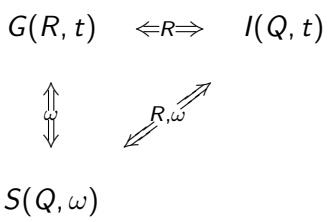

Figure 3.3: Diagram that illustrates the Fourier relations between $S(Q,\omega)$, $G(R,t)$, and $I(Q,t)$. Double arrows stand for Fourier transformation with respect to the noted vector space.

Scattering Length and Nuclear Spin Scattering

As we have seen in Eq. (3.20), the form factor in neutron scattering is expressed via the scattering length b, which is independent of Q. However, b is highly dependent of the isotope, from which the neutron scatters. This gives rise to incoherent scattering from a material that consists of different isotopes. For a given element with an isotopic composition, a coherent and incoherent scattering cross section σ can thus be defined. Tab. 3.2 lists the experimental values for the coherent and incoherent scattering cross section for the case of hydrogen (H), deuterium (D) and carbon (C), together with the absorption cross section. Evidently, H exhibits a very high incoherent scattering cross section while scattering from D and from C is mainly coherent.

	Z	σ_{coh} [barn]	σ_{inc} [barn]	σ_{abs} [barn]
^{1}H	1	1.8	80.2	0.3
(D) ^{2}H	1	5.6	2.0	0.0005
C	6	5.6	0.001	0.003

Table 3.2: List of the neutron scattering cross sections of the element carbon (C) and the hydrogen isotopes (H) and (D). Z: atomic number; σ_{coh}: coherent cross section; σ_{inc}: incoherent cross section; σ_{abs}: absorption cross section (1 barn = 10^{-10} m^2).

The existence of incoherent scattering from a single isotope stems from spin scattering. Since the neutron is a spin $\frac{1}{2}$ particle, during scattering from a nucleus with spin I the interacting system has a combined spin $I \pm \frac{1}{2}$. These two processes have different scattering lengths b, which gives rise to coherent and incoherent scattering, even for a single isotope. The probability with which a neutron scatters to a certain combined spin state can be calculated by comparing the total number of states associated with that spin state. For scattering from a single isotope with nuclear spin I, there are two combined states. The number of states with spin $I + \frac{1}{2}$ are:

$$2(I + \frac{1}{2}) + 1 = 2I + 2, \tag{3.29}$$

and the states associated with spin $I - \frac{1}{2}$:

$$2(I - \frac{1}{2}) + 1 = 2I. \tag{3.30}$$

Isotope	Combined spin	b [fm]
^{1}H	1	10.85
^{1}H	0	-47.50
^{2}H	$\frac{3}{2}$	9.53
^{2}H	$\frac{1}{2}$	0.98

Table 3.3: Scattering lengths b for combined spin states of a neutron with hydrogen isotopes (from [17]).

The relative frequencies for these states to occur are thus obtained by dividing through the total number of possible states $4I + 2$:

$$f_+ = \frac{2I+2}{4I+2} = \frac{I+1}{2I+1} \tag{3.31}$$

$$f_- = \frac{2I}{4I+2} = \frac{I}{2I+1}. \tag{3.32}$$

The coherent and incoherent neutron scattering cross sections are proportional to the mean square and the statistical variance of the scattering lengths b_+ and b_-, respectively:

$$\sigma_{coh} = 4\pi\bar{b}^2 = 4\pi[\sum_{i=+,-} f_i b_i]^2 = 4\pi[f_+ b_+ + f_- b_-]^2 \tag{3.33}$$

$$\sigma_{inc} = 4\pi\left(\bar{b^2} - \bar{b}^2\right) = 4\pi\left(\sum_{i=+,-} f_i b_i^2 - [\sum_{i=+,-} f_i b_i]^2\right). \tag{3.34}$$

The hydrogen atom exhibits a large negative scattering length b for a combined spin of zero (Tab. 3.3). This gives rise to an extremely high incoherent scattering cross section, as listed in Tab. 3.2. Deuterium, on the other hand, exhibits a larger coherent scattering cross section. Deuteration of samples is therefore a common technique in situations, where the large incoherent cross section of hydrogen would pose a problem.

3.2.2 Elastic Neutron Scattering – Diffraction

In neutron diffraction, the angular distribution of neutrons that scatter from a sample is measured. In a periodic structure, coherent diffraction occurs under the Bragg

condition

$$n\lambda = 2d \sin\theta, \tag{3.35}$$

where n is an integer number, d is the distance between repeating elements in the structure, and θ is the scattering angle. From the angular distribution of the scattering signal, information of the *structure* of a system can thus be retrieved. The Bragg law is equal to the condition that the vectorial transfer Q between initial and final neutron momentum equals a vector τ that connects two lattice elements in reciprocal space $Q = k - k' = \tau$ [17]. In a typical neutron scattering experiment, where a detector bank counts scattered neutrons over a range of angles, a periodic structure will thus scatter neutrons only into certain angles, namely the direction of the outgoing scattering vector. The scattering angle is therefore directly related to the occurrence of a periodic structure, and a determination of a whole angular spectrum permits e.g., the reconstruction of the positions of atoms in a material. In a single crystal, Bragg diffraction creates scattering peaks in certain well-defined solid angles. It happens that the sample consists of a powder of small, randomly oriented crystal lattices. In this case, the outgoing wave-vector k' lies on the so-called *Debye-Scherrer cone*. Only the information about the absolute value $|\tau|$ can be extracted in this case.

The Neutron Diffractometer D20

In this thesis, I present the analysis of data obtained from the two-axis neutron spectrometer D20 at ILL. Fig. 3.4 shows an illustration of the instrument. The neutron beam first passes a collimator that strips off diverging parts of the beam. Monochromatisation is then achieved by (002) Bragg reflection from a highly ordered pyrolytic graphite (HOPG) or a Cu crystal. After a second collimation stage, the beam scatters from the sample into a detector bank consisting of 48 detector plates, each containing 32 cells. Each cell spans 0.1°, the entire detector spans an angular range of 160°.

The sample, an exfoliated graphite named Papyex, exhibits random orientation of graphite crystal planes in two dimensions and a finite angular spread in the third dimension. The obtained angular spectra correspond highly to a powder diffraction spectrum. The experiment and the results are discussed in detail in Chap. 6.

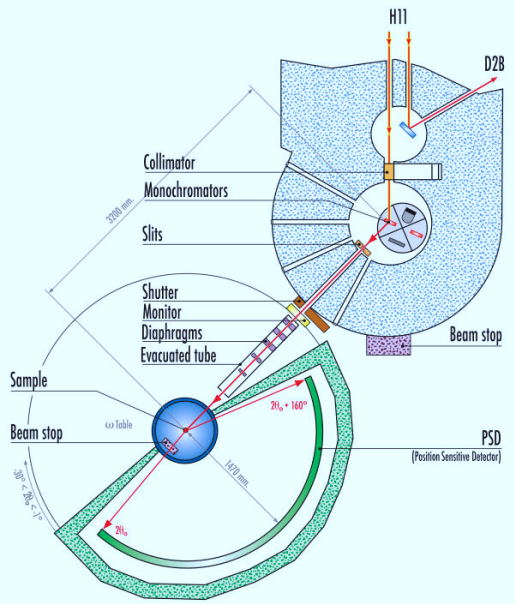

Figure 3.4: Illustration of the neutron diffractometer D20 at ILL. From [20].

3.2.3 Inelastic Neutron Scattering - Time-of-Flight Spectroscopy

Time-of-Flight (TOF) spectrometers measure velocity changes upon scattering from a sample of a pulsed, monochromatic neutron beam. Monochromatisation is necessary in order to know the incoming neutron velocity v_i. Pulsation of the beam, which is achieved either by a pulsed neutron source, or by a beam chopper, allows calculation of the outgoing neutron velocity v_f from the time of arrival at the detector. From this, the energy transfer ω and momentum transfer Q of the neutron can be calculated [19]. By normalizing the signal distribution in ω and Q with an instrumental resolution function, usually obtained from a measurement of an incoherent scatterer, the DSF $S(Q, \omega)$ can be retrieved. Here, we will briefly introduce the TOF spectrometers, at which we have performed measurements which contribute to this thesis.

The Neutron Time-of-Flight Spectrometer IN6

IN6 is a TOF spectrometer at ILL that operates with a continuous white beam of cold neutrons. Monochromatisation is achieved by three composite graphite monochromators that select only neutrons of a defined wavelength in the range 4.1 – 5.9 Å via Bragg diffraction [21] (details in Sec. 8.2.3). The beam is then cut into pulses by a

chopper and collimated before scattering from the sample. A large panel of detectors is placed in an array that spans about 120°, enabling measurement of a huge momentum transfer range at once. This kind of instrument is referred to as a direct geometry spectrometer, since monochromatisation and chopping take place before the beam scatters from the sample. Fig. 3.5 shows an illustration of the instrument.

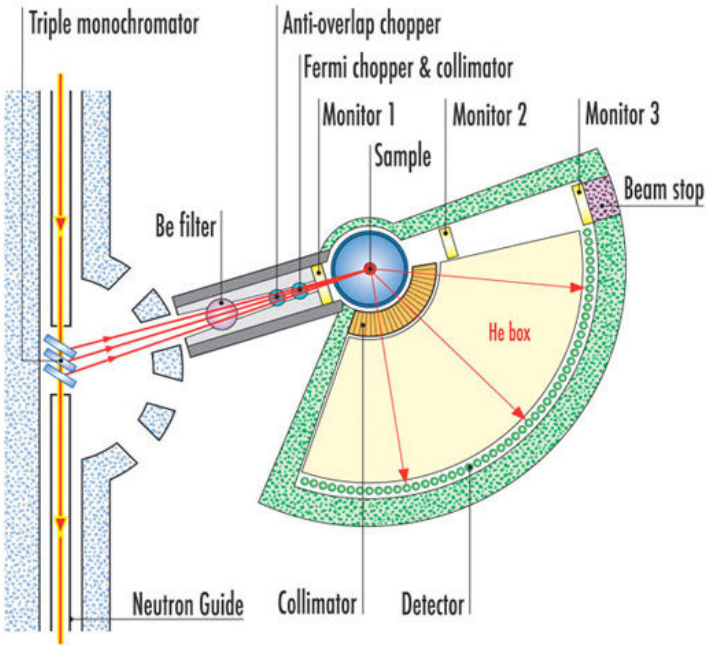

Figure 3.5: Schematic drawing of the instrument IN6 at ILL. From [20].

The Neutron Backscattering Spectrometer OSIRIS

OSIRIS is a backscattering spectrometer at ISIS that makes use of the TOF principle. Since it is operated at a pulsed source of cold neutrons, it does not require a priori beam chopping. There is, however, a set of choppers for selecting a wavelength window. Monochromatisation is achieved by Bragg reflection from a graphite analyser bank that spans 170°. The selected wavelength is reflected back towards a detector assembly that is situated beneath the sample. Since the beam is monochromatised after scattering from the sample, OSIRIS is classified as an inverted geometry spectrometer. The large analyser bank allows scattering over a large Q-range (details in Sec. 9.2.3). Fig. 3.6 shows an illustration of OSIRIS. The energy resolution obtainable with OSIRIS is twice as high as the highest resolution of IN6.

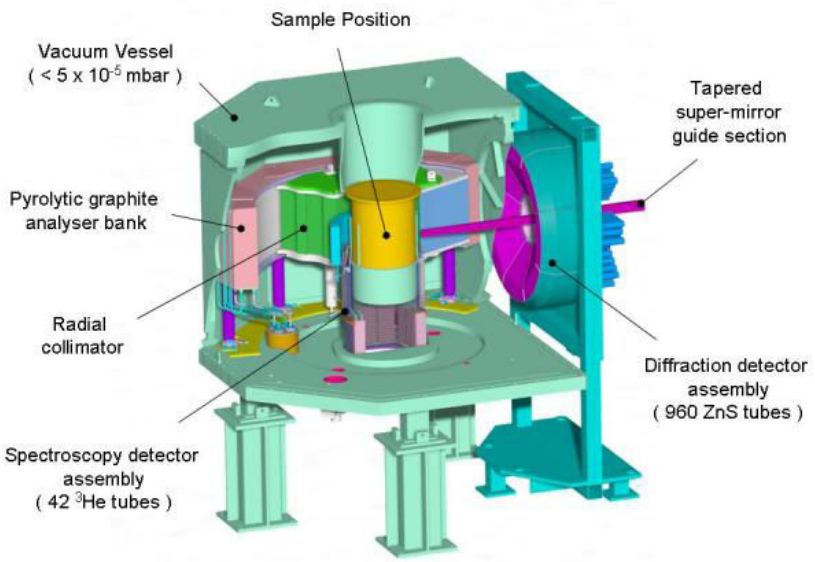

Figure 3.6: Schematic drawing of the instrument OSIRIS at ISIS. From [22]

3.2.4 Neutron Spin-Echo Spectroscopy

The drawback of the above described conventional TOF techniques is the huge loss in neutrons due to the choppers and monochromatisers, or more general, the necessary compromise between flux and energy or momentum resolution which stems from the equal distribution of the neutrons in their available phase space as predicted by the fundamental Liouville theorem. A closer look at the neutron phase space in a TOF experiment reveals that it spreads over the six dimensions of the independently measured variables v_i and v_f. However, only four variables, namely ω and the three components of Q, are being used to interpret the acquired data. This exhibits the reason for the high loss in neutrons, as two dimensions of the phase space have to be "cut out" and it also lets the question for a possible different measurement technique arise. Since no technique is known that measures in a global manner directly the variables of interest Q and ω, we demand this condition to be satisfied at least locally, i.e. we are looking for a measurement that is locally a function of Q and ω:

$$\delta\varphi = \boldsymbol{\alpha}\delta Q + \beta\delta\,\omega, \tag{3.36}$$

where $\boldsymbol{\alpha}$ and β are constants. Q and ω are connected to v_i and v_f via: :

$$\hbar Q = m(v_f - v_i) \tag{3.37}$$

$$\hbar\omega = \frac{m}{2}(v_f^2 - v_i^2), \tag{3.38}$$

therefore the measurement would need to determine the vectorial and the squared change in neutron velocity independently of the velocity of the incoming neutron.

Allowing for a velocity spread means that even if an initial beam chopping was used, neutrons would be continuously detected. A change in velocity therefore has to be measured using an internal "clock" of the neutron. In the energy range discussed here, the only internal degree of freedom of the neutron is its spin and the only way for it to evolve with time is by Larmor precession in a magnetic field. In order for a velocity change of the neutron while scattering at a sample to be registered by Larmor precession, magnetic fields have to act on the neutron before and after scattering in such a way that equation (3.36) is satisfied. The straightforward way is to identify φ as the Larmor precession angle, it will later become evident that this is justified. It follows directly that β has the dimension of time; it is referred to as the spin-echo (SE) time or Fourier time t.

Larmor precession describes the precession of the magnetic moment of a particle in an external magnetic field. The classical spin vector S experiences a torque that acts perpendicularly on the magnetic field H and on S. If a polarised neutron (i.e. with a measured spin) travels through a magnetic field H over a distance l, it will precess by an angle φ:

$$\varphi = \gamma\frac{Hl}{v}, \tag{3.39}$$

with the neutron velocity v and γ the gyro-magnetic ratio γ = -1.8324·$10^8 \mathrm{s}^{-1}\,\mathrm{T}^{-1}$.

Polarisation analysis selects only one component of the neutron polarisation. With respect to the initial direction x, this selects the component P_x:

$$P_x = \langle\cos\varphi\rangle = \int f(v)\cos(\frac{\gamma Hl}{v})\,\mathrm{d}v, \tag{3.40}$$

where the average has been taken over the neutron velocities v with distribution

$f(v)$. This is effectively the Fourier transform of the distribution function for the inverse velocity $\frac{1}{v}$ since $f(v)\,\mathrm{d}v = f(v)v^2\,\mathrm{d}\frac{1}{v} = f(\frac{1}{v})'\,\mathrm{d}\frac{1}{v}$. With $\lambda = \frac{h}{mv}$ it becomes evident that this is the wavelength spectrum [23]. When the neutron beam travels through the field by an increasing length l, more and more polarisation is lost due to a finite wavelength distribution (A to B in Fig. 3.7).

The Spin-Echo Principle

In order to recover the information that seems to be lost in the dephased neutron wave, the precession process has to be inversed by passing the neutron beam through a second magnetic field H_1 that is opposite to H_0 after scattering. The effective precession angle for a given velocity v is then:

$$\varphi = \varphi_{AB} - \varphi_{BC} = \gamma(H_0 l_0 - H_1 l_1)/v, \tag{3.41}$$

where the distances AB and BC are indicated in reference to Fig. 3.7. When the field integrals are exactly of opposite and equal strength, i.e. $H_0 l_0 = H_1 l_1$, the precession is exactly reversed independently of the velocity (B to C in Fig. 3.7). The dephasing is therefore reversed and a spin echo is obtained. In the region close to this "spin-echo point", polarisation is partly recovered, this is the so-called spin-echo group. As pointed out before, it is the Fourier transform of the inverse velocity distribution. The average velocity v defines the oscillation frequency, while the spread of the v distribution determines how fast the spin-echo group decays when moving away from the spin-echo point.

Our aim is to measure interaction of the neutron beam with a sample. The only reasonable configuration would be to let the beam scatter from a sample between the two precession fields (point B in Fig. 3.7). Inelastic scattering changes the neutron velocity from v_0 to v_1 resulting in a precession angle:

$$\varphi = \gamma \left[\frac{l_0 H_0}{v_0} - \frac{l_1 H_1}{v_1} \right]. \tag{3.42}$$

As pointed out before, the goal is to find a measurement that depends locally only on the velocity change, not on the absolute velocities. For an average incoming neutron velocity $\bar{v}_0$ and a given energy transfer $\hbar\omega_0$, the average outgoing neutron

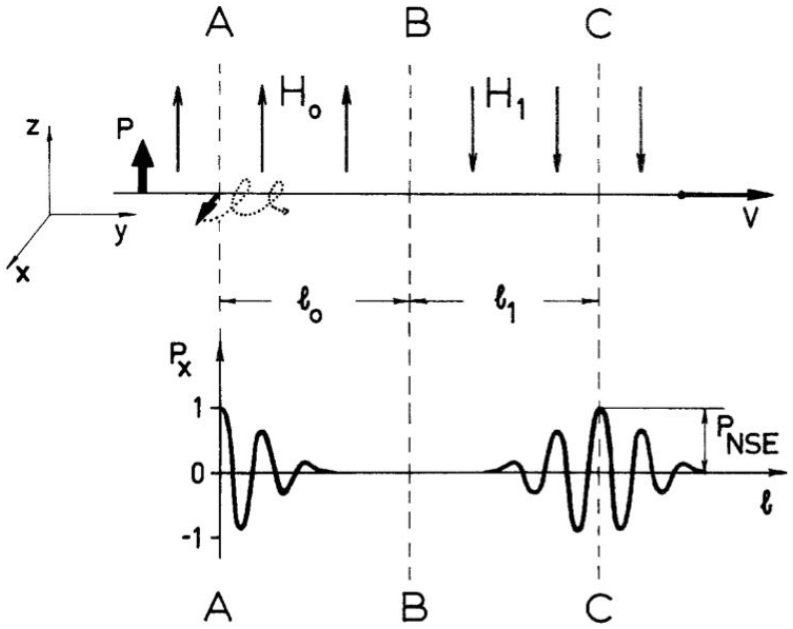

Figure 3.7: Basic illustration of dephasing of the neutron spin through Larmor precession and spin echo from [23]. A precession field H_0 between A and B causes dephasing. After passing through an inverse but equal precession field H_1, a spin echo is obtained around point C.

velocity $\bar{v}_1$ is defined by equation (3.38). We require equation (3.36) to be fulfilled locally, i.e.:

$$\varphi - \bar{\varphi} = t(\omega - \omega_0), \tag{3.43}$$

with $\bar{\varphi} = \varphi(\bar{v}_0, \bar{v}_1)$ and t being a constant. Small variations in the neutron velocity cause a variation in φ:

$$\varphi - \bar{\varphi} = \gamma \left[-\frac{l_0 H_0}{\bar{v}_0^2} \delta v_0 + \frac{l_1 H_1}{\bar{v}_1^2} \delta v_1 \right], \tag{3.44}$$

with variations in velocity $\delta v_i = v_i - \bar{v}_i$. For the energy change this small variation yields:

$$\omega - \omega_0 = \frac{m}{\hbar} \bar{v}_1 \delta v_1 - \frac{m}{\hbar} \bar{v}_0 \delta v_0 \tag{3.45}$$

Combining these two equations yields, independently for $v_i = v_0, v_1$:

$$\gamma l_i \frac{H_i}{\bar{v}_i^2} = t \frac{m}{\hbar} \bar{v}_i. \tag{3.46}$$

This gives the necessary magnetic fields H_0, H_1 to perform a measurement at the Fourier time t.

It is important to note that the spin echo condition can generally be fulfilled for any energy change ω_0, not just for the elastic case. Required is simply an appropriate tuning of the magnetic field.

Combining equation (3.40) and equation (3.43) yields:

$$P_{NSE} = P_S \langle \cos(\varphi - \bar{\varphi}) \rangle = P_S \frac{\int S(Q,\omega) \cos[t(\omega - \omega_0)] \, \mathrm{d}\omega}{\int S(Q,\omega) \, \mathrm{d}\omega}, \tag{3.47}$$

where the integral is now running over ω instead of the velocity v and therefore $f(v)$, the probability that a neutron has a velocity v has become a function of the energy transfer $f(\omega)$. It describes the probability that (for a given Q) a neutron scatters with an energy change ω. It is thus nothing else but the scattering function $S(Q,\omega)$. P_S accounts for scattering events that change the neutron polarisation such as spin or magnetic scattering. For the moment we assume $P_S = 1$. The spin-echo Signal P_{NSE} is thus the cosine Fourier transform of the scattering function. This is the real part of the ISF, $\Re I(Q,t)$. This identity holds only for a restricted range since the locality condition of small velocity changes requires a certain monochromatisation of the incoming neutron beam. In general, a velocity distribution of $\mathrm{d}v/v = 15\,\%$ is sufficient for most spectrometers. Since $S(Q,\omega)$ is the double Fourier transform of the particle correlation function $S(R,t)$ and the Fourier transform in time of the measured polarisation $I(Q, t_{NSE})$, the Fourier time can be identified as real, physical time.

The Spin-Echo Spectrometer IN11

Here, we will describe the technical application of the spin-echo principle using the NSE spectrometer IN11 at ILL as an example. The instrumental layout is illustrated in Fig. 3.8. The numbers correspond to the different parts of the instrument, which play a role for the measurement.

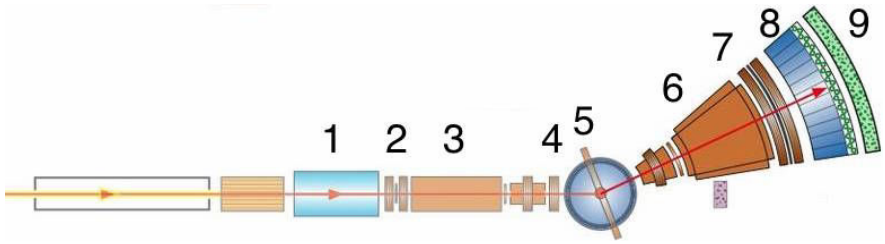

Figure 3.8: Schematic drawing of the instrument IN11 at ILL. The neutron beam is depicted by a red arrow. The numbers highlight parts of the instrument that are explained in the text. From [20].

1. **Polarisation**: Reflections from supermirrors polarise the neutron beam parallel to a magnetic guide field with 99 % efficiency. A guide field is maintained through the whole trajectory of the neutron, to "shield" it from magnetic perturbations like the Earth's magnetic field that would otherwise change the polarisation and thus destroy the information that is encoded in it.

2. $\pi/2$ **Flip #1**: A thin, flat coil placed perpendicular to the beam causes a Larmor precession of $\pi/2$ (or 90 degrees), turning the neutron spin perpendicular to the guide field. This "switches on" the Larmor precession of the neutron.

3. **Larmor Precession #1**: A first main solenoid creates a tunable magnetic field H. A neutron travelling through the solenoid with a velocity v will experience a precession through an angle $\phi = \gamma H l / v_i$. The initial velocity v_i is therefore encoded in the polarisation phase ϕ.

4. **Scattering From the Sample**: The neutron scatters from the sample with a momentum transfer $\hbar Q = m v_i - m v_f$ and energy transfer $\hbar\omega \approx m v_i (v_i - v_f)$. The sample is usually embedded in a sample environment, a so-called "orange" ILL cryostat or cryo-furnace that allows controlled cooling and heating of the sample [20].

5. π **Flip**: Similar to the $\pi/2$ flipper, this small flat coil causes a precession by π (or 180 degrees) of the spin in a direction perpendicular to the precession plane. This adds a phase of π to only one component of the precession, having the effect that the phase angle ϕ is inverted.

6. **Larmor Precession #2**: A second main solenoid with a comparable field strength causes a precession ϕ'. Since the initial precession angle ϕ has been

inverted by the π flipper, the total precession angle after the second field consists of the difference:

$$\phi - \phi' = \gamma HI/v_i - \gamma HI/v_f \approx \gamma HI \frac{v_i - v_f}{v_i^2} \approx \frac{\gamma HI}{m v_i^3} \hbar\omega = t\omega, \tag{3.48}$$

where use has been made of the definition of the Fourier time t (Eq. (3.46)).

7. $\pi/2$ **Flip #2**: A second $\pi/2$ flipper turns a component of the polarisation parallel to the guide field, the precession is stopped.

8. **Polarisation Analysis**: A polarisation analyser (supermirror or ^{3}He analyser) projects the spin on the parallel axis.

9. **Detection**: In an array, 41 ^{3}He detectors are distributed over an angle of 30°. This array allows to collect data simultaneously for different Q.

In practice, to account for instrumental effects, the spectrometer is calibrated by performing a measurement on a sample that produces only elastic, spin-coherent and isotope-incoherent scattering. Any deviations in this measurement stem from finite polarisation efficiency and dephasing effects in the magnetic fields. Since the overall function is the product of this resolution function with the "clean" ISF, one simply has to divide the measured polarisation by this resolution measurement to recover the response to the physics in the system.

3.2.5 Neutron Scattering Signatures of Diffusion

QENS spectroscopy is a powerful tool for the investigation of surface diffusion. In contrast to inelastic scattering from excitations, the energy transfer of a neutron that scatters from a diffusing molecule is small (in the order of μeV to a few meV), originating from typical time-scales of diffusion in the order of picoseconds. In a spectroscopy experiment, this causes a quasi-elastic broadening of the elastic line [19]. Many different models exist for the various kinds of diffusion, we will present here, in brief, a summary of those diffusion models, which are relevant to this thesis. Most of these diffusion models express the *self-diffusion* of a particle, in contrast to chemical transport-diffusion, which assumes a concentration gradient. The connection between the motion of a diffusing particle and the neutron measurement lies in the Van Hoove self-correlation function $G_{inc}(R, t)$. It expresses on the one hand in the

classical approximation the probability of finding a particle at a time t displaced by r, given it is at the (arbitrary) origin at $t = 0$. On the other hand, it is connected via Fourier transformation to the *incoherent* scattering cross section (see Fig. 3.3 and Eq. 3.23). For comparison, *coherent* scattering is connected in the same way to the cross-correlation function $G_{coh}(R, t)$, which expresses the probability of finding a particle at a position r at time t, given that *any* particle is found at the origin at time $t = 0$. It expresses thus a relaxation of the structural configuration of particles [19].

Brownian Motion and Anomalous Diffusion

A common type of molecular diffusion on surfaces is the Einstein diffusion caused by Brownian motion [24, 19]. In this model, point-like particles perform random walks on the surface by moving freely along straight lines between singular collisions. This system is described by a second order differential equation named Fick's law:

$$\tau \frac{\partial G_s(r,t)}{\partial t} = \frac{\langle l^2(\tau)\rangle}{6} \nabla^2 G_s(r,t). \tag{3.49}$$

If subsequent steps are uncorrelated (no memory), then Eq. (3.49) yields a simple solution, the diffusion constant D:

$$D = \frac{\langle l^2\rangle}{4\tau} = \frac{k_B T}{m\eta}, \tag{3.50}$$

where m is the particles mass, k_B is the Boltzmann constant and η is the kinetic friction. The factor 1/4 holds for two-dimensional diffusion and would be replaced by 1/6 in the 3D case. The latter equation is referred to as Einstein's equation of diffusion.

Modern microscopical and spectroscopy techniques have made it possible to study adparticle diffusion at its proper length scale, i.e. the angstrom range. The momentum transfer Q is the conjugate variable of the vector R of the displacement of an adparticle, and thus a neutron scattering response at a certain Q corresponds to the observation of a certain conjugate length scale R. Depending on the system, the momentum transfer Q may be smaller or bigger than the value that corresponds to the mean free path l of a diffusing adparticle. In the range of Q that corresponds to distances that are larger than the mean free path of a diffusing particle, and the

macroscopic observation of Eq. (3.50) that D is a constant, holds. Eq. (3.49) can be solved and a Fourier transformation yields the ISF:

$$I(Q,t) = \exp(-DQ^2|t|). \tag{3.51}$$

For higher values of Q, collision free motion of the adparticle is observed. Diffusion in this length scale is in general described by super-diffusion, i.e. diffusion with a faster than linear increase of the mean square displacement with time. The special case of a free flight gives rise to a quadratic time dependence and is referred to as ballistic diffusion [25]:

$$\langle l^2 \rangle = \frac{k_B T}{2m} \tau^2, \tag{3.52}$$

where m is the mass of the diffusing particle. Neutron scattering from ballistically diffusing particles gives rise to a QENS broadening that follows a Gaussian distribution [17]:

$$I(Q,t) = \exp[-\frac{1}{2} Q^2 \frac{2k_B T}{m} t^2]. \tag{3.53}$$

If the character of the diffusive motion is not ad hoc known, a more general model exists, that contains a shape parameter $\chi(Q) = \sqrt{\langle v^2 \rangle} Q/\eta_T$ [26, 27]. The mean square velocity $\langle v^2 \rangle$ is determined by the system temperature via Maxwell-Boltzmann statistics. Depending on the friction parameter η_T, the incoherent DSF varies its shape continuously between a Lorentzian shape in the case of purely Brownian diffusion to a Gaussian shape in the case of a "ideal 2D gas" of freely moving adparticles. This is achieved by developing the incoherent DSF as a series of Lorentzian distributions [28]:

$$S(Q,\omega) = e^{\chi^2(Q)} \sum_{n=0}^{\infty} \frac{[-\chi^2(Q)]^n}{\pi n!} \frac{[n+\chi^2(Q)]\eta_T}{[n+\chi^2(Q)]^2 + (\hbar\omega)^2}. \tag{3.54}$$

The QENS broadening gives, depending on a dimensionless parameter ν, the half width at half maximum (HWHM) of a Lorentzian distribution ($\nu = 1$) or that of a Gaussian distribution ($\nu = 0$).

$$\Gamma(Q) = \hbar[\nu\eta_T\chi^2(Q) + (1-\nu)\sqrt{2\ln 2}\eta_T\chi(Q)] \tag{3.55}$$

The Rough Hard Disc Model

It has been shown that for the case of a non-negligible exchange of angular momentum between two molecules during collision, this exchange has to be taken into account because the kinetic friction is in this case substantially increased. This led to the development of a model of colliding rough hard spheres by Chandler [29, 30, 31]. Based on this model, we developed a corresponding two dimensional model of colliding disks, the RHD model [32]. This model yields a collisional friction parameter η_{coll}:

$$\eta_{coll}(\theta, T) = \frac{3\kappa + 2}{2\kappa + 2} \frac{d g_d(d+) \theta}{A} \sqrt{2\pi} \sqrt{\frac{k_B T}{\mu}}, \tag{3.56}$$

where $\kappa = 2I/\mu d^2$ is a dimensionless indication for the distribution of mass in a colliding sphere with $0 \leq \kappa \leq 1$. d is the colliding disk diameter, it corresponds to the distance between the centre of mass (CoM) of two colliding disks at the moment of impact and $g_d(d+)$ corresponds to the radial distribution function evaluated at d. This accounts for the apparent number density from the disks view and the resulting collision probability. A corresponds to the surface area that is occupied by a single adparticle at monolayer coverage and θ is the relative surface coverage in ML. The derivation of Eq. (3.56) is developed in the Appendix of [32].

Activated Jump Diffusion

For the case that the adparticle motion is governed by the interaction of the particle with a strongly corrugated surface, its motion can be well described by the Chudley-Elliott (CE) model of jump diffusion [33, 19]. It assumes that a particle rests adsorbed for a time τ at an adsorption site, before it moves instantaneously to another adsorption site. In the most simple case, motion happens on a Bravais lattice. The system can then be described by a rate equation:

$$\frac{\partial}{\partial t} P(r, t) = \frac{1}{n\tau} \sum_{l_i} \left[P(r + l_i, t) - P(r, t) \right], \tag{3.57}$$

with the probability $P(r, t)$ of finding an adparticle at a position r at a time t and the probability $P(r + l_i, t)$ of finding it at $r + l_i$, where l_i is the jump vector, which

connects the initial with the final position of a jump. $P(r,t)$ is identical to the self correlation function, $G_{inc}(r,t) = P(r,t)$. The differential rate equation can be solved by Fourier transformation, where the Fourier transform of $G_{inc}(r,t)$ is identified with the incoherent ISF $I_{inc}(Q,t)$:

$$\frac{\partial}{\partial t} I_{inc}(Q,t) = \frac{1}{n\tau} \sum_{l_i} I_{inc}(Q,t)[e^{-iQ.l_i} - 1]. \tag{3.58}$$

The solution is then given by an exponentially decaying ISF:

$$I_{inc}(Q,t) = I_{inc}(Q,0)e^{-\Delta\omega(Q)t}, \tag{3.59}$$

where the exponential decay rate $\Delta\omega(Q)$ has been defined as:

$$\Delta\omega(Q) = \frac{1}{n\tau}\sum_{l_i}[1 - e^{-iQ.l_i}] = \frac{1}{n\tau}[n - 2\sum_{l_i>0}\cos(Q.l_i)] = \frac{4}{n\tau}\sum_{l_i>0}\sin^2(\frac{Q.l_i}{2}), \tag{3.60}$$

where use has been made of the fact that forward and backward jumps are equivalent. This result relates the diffusion to the neutron scattering signal measured in an experiment. In a spin-echo experiment, where the ISF is measured via the beam polarisation, a single exponential decay is observed. In a TOF experiment, the measurement in energy space yields its Fourier transform. The DSF thus becomes a Lorentzian function:

$$S(Q,\omega) = \frac{1}{\pi}\frac{\Delta\omega(Q)}{\Delta\omega(Q)^2 + \omega^2}. \tag{3.61}$$

In the case that hopping occurs on a non-Bravais lattice, more complex models have to take into account energetical and geometrical site inequivalences [34, 35]. An illustration of the possible jumps on the graphene/Ni(111) and on the Ni(111) lattice can be seen in Fig. 3.9. Jumps between **hollow** sites on graphene and **top** sites on Ni(111) are geometrically identical and form a Bravais lattice. Jumps between **top** sites on graphene and **hollow** sites on Ni(111) form two Bravais sub-lattices that may be energetically non-degenerate, giving rise to two different diffusion rates.

If the scattered sample is not a single crystal, isotropic angular averaging has to be performed since the scattered neutron signal "sees" the jumping adparticle from

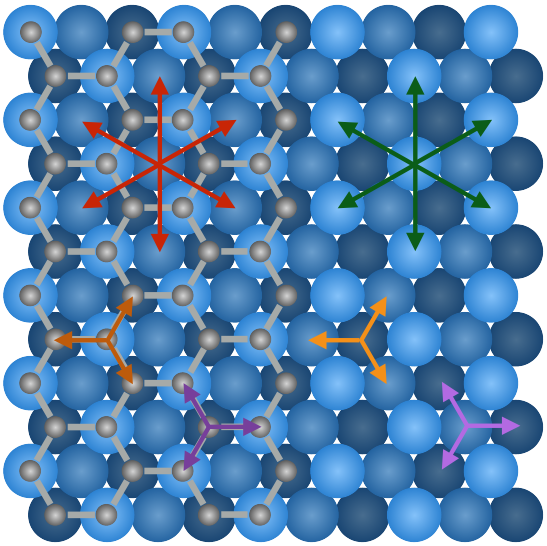

Figure 3.9: Illustration of possible jumps between adsorption sites on the (0001) basal plane of graphene/Ni(111). Red: **hollow–hollow** jumps on the graphene surface; Green: **top–top** jumps on Ni(111); Dark Orange and Purple: Two possibilities of **top–top** jumps on graphene; Light Orange and Purple: Two possibilities of **hollow–hollow** jumps on Ni(111).

all possible directions. A common approach to this averaging consists in angular averaging of Eq. (3.60). In the case of 3D isotropy, this integration yields [36, 34]:

$$\Delta\omega(Q) = \frac{1}{4\pi}\int \mathrm{d}\sin\theta\,\mathrm{d}\phi\frac{1}{\tau}[1 - e^{-\mathrm{i}Ql\sin\phi\sin\theta}] = \frac{1}{\tau}[1 - \frac{\sin Ql}{Ql}] = \frac{1}{\tau}[1 - J_{1/2}(Ql)], \quad (3.62)$$

where $J_{1/2}(Ql)$ is the zeroth order spherical Bessel function of the first kind. In the case of 2D isotropy, integration over ϕ yields:

$$\Delta\omega(Q) = \frac{1}{2\pi}\int \mathrm{d}\phi\frac{1}{\tau}[1 - e^{-\mathrm{i}Ql\sin\phi\sin\theta}] = \frac{1}{\tau}[1 - J_0(Ql\sin\theta)], \quad (3.63)$$

where $J_0(Ql\sin\theta)$ is the zeroth order cylindrical Bessel function. However, even in the early publications it has been pointed out that this approach is approximative in the sense that inserting the averaged $\Delta\omega(Q)$ into Eq. (3.61) assumes a single Lorentzian broadening, while the "correct" way to average directly Eq. (3.61) over all angles, results in general in a non-Lorentzian QENS broadening [36]. This calculation has to be performed numerically, such a calculation is discussed in detail in Sec. 9.3.

3.3 Helium Atom Scattering

3.3.1 Thermal Helium Atom Scattering Theory

Helium atoms with thermal kinetic energies are well suited for studying surfaces for several reasons (see Fig. 3.10 for a comparison of the spectral range of several surface science techniques): Thermal energy helium atoms have a wavelength that corresponds roughly to the normal inter-atomic spacing. Their low kinetic energy permits a highly non-destructive observation and allows a very high energy resolution which permits studying very slow processes. The helium atoms are chemically inert and uncharged and therefore interact with the surface only through electrostatic and Van der Waals interactions. This makes the helium atom an entirely surface sensitive particle.

He-Surface Interaction Potential

The interaction of a helium atom with the substrate is attractive at large distances due to dipole-dipole interactions (London dispersion force) that decay with the distance from the surface z by z^{-3} (see Fig. 3.11). At short distances, overlapping of the helium electron cloud with the substrate valence (or conduction) electrons causes a strong, short ranged repulsion [38]. Fig. 3.11 a) illustrates the different possibilities for the interaction of a helium atom with the surface. It may either scatter elastically (1), inelastically (2), undergo a selective adsorption process (3), or become trapped at the surface (4). The latter two processes do not play a role in this work and are only mentioned for completeness. The repulsive part of the interaction potential $V(R)$ can be approximated by the charge density $\rho(R)$ at the surface [39]:

$$V(R) \propto \rho(R). \tag{3.64}$$

In order to describe in a simplified way the refractive effect of the interaction potential on scattering dynamics, a laterally averaged surface potential is assumed [40]. The effect of an attractive surface potential of well-depth V on the incident energy E_i and incident momentum k_i of the helium atom is expressed by replacing E_i with

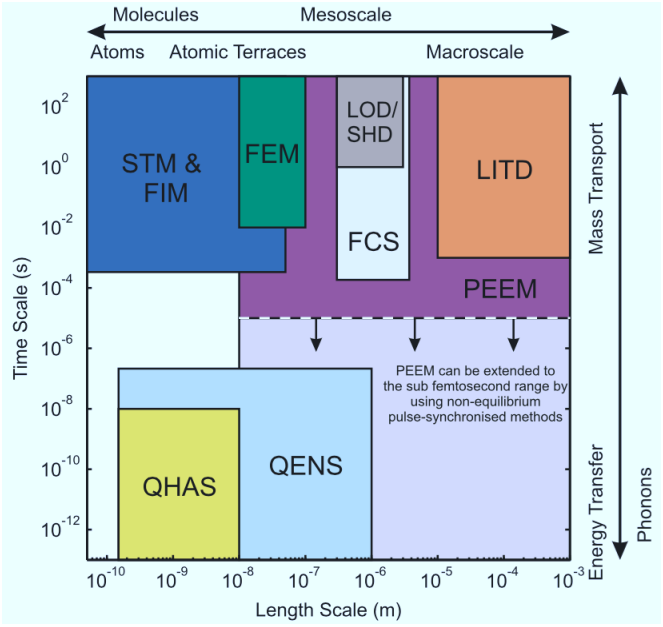

Figure 3.10: Comparative illustration of a selection of different techniques for measuring surface dynamics with regard to length and time scales of the dynamic system: microscopic techniques are scanning tunnelling microscopy (STM), field emission microscopy (FEM), field ion microscopy (FIM) and photoemission electron microscopy (PEEM); optics based techniques are laser induced thermal desorption spectroscopy (LITD), fluorescence correlation spectroscopy (FCS), linear optical diffraction (LOD) and second-harmonic diffraction (SHD); scattering based techniques are Quasi-elastic helium atom scattering (QHAS) and neutron scattering (QENS). Figure from [37].

$E_i' = E_i + V$ [41] (this is the so-called Beeby correction). This implies for the perpendicular component of the incoming momentum $k_{i,\perp}$:

$$k_{i,\perp}' = \sqrt{k_{i,\perp}^2 + 2mV/\hbar}, \tag{3.65}$$

where m is the mass of the helium atom and $\hbar$ is the Planck constant. The corrected perpendicular momentum transfer $\Delta k_\perp' = k_{i,\perp}' - k_{f,\perp}'$ now reads:

$$\Delta k_\perp' = k_i \left[\sqrt{\cos^2\theta_i + \frac{V}{E_i}} + \sqrt{\cos^2\theta_f + \frac{V}{E_i}} \right], \tag{3.66}$$

with the incoming and outgoing angles θ_i and θ_f, respectively, relative to the surface normal. To adopt the common notation for helium scattering, the momentum transfer will be denoted by Δk in the chapters that discuss helium scattering studies, even if the physical meaning is the same as that of Q in neutron scattering.

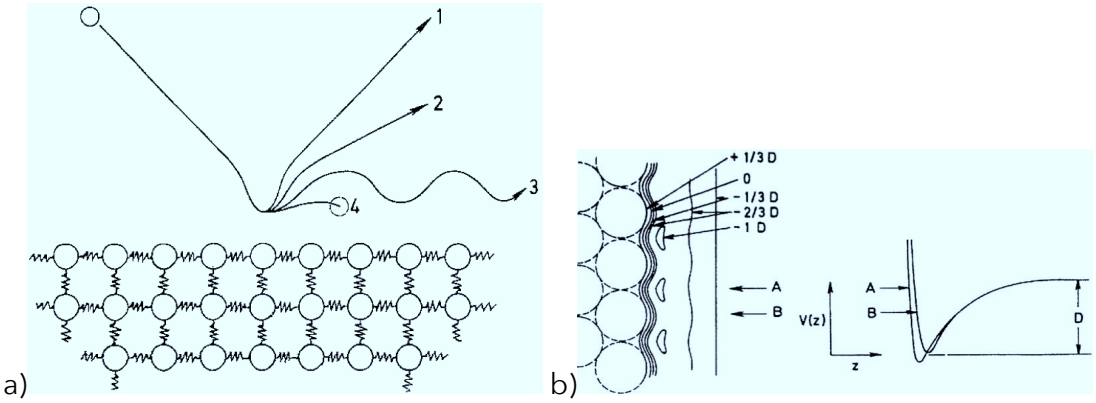

Figure 3.11: Illustration of a helium atom scattering from an ordered surface. a) Possible scattering processes. 1: elastic scattering; 2: inelastic scattering; 3: selective adsorption; 4: trapping. From [42]. b) Illustration of the equipotential lines of the helium-surface interaction and the potential well depth D as a function of the distance z to the surface at two positions A and B. From [43].

Assuming a rigid surface, scattering is purely elastic and occurs only under diffraction condition, resulting in distinct diffraction peaks. By far the brightest signal stems from 0th order diffraction, or specular reflection ($k_f = k_i$). However, a sample at a finite temperature is never fully rigid; atom vibrations in the lattice cause inelastic scattering of the He atom. This behaviour is in many cases well described by the Debye-Waller law [44]. A reduction of the elastic signal is referred to as *attenuation*; its observation is a common approach to study e.g. the adsorption of adparticles.

He-Adsorbate Interaction Potential

An isolated adparticle causes a large geometrical perturbation of the otherwise very flat interaction potential of the graphene substrate surface that we have used in this study. Attractive dispersion force between the He atom and the adparticle is felt even at relatively large distances, giving rise to diffuse scattering over a wide area [38] (illustrated in Fig. 3.12). This area is referred to as *giant scattering cross section*, it is usually denoted as Σ. Since an adparticle is not a flat object, scattering

at a finite angle increases the zone of influence even further, giving rise to a larger apparent scattering cross section. For scattering at an incoming angle θ_i with respect to the surface normal, the apparent scattering cross section Σ' is given in a rough approximation by [38]:

$$\Sigma' = \Sigma / \cos(\theta_i). \tag{3.67}$$

In our studies, we used an incoming angle of 22.2°, for which the above approximation is largely sufficient.

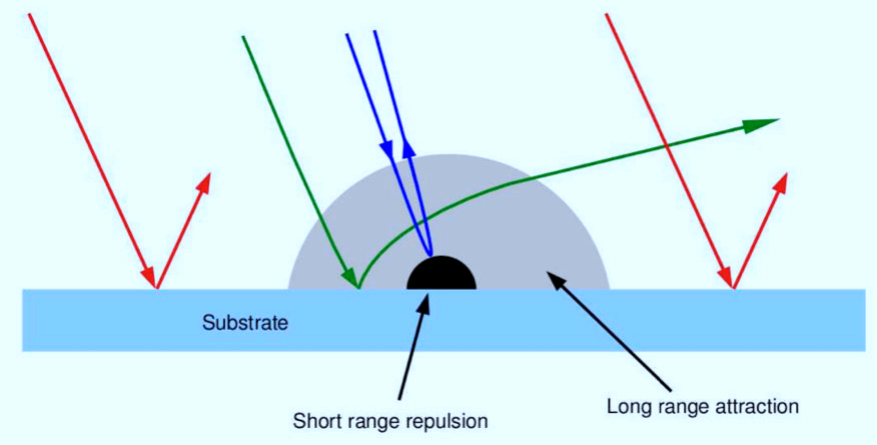

Figure 3.12: Illustration of the giant helium scattering cross section, caused by long range attractive forces. From [45].

Monitoring Adsorption with Specular Reflection

The high sensitivity to surface perturbations makes elastic helium scattering a very effective probe for the adsorption of adparticles. If, in a first approximation, we assume the adparticles as perfect diffusive scatterers that are randomly distributed over the surface (in contrast to attractive or repulsive rearrangement), an exponential decay of the specular reflected signal I is observed [38]:

$$I/I_0 = e^{-\theta \Sigma n_s}, \tag{3.68}$$

where θ is the relative surface coverage, Σ is the helium scattering cross section of the adparticle, and n_s is the surface area that an adparticle occupies at monolayer

coverage. The exponential law stems from the fact, that the probability of an incoming adparticle to encounter an already occupied part of the surface is proportional to the surface coverage.

For adsorption that happens exclusively on lattice sites of the substrate, a power law is observed instead [38]:

$$I/I_0 = (1 - \Theta)^{\Sigma n_s}. \tag{3.69}$$

In the case of strong repulsion between the adparticles, overlap of the scattering cross sections is minimised. Specular attenuation thus happens at a much faster rate for increasing coverage since each adparticle covers a maximum surface area. A faster-than-exponential decay of I is observed. In the case of strong attraction between adparticles, scattering cross section overlap, giving rise to a slower-than-exponential decay of i. For large enough islands, Σ approaches the area A that an adparticle occupies within the island, $\Sigma \to A$.

Quasi-Elastic Helium Scattering

Since the helium interaction potential is rather complex in contrast to the Fermi pseudo potential applied in neutron scattering, establishing a relation between the differential scattering cross section and particle correlation functions is not a simple proportionality. The scattered intensity $R(\Delta k, \omega)$ depends on the DSF $S(\Delta k, \boldsymbol{\omega})$ as well as on the form factor $F(\Delta k, \omega)$, represents the Fourier transform of the spatial density of an adparticle, as seen by the helium atom. The determination of $F(\Delta k, t)$ is in general quite complex, however in the case of scattering from a dilute phase of adparticles of a single type, the kinematic approximation can be made, which separates the form factor and the structure factor [46]:

$$\tilde{I}(\Delta k, \omega) = |F(\Delta k, \omega)|^2 \cdot S(\Delta k, \omega). \tag{3.70}$$

3.3.2 The Cavendish ^{3}He Spin-Echo Spectrometer

Detailed descriptions of the HeSE instrument have been published by P. Fouquet [47] and A. P. Jardine [13]. This subsection will only give a brief overview over the basic functioning of the instrument.

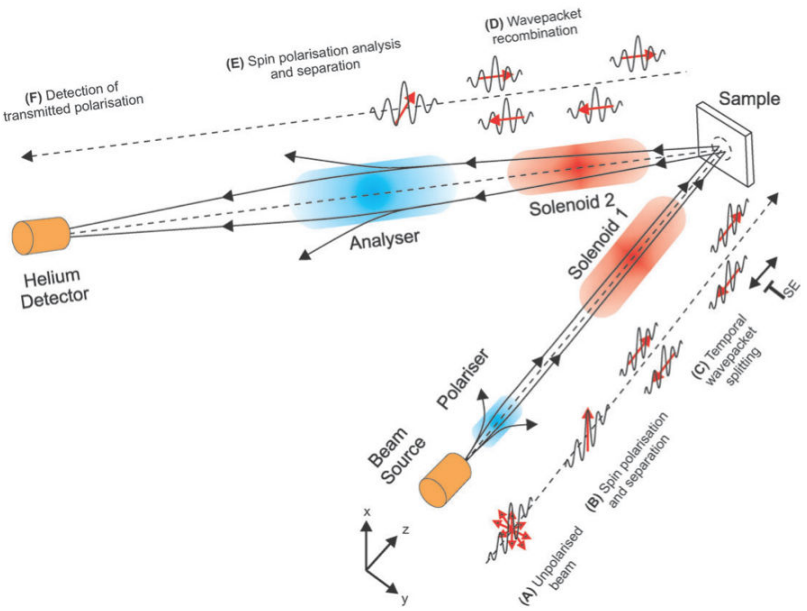

Figure 3.13: Schematic drawing of the HeSE instrument at the Cavendish Laboratory. Explanations of the different parts are given in the text. From [48].

Beam Production and Detection

The helium beam is created using a high pressure (50 – 80 bar) of helium. Contrarily to the helium TOF spectrometer, the ^{3}He isotope is used since its half-integer nuclear spin is necessary for beam polarisation. In order to create a beam of high collimation (and thus intensity) and high monochromaticity, it is expanded supersonically through a 10 μm wide Cambridge type nozzle into a low pressure vacuum chamber. The nozzle is cooled to low temperature in order to create a low energy beam (normally 37 K for an 8 meV beam). The beam is collimated using a 0.5 mm wide skimmer (point A in Fig. 3.13). Differential pumping stages throughout the entire experimental setup reduce the background pressure. The world wide shortage of ^{3}He and the resulting high price make a hermetically sealed recycling system necessary that passes the ^{3}He from the pumping stages to a cleaning system and re-compresses the recycled ^{3}He.

Switching to the far end of the instrument, the ^{3}He atoms enter a custom built detector, where they become ionised through solenoidal, magnetically confined electron bombardment [49], aiming at high detection efficiency and low multiple ionisation (point F in Fig. 3.13).

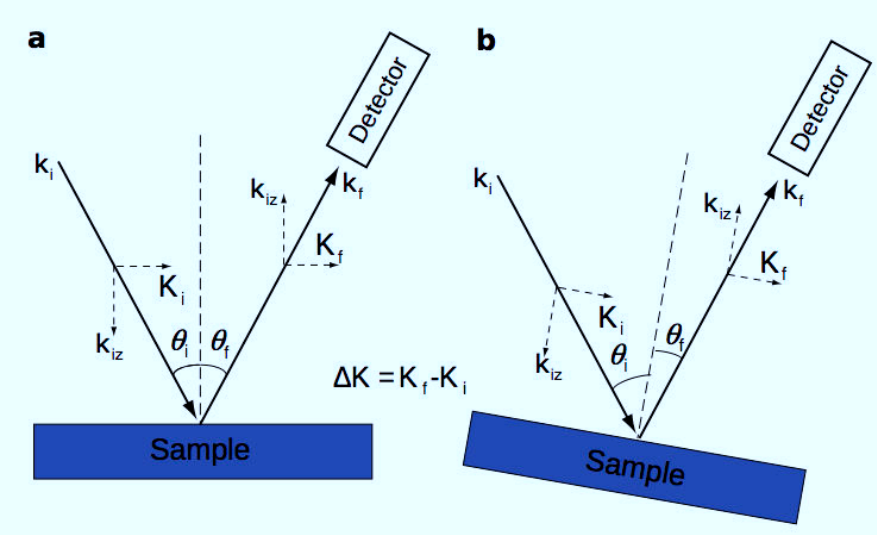

Figure 3.14: Scattering geometry at the HeSE spectrometer for specular scattering (a) and off-specular scattering (b). The total scattering angle is fixed at 44.4° and momentum transfer is achieved by tilting the scattering plane. From [50].

Scattering Geometry

The central part of the instrument consists of a rotatable sample mount in the centre of a ultra high vacuum (UHV) chamber, where scattering from a sample takes place. The incoming and outgoing beam are fixed at an angle of 44.4°, while a momentum transfer $\Delta p = \hbar \Delta k$ is achieved by rotating the sample plane (see Fig. 3.14). For elastic scattering, the parallel and perpendicular momentum transfer, $\Delta k_{\parallel}$ and $\Delta k_{\perp}$, can be calculated from simple trigonometry:

$$\Delta k_{\parallel} = |k_i| \sin\theta_i |k_f| \sin\theta_f = |k_i| \sin\theta_i |k_f| \sin(\theta_{total} \theta_i) \tag{3.71}$$

$$\Delta k_{\perp} = |k_i| \cos\theta_i |k_f| \cos\theta_f = |k_i| \cos\theta_i |k_f| \cos(\theta_{total} \theta_i). \tag{3.72}$$

Furthermore, the sample can be rotated in the surface plane, allowing to direct the momentum transfer towards different crystal directions. As mentioned before, the momentum transfer is commonly denoted by Δk, in contrast to Q in neutron scattering. Furthermore, we will refer by Δk to the *parallel* contribution of the momentum transfer only, since we are studying structure and dynamics at a flat substrate surface, $\Delta k := \Delta k_{\parallel}$. Also, the perpendicular contribution $\Delta k_{\perp}$ is in our instrumental

setup very high, but almost constant. Assuming a 7 meV attractive potential and beam energy of 8 meV, in the accessible angular range of about $\pm 45\,^{\circ}$ off-specular scattering, the perpendicular momentum transfer is limited to $8 \leq \Delta k_{\perp} \leq 9\,\text{Å}^{-1}$.

Spin-Echo Creation

The helium beam passes a 1.1 T hexapole magnet with a linear field gradient that focusses one spin component of the beam and defocusses the other one (point B in Fig. 3.13). The ^{3}He atoms of the defocussed beam are pumped away and what remains is a highly focussed, spin polarised ^{3}He beam. Spin precession is then achieved by two precession solenoids of 0.75 m length each in the incoming and outgoing beam, that create a maximum field of 0.15 T at a maximum electrical current of 8 A (point C and D in 3.13). Finally, the beam passes a hexapole analyser that uses the same functioning as the polariser (point E in 3.13).

Helium Spin-Echo Spectroscopy

The spin-echo principle for helium scattering works in analogy to its counterpart in neutron scattering (see Sec. 3.2.4), expect for the discussed differences in the scattering process.

The measured polarisation amplitude at the spin-echo point corresponds, ignoring for the moment the form factor, to the real part of the normalised ISF $\Re(I(\Delta k, t))$. By introducing an additional phase shift of $\pi/2$, the imaginary part $\Im(I(\Delta k, t))$ can be measured as well. The two contributions correspond to the symmetrical and anti-symmetrical contributions in ω of $S(\Delta k, \omega)$, respectively. While surface diffusion processes are entirely symmetric in ω, adsorbate vibrational modes or substrate phonons may introduce asymmetric contributions. The full $S(\Delta k, \omega)$ can be reconstructed by Fourier transformation from both parts [48].

3.3.3 De Gennes Narrowing in Helium Spin-Echo

De Gennes, after whom the effect was named, was the first to give an explanation for an apparent narrowing of the QENS broadening of the DSF $S(Q, \omega)$, which mirrored $S(Q)$. By calculating higher order moments of $S(Q, \omega)$, he showed that in the case of

diffraction, velocity correlations of neighbouring atoms result in a slower decorrelation in diffusion, and thus a narrowing of $S(Q,\omega)$ for the case of coherent scattering [51]. Pusey found a similar result in dynamic light scattering, a technique that basically measures the ISF $I(Q,t)$ [52]. He stated that for Brownian-type diffusion, where the ISF is given by $I(Q,t) = I(Q,0)\exp(-DQ^2t)$ with the diffusion constant D, an effective diffusion constant D_{eff} is observed with $D_{eff} = D/I(Q,0)$.

Since thermal helium atoms scatter coherently, an ISF measured in a HeSE measurement is subject to de Gennes narrowing. With regard to surface diffusion, this fact complicates data analysis, since most diffusion models assume incoherent scattering. If the structure factor $S(\Delta k)$ is known, an incoherent diffusion constant, corrected by the structural effects from de Gennes narrowing, can be calculated by simple multiplication with $S(\Delta k)$. However, in helium scattering the form factor has an important effect on the scattering amplitude, which complicates a determination of $S(\Delta k)$.

What we will discuss in the following is a preliminary correction procedure, which we have not yet understood in detail, but which seems to allow us to calculate the incoherent exponential decay rate $\alpha_{inc}(\Delta k)$ of a surface diffusion process from its coherent counterpart, $\alpha(\Delta k)$, which is obtained by measurements.

In the HeSE measurements that are discussed in this thesis, namely in the system of diffusing benzene molecules on graphene/Ni(111) (Chap. 7) and in the system of diffusing H_2O molecules on graphene/Ni(111) (Chap. 5), an *increase* of the decorrelation rate $\alpha(\Delta k)$ was observed, that is proportional to the quasi-elastic ISF $I_{qe}(\Delta k, t)$, a behaviour which seems at first glance to be the inverse of a de Gennes narrowing (a narrowed $S(\Delta k,\omega)$ would correspond to a *decrease* in $\alpha(\Delta k)$). We have the idea that this apparent inversion of the de Gennes effect stems from normalisation of the ISF.

Let us assume a system that consists of diffusing molecules on a surface, where the diffusion causes an exponential decay of the ISF with a Δk-dependent coherent decay rate $\alpha_{coh}(\Delta k)$, then the ISF is in general given by:

$$\tilde{I}(\Delta k, t) = \tilde{I}_{qe}(\Delta k)\exp[\alpha_{coh}(\Delta k)\cdot t] + \tilde{I}_{el,ad}(\Delta k) + \tilde{I}_{el,su}(\Delta k), \tag{3.73}$$

where $\tilde{I}_{qe}(\Delta k)$ is the quasi-elastic amplitude that stems from scattering from diffusing molecules, and $\tilde{I}_{el,ad}(\Delta k)$ is the elastic amplitude that stems from scattering from

immobile adsorbate molecules. $\tilde{I}_{el,su}(\Delta k)$ is the elastic amplitude from scattering of the substrate. The decay rate is subject to de Gennes narrowing, which relates the incoherent to the coherent decay rate, $\alpha_{coh}(\Delta k) = \alpha_{inc}(\Delta k)/S_{ad}(\Delta k)$, with the *structure factor* of the adsorbate:

$$S_{ad}(\Delta k) = S_{qe}(\Delta k) + S_{el,ad}(\Delta k), \tag{3.74}$$

where we assume that $\tilde{I}_{qe}(\Delta k) = |F_{ad}(\Delta k, \omega)|^2 \cdot S_{qe}(\Delta k)$ and $\tilde{I}_{el,ad}(\Delta k) = |F_{ad}(\Delta k, \omega)|^2 \cdot S_{el,ad}(\Delta k)$, with the form factor of the adsorbate $F_{ad}(\Delta k, \omega)$ (Eq. (3.70)).

In a HeSE measurement, the polarisation corresponds to an ISF that is normalised by $I(\Delta k, t) = \tilde{I}(\Delta k, t)/\tilde{I}(\Delta k, 0)$:

$$I(\Delta k, t) = I_{qe}(\Delta k) \exp[\alpha_{eff}(\Delta k) \cdot t] + I_{el,ad}(\Delta k) + I_{el,su}(\Delta k). \tag{3.75}$$

with the normalised amplitudes $I_{qe}(\Delta k)$, $I_{el,ad}(\Delta k)$ and $I_{el,su}(\Delta k)$. Further, we note that:

$$I_{qe}(\Delta k) = \frac{\tilde{I}_{qe}(\Delta k)}{\tilde{I}(\Delta k, 0)} = \frac{S_{qe}(\Delta k)|F_{ad}(\Delta k, \omega)|^2}{S_{ad}(\Delta k, 0)|F_{ad}(\Delta k, \omega)|^2 + S_{su}(\Delta k, 0)|F_{su}(\Delta k, \omega)|^2}, \tag{3.76}$$

with the substrate form factor $F_{su}(\Delta k, \omega)$. For the coherent decay rate $\alpha_{coh}(\Delta k)$, rearranging the above equation implies for the de Gennes narrowing:

$$\alpha_{inc}(\Delta k) = \alpha_{coh}(\Delta k) \cdot \left(\frac{S_{qe}(\Delta k)}{I_{qe}(\Delta k)} - |r|^2 \cdot S_{el,su}(\Delta k) \right), \tag{3.77}$$

with the ratio between the form factors $r = F_{su}(\Delta k, \omega)/F_{ad}(\Delta k, \omega)$. This result could explain our observations: in regions, where we assume the contribution of the substrate $S_{el,su}(\Delta k)$ to be negligible, i.e. everywhere except for small regions around diffraction peaks, the exponential decay is altered by a factor that is the ratio between the normalised quasi-elastic amplitude and its structure factor. For a disordered, dilute adsorbate phase, that undergoes the simplest forms of surface diffusion, i.e. Brownian-type diffusion, ballistic diffusion, or jump diffusion on a Bravais lattice, $S_{qe}(\Delta k)$ would be independent of Δk. In these cases, $\alpha_{inc}(\Delta k)$ can be calculated by dividing $\alpha_{coh}(\Delta k)$ by the measured amplitude of the exponential decay, $I_{qe}(\Delta k)$ and subsequent rescaling of $\alpha_{inc}(\Delta k)$ by a constant such that $\alpha_{coh}(\Delta k) = \alpha_{inc}(\Delta k)$

in regions where no structural contribution is expected. However, this result does not apply in the vicinity of substrate diffraction peaks (where an additional correction by $|r|^2 \cdot S_{el,su}(\Delta k)$ would be necessary).

To obtain a rough approximation of the form factors of the studied adsorbate molecules H_2O and benzene, we have the Fraunhofer scattering intensity in the hard hemisphere approximation (see Fig. 3.15). Its hull function follows approximately a Δk^{-3} dependence. The calculation follows the description in [53], where we have assumed a CoM distance at the turn-over point of 2.65 Å for H_2O and 3.65 Å for benzene. The form factor of the substrate, a graphene/Ni(111) surface can be seen in a diffraction scan in Fig. 4.5.

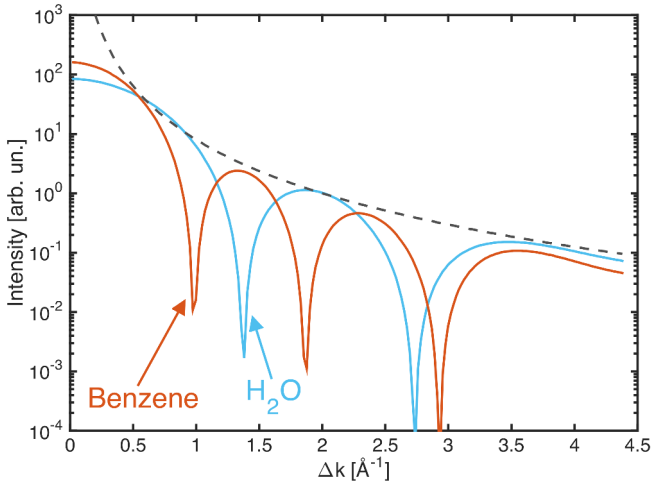

Figure 3.15: Calculated Fraunhofer intensity versus Δk in the hard hemisphere approximation for H_2O and benzene. Grey dashed line: Δk^{-3} approximation.

4 Epitaxial Graphene Growth on the (111) Surface of a Nickel Crystal

4.1 Introduction

Graphene as a truly two dimensional material exhibits unique properties that have attracted large attention in the last decade. It is a single layer of carbon atoms that arrange in a hexagonal honeycomb lattice structure with a C-C bond distance of 1.42 Å. In this plane, one 2s and the $2p_{x,y}$ orbitals hybridize to form strong Σ bonds between C atoms. The $2p_z$ orbital forms a π band that is half filled, where the conduction band and the valence band meet at the Fermi level [54]. This makes graphene a zero-gap semiconductor.

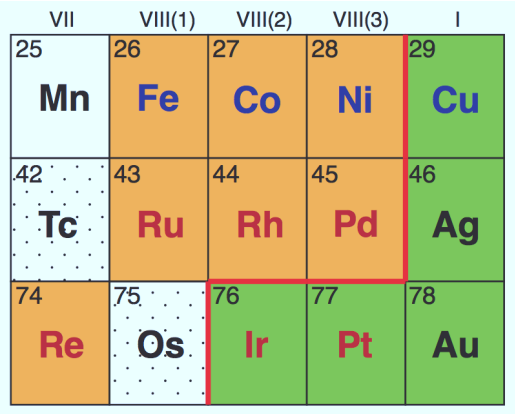

Figure 4.1: View of the periodic table of transition metals that allow epitaxial graphene growth. Orange and green highlighted panels: strongly and weakly interacting graphene, respectively. Blue and red labelled elements: lattice matched and lattice mismatched systems, respectively. From [55].

Graphene can be grown epitaxially on several metal surfaces by chemical vapour deposition, where the metal surface acts as a catalyst on carbohydrate precursors, which leave carbon behind at the surface [56]. Epitaxial graphene growth on the

Ni(111) surface has been reported as early as 1983 [57, 58]. Since then, epitaxial graphene growth by chemical vapour deposition has been successful on a dozen of transition metal surfaces. They differ in general in two qualities, by which each system can be classified: The graphene and metal system can interact weakly or strongly, which for a strongly interacting system results in a shift of the Fermi level and the appearance of a band gap, while for a weakly interacting system, the properties of free standing graphene are largely preserved [55]. In general, the quality of these graphene layers is very high, with a very large structural coherence [59]. The second classification is structural. The graphene layer may either be matched or mismatched with respect to the metal surface, depending on the unit cell size of the metal surface and the interaction strength. Fig. 4.1 shows a comparison of the known transition metal – graphene systems. Since graphene/Ni(111), is a strongly binding system and the lattice constants of free-standing graphene and the Ni(111) surface differ only by 1.2 %, the graphene layer matches the metal surface [56, 55]. (The lattice constants of the hexagonal unit cell are a_{Ni} = 2.49 Å and a_{GR} = 2.46 Å, respectively.) The strong interaction also causes the graphene layer to be located relatively close to the Ni surface, with a separation of 2.1 Å, compared to 3.3 Å inter-layer distance in graphite.

Fig. 4.2 illustrates the geometry of the graphene/Ni(111) surface. The graphene unit cell is indicated by red arrows ($a_1 = a_2 = 2.49$ Å). The reciprocal space unit vectors b_1 and b_2 are drawn in purple ($b_1 = b_2 = 4\pi/\sqrt{3}a$). The Brillouin zone (BZ) is rotated by 30° with respect to the orientation of the real space graphene hexagon. The two principal azimuthal directions in Brillouin zone are denoted by $\overline{\Gamma}\overline{\mathrm{M}}$ and $\overline{\Gamma}\overline{\mathrm{K}}$ connecting the $\overline{\Gamma}$ point with the $\overline{\mathrm{M}}$ and the $\overline{\mathrm{K}}$ points, respectively. In terms of directions, along which helium scattering is performed, $\overline{\Gamma}\overline{\mathrm{M}}$ corresponds to scattering along the [110] direction in real space, and $\overline{\Gamma}\overline{\mathrm{K}}$ corresponds to the $[1\bar{1}0]$ direction. Since the geometry of the HeSE instrument is fixed to 44.4° and the sample is tilted for diffraction measurements, at 8 meV beam energy, a range in Δk up to about ± 5 Å^{-1} is accessible. In this range, we can access only one diffraction condition, the first order Bragg diffraction (see Fig. 4.4 and 4.5 in the next section). The orange lines in Fig. 4.2 illustrate the scattering planes that correspond to this Bragg condition.

Since the interaction between an organic molecule and the substrate is typically weak, conventional techniques such as X-ray scattering and high-energy electron diffraction can often become destructive. Due to the low energies (5 – 100 meV), neutral He atoms are perfectly suited to probe these systems in an inert, completely

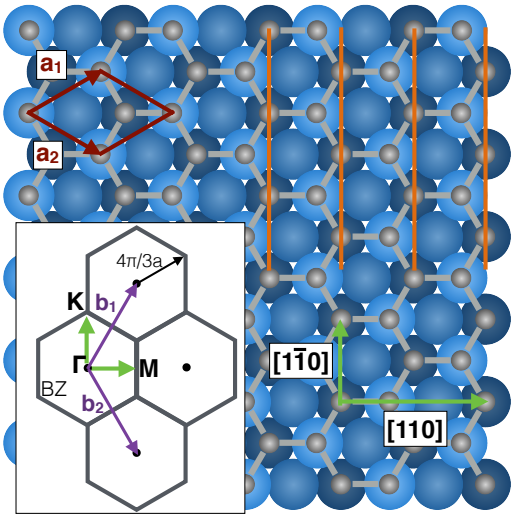

Figure 4.2: Illustration of real space and reciprocal space geometry of the graphene/Ni(111) surface. Dark red: unit cell in real space; Purple: unit cell in reciprocal space; BZ: first Brillouin zone; The green arrows indicate the principal directions in real space, [1$\bar{1}$0] and [110], and in reciprocal space, $\overline{\Gamma M}$ and $\overline{\Gamma K}$. The orange lines indicate the scattering planes of the first order diffraction peak that is situated in the [110] $\overline{\Gamma M}$ direction at 2.93 Å^{-1}.

non-destructive manner [60, 61, 41].

In this chapter, we will discuss our growth procedure of an epitaxial graphene on the (111) surface of a Ni crystal. We will then present structural studies from helium diffraction. Finally, we will discuss the spectra of two observed surface excitations in the very low energy regime, namely the longitudinal resonance mode and the Rayleigh mode. These modes hold important information about the thermal conductivity of graphene which is dominated by contributions from acoustic phonons near room temperature. It also shows the importance of the graphene-substrate interaction which can easily modify the corresponding dispersion curves.

4.2 Experimental Details

The Ni(111) single crystal used in the study was a disc with a diameter of 10 mm and a thickness of 1 mm. Fig. 4.3 shows the single crystal sample mounted on a sample holder (see Fig. 4.3). The sample holder can be heated using a radiative heating

from a filament on the backside of the crystal. For cooling, heat is transferred from the sample via a sapphire crystal and a subsequent stack of flexible copper bands to a reservoir of liquid nitrogen or liquid helium, which allow cooling to 100 K and 75 K, respectively. Sapphire exhibits a very good heat conductivity at low temperatures and a flexible heat conductor is necessary to rotate the sample holder. The sample temperature was measured using a chromel-alumel thermocouple. Prior to the

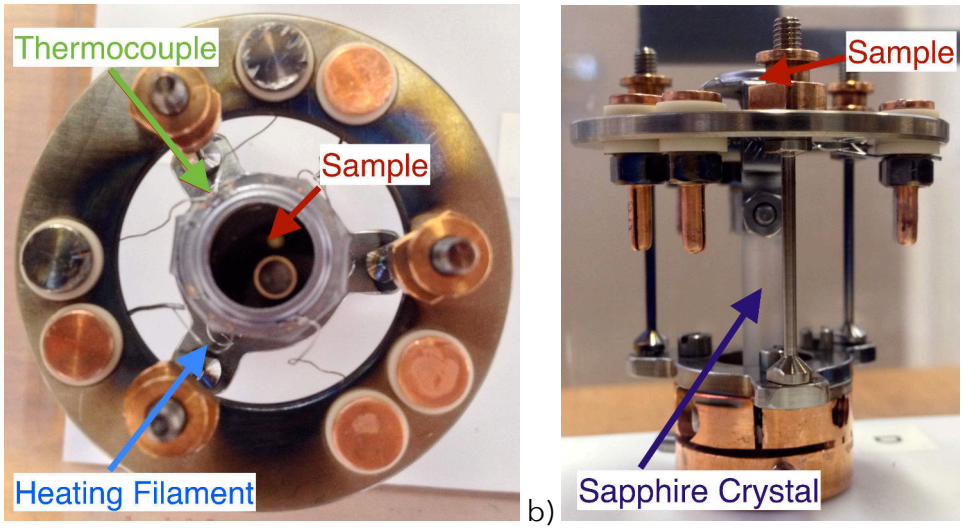

Figure 4.3: The Ni(111) single crystal mounted on a sample holder. a) Top view. The crystal surface reflects the lens of the camera. b) side view.

measurements the surface was cleaned by Ar^+ sputtering and annealing to 870 K. A monolayer of graphite on Ni(111) was then grown by dosing ethene (C_2H_4) while heating the Ni crystal (730 K) over several hours [62]. This process gives rise to an epitaxial graphene layer which is not rotated with respect to the substrate. The formation of a single domain of the graphitic lattice causes a diffraction pattern which exhibits the same symmetry as the hexagonal Ni(111) surface.

4.3 Structure of Graphene/Ni(111)

We have performed helium diffraction studies on the prepared graphene/Ni(111) surface. Fig. 4.4 shows a three-dimensional polar plot of the scattered intensity. Here, the radial coordinate corresponds to the incident angle θ_i and the polar angle corresponds to the azimuthal orientation of the crystal. The z-axis indicates the scattered intensity which is plotted on a logarithmic scale. The two first order diffraction

peaks which are contained in the scanned azimuthal range are clearly visible. They are located at the same position as the peaks of the Ni substrate, which suggests a (1 x 1) structure on the underlying Ni(111) surface.

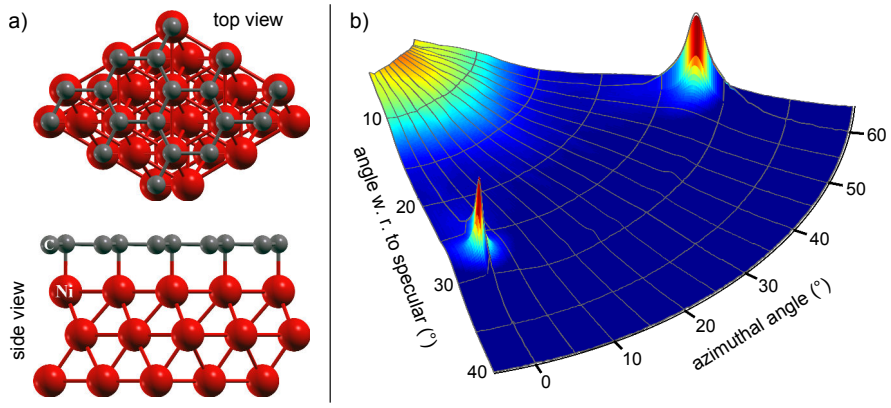

Figure 4.4: a) Top and side view of the graphene/Ni(111) surface structure (according to [63]). b) Three-dimensional polar plot of the scattered He intensity for graphene/Ni(111) where the z-axis corresponds to the scattered intensity on a logarithmic scale. The scan was taken with an incident beam energy of $E_i = 8$ meV and the surface at 150 K. The two diffraction peaks which are contained in the scanned azimuthal range are clearly visible. The specular peak is not shown in the plot due the high intensity compared to the diffraction peaks.

Several possible configurations exist for the position of the carbon atoms in the graphene layer, relative to the Ni(111) substrate. Recent density functional theory (DFT) calculations have shown that the energetically most favourable graphene/Ni(111) configuration is the top-fcc one (see Fig. 4.4a)) followed by the top-hcp structure [64, 65, 66]. The energy difference between these two structures has been reported to be quite small and domains with both configurations have been observed in experiments [65, 66]. Unfortunately we cannot distinguish the two configurations from diffraction. However, based on about 20 % He reflectivity of the graphene covered surface and the small width of the specular peak, we expect to have predominantly one configuration since the number of defects and domain boundaries must be small in order to achieve the high observed reflectivity [41].

Note in particular that the specular reflectivity for He is similar to the reflectivity of the graphene/Ru(0001) system where a reflectivity of up to 23 % was reported [67, 61]. Not only exhibits graphene/Ni(111) a high He reflectivity as recently predicted [61], its reflectivity remains also unchanged after O_2 exposure at $2 \cdot 10^{-7}$ mbar for

15 minutes similar to the graphene/Ru(0001) system [67].

In Fig. 4.5 the scattered intensity versus Δk is plotted for both graphene/Ni(111) and Ni(111) along the $\overline{\Gamma}\overline{\mathrm{M}}$ direction. On the graphene covered surface the intensity of the diffraction peak is increased by two orders of magnitude indicating a larger corrugation of the surface electron density compared to the clean Ni(111) surface. According to the peak area, the intensity of the first order diffraction peak is only 0.003 % of the specular intensity for Ni(111) and 1 % for graphene/Ni(111), respectively.

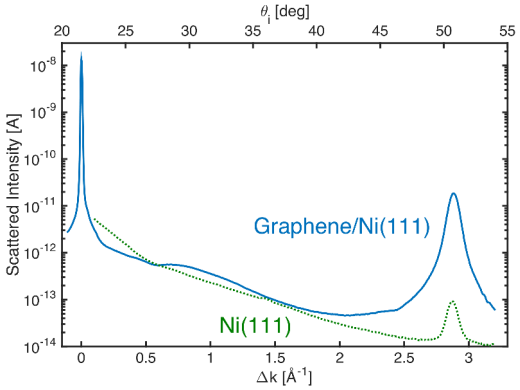

Figure 4.5: Comparison of the scattered intensities for graphene/Ni(111) and clean Ni(111) versus Δk. Both scans were taken along the $\overline{\Gamma}\overline{\mathrm{M}}$ direction with the crystal at room temperature and a beam energy of 8 meV. The intensity of the diffraction peak is increased on the graphene covered surface which indicates a larger corrugation of the surface electron density compared to the pristine Ni surface.

We used purely elastic close-coupling calculations to determine the corrugation of the surface electron density quantitatively. In the close-coupling approach, the surface is considered to be statically corrugated and periodic and helium atoms are viewed as structureless [68]. The surface potential was approximated by a corrugated Morse potential, which is a common approach in combination with close-coupling calculations. With this approach, the electronic corrugation can be calculated by solving the Schrödinger equation with the corrugated Morse potential iteratively, to match the experimental diffraction peak intensities [68]. We thus found that the peak-to-peak height of the surface electron density corrugation for graphene/Ni(111) is 2.5 % of the Ni surface lattice constant and 0.22 % in case of the pristine Ni surface, respectively. While the surface electron density corrugation for graphene/Ni(111) is considerably larger than on clean Ni, this corresponds to a

peak to peak height of 0.06 Å. This is still comparable to the findings of some metal surfaces [41]. It is also smaller than the corrugation on graphite [69]. Compared to graphene/Ru(0001) (0.15 Å [70]) and graphene/Rh(111) (0.9 Å [71]) this is the smallest surface electron density corrugation that has been reported for graphene/metal systems so far.

We used the fact that the graphene covered surface has a larger electron density corrugation than the Ni(111) surface to monitor the graphene growth. Fig. 4.6 shows the intensity of the first order diffraction peak during graphene growth. The intensity first drops upon formation of nickel carbide domains [62]. Upon conversion into graphene the intensity increases again and finally reaches a value above the initial intensity when the graphene layer is completed, due to the higher corrugation.

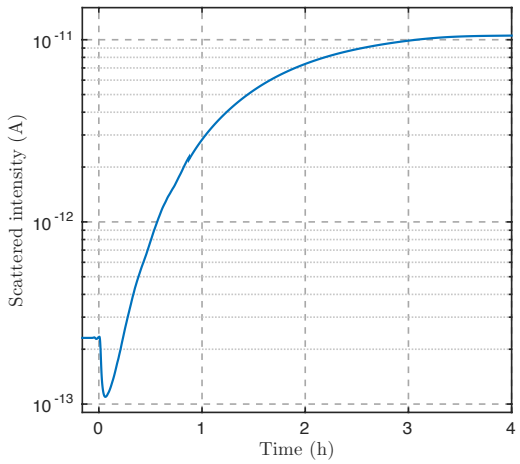

Figure 4.6: The growth of graphene on Ni(111) can be followed by monitoring the first order diffraction peak while dosing ethene (C_2H_4). Here the time $t = 0$ on the abscissa corresponds to starting the dosing of ethene. First nickel carbide forms and the intensity drops. As soon as this converts to graphene the intensity increases since graphene exhibits a larger corrugation than Ni(111). The whole growth process continuous over several hours.

4.4 Phonon Spectra for Graphene/Ni(111)

In the HeSE instrument, the two precession coils for the incoming and the outgoing beam can be steered by two independent power supplies. In this configuration, they can thus be seen as energy analysers that allow us to select the wavelength

of the incoming and outgoing ^{3}He atoms independently (see [72] for details). We have measured several energy analysed scattering spectra along the $\overline{\Gamma M}$ direction. Fig. 4.7 shows the 2D wavelength intensity map for graphene/Ni(111) at an incident angle $\theta_i = 18.2°$. The only noticeable feature except for the elastic peak at $\lambda_f = \lambda_i$ is the Rayleigh mode of Ni(111) on the phonon creation side (at larger λ_f). This suggests that there is no significant difference in the surface phonon dispersion relation for Ni(111) and the graphene covered surface within the energy range accessible with a 8 meV beam.

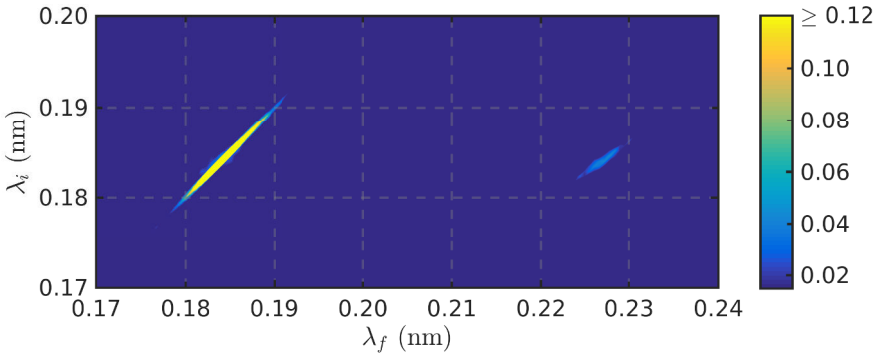

Figure 4.7: 2D wavelength intensity matrix for graphene/Ni(111) along $\overline{\Gamma M}$ recorded at $\theta_i = 18.2°$, a beam energy of 8 meV and a sample temperature of 150 K. The plot shows the measured probability for detecting a scattered He atom with wavelength λ_f versus the incoming wavelength λ_i. The only two visible features are the elastic peak (at $\lambda_f = \lambda_i$) and the Rayleigh mode on the creation side (at larger λ_f).

At first glance, one might expect to detect phonon modes similar to the ones in graphite [73, 74] or free-standing graphene [75, 76] on graphene/Ni(111). The three acoustic modes (ZA, TA and LA) should be at a detectable energy within the vicinity of the $\overline{\Gamma}$-point. However, previous measurements of the graphene/Ni have only covered phonon events at energies greater than 20 meV [77, 78, 59, 56].

The experiments presented in this work have been performed for in plane scattering along the $\overline{\Gamma M}$ azimuth of the crystal. In this case the scattering plane, defined by the incoming and scattered He beam, coincides with a mirror plane of the surface. Hence the TA mode cannot be excited since it is anti-symmetric with respect to the scattering plane [79, 80]. As shown by de Juan et al. [79] this symmetry is not broken by bonding of the graphene layer to the substrate in the case of Ni(111). However, the bonding to a perfectly commensurate triangular substrate gives rise to a lifting of the ZA mode [79] which brings the ZA mode out of the detectable energy range

of our instrument.

Hence the LA mode is the only phonon mode present in graphene/Ni(111) that would be experimentally accessible within the framework of this study. Yet this mode has the largest slope of the acoustic phonon modes and would only be detectable close to $\overline{\Gamma}$. While in the current spectra there are no indications for this mode it would require a more thorough investigation at specific scattering conditions to make any sound conclusions regarding this. In particular, since on other graphene/metal systems low energy phonon modes have been found [81, 82, 61].

Nevertheless, an important result of this study is that the Rayleigh mode and the longitudinal resonance of the Ni(111) substrate [83, 84] are observable on the graphene covered surface, even though the Ni atoms are screened out by the graphene sheet. An exemplary phonon spectrum is shown in Fig. 4.8 together with a spectrum taken on Ni(111) under the same experimental conditions.

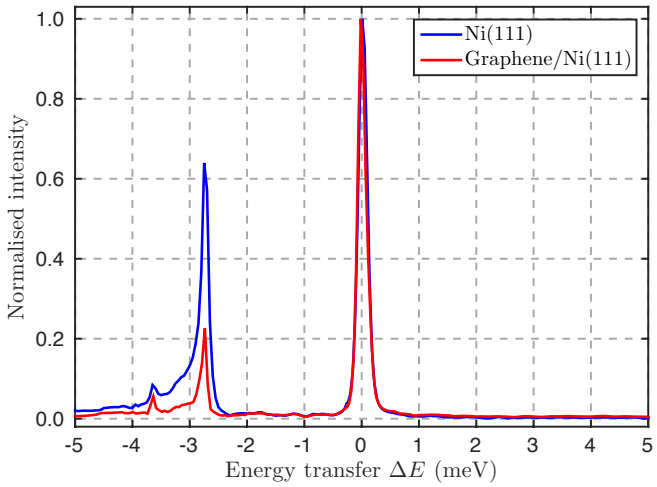

Figure 4.8: Comparison of the phonon spectra for graphene/Ni(111) and Ni(111). The spectrum was taken along the $\overline{\Gamma M}$ azimuth at an incident angle $\theta_i = 18.2°$, $E_i = 8$ meV and the sample was cooled down to 150 K. Despite the diffuse elastic peak at 0 energy transfer both the Rayleigh mode at -2.7 meV and the longitudinal resonance at -3.6 meV can clearly be seen. The intensity of the Rayleigh mode is smaller on the graphene covered surface.

Both spectra have been normalised so that the intensity of the diffuse elastic component at zero energy transfer corresponds to one. Despite the diffuse elastic component the Rayleigh mode and the longitudinal resonance can be seen on the creation

side. The intensity of the Rayleigh mode is clearly reduced on the graphene covered surface with respect to the intensity on Ni(111). This seems to be a general effect when comparing intensities of several spectra throughout the $\overline{\Gamma M}$ direction.

Since the inelastic scattering of ^{3}He atoms due to phonons involves scattering by phonon-induced charge density oscillations it has been shown that subsurface phonon modes are accessible for HAS due to the electron-phonon coupling. The electron-phonon coupling parameters found for graphite and graphene/metal systems have been reported to be close to 1 [85] which is similar to the value reported for other systems where subsurface phonon modes could be detected with HAS [86, 87].

Moreover, the observation of the Rayleigh mode from the substrate is consistent with measurements of graphene/Ru(0001) where a strong intensity of the Rayleigh mode from the Ru(0001) substrate was found [61]. Maccariello at el. demonstrated that surface charge density oscillations are the main contribution for this observation on graphene/Ru, although the graphene layer also oscillates with the underlying Ru surface due to the strong bonding to the substrate [61].

When performing HeSE measurements, ISFs at low Fourier times (about < 1 ps) include contributions from low energy surface phonons. This will be discussed in detail in chapter 5, where in the same Fourier time range, a decay of the Rayleigh mode and a fast diffusion process are observed.

4.5 Summary and Conclusion

In this chapter, we have discussed the preparation of a graphene/Ni(111) layer by chemical vapour deposition. By comparing specular and diffraction peak intensities, we found that the epitaxial graphene layer exhibits an electron density corrugation with a peak to peak height of 0.06 Å upon scattering of ^{3}He with a beam energy of 8 meV. This corrugation is smaller than the values reported for graphene/Ru(0001). The graphene/Ni(111) surface shows a similar reflectivity of ≈ 20 %.

Measurements of the surface phonons modes in the low energy region basically show the same modes as on the pristine Ni surface. While 2 of the acoustic graphene modes are not accessible in our setup, the observation of the Ni(111) surface modes is ascribed to the ability of HAS to detect subsurface phonon modes due to the

electron-phonon coupling. The intensity of the Rayleigh mode is generally smaller on the graphene coated surface compared to the Ni surface. The similarity of these findings with atom scattering results from graphene/Ru[61] perfectly confirms the theory that strongly interacting graphene-metal systems should give rise to a high He reflectivity.

5 H_2O Adsorbed on Graphene/Ni(111)

5.1 Introduction and State of Current Research

H_2O adsorbed on graphene and graphite surfaces can be regarded as a fundamental system for studying physisorption. The system shows electrostatic, van der Waals, and hydrogen bonding interactions in a complex way and the existence of strong hydrogen bonds makes it an interesting adsorbate to study cluster formation on the graphene surface [88]. In general, H_2O is expected to behave much differently on the strongly hydrophobic graphene surface [89, 90, 91] in comparison to its behaviour in bulk liquid water or ice. The adsorption properties of water on graphene have attracted much attention since resistivity measurements have shown the existence of a tunable band-gap of 0.2 eV in graphene on a SiO_2 substrate by exposition of the surface to humidity [92]. The exact structure of the adsorbed H_2O might play an important role for the influence of the adsorbate on the electronic properties in graphene, as DFT calculations suggest [54].

In order to simplify the discussion of water adsorption on graphene in terms of geometry, it is helpful to introduce abbreviations: possible adsorption sites are on **top** of a C atom (T), above a **bridge** site between two C atoms (B), and above the **hollow** centre of the graphene hexagon (H). Furthermore, the water molecule might be oriented in different ways: both h atoms pointing symmetrically upward (u) or downward (d), lying flat parallel to the surface (f), or with one H atom parallel to the surface and the second pointing downward (v).

Experimental investigations

The experimental investigations so far have been limited mostly to macroscopic investigations, such as calorimetric and thermal desorption measurements. For com-

parison, we also include results from H_2O on the surface of graphite, as well as from H_2O on graphene with different metal substrates.

The only experimental value for the binding energy of H_2O to a graphite surface stems from micro-calorimetric measurements, where a differential heat of adsorption of 156 meV at the zero coverage limit was observed [93]. Several groups have conducted TDS measurements of water on the (0001) basal plane of graphite. Consistently, a single desorption peak was observed that corresponds to a desorption energy in the range of 0.4 to 0.5 eV. (Chakarov et al.: (0.48 ± 0.03) eV [94, 95], Ulbricht et al.: (eV [15], Bolina et al.: (0.416 ± 0.003) eV [96]). This value is close to the sublimation enthalpy of ice at 0 K, 0.49 eV [94]. This energy was observed not to change with coverage, indicating de-wetting of the graphene surface [15]. Furthermore, sub-monolayer desorption seems to be of approximately 0th order and the sticking coefficient seems to be coverage independent [94, 96]. For coverages approaching the monolayer, 1st order desorption has been observed [94]. On the surfaces of graphene/Ni(111) and of graphene/Li(111), TDS spectra reveal pseudo-zeroth order desorption (see Fig. 5.1). Desorption energies of (356 ± 23) meV in the first case, and (585 ± 31) meV in the latter case, respectively, were found.

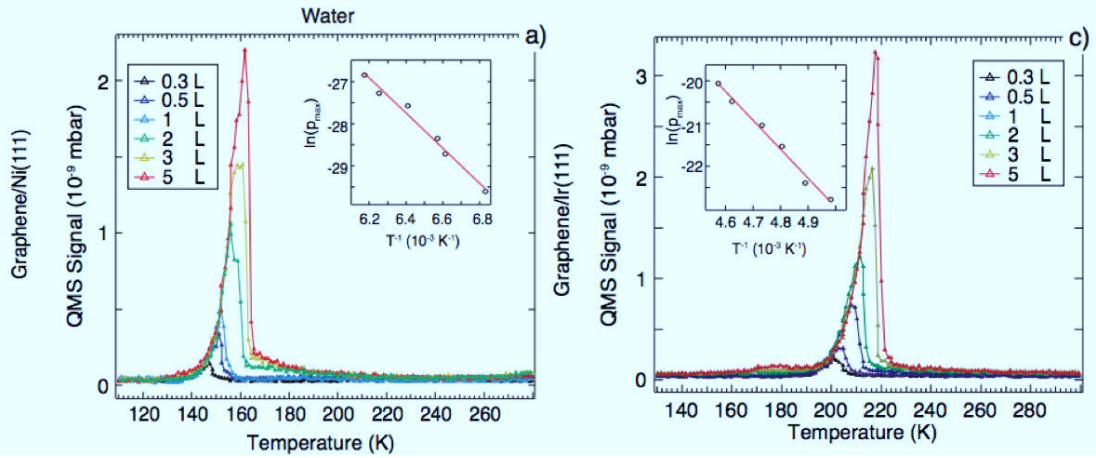

Figure 5.1: Thermal desorption spectroscopy of H_2O adsorbed on the surfaces of graphene/Ni(111) and of graphene/Li(111). From [55].

From LEED and rare-gas adsorption/desorption measurements, a metastable ice I_h bilayer on graphene/Pt(111) has been reported at 125 K that de-wets and forms 3D ice I_c islands upon heating to 135 K [89].

HREELS studies of H_2O on HOPG revealed the formation of hydrogen bonded clusters that exhibit the same vibrational spectra as bulk ice for coverages in the sub-

monolayer range [97]. For H_2O on the surface of graphene/Pt(111), an almost identical spectrum was found, with an additional sharp O–H vibrational band at 457 meV, which is seen as evidence for non-H-bonded water molecules at the water/graphene interface [88].

On graphene/Ru(0001), intercalation of water has been observed with STM measurements [98]. We have observed no comparable phenomena, but it has to be noted that graphene is more strongly bound to the Ni(111) surface than to the Ru(0001) surface.

The formation of a amorphous ice layers on surfaces, commonly named amorphous solid water (ASW) has been observed since the 1960s [99]. In the bulk state, at ≈ 135 K ASW undergoes a glass transition to a viscous liquid, where a coexistence of amorphous and cubic crystalline regions have been observed [100]. In isothermal desorption measurements of H_2O on HOPG at ≈ 100 K, the glass transition was observed by a change in desorption rate and a growth of 3D water islands rather than a wetting of the graphite surface [101, 102]. TDS measurements over a large range of surface coverages of H_2O on HOPG revealed the existence of four desorption peaks corresponding to desorption from 2D and 3D islands, as well as from two ice structures, ice I_h and potentially ice I_c, as can be seen in Fig. 5.2.

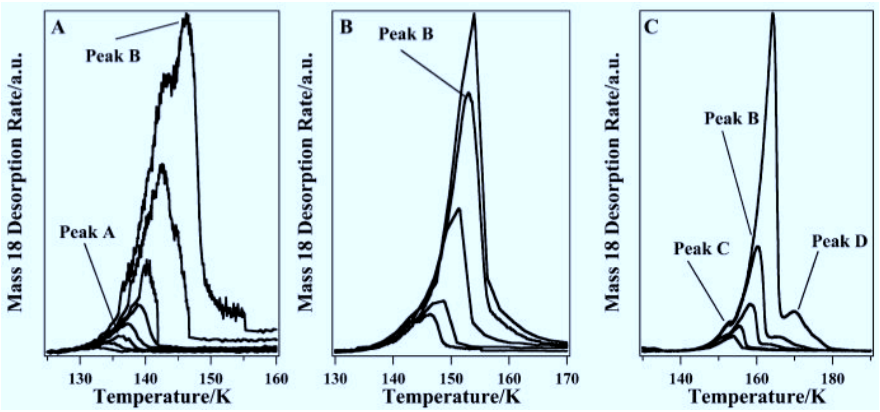

Figure 5.2: TDS spectra of water on HOPG, from [96]. Spectra following exposures A: from 0.04 – 2 L; B: from 2 – 15 L; C: from 15 – 275 L. Peak A: desorption from 2D islands or the edges of 3D islands; Peak B: desorption from the surface of 3D islands; Peak C and D: desorption from ice I_c and I_h, respectively after phase transition.

HAS measurements of water on HOPG revealed the formation of an ice layer on the surface in a temperature range or 100 – 140 K and the formation of 3D structures in

the range 140 – 180 K. For higher temperatures, an onset of mobility was observed, corresponding to the formation of a quasi-liquid water layer [103, 104]. In quasi-elastic helium atom scattering (QHAS) measurements of a 1000 Å thick ice I_h crystal grown on a Pt(111) surface, a Rayleigh surface mode was observed, as well as a dispersion-less phonon branch at $\hbar\omega = 5.4$ meV, which was attributed to frustrated translational vibrations of isolated water molecules [105].

Angle-resolved photoelectron spectroscopy of GR/Ni(111) revealed the existence of interface states, originating from the strong hybridization of the graphene π and spin-polarized Ni 3d valence band states [54]. Adsorption of 0.5 ML H_2O on the GR/Ni(111) surface resulted in p-doping, although the electronic structure of the graphene π and Ni 3d states remained in this case mostly intact. The structural change could be interpreted in terms of a preferential adsorption on either hollow or bridge adsorption sites.

Molecular dynamics and density functional theory calculations

A large number of calculations have been performed in the last ten years to determine to sufficient precision the adsorption location and energy of single and multiple H_2O molecules on graphene and graphite surfaces, as well as on acenes, serving as "miniature graphene".

Most calculations have hereby been done using the DFT approach. However, it has been pointed out that DFT often fails to describe physisorption correctly, since contrary to the local chemical interaction, the dispersion interactions originate from long-range electron correlation effects and they are not captured by the standard DFT approach because of the local character of commonly used functionals [106]. Several calculations used an exchange-correlation functional named the van der Waals-density functional (vdW-DF) developed by Dion et al [107], in order to improve accuracy.

Single molecule adsorption

Molecular dynamics calculations indicate that the binding energies of water with a single graphene layer are comparable to those of water bound on graphite [108].

Furthermore, the similarity of water adsorbed on graphene and on other hydrophobic surfaces suggests that the hydrophobicity plays a more important role than the detailed structure of the surface [108].

The density functional approach has been applied a number of times, showing a strong hydrophobicity of the graphene layer [109, 90]. The influence on the electronic structure of the graphene is rather small and highly oriented water clusters can lead to the doping of graphene [110, 90]. The DFT calculations generally agree that the potential energy surface is rather flat and that the binding energy depends more on the orientation than on the position of the adsorbent [110, 90, 111].

A summary of the results from DFT calculations by various groups is shown in Tab. 5.1. The table shows the preferential adsorption site (H: **hollow**, T: **top**) together with the most favourable orientation (d: H both atoms pointing downward, v: one H atom parallel to the surface, and the second one pointing downward). Most calculations predict a preferential H adsorption with a d orientation. An adsorption energy E_a in the range of about 130 meV is calculated, but results vary considerably. A general agreement on an adsorption distance of about 3.3 Å can be observed.

Site	orientation	E_a [meV]	d [Å]	Reference
H	v	47	3.50	[112]
H	d	123	2.55	[54]
H	d	144	3.23	[113]
H	d	156	3.26	[114]
H	d	70–98	3.4–4.0	[115]
T	d	135	3.23	[106]
H	d	130	3.36	[116, 111]
H	d	183	2.31	[117]*

* Values for graphene/Ni(111)

Table 5.1: Summary of DFT calculation results for a single H_2O molecule on a graphene surface. E_a: adsorption energy; d adsorption distance.

Cluster adsorption

The structure of H_2O clusters adsorbed on graphite has been calculated by several groups. The results agree in finding that almost no structural change happens in the cluster-graphite system in comparison to the free cluster. The association energy to the cluster is in the range of 450 – 500 meV, while the binding energy of a molecule

to the graphene surface is much lower, and also lower than for a single molecule (70 meV [109], 15 meV [90]). It was further predicted that single molecules, clusters up to 5 molecules and a single layer of ice I_h do not cause doping of the graphene [110, 112, 90]. However, bilayers and four layers of ice I_h would cause a band gap tuning [110]. The difference is caused by the orientations of the H_2O molecules in the ice clusters. MD simulations of a large number of molecules on a graphene surface at room temperature suggest the distinct existence of an ordering into layers with roughly 3 Å distance [108]. The interaction between an ice-bilayer and a Ni(111) supported graphene layer has been calculated with DFT by Li et al., exhibiting a small band gap opening of ≈ 40 meV around the Fermi level [117].

Dynamics

The diffusion of water on graphene has been studied by means of molecular dynamics (MD) simulations. Ab initio MD by Tocci et al. predict a substantially lower macroscopic friction coefficient in comparison to adsorption on a hexagonal boron nitride surface [118]. A fast diffusion with diffusion constant D =2.6 Å^2/ps is suggested at room temperature by calculations from Park et al. This fast diffusion is suggested to be connected with preferential ordering of the molecules into an ice I_h structure where first layer molecules are situated above the hollow graphene sites [119]. MD simulations at 100 K by Ma et al. predict a diffusion constant $D = 0.6$ Å^2/ps. The authors further stated that observation of diffusing H_2O molecules would be very difficult to achieve, as due to the "ultra-fast diffusion", H_2O molecules would very rapidly agglomerate into clusters [115].

Outline of this chapter

In the present chapter, we present results of HeSE studies on the structural and dynamical properties of water adsorbed on the surface of graphene/Ni(111).

The results from adsorption and diffraction studies show that water adsorbs at low temperature (< 105 K) as amorphous ice, while upon heating, it rearranges into clusters, de-wetting the graphene surface. Above about 120 K, desorption occurs. Thermal and isothermal studies allowed us to determine a desorption energy of 515 meV, which suggests that we are observing desorption from the clusters.

Spin-echo measurements revealed a jump diffusion of H_2O molecules between hollow adsorption sites over a diffusion barrier $E_a = (51 \pm 12)$ meV with a hoppingate of $\eta = (1.81 \pm 0.07) \cdot 10^{-2}\,\mathrm{ps}^{-1}$ at 125 K. Furthermore, the existence of Rayleigh phonon modes from the graphene/Ni(111) surface, as well as from islands has been observed.

5.2 Adsorption and Desorption

5.2.1 Isothermal Adsorption

We have carried out isothermal adsorption measurements of H_2O on a graphene/Ni(111) surface (preparation described in Chap. 4) with the HeSE spectrometer by monitoring the specular reflected helium signal while dosing H_2O onto the surface through a ≈ 1 m dosing arm with length at a 50 mm distance from the opening to the surface. Partial pressure at the surface has been estimated with the use of a correction factor from a previous calibration measurement. In this calibration, adsorption measurements obtained while using the dosing arm were compared with the same measurements while dosing by back filling the vacuum chamber [120]. Taking into account a change in the distance of the dosing arm after installation of an alignment segment, we could interpolate a multiplication factor to convert from the measured background pressure to the actual surface pressure at 50 mm distance. This calculation risks the introduction of a systematic error, that we can only estimate to about 10 %. In addition, the monitored pressure readings from the ionisation gauge need to be corrected by a factor of 1.12 to account for the ionization efficiency of the H_2O molecule [121]. A precise pressure control has been obtained with the use of a leak valve that is attached to the top of the dosing arm. The leak valve itself was usually regulated by a feedback control system in order to maintain a constant pressure. Adsorption has been monitored at 100, 110, 125, 130, and 150 K at a dosing pressure at the surface of about $6 \cdot 10^{-8}$ mbar. The water sample used for the experiments was created in-house by an extensive series of distillation and de-ionization cycles, ensuring a very high water purity. Prior to every series of adsorption, diffraction, or HeSE measurements, the water contained in a glass sample support was purified by several freeze-thaw cycles. In addition, at regular intervals a mass spectrometer signal was monitored to exclude a contamination of the water sample.

Since we expect water not to wet the graphene surface, we cannot technically speak of a monolayer. However, in literature, a monolayer equivalent has been defined in several cases for water on graphite and graphene, where 1 ML corresponds to 0.115 molecules/Å^2 = 0.603 molecules/uc (uc: graphene unit cell), which is equivalent to the density of an ice I_h over-layer [94, 122]. With the theory of kinetic gases (Eq. 3.1), we can relate the exposure to the expected surface coverage, making use of: the gas temperature $T = 289.15$ K, the mass of the water molecule $m = 18.0153$ g/mol, and the pressure p. An exposure of 1 L corresponds therefore to a surface coverage equivalent of 0.0486 Å^{-2} = 0.422 ML, assuming a sticking coefficient of unity.

Adsorption in the range of 100 K – 120 K

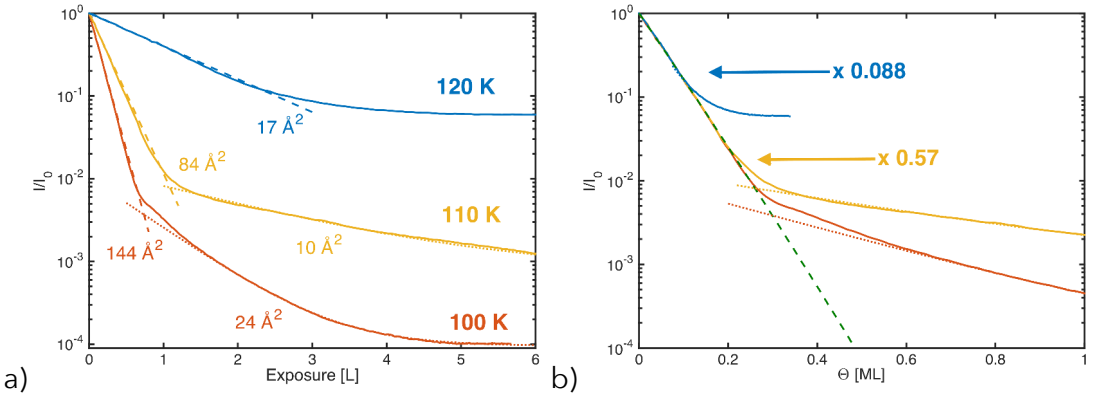

Figure 5.3: Normalized specular helium signal I/I_0 versus exposure for the adsorption of H_2O onto the GR/Ni(111) surface at three temperatures 100 K, 110 K, and 120 K. I/I_0 is shown on a logarithmic scale. Dashed lines indicate the initial signal attenuation with the corresponding helium scattering cross section Σ_1. Dotted lines show an exponential fit to the helium signal at higher coverage, where a lower helium scattering cross section Σ_2 is found.

At 100 K, the specular signal drops exponentially up to an exposure of about 0.6 L, where a second, slower exponential decay sets in. The signal decays to full attenuation and does not recover when the dosing pressure is decreased, which is in accordance with the growth of an amorphous layer. At 110 K and 120 K, the same two decays are observed, but the signal does not fully attenuate. The normalized specular intensity as a function of coverage for measurements at these temperatures is shown in Fig. 5.3 a).

The rapid initial decay of the specular signal, which happens in the very low coverage regime, is characteristic of the adsorption of a non-interacting gas. We have fitted an exponential law $I/I_0 = exp(-\Sigma \cdot n \cdot \theta/\cos(\vartheta_i))$ (Eq. (3.68)), as expected for random adsorption, and a power-law $I/I_0 = (1-\theta)^{\Sigma \cdot n \cdot / cos(\vartheta_i)}$ (Eq. (3.69)), as for the case of lattice adsorption, to the data. Both models worked equally well and produced the same results within the statistical uncertainty, thus we cannot conclude which description is more appropriate. Here, Σ_1 is the helium scattering cross section, $n = 8.69\,\text{Å}^2$ is the surface area that an H_2O molecule occupies at (hypothetical) monolayer coverage, and the term $\cos(\vartheta_i)$ corrects for the increase of the apparent scattering cross section since scattering happens at an initial angle $\vartheta = 22.2°$ with respect to the surface normal. By assuming the relation between exposure and surface coverage equivalent described above and assuming a sticking coefficient of unity we can determine the helium scattering cross section by fitting an exponential function to the data. We repeated the procedure for the high coverage regime, where a second exponential decay is observed. The results are summarized in Tab. 5.2. The

Temperature [K]	Σ_1 [Å^2]	Σ_2 [Å^2]	final I/I_0
100	144 ± 1	23.5 ± 0.5	0
110	(84 ± 1)	10.0 ± 0.2	$(7.2 \pm 0.4)\cdot 10^{-4}$
125	(17.4 ± 0.4)	-	$(5.80 \pm 0.01)\cdot 10^{-2}$

Table 5.2: Helium scattering cross sections and sticking coefficients determined by the slope of specular helium uptake curves. Σ_1 is the scattering cross section of the initial adsorption process, the values for 110 K and 125 K are in brackets since they are apparent cross sections due to a lower sticking coefficient. Σ_2 is the scattering cross section attributed to the second adsorption process at lower coverage. final I/I_0 is the extrapolated value for the final specular signal.

scattering cross section of H_2O has been observed not to change with temperature [38] and this assumption would seem unreasonable. The apparent change in cross section could rather express either a change in sticking probability, an onset of desorption, or an onset of island formation. In the literature, the scattering cross section of H_2O has been measured to be 130 Å^2 (no uncertainty was given) [123], which is lower than the (144 ± 1) Å^2 obtained here, but still in reasonable agreement, if an estimated 10 % uncertainty of the dosing pressure at the surface are taken into account. We thus assume the initial sticking coefficient at 100 K to be close to unity. The dramatic change in the apparent scattering cross section at 110 K and 120 K is unlikely to be due to a change in the initial sticking coefficient. Desorption is still

very slow at 110 K and 120 K. We thus expect the apparent cross section to reflect an onset of island formation that we have observed to start at 105 K, and that would accelerate with higher temperature due to faster surface diffusion. Fig. 5.3 b) shows the specular signal at 110 K and 125 K in comparison to 100 K after rescaling of the surface coverage to account for the change in the apparent scattering cross section.

At 100 K and 110 K, a distinct kink is observed in the specular signal at an exposure of about 1 L, which corresponds to about 0.3 ML surface coverage. The apparent scattering cross sections drop by a factor of 6 and 8.4 at 100 K and 110 K, respectively. At higher coverages, an arriving molecule would statistically have a very high chance to adsorb in the direct neighbourhood of at least one other molecule. Since their cross sections overlap, the effective cross section is reduced. The apparent cross section of 10 Å^2 at 110 K is close to the surface area covered by a single molecule, 8.7 Å^2. This indicates the formation of islands. At 100 K, the cross section is higher by a factor of three. Diffraction measurements suggest that at this temperature, an amorphous ice layer grows on the surface, as will be discussed in the next section. This means that, instead of island formation, a formation of oligomers is more probable.

Adsorption above 120 K

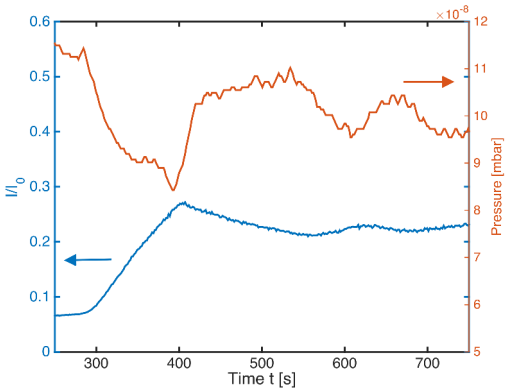

Figure 5.4: Normalized specular helium signal I/I_0 and dosing pressure versus measurement time t at 125 K. The lower, blue curve indicates I/I_0, the upper, red curve the dosing pressure.

At 130 K and 125 K, the specular signal also drops with increasing dosing pressure, indicating adsorption. However, in contrast to sample temperatures below 120 K,

when reducing pressure, the signal recovers at a very fast rate. The system is, thus, in an adsorption-desorption equilibrium. Fig. 5.4 shows an example for the response of specular reflectivity to a change in pressure. At 150 K, no adsorption has been observed even when dosing up to $1.5 \cdot 10^{-7}$ mbar.

5.2.2 Thermal and Isothermal Desorption

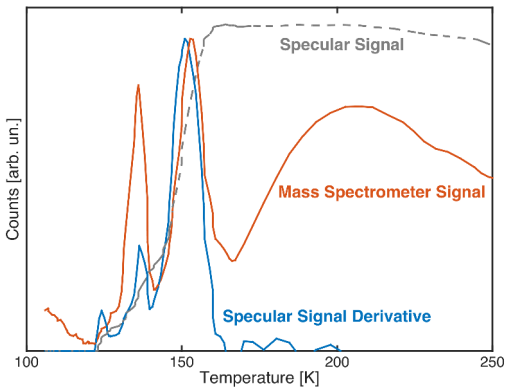

Figure 5.5: Mass spectrometer signal and derivative of the specular helium signal $\mathrm{d}I/\mathrm{d}T$ versus temperature T during thermal desorption of water from graphene/Ni(111), dosed at 100 K. The applied heating rate in the range 130 – 180 K was $\beta = 0.11$ K/s. Orange solid line: mass spectrometer signal. Blue solid line: derivative of specular signal $\mathrm{d}I/\mathrm{d}T$. Grey dashed line: specular signal.

Thermal desorption spectroscopy has been performed while monitoring the $m/z = 18$ peak on a mass spectrometer and simultaneously measuring the specular reflected signal. Fig. 5.5 shows a typical desorption measurement. Clearly visible are two distinct mass spectrometer peaks with maxima at 136 K and 153 K, which coincide with a rapid recovery of the specular signal. The mass peaks at higher temperatures must stem from desorption from other surfaces, such as the sample holder, since no change in specular signal is observed during desorption.

Heating rate [K/s]	$T_{max,1}$	$T_{max,2}$	E_{d1} [meV]	E_{d2} [meV]
0.11	137 ± 2	151 ± 5	444 ± 6	494 ± 16
0.21	144 ± 4	166 ± 5	463 ± 13	536 ± 17

Table 5.3: Desorption energies calculated from the maximum gradient of specular intensity from thermal desorption spectra using the Redhead formula. The measurement uncertainty is based on the peak width.

In order to estimate the desorption energy E_d, we relied on the estimation from Ulbricht et al. [15] for the pre-exponential factor $\nu = 9 \cdot 10^{14}\ s^{-1}$. Applying the Redhead equation [16] to the temperatures at the two peak maxima of the specular intensity gradient yields estimates for desorption energies around 450 meV and 510 meV, respectively. The exact values can be found in Tab. 5.3. The lower energy peak would unlikely stem from desorption from the graphene surface, since calculations predict a much lower desorption barrier of about 100 meV. More likely is the case of desorption from the edge and from the centre of islands, respectively, for the first and second desorption peak.

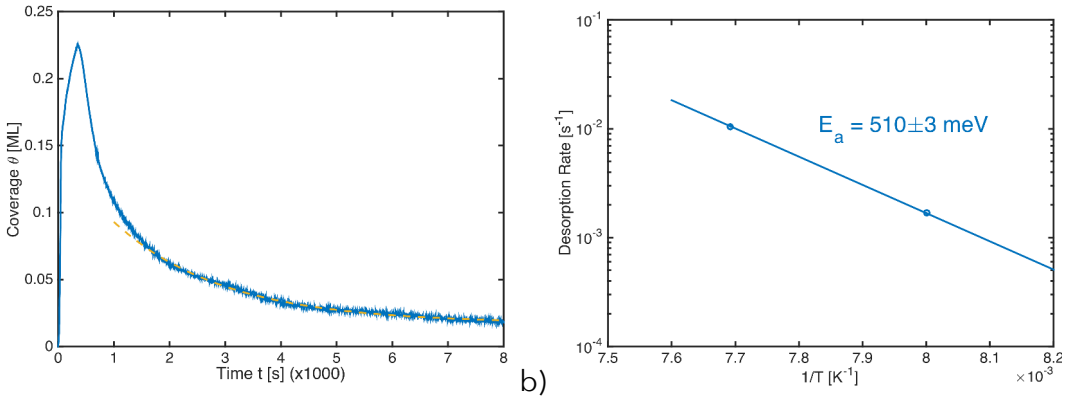

Figure 5.6: Isothermal desorption of water from graphene/Ni(111). a) Surface coverage versus time at 125 K. After 350 s, the dosing valve was closed. Yellow dashed line: Exponential fit to the coverage. b) Logarithm of initial desorption rate versus inverse temperature in an Arrhenius plot. Solid blue line: Linear fit in the range 125 – 130 K. The slope indicates a desorption barrier of 515 meV.

For the isothermal desorption measurement, we exposed the surface to $6 \cdot 10^{-8}$ mbar H_2O overpressure and waited until the system was in equilibrium. We then turned off the exposure and monitored the specular signal recovery. From this we calculated the corresponding surface coverage as a function of time. An example is shown in Fig. 5.6 a): the surface coverage first rises during exposure and then decays exponentially after exposure has been stopped after about 300 s. Unfortunately, we have only measured this desorption rate at 125 K and at 130 K. At 110 K, no desorption was observed and at 150 K, a substantial drop in specular signal could not be observed in the technically available pressure range. The initial desorption rate, which is identical to the exponential decay rate, exhibits an activated temperature dependence at 125 K and at 130 K. Fig. 5.6 b) shows an Arrhenius plot of the desorption rate. The slope of the Arrhenius law corresponds to an activation energy

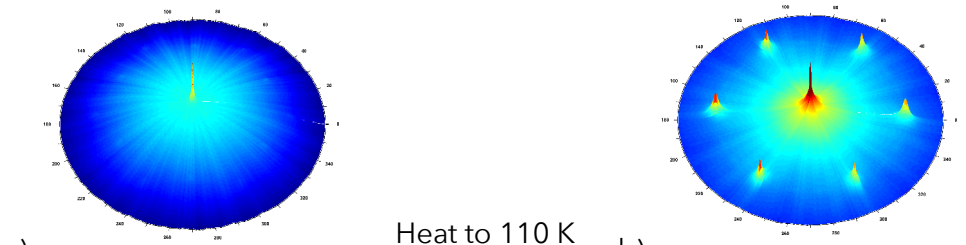

Figure 5.7: Helium diffraction patterns of water adsorbed on a graphene/Ni(111) surface. a) When dosed at 100 K, H_2O forms amorphous ice on the graphene surface; all diffraction signal is lost. b) When heated to 105 K, the original graphene diffraction pattern is recovered (pattern shown was measured at 110 K), showing only the first order (110) diffraction peak and its equivalents in the hexagonal symmetry.

of desorption of (510 ± 3) meV. Since this analysis relies on only two measurement points, the result needs to be viewed with a critical eye. The uncertainty in the energy was established based on the uncertainties of the measured desorption rates and is certainly underestimated.

The results from both desorption studies are higher than the (356 ± 23) meV previously measured by TDS on the graphene/Ni(111) surface, where only a single desorption peak was observed [55] (see Fig. 5.1). They are rather in the range of the reported results from TDS measurements on graphite ((414 ± 80) meV [96], (450 ± 30) meV [94], (480 ± 30) meV [15]).

5.3 Adsorbate Structure

We have performed helium diffraction measurements on the graphene/Ni(111) sample with approximately 1 ML of water adsorbed at different temperatures. Fig. 5.7 shows a comparison between the diffraction pattern of water/graphene at 100 K and at 110 K, where the radial coordinate corresponds to an inclination of the surface plane away from specular geometry and the angular component corresponds to the azimuthal angle of the surface plane (see Sec. 3.3.2 for illustration). After adsorption of H_2O at 100 K, the diffraction scan exhibits no diffraction signal except for specular reflection. We interpret this as being due to the formation of amorphous

solid water (ASW) at the surface. After heating the surface to 110 K, diffraction scans reveal peaks at the same position as the 1st order diffraction of graphene. From subsequent thermal desorption measurements, we can conclude that no desorption occurs at this temperature. The diffraction pattern could thus stem only from a perfect (1 x 1) H_2O over-structure, or from de-wetting of the graphene surface upon melting, which would expose free graphene to the helium atoms. Comparison with the structures of ice I_h and ice I_c, which would be the only reasonable assumptions here, shows that a structure that is closer packed than a ($\sqrt{3}$ x $\sqrt{3}$) over-structure, cannot be assumed. We thus conclude in accordance with the strong hydrophobicity of graphene and graphite, that de-wetting occurs at 105 K, as revealed by a subsequent monitoring of the diffraction peak during slow heating.

5.4 Adsorbate Dynamics

We measured intermediate scattering functions for a range of momentum transfers Δk at a temperature of 125 K along the two principal axes of the hexagonal graphene surface, $\overline{\mathbf{\Gamma}\mathrm{K}}$ and $\overline{\mathbf{\Gamma}\mathrm{M}}$. In both directions, measurements have been performed over a momentum transfer range from 0 to 3.2 Å^{-1}. A first series of measurements was obtained using a power supply that delivers a current of up to 10 A, allowing us to access a Fourier time range from 0.6 to 600 ps. Measurements were then repeated under the same conditions with a different power supply that delivers up to 1 A, but at higher precision, allowing us to focus on smaller Fourier times in the range from $5 \cdot 10^{-2}$ to 60 ps.

We monitored the specular signal before each measurement to ensure a constant surface coverage of H_2O on the graphene surface. The surface coverage was controlled throughout the measurements by applying a constant H_2O overpressure. The specular attenuations and corresponding calculated surface coverages, at which spin-echo measurements have been performed, are shown in Tab. 5.4. We generally observed the existence of two exponential decays, a faster one with decay rates in the order of several ps^{-1} and a slower one with decay rates in the order of 0.01 ps^{-1}.

I/I_0	θ [ML]
1/3	0.06
1/5	0.09
1/40	0.20

Table 5.4: Relative specular reflectivities I/I_0 and corresponding surface coverages θ, at which HeSE measurements have been performed.

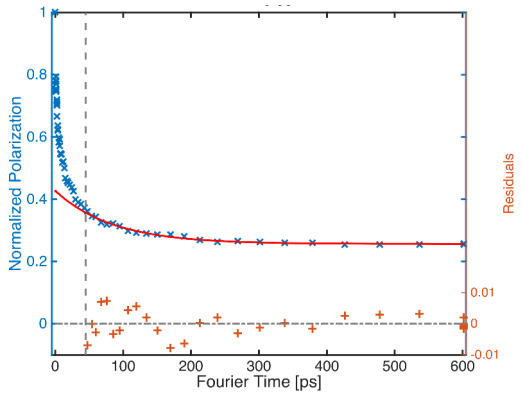

Figure 5.8: Normalized polarization versus Fourier time t at $\Delta k = 0.38\,\text{Å}^{-1}$ in $\overline{\Gamma M}$ direction. Blue crosses: ISF of 0.06 ML H_2O on the graphene surface at 125 K. Red line: single exponential decay fitted to the experimental data. Orange crosses: Residuals. Grey dashed line: lower threshold at 45 ps.

5.4.1 Surface Diffusion

We have analysed the SE measurements by MATLAB (using the built-in non-linear least squares, trust-region algorithm) fitting a single exponential decay to the real part of the ISF:

$$I(\Delta k, t) = I_{qe}(\Delta k) \cdot \exp[-\alpha(\Delta k)t] + I_{el}(\Delta k), \tag{5.1}$$

with the elastic and quasi-elastic polarization amplitudes $I_{el}(\Delta k)$ and $I_{qe}(\Delta k)$, respectively, and an exponential decay rate $\alpha(\Delta k)$. An example for a measured ISF is shown in Fig. 5.8, depicting the measurement points as crosses, together with a solid line that represents the fitted model function from Eq. (5.1). Values at lower times than a certain threshold have not been taken into account in the fitting to avoid inference of a second, rapid decay. The threshold has been decided individually for each ISF by analysing the distribution of the residuals. It lies in general in a range from 20 to 50 ps.

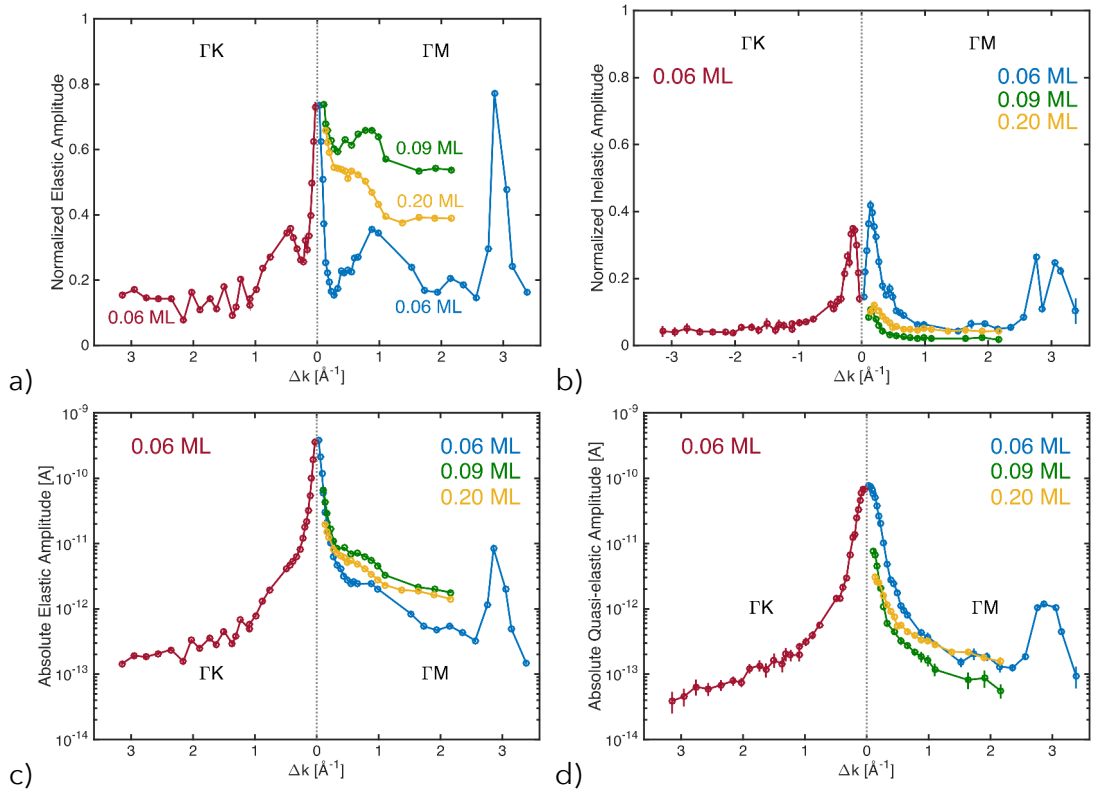

Figure 5.9: Quasi-elastic and elastic amplitudes of different H_2O coverages at 125 K versus Δk. a) and c) relative and absolute elastic polarization amplitudes $I_{el}(\Delta k)$ and $\tilde{I}_{el}(\Delta k)$, respectively; b) and d) relative and absolute quasi-elastic polarization amplitudes $I_{el}(\Delta k)$ and $\tilde{I}_{el}(\Delta k)$, respectively.

The resulting quasi-elastic and elastic amplitudes, $I_{qe}(\Delta k)$ and $I_{el}(\Delta k)$, respectively, are relative contributions due to the normalisation of the ISF. Multiplication with $\tilde{I}(\Delta k, t = 0)$ yields the absolute amplitudes. Both are shown in Fig. 5.9 for different surface coverages and along the two principal directions. $I_{el}(\Delta k)$ is depicted in Fig. 5.9 a); it exhibits sharp peaks at the positions of specular reflection and first order diffraction from graphene, as well as broader peaks at about 1 $Å^{-1}$ in the $\overline{\Gamma M}$ direction and 0.5 $Å^{-1}$ in the $\overline{\Gamma K}$ direction. Looking at the absolute elastic amplitude in c) leads to the suspicion that instead of separate peaks, rather a very broad peak around $\Delta k = 0$ is seen here. The reason for the occurrence of this peak will be discussed again at a later point in this section.

Fig. 5.9 b) shows $I_{qe}(\Delta k)$, which exhibits asymmetrical peaks that seem to be positioned on the edges of the mentioned diffraction peaks. Strangely, there is no linear dependence of the amplitudes on the surface coverage. At 0.20 ML, $I_{el}(\Delta k)$

is higher than at 0.06 ML, but lower than at 0.09 ML coverage. The opposite behaviour is found for $I_{qe}(\Delta k)$. The absolute amplitude shown in d) makes it clear that this strange shape stems from the normalization of broad peaks around specular and first order diffraction; in the relative amplitude, the sharp elastic peak has been "cut out", giving rise to this peculiar shape. The broad peaks in the absolute amplitude can be interpreted as the form factor of the H_2O molecule, as approximately shown in Fig. 3.15.

The exponential decay rate $\alpha(\Delta k)$ is shown in Fig. 5.10 a); except for 0.20 ML the decay rates exhibit a steep initial rise, which we expect to be linked to de Gennes narrowing. As discussed in Sec. 3.3.3, we can tentatively calculate the incoherent decay rate $\alpha_{inc}(\Delta k)$. Since $\alpha_{inc}(\Delta k)$ contains only information about the self-correlation function of a diffusing molecule, this simplifies a comparison to incoherent self-diffusion models considerably. The calculation of $\alpha_{inc}(\Delta k)$ follows Eq. (3.77). Neglecting effects of substrate diffraction, which plays a role only locally around the diffraction peaks, we divide $\alpha(\Delta k)$ by $I_{qe}(\Delta k)$ and subsequently need to multiply by the quasi-elastic structure factor $S_{qe}(\Delta k)$. We have no experimental measurement of the (pure) structure factor, however, we expect that in regions, where no diffraction from substrate or ordered over-structures appears, the coherent and the incoherent decay rates are approximately the same, $\alpha(\Delta k) = \alpha_{inc}(\Delta k)$, from which follows that in these regions $I_{qe}(\Delta k) = S_{qe}(\Delta k)$. Looking again at Fig. 5.9 b), we observe that $I_{qe}(\Delta k)$ is flat except for the regions around diffraction peaks. We thus used a constant value derived from averaging the flat region of $I_{qe}(\Delta k)$ to re-scale $\alpha(\Delta k) I_{qe}(\Delta k)$. We refer to the result as $\alpha_{inc}(\Delta k)$, even if it is not an incoherent decay rate. It still contains a contribution by $S_{qe}(\Delta k)$, but for an dilute adsorbate phase without significant structural ordering, it approaches $\alpha_{inc}(\Delta k)$. The results need thus to be interpreted with care.

The incoherent decay rate $\alpha_{inc}(\Delta k)$ is shown in Fig. 5.10 b). It exhibits a sinusoidal Δk dependence that is characteristic of jump diffusion; the periodicity of about 2.9 $Å^{-1}$ in $\overline{\Gamma M}$ direction suggests a jump distance that corresponds to the size of the graphene unit cell. In the measured Δk-range, the decay rate is in the order of 0.01 ps^{-1} at 125 K. This temperature corresponds to a mean kinetic energy in the order of 10 meV. As discussed in the introduction, the adsorption energy of an H_2O molecule in an ice cluster is predicted to be in the order of 500 meV [90, 109], while for the adsorption energy of a molecule on the graphene surface, values in the order of 100 meV have been calculated (see. Tab. 5.1). We thus expect to observe the

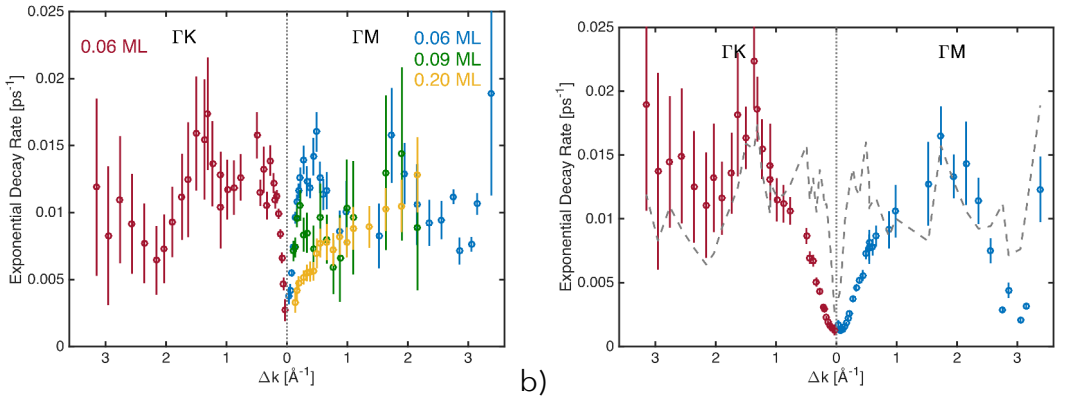

Figure 5.10: Exponential decay rate of H_2O on graphene at 125 K versus Δk. Blue and red: 0.06 ML coverage; green: 0.09 ML coverage; yellow: 0.20 ML coverage; a) Observed decay rate when fitting Eq. (5.1). b) Decay rate at 0.06 ML coverage after correction as described in Sec. 3.3.3. Grey dashed line: uncorrected decay rate for comparison.

diffusion of H_2O on graphene, rather than on the surface of an ice cluster.

Fig. 5.11 shows $\alpha(\Delta k)$ in comparison to the decay rate of hopping on a hexagonal Bravais lattice with $a = 2.49$ Å hopping distance. Fitting a sum of jumps to nearest, next-nearest, and next-next-nearest neighbours produced a most probable fit with a hopping rate $\tau^{-1} = (1.81 \pm 0.07) \cdot 10^{-2}$ ps^{-1} and a relative contribution of $p_n = (57 \pm 6)$ %, $p_{nn} = (31 \pm 7)$ %, and $p_{nnn} = (12 \pm 6)$ % for nearest, next-nearest, and next-next-nearest neighbour jumps, respectively. For an illustration of these three jumps, see Fig. 5.12. For each distance, jumps to six positions are possible, as indicated by the coloured dots. Also significant is the occurrence of a Δk-independent offset $C = (1.1 \pm 0.1) \cdot 10^{-3}$ ps^{-1}. We interpret this as a motion of the molecules in the z-direction since the parallel component of Δk vanishes in the specular reflection condition. However, it has to be kept in mind, that the correction, which has been applied to the exponential decay rates, is not valid in regions very close to substrate diffraction peaks (i.e. at (0 ± 0.2) Å^{-1} and at (2.9 ± 0.2) Å^{-1}).

We assume that hopping occurs between hollow adsorption sites on the graphene surface. However, jumps from **top** to **top**, as well as from **bridge** to **bridge** adsorption sites are also important options to consider since they bear a very similar signature. Looking at the first case, the **top** adsorption sites are in general not degenerate because of the Ni(111) surface that lies below the graphene layer (see Fig. 3.9); instead the geometry can be described by two hexagonal Bravais lattices with different adsorption energies. A generalized jump diffusion model for non-equivalent

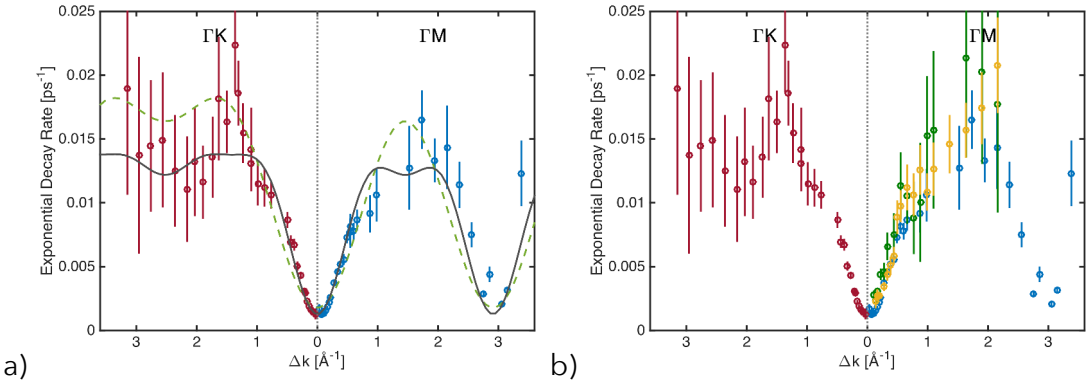

Figure 5.11: Corrected exponential decay rate of H_2O on graphene at 125 K versus Δk. Blue and red: 0.06 ML coverage; green: 0.09 ML coverage; yellow: 0.20 ML coverage. a) Black solid line: CE model with possible jumps to the three closest sites. Green dashed line: CE model with jumps to only neighbouring sites; b) Comparison of decay rates at different surface coverages.

adsorption sites has been established by Tuddenham et al. [35]. We would only expect a small non-degeneracy between the sites since hydrogen atoms adsorbed on the pure Ni(111) layer show almost perfect degeneracy [50] and since we expect the additional highly symmetric graphene layer not to increase the energetical asymmetry between sites. For the degenerate case, the observed decay rate is by a factor two larger along the $\overline{\mathbf{\Gamma}\mathrm{K}}$-direction than along the $\overline{\mathbf{\Gamma}\mathrm{M}}$-direction. For non-degenerate sites, a second, faster decay appears, with an amplitude that is very low up to about 1.5 Å^{-1}, and then rises steeply (see Figs. 6 and 7 in [35]). We do not observe such a contribution, however the existence of surface phonons and a fast rotational diffusion make a judgement difficult. **Bridge** to **bridge** jumps bear a similar geometry **top** jumps. By the same reasoning, we do not expect this to be an option, since for the case of very small non-degeneracies, the decay rate in $\overline{\mathbf{\Gamma}\mathrm{K}}$-direction is significantly higher. However, further investigation are needed to test our assumption that the observed process corresponds to jumps between **hollow** sites.

HeSE measurements at different temperatures revealed an activated temperature dependence of $\alpha(\Delta k)$ (see Fig. 5.13). To ensure a constant surface coverage of 0.06 ML at all temperatures, an over-pressure was applied for each measurement, which corresponded to $I/I_0 = 1/3$ specular reflected signal. The observed activation energy, which is given by the slope of the logarithm versus inverse temperature, seems to differ between the two momentum transfers Δk, at which measure-

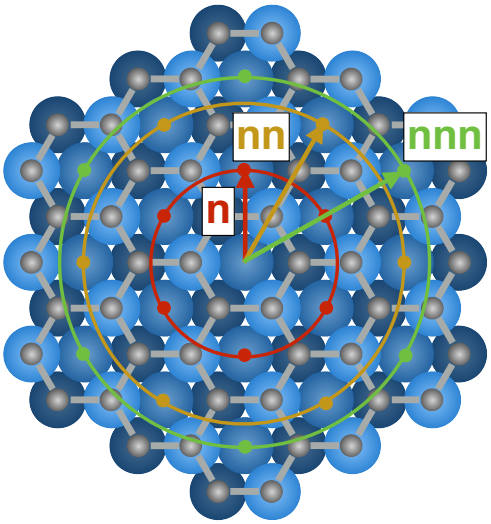

Figure 5.12: Illustration of nearest (n), next-nearest (nn) and next-next-nearest neighbour jumps between **hollow** adsorption sites on the graphene/Ni(111) lattice.

ments have been performed. This might be linked to a change in the relative contributions of elastic and quasi-elastic amplitudes, which is connected to $\alpha(\Delta k)$ by the de Gennes narrowing discussed above. It has to be noted that a calculation of $\alpha_{inc}(\Delta k)$, as applied before over a momentum transfer range, has not been applied here, as measurements at two Δk points do not contain sufficient structural information. In the lack of means for further investigation, we take the average value $E_a = (51 \pm 12)$ meV as an approximative result for the activation barrier of jump diffusion. In the case of the expected jump diffusion between **hollow** sites, this activation energy would correspond to the potential energy difference between a **hollow** and a **bridge** adsorption site, which would need to be overcome during a jump. This value is quite high in comparison to what is expected from DFT calculations. As discussed in the introduction of this chapter, adsorption energies are predicted to be in the range of 130 meV (see Tab. 5.1). The calculated differences of adsorption energies between **hollow** and **bridge** sites are in most studies in the order of only a few meV (e.g. 10 meV [54], 13 meV [113], 7 meV [117]).

5.4.2 Surface Phonon Decay and Rotational Diffusion

We have repeated the SE measurements at 0.06 ML surface coverage at 110 K and at 125 K with the use of a different power supply for the precession coils, which de-

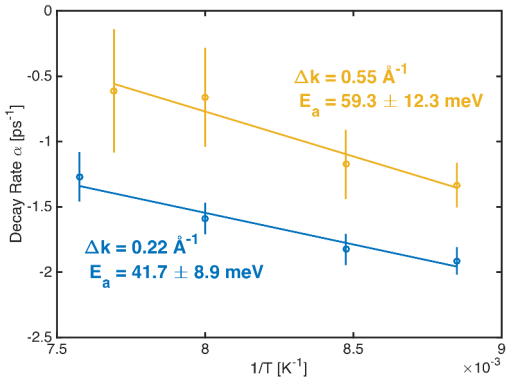

Figure 5.13: Arrhenius plot of $\alpha(\Delta k)$ versus inverse surface temperature of 0.06 ML H_2O on graphene at $\Delta k = 0.22\,\text{Å}^{-1}$ and $\Delta k = 0.55\,\text{Å}^{-1}$. The straight solid lines indicate fits to an Arrhenius-type model function.

livers a lower current at a higher precision, which enabled us to measure at a range of Fourier times from $5 \cdot 10^{-2}$ to 60 ps. In this time range, the fast decay of the polarization is well resolved.

We have calculated a DSF from each ISF measurement at different off-specular angles γ by Fourier transformation. This can be used to create a map of the DSF along γ and along ΔE. Since HeSE measurements had been undertaken using an exponential spacing between the Fourier time points, interpolation of the ISF prior to Fourier transformation was necessary. This procedure could in general introduce non-physical artefacts. We varied the sampling rate of the interpolation to test for the possible appearance of such artefacts, but none were observed in the low energy range that we are interested in. The final results were obtained by interpolating 2^8 linearly spaced query points. Furthermore, a Hann window function [124] was used for the Fourier transformation, which was carried out by using a standard fast Fourier transform (FFT) algorithm.

Fig. 5.14 shows the $S(\gamma, \Delta E)$ map that was extracted from the measurements. The Rayleigh mode and the longitudinal resonance, which we had previously observed on the bare graphene surface are clearly visible. Rough estimates of the initial slopes are shown in Fig. 5.14 b) for the Rayleigh mode (yellow dashed line) and for the longitudinal resonance (grey dotted line).

The inelastic peak of a phonon at ΔE for a given Δk appears in $I(\Delta k, t)$ in the form of oscillations of exponentially decaying amplitude with frequency $\omega = \frac{\Delta E}{\hbar}$. The exponential decay rate is linked to the physical decay rate of the coherence of a phonon,

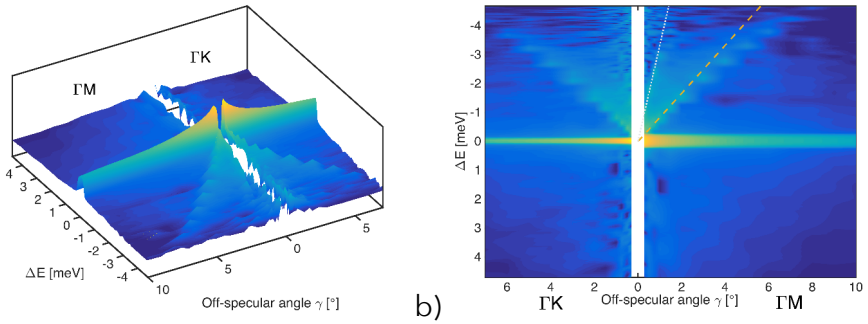

Figure 5.14: Colour plots of $S(\gamma, \Delta E)$ of 0.06 ML H_2O on GR at 110 K along $\overline{\Gamma K}$ and $\overline{\Gamma M}$; Heights and colours are scaled logarithmically and in the 3D view, smoothing has been applied for a better elucidation. a) 3D colour plot to emphasize the existence of the specular reflection peak and of the phonon branches. b) The same plot in 2D view. The bright horizontal line corresponds to elastic scattering; Yellow dashed line: initial slope of the graphene/Ni(111) Rayleigh mode. Grey dotted line: initial slope of the ice Rayleigh mode.

but depends on the slope of the phonon dispersion line relative to the direction of the measurement in the ΔE–Δk plane. This would theoretically allow us to include an oscillating term in the model function for the fitting procedure. However, the high oscillation frequency and the fact that contributions from two surface phonon modes occur, makes this process too unstable to be successful. At short Fourier times we observed the coexistence of a fast exponential decay, and of decaying oscillations from the surface phonons. We have not succeeded in separating the two, instead an approximative approach turned out to work, which includes the use of a sum of two exponential decays together with a constant term as a model function:

$$I(\Delta k, t) = I_{fa}(\Delta k) \cdot \exp[-\alpha_{fa}(\Delta k)t] + I_{qe}(\Delta k) \cdot \exp[-\alpha_{qe}(\Delta k)t] + I_{el}(\Delta k), \qquad (5.2)$$

where $I_{fa}(\Delta k)$ and $I_{qe}(\Delta k)$ are the amplitudes of the fast and of the slow exponential decay, respectively. $I_{el}(\Delta k)$ is the elastic amplitude. $\alpha_{fa}(\Delta k)$ is the decay rate of the fast exponential decay and $\alpha_{qe}(\Delta k)$ is the decay rate of the slow quasi-elastic component, which stems from the jump diffusion that we have already observed in the long Fourier-time measurements. In this approach, the first, faster decaying exponential function needs to be seen as an approximation that allows us to identify the nature of the fast decay. Fig. 5.15 a) shows an exemplary ISF of the clean graphene surface in comparison with the ISF of 0.06 ML H_2O coverage at the same Δk. The

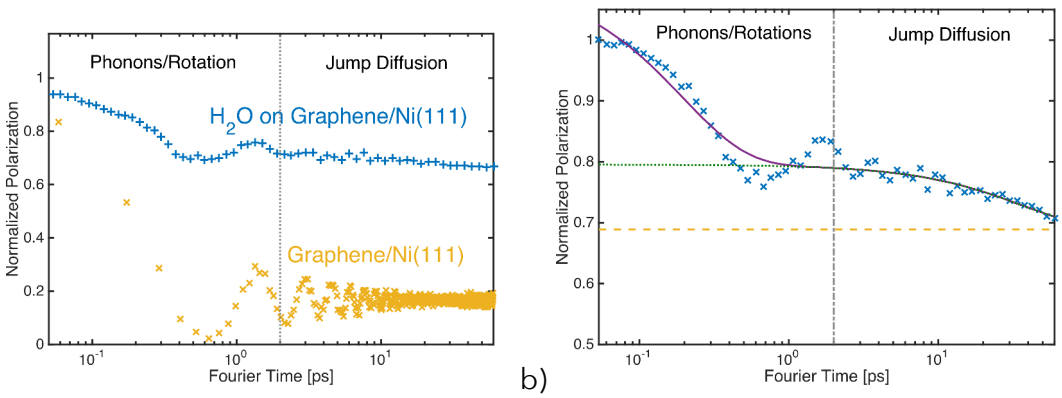

Figure 5.15: Examples of ISFs for H_2O covered and clean graphene. a) normalized polarization versus Fourier time, $\Delta k = 0.33$ Å^{-1}; Yellow "x" symbols: Clean graphene at 150 K; Blue "+" and diamond symbols: 0.06 ML H_2O on graphene at 125 K. b) normalized polarization versus Fourier time, for 0.06 ML H_2O on graphene at 125 K, $\Delta k = 0.27$ Å^{-1}. Lines show fit parameters from fitting Eq. (5.2). Yellow dashed line: elastic contribution; green dotted line: Slow decay plus elastic contribution; purple solid line: Entire fitted function, including fast decay.

ISF of the clean graphene surface decays rapidly to a low, constant polarization, due to surface phonons. Fig. 5.15 b) shows an ISF of 0.06 ML H_2O coverage at a similar Δk, together with the results from fitting Eq. (5.2). It is important to notice that the time scale is plotted logarithmically in both figures, in order to visualise both decays, which are separated by two orders of magnitude in terms of the decay rate. This is also the reason why an exponential Fourier time spacing was chosen for the measurements: in order to be able to measure over a very large time range and with a high resolution in time, but still at reasonable data acquisition times. The different components of Eq. (5.2) as a result of the fitting are shown separately in the figure. The oscillations are clearly visible, with a seemingly increasing frequency due to the logarithmic time scale.

The fast decay rate $\alpha_{fa}(\Delta k)$ is shown in Fig. 5.16. At both temperatures and in both crystal directions, it exhibits a steep initial rise up to about 0.7 Å^{-1}, where a distinct kink is visible. At higher Δk, a sort of sinusoidal shape follows. A comparison with $S(\Delta k, \Delta E)$ (Fig. 5.14) shows that it is at the momentum transfer, where the kink is found, that the graphene Rayleigh mode reaches an energy at the limit on the creation side, given by the energy of the incoming helium atoms (or rather by the Fourier time spacing of the measurement, which determines the maximum observable energy by the Fourier relation between time and energy space).

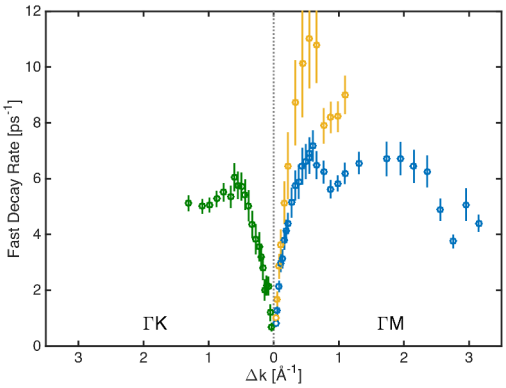

Figure 5.16: Fast decay rate $\alpha_{fa}(\Delta k)$ of 0.06 ML H_2O on graphene versus Δk. Blue and green: temperature 125 K; yellow: temperature 110 K.

Fig. 5.17 a) shows the relative amplitude $I_{fa}(\Delta k)$ of the fast decay. It rises steeply up to about 0.4 Å^{-1}, where it drops up to about 0.9 Å^{-1}. We interpret this as the contribution from the surface phonons by the same reasoning as for $\alpha_{fa}(\Delta k)$. For Δk above 0.9 Å^{-1}, the amplitude rises again and drops sharply at the position of the first order diffraction peak. We tentatively attribute this behaviour to a contribution from rotational diffusion of the H_2O molecules. For uni-axial rotational diffusion in the surface plane, the incoherent ISF is given by [125]:

$$I_{inc,rot}(\Delta k, t) = \sum_{l=0}^{\infty} j_l^2(\Delta k \cdot R) \exp[-l^2 D_R t], \tag{5.3}$$

where j_l is the cylindrical Bessel function of the first kind, R is the radius of rotation and D_R is a rotational diffusion constant. D_R is Δk-independent, but the relative contributions of the Bessel functions in the summation depend on Δk. For R, we have chosen the distance of the hydrogen atoms in the H_2O molecule to its centre of mass, $R = 0.912$ Å. This would be exactly correct for the case of neutron scattering, but can only serve as an approximation here, since the helium atom scatters from the valence electron cloud of the molecule. The amplitudes $j_l^2(\Delta k \cdot R)$ for $l = 1 \ldots 4$ from Eq. (5.3) are also plotted in Fig. 5.17 a). From the plots it can be seen, that only the first four terms in the summation contribute in the Δk range that we are studying. For the case of isotropic rather that uni-axial rotation, a law similar to Eq. (5.3) is found, but with spherical Bessel functions, which seem to agree less with $I_{fa}(\Delta k)$ than the cylindrical ones (see grey dashed line in Fig. 5.17 a) for the $l = 1$ contribution of isotropic rotations). Here, we made the comparison between rotational diffusion

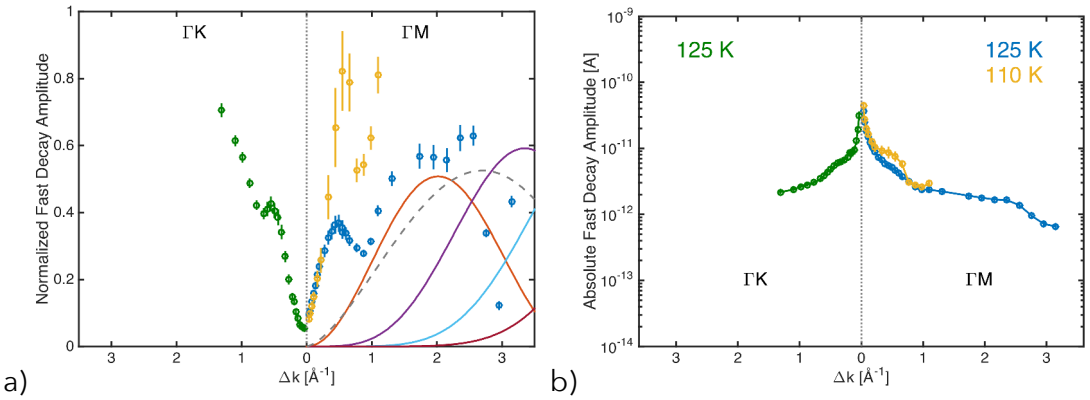

Figure 5.17: Fast decay amplitude of 0.06 ML H_2O on graphene versus Δk. Blue and green: temperature 125 K; yellow: temperature 110 K. a) relative amplitude $I_{fa}(\Delta k)$. b) absolute amplitude $\tilde{I}_{fa}(\Delta k)$. Solid lines: expected contributions from rotational diffusion, as explained in the text. Bright red line: $l = 1$; purple line: $l = 2$; blue line: $l = 3$; dark red line: $l = 4$; grey dashed line: first order spherical Bessel function for isotropic rotations.

and the *relative* decay amplitude. This has to be viewed with suspicion, since relative contributions from the slow exponential decay and from the elastic signal might interfere. However, in the Δk range of interest, i.e., 1 – 2.7 Å^{-1}, the observed slow decay amplitude and the elastic amplitude are rather constant in Δk. Fig. 5.17 b) shows the absolute amplitude of the fast decay. It is very flat in comparison to the elastic and the slow decay amplitudes, but the form factor makes a comparison with rotational diffusion impossible. A straightforward procedure to test the idea of rotational diffusion would be to fit Eq. (5.3) to the measured ISFs. This idea should be tested as a next step in future research.

Rotational diffusion also gives rise to an elastic contribution, which corresponds to the $l = 0$ term of Eq. (5.3):

$$I_{el,rot}(\Delta k) = j_0^2(\Delta k \cdot R). \tag{5.4}$$

Fig. 5.18 shows the sum of $I_{qe}(\Delta k)$ and $I_{el}(\Delta k)$, from the measurements at long Fourier times, together with a plot of Eq. (5.4), incorporating an offset of 0.2 to approximately match the data (relative to the short time scales of the fast decay, the slow decay needs also to be treated as elastic). While it does not exactly match the data, it may serve as an explanation of the observed broad peaks around 1 Å^{-1}. This interpretation might at first seem contradictory to the absence of rotational diffusion

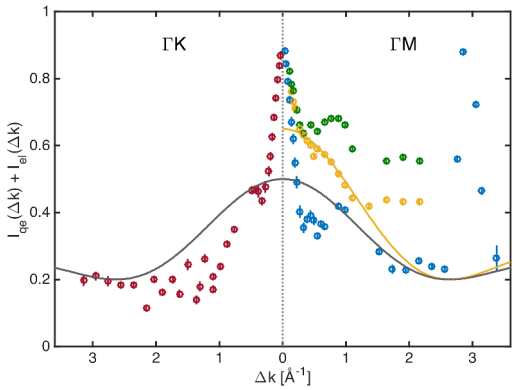

Figure 5.18: Sum of slow quasi-elastic amplitude $I_{qe}(\Delta k)$ and elastic amplitude $I_{el}(\Delta k)$ versus Δk. Blue and red: 0.06 ML coverage; green: 0.09 ML coverage; yellow: 0.20 ML coverage. Grey and yellow lines: zeroth order Bessel function $j_0^2(\Delta k \cdot R)$ with an arbitrary amplitude plus an offset of 0.2 to match the experimental data.

in the benzene/graphene data discussed in Chap. 7. Our idea is that, since the benzene molecule exhibits a de-localized π-band, rotations might not be visible to the helium atom. The H_2O molecule, on the other hand, exhibits a significant dipole moment and a scattered helium atom would thus be sensitive to rotations.

5.5 Conclusions

We have studied the adsorption, structure and dynamics of sub-monolayer H_2O adsorbed on a graphene/Ni(111) surface.

Specular ^{3}He reflection measurements of the adsorption of H_2O on the graphene surface revealed an initial adsorption with low interaction between molecules that allowed us to determine a helium scattering cross section for the benzene molecule, $\Sigma = (144 \pm 1)$ Å^2. No formation of an H_2O monolayer was observed, indicating that the H_2O does not wet the graphene surface. Instead, a decrease of the apparent helium scattering cross section was observed at high sub-monolayer coverage, indicating the formation of islands.

Isothermal desorption measurements of sub-monolayer coverages exhibit an exponentially decaying surface coverage. The initial desorption rate obeys an activated temperature dependence with an activation energy of desorption of (510 ± 5) meV. TDS measurements revealed the existence of two desorption peaks. Analysis of the

dependence of desorption temperature with heating rate via the Redhead formula yields activation energies of desorption of about 450 meV and 510 meV from the two desorption peaks. We tentatively attribute them to desorption from the edge and the surface of an island.

We have performed helium diffraction measurements of about 1 ML of H_2O at 100 K and at 110 K. At 100 K, no diffraction was observed and the graphene diffraction peak was completely suppressed. We attribute this to the formation of amorphous ice. At 110 K, a recovery of the graphene diffraction peaks was observed, with no additional diffraction. This has been interpreted as a de-wetting of the graphene surface upon heating, resulting in island formation.

HeSE measurements at 125 K in the coverage range 0.06 – 0.12 ML revealed the existence of a slow activated diffusion with an activation energy for diffusion $E_a = (51 \pm 12)$ meV. Applying a tentative calculation of the incoherent ISF decay rate revealed jump diffusion between hollow adsorption sites. At 125 K, we found a hopping rate $\tau^{-1} = (1.81 \pm 0.07) \cdot 10^{-2}\,\mathrm{ps}^{-1}$ and a relative contribution of $p_n = (57 \pm 6)\,\%$, $p_{nn} = (31 \pm 7)\,\%$, and $p_{nnn} = (12 \pm 6)\,\%$ for nearest, next-nearest, and next-next-nearest neighbour jumps, respectively.

At short Fourier times, a fast decay was observed, which we tentatively attribute to uni-axial rotational diffusion of H_2O molecules on the graphene surface. In addition, oscillations are visible, which stem from the Rayleigh surface phonon and from the longitudinal resonance of the graphene surface.

6 The Structure of Deuterated Benzene Adsorbed on the Graphite (0001) Basal Plane

6.1 Introduction

The purpose of this chapter is to discuss the structure of benzene adsorbed on the graphite plane at coverages below and above the monolayer. While no dynamics are studied in this chapter, the implications of the adsorbed structure on surface diffusion are quite important. In the following chapter (Chap. 7), we will then discuss surface diffusion of benzene on the graphene/Ni(111) layer.

The neutron data, on which this chapter is based, have been measured by H. Hedgeland, A.P. Jardine and P. Fouquet some years ago. They have been included in the doctoral thesis of H. Hedgeland together with a basic structural discussion on the raw data [126]. This chapter is based on the same data, but my analyses carry the structural discussion to a significantly more detailed level and draws conclusions hitherto undiscovered. We have also published the work of this chapter in 2014 [127].

The structure of adsorbed benzene has been studied for several decades and yet continues to be of active interest [128, 129]. From a fundamental point of view, benzene is of great importance as it represents the smallest building block of a layered hexagonal carbon system and in spite of its high symmetry it gives rise to complex structures and dynamics [130, 131, 132, 133, 134, 135, 136].

A detailed understanding of benzene physisorption is also important for the development and improvement of filtering systems. Benzene is a highly toxic and carcinogenic aromatic carbohydrate that occurs naturally in crude oil and coal deposits and its safe removal is thus of great concern for petrochemistry [137, 138]. Finally, benzene on carbon surfaces has been considered as an important prototype for

studying elementary dynamic processes and friction in view of the development of nanometre size motorization systems [135, 139].

The structure of bulk crystalline benzene has been studied for more than fifty years [140, 141, 142]. The benzene's multipole moments cause a perpendicular relative orientation of adjacent molecules (the symmetry of the molecule suppresses net charge and dipole moment). Recently, the structure of liquid benzene has also been investigated in detail [143].

The sub-monolayer structure of benzene adsorbed on graphite has been the subject of much debate. Whilst authors using nuclear magnetic resonance (NMR) [130, 144] and QENS measurements [131] suggested that the molecules stood upright on the graphite surface, neutron diffraction studies suggested flat lying molecules and a commensurate $(\sqrt{7} \times \sqrt{7})\mathbf{R}19°$ monolayer structure [132]. The flat adsorption geometry was confirmed several years later by low-energy electron diffraction (LEED) [145, 146], X-ray diffraction [147], and further NMR measurements [148, 149]. These heterogenous results were also reflected in the theoretical work on benzene on graphite: First MD simulations produced a structure that consisted mainly of flat lying molecules, but contained also a non-negligible fraction of upright molecules [150, 151, 152, 153, 154, 155].

A recent Grand Canonical Monte Carlo (GCMC) simulation in the liquid phase (273 – 373 K) produced a monolayer consisting of mostly flat lying molecules [156]. It is worth noting that in the latter publication the importance of including a quadrupole interaction in the calculation is discussed. This is to be expected in view of the alternating structure of the benzene crystal that is mainly due to dominant quadrupole interactions [140]. The existence of a second surface layer has been discussed at several occasions. Whilst, to our knowledge, no experiment before has aimed to study it, several simulations on this question have been performed [150, 152, 153, 155, 156]. The results differ, but suggest in their majority the existence of a disordered, liquid-like second layer [156, 155, 153]. Finally, there have been structural studies using a density functional theory (DFT) approach [157]. The latter do not consider, however, lateral interactions.

Here, we report on neutron diffraction measurements on fully deuterated benzene, C_6D_6 adsorbed on the basal plane surface (0001) of exfoliated graphite. These measurements cover for the first time relative surface coverages between 0.15 and 2 ML

in a coherent experiment. This represents a full overview of the structure from isolated molecules to a dense double layer. Our data indicate the transition to a three-dimensional liquid at coverages of more than 1 ML. The structure was followed from low temperature across the melting transition up to 250 K.

This chapter is organised as follows: After this general introduction, we describe the sample preparation procedure and the instrument parameters used for the measurements. In the subsequent section, we present the experimental results and the analysis. We finish the chapter with a discussion of the results in view of past results and future research.

6.2 Experimental

6.2.1 Sample Preparation

As explained in the introduction, the sample preparation and the experimental procedure have not been undertaken by me, but by H. Hedgeland, A. P. Jardine and P. Fouquet. For completeness, I will nevertheless include their description in this sub-section.

Neutron and x-ray diffraction experiments of hydrocarbon molecules adsorbed on graphite require the use of high surface density substrates due to the small surface signal. Here, chemically exfoliated graphite has been used, which is a widely used high surface density material that typically has a specific surface area of about $20\,m^2g^{-1}$ and retains a sufficiently low defect density [158, 159]. In addition, exfoliated graphite samples show a preferential orientation of the basal plane surfaces. This was exploited by orienting the basal planes parallel to the scattering plane of the neutrons. 25 g of Papyex exfoliated graphite of grade N998 (> 99.8 % C, Carbone Lorraine, Gennevilliers, France) was prepared in the form of exfoliated graphite disks of 2 cm diameter that were heated to 973 K under vacuum for 4 days and subsequently transferred to a cylindrical aluminium sample holder under protective atmosphere. The sample holder was sealed by a lid with a steel knife edge and connected to a gas sorption system via a heated steel capillary. The surface density of the sample was measured *in-situ* by Brunauer-Emmett-Teller (BET) nitrogen adsorption isotherms that were obtained using a high precision absolute pressure gauge (Baratron 690A, MKS Instruments). A specific surface area of $23\,m^2g^{-1}$ was found.

Fully deuterated benzene (99.6 % D, CEA Saclay) was used in this experiment to enhance coherent scattering. Here, the relative surface coverage, θ, is defined by the ratio of the molecular density, ρ, divided by the density of the $(\sqrt{7}\,\mathrm{x}\,\sqrt{7})\,\mathbf{R}19°$ structure ($\rho_{ML} = 1/36.7\,\text{Å}^{-2}$, [146]): $\theta = \rho/\rho_{ML}$. The density, ρ, was given by the change in pressure of the benzene during adsorption (exploiting the finite vapour pressure of benzene at room temperature) and by the known surface area of the sample.

6.2.2 Diffraction Measurement

Neutron diffraction measurements were carried out using the high intensity powder diffractometer D20 at ILL (see Sec. 3.2.2), using a wavelength of $\lambda = 2.4\,\text{Å}$ [160]. Data were taken in a range of momentum transfers $Q = |k_f - k_i|$ from 0.2 to 5.1 Å^{-1}, where k_i and k_f are the neutron wave-vectors before and after scattering from the sample, respectively. Measurements were performed at relative surface coverages of 0.15 ML, 0.5 ML, 0.8 ML, and 1.3 ML, respectively, and at temperatures in the range from 80 to 250 K. The temperature was controlled using a standard liquid helium cryostat ('orange' cryostat, [161]). Additional diffraction measurements of the clean graphite sample were performed at all temperatures. The graphite substrate and its orientation remained the same throughout all measurements. Subsequently, the clean graphite data were subtracted from the diffraction data of the adsorbate systems at equal temperature (see Fig. 6.1). Five regions in the data show very strong signal from the graphite substrate that masks the signal from the benzene adsorbate and makes a meaningful interpretation of the benzene signal impossible. These regions, as well as the low Q region, are marked by a grey shadowing in Fig. 6.1 and excluded in our further data analysis.

6.2.3 Neutron Spin-Echo Measurement

Supplemental NSE measurements were performed on the neutron spin echo spectrometer IN11 at ILL using the high signal 30 degree detector set-up IN11C [162]. Here, we used a wavelength of $\lambda = 5.5\,\text{Å}$ for maximum signal. The spectra were normalized using a standard procedure: All data were divided by a spectrum obtained at the cryostat base temperature of 1.5 K, where the system can safely be assumed to be static in the dynamic window of the spectrometer. The experiment covered a range of momentum transfers of $Q = 0.2$ to 0.7 Å^{-1}.

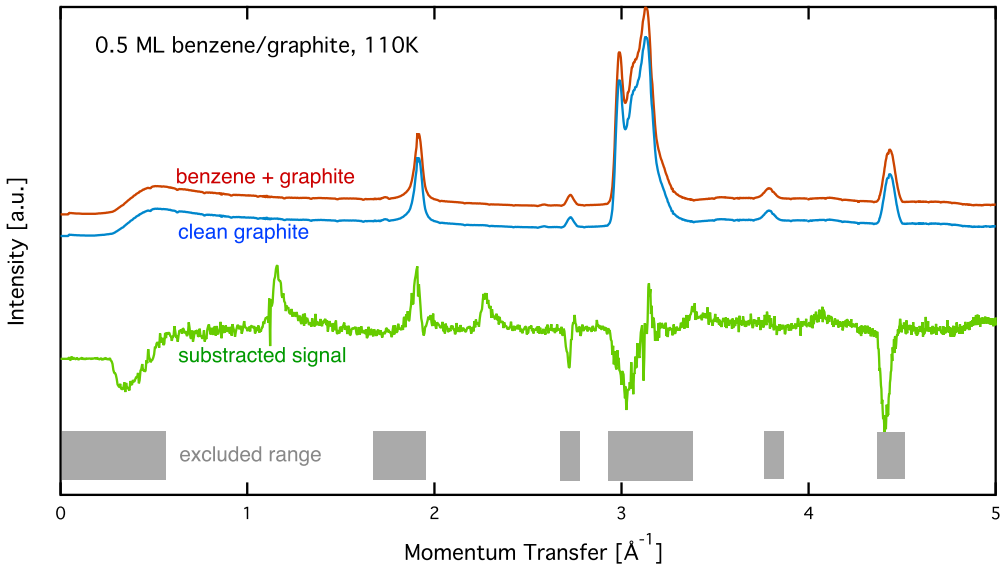

Figure 6.1: Diffraction data at 110 K for the empty graphite sample and a coverage of 0.5 ML are shown together with the subtracted data. Regions with strong graphite signal are indicated by a grey pattern. These regions are omitted in the analysis in this paper.

6.3 Results and Discussion

Fig. 6.2 displays an overview of the coverage dependence of the diffraction patterns of benzene/graphite at a temperature of 110 K. The graphs show significant structural differences between the sub-monolayer and the multi-layer regime as new peaks appear above 1 ML. Hence, for the sake of clarity of the description, we will describe the data from these two regimes in separate sections.

6.3.1 Diffraction Data and Structural Refinement - Sub-Monolayer Regime

The diffraction pattern of the monolayer of benzene/graphite at low temperature has been studied many times before and there exists general agreement on a $(\sqrt{7}\,x\,\sqrt{7})\mathbf{R}19°$ pattern with respect to the graphite (0001) surface structure [145, 146, 147, 148]. However, the capabilities of neutron powder diffractometers and the corresponding data treatment methods have advanced tremendously since the last data where published and we can now study the structural changes upon heating up to the monolayer desorption temperature of 150 K [163]. In addition,

the strong signal of the D20 diffractometer allows us to study several sub-monolayer coverages.

We start our analysis with the lowest measured coverage of 0.15 ML (see Fig. 6.2). At 0.15 ML, no diffraction peaks are observed, which signifies that no long range order arises. The graphs of the two higher sub-monolayer coverages 0.5 ML and 0.8 ML show four strong peaks outside of the regions that are dominated by graphite peaks. These peaks remain at the same position up to 1 ML coverage and have an asymmetrical shape that is typical for diffraction patterns of two-dimensional (poly)-crystalline systems that show random domain orientation with respect to the surface normal [164, 165].

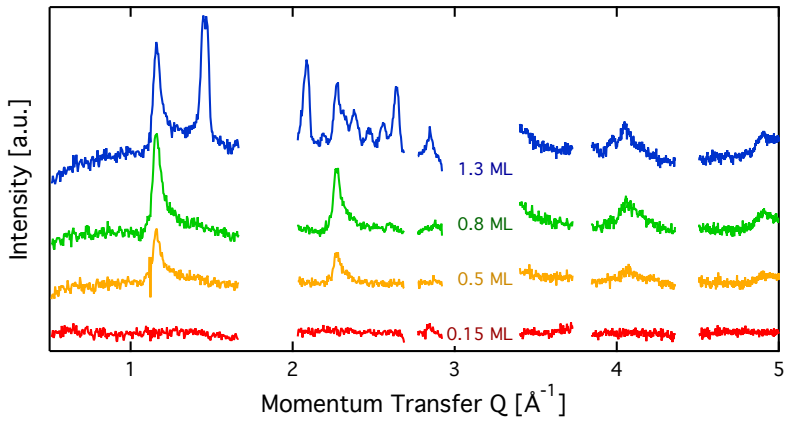

Figure 6.2: Diffraction patterns for varying coverages at 110 K. Regions with strong graphite signal are omitted in the graph. At a coverage of 0.15 ML no structural peaks are seen. At a coverage of more than 1 ML additional peaks appear, which cannot be explained in the framework of a flat benzene structure.

For a more detailed analysis of the sub-monolayer and monolayer structures we have simulated neutron diffraction patterns of a flat lying monolayer using the software package *nxpattern*, which allowed us to adjust a number of parameters manually [166]. The results of such a manual structural refinement are displayed in Fig. 6.3. The positions of the atoms in the deuterated benzene molecule were calculated based on results from neutron diffraction data [142] to account for the bond length difference between hydrogenated and deuterated benzene molecules. We have then adjusted the lattice parameters and found clear consistency with the model of a monolayer of densely packed flat lying benzene molecules. In a next step we have simulated results for out-of-plane tilting of molecules and in-plane rotations. We can

exclude a rotation greater than 1 degree and a tilt greater than 10 degrees, due to the subsequent mismatch of the calculated and the measured peak positions.

Further information could be drawn from the line-shape: in-plane neutron scattering from a flat, two dimensional layer of ordered islands that are randomly oriented produces diffraction peaks that drop sharply for lower angles and exhibit a Lorentzian decay for higher angles [164]. Even better results were obtained in our case by using a squared Lorentzian peak shape that has been theoretically shown to be an indication of random layer lattices that undergo strain effects [167]. The peak width of the simulated diffraction patterns depends on the size of the islands. For the 110 K data we obtained an average island diameter of (200 ± 50) Å. The graphite layers in the compressed exfoliated graphite exhibit a preferred orientation in the plane with a mosaic spread of the surface normal of 20 – 30 degrees full width half maximum (FWHM) [168, 169]. This also influences the peak shape and has been taken into account in the simulation of the pattern. The *width* of the diffraction peaks is mainly determined by the correlation length, which is given by the average ordered island size after the instrument resolution effects from the diffractometer D20 have been corrected for with the instrumental resolution function. Finally the Debye-Waller factor, given by $DWF = \exp[-Q^2 \langle u^2 \rangle / 3]$ ($\langle u^2 \rangle$ is the mean square displacement of the atoms) has a significant influence on the relative amplitudes of the measured peaks (see Fig. 6.3): the intensity of the diffraction peaks drops with increasing momentum transfer.

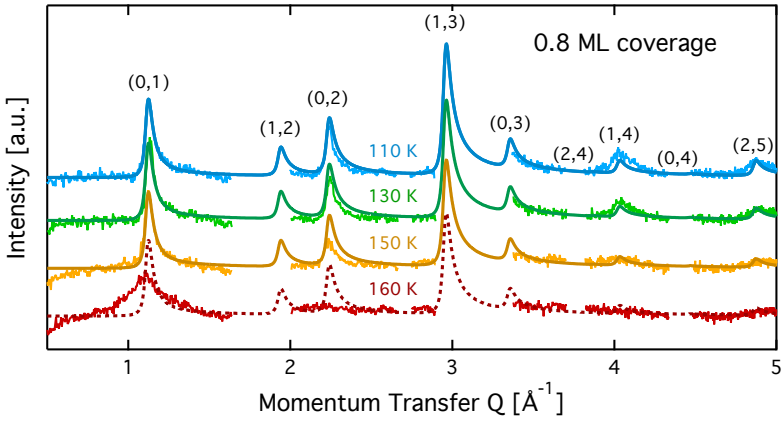

Figure 6.3: Diffraction patterns for varying temperatures at a coverage of 0.8 ML. The calculated diffraction pattern for a commensurate $(\sqrt{7} \times \sqrt{7})\mathbf{R}19°$ monolayer is shown by the (dotted) line.

The diffraction graph resulting from the structural refinement for the coverage 0.8 ML

Index	Measured Position	Simulated Position
(0,1)	1.124 ± 0.011	1.116
(1,2)	hidden	1.933
(0,2)	2.220 ± 0.022	2.232
(1,3)	hidden	2.953
(0,3)	hidden	3.486
(2,4)	hidden	3.867
(1,4)	4.042 ± 0.040	4.024
(0,4)	hidden	4.465
(2,5)	4.894 ± 0.049	4.865

Table 6.1: Measured and calculated positions of the diffraction peaks of the submonolayer structure at a coverage of 0.8 ML. All values are in units of $Å^{-1}$.

is shown in Fig. 6.3. The agreement with the measured diffraction data confirms the formation of a $(\sqrt{7} \times \sqrt{7})\mathbf{R}19°$ structure up to a temperature of 150 K. Above this temperature, desorption sets in. The measured diffraction peak positions and the simulated peak positions in the Q-range of our data are compared in Tab. 6.1. The four available peaks are reproduced well within the experimental error bar. The $(\sqrt{7} \times \sqrt{7})\mathbf{R}19°$ structure is depicted in Fig. 6.4. Here, we propose two possible variants. The structure in Fig. 6.4 a) assumes the positions of the benzene hydrogen atoms on top of the underlying carbon atoms. This structure has been preferred recently by other authors [157]. In the structure of Fig. 6.4 b) the hydrogen atoms are turned to take a maximum distance from the top layer carbon atoms. Since the scattering plane is concomitant with the surface planes our diffraction data cannot distinguish between the two orientations, but orientation b) is preferred by our MD simulations [136], where the orientation of the benzene rings with respect to the carbon structure is found to be turned by about 20° with respect to the graphite top layer. An I-V analysis of low intensity LEED measurements might resolve this issue, but it has to be kept in mind that the benzene islands remain highly dynamic even at temperatures of 60 K as shown by recent spectroscopy data [32].

6.3.2 Comparison to Neutron Spin-Echo Data

NSE spectroscopy measures the decay of structural correlation with time. NSE spectra for temperatures between 120 and 150 K are shown in Fig. 6.5. The NSE spectra show a decay that can be expressed by a simple exponential decay that reaches a plateau value A at large time whose value strongly depends on temperature:

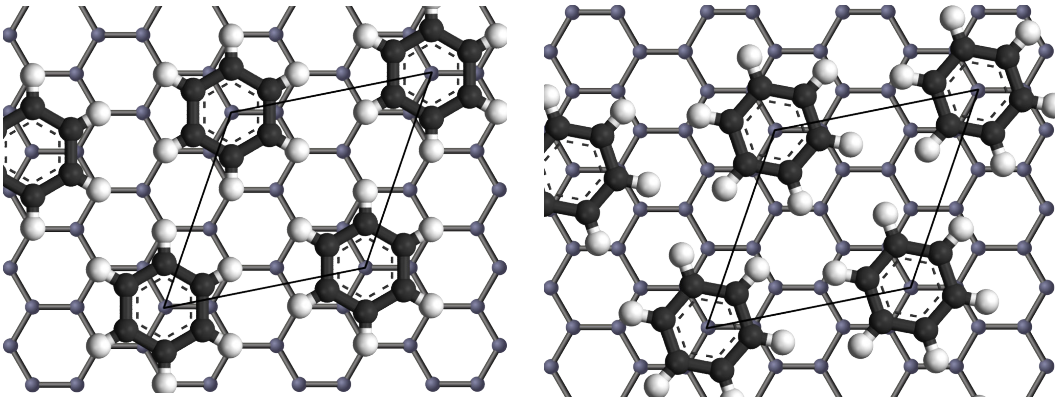

a) b)

Figure 6.4: Illustrations of the commensurate $(\sqrt{7}\,x\,\sqrt{7})\,\mathbf{R}19°$ structure. a) The hydrogen atoms are positioned on top of first layer carbon atoms. b) The hydrogen atoms are turned away from the carbon atom positions. This orientation agrees with our recent MD calculations [136].

$I(Q,t)/I(Q,0) = (1-A) \times \exp[-t/\tau(Q)] + A$, where $\tau(Q)$ is the decay time of the structural correlation function. The plateau represents the scattering from the static fraction of the sample, i.e., from the graphite substrate and from immobile clusters of benzene. The change of the level of the plateau indicates a *gradual* melting of the layer, which should also influence the diffraction signal. In the diffraction data we observe a change of the peak intensities with temperature, which is most pronounced for the higher diffraction orders, and we see that the peak positions do not shift with temperature. In Fig. 6.5, we compare the area of the (0,2) and (1,4) peaks (averaged to decrease the size of the experimental error bar) with the A parameter extracted from fitting the NSE data at a momentum transfer $Q = 0.4\,\text{Å}^{-1}$. From our diffraction and NSE data we can, thus, deduce that islands are formed at 0.5 and 0.8 ML coverages below 150 K that are ordered in the $(\sqrt{7}\,x\,\sqrt{7})\,\mathbf{R}19°$ monolayer structure and that increase in size with decreasing temperature.

6.3.3 Diffraction Results and Structural Refinement - Coverage Exceeding 1 ML

Diffraction data for a coverage of 1.3 ML are shown in Fig. 6.6. Up to a temperature of 160 K additional peaks are clearly visible and the peaks that are found for the submonolayer structure remain. We have performed structural refinement by assum-

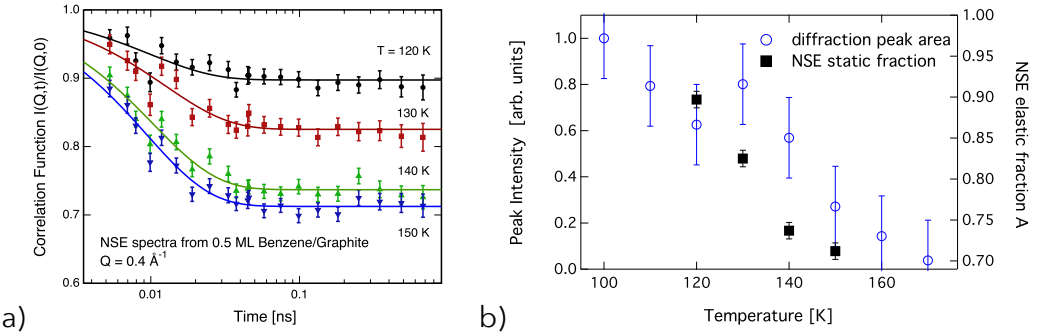

Figure 6.5: a) Neutron spin echo spectra of an 0.5 ML benzene layer on exfoliated graphite measured at temperatures between 120 and 150 K at a momentum transfer of $Q = 0.4\,\text{Å}^{-1}$. The solid lines are exponential function fits to the data.b) Comparison of the total area of the (0,2) and (1,4) diffraction peaks (blue circles) to the static scattering A parameter from NSE spectroscopy at a momentum transfer $Q = 0.4\,\text{Å}^{-1}$(black squares). The signal from the two diffraction peaks has been integrated to reduce the experimental error bar.

ing either flat double layers or compressed layers with alternating flat and upright molecules in various geometries. None of these models reproduced the observed additional lines for the 1.3 ML coverage. Furthermore, we observed that the additional peaks that appear above 1 ML coverage (see Fig. 6.6) disappear at around 200 K and thus at a temperature that is 50 K above the monolayer desorption temperature. We conclude, that a second layer formation is not found here. Instead, we propose the formation of bulk crystalline benzene when the first layer is complete. In Fig. 6.6 we also compare our data with neutron diffraction data from bulk benzene by Craven *et al.* measured at the instrument D2B at ILL [141]. The similarity to the bulk data provides clear evidence that the additional structure at above monolayer coverage is bulk crystalline benzene. The creation of the bulk structure at coverages with a relatively modest excess over 1 ML is at odds with the widely spread picture of structure creation in the low coverage regime [170].

6.4 Conclusions

In this chapter, the analysis of neutron diffraction studies of benzene mono- and multilayers on exfoliated graphite was presented. For a low coverage of 0.15 ML no ordered structure was observed. For coverages between 0.5 ML and 1 ML, the exis-

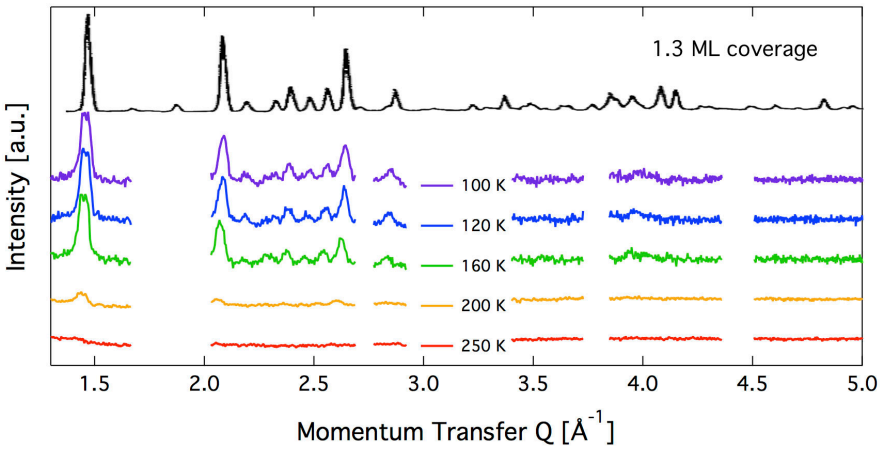

Figure 6.6: Diffraction patterns for varying temperatures at a relative benzene coverage of 1.3 ML. Due to the subtraction of very intense peaks, the noise has increased substantially. The black line shows a neutron diffraction pattern from bulk benzene at 105 K that has been inserted into the figure and has originally been obtained by *Craven et al.* [141].

tence of a flat $(\sqrt{7} \times \sqrt{7})\mathbf{R}19°$ structure has been observed that can be shown to be caused by ordered islands of at least 200 Å diameter. The structure does not compress, within the experimental error bar, upon increasing the coverage. At a coverage of 1.3 ML, a bulk crystalline benzene structure appears rather than a second layer. This structure differs strongly from a compressed ordered structure suggested recently [170].

7 Benzene Adsorbed on Graphene/Ni(111)

7.1 Introduction

The interaction of aromatic carbohydrates with the graphene and graphite surface displays a model system for the fundamental research on friction [171, 172, 173, 174]. Graphite has since long been known as an excellent lubricant, but recently super-lubricity, i.e., negligible friction of graphene sheets on a graphite surface has been discovered by scanning force microscopy [175, 176]. Technological interest in the field of nano-robotics exists in the search of low friction building blocks [135, 139].

The adsorption of benzene on the graphite surface has already been discussed in detail in the preceding chapter. Benzene adsorption on graphene has been studied in a series of DFT calculations in recent years [177, 178, 179, 180, 181, 182]. In general, an energetic preference of adsorption in the **stack** configuration, i.e. the centre of the benzene molecule atop of a C atom has been predicted, with an adsorption configuration above a hollow centre being the least favourable one. Reported energy differences between the two configurations are roughly 80 meV [177], 50 meV [178], and 40 meV [180]. The distance of the molecule to the surface in the **stack** configuration was calculated to be 3.34 Å [179], 3.2 Å [180], 3.5 Å [178], and 3.17 Å [177]. Only a very small charge transfer has been calculated, resulting in an almost intact graphene band structure with an intact zero-gap at 0 K [177, 178]. On the other hand, considerable influence of adsorbed benzene on the electronic structure of graphene has been observed by Raman spectroscopy [183]. MD forcefield simulations on a graphite surface have been conducted to calculate the potential energy surface and diffusional dynamics of single and multiple benzene molecules. A very low potential barrier of only a few meV has been found for a single molecule, evaluation of diffusion calculations bear a potential barrier at 0.5 ML surface coverage of only 11 meV and predict Brownian-type diffusion rather than jump diffusion [136].

From HeSE and NSE studies of benzene on an HOPG substrate, under comparable conditions to the ones presented here, a Brownian-type diffusion has been reported, where the friction consists of both, static and kinetic friction [136, 4].

The kinetic friction η was first related to the diffusion constant D in the Einstein relation of diffusion [24], which is a fluctuation-dissipation relation. It can be restated in the fluctuation-dissipation theorem by Kubo [184]:

$$D = \frac{k_B T}{m\eta}, \tag{7.1}$$

where k_B is the Boltzmann constant, T the temperature and m the mass of the particle. The observed friction can be either caused by the kinematic viscosity ν via $\eta = 2\pi d\nu/m$, where d is the diameter of an atom in a liquid [185]. The friction η could, on the other hand, be caused by energy dissipation via surface phonons (surface friction). Neutron TOF and NSE measurements at different surface coverages of benzene on exfoliated graphite have shown a large part of the kinetic friction could be successfully described by a RHD model, where coupling of translational and rotational momentum are described by a system of colliding disks and that only a small part of the friction is caused by surface friction.

In this chapter, we present HeSE studies of low coverages of adsorbed benzene on the surface of graphene/Ni(111). Section 7.2 discusses specular reflectivity studies of the adsorption and desorption of the adsorbate, where we observe a wetting of the graphene surface with a possible simultaneous adsorption on top of the first layer. Thermal and isothermal desorption studies let us determine a precise value for the desorption barrier. In section 7.3, we discuss helium diffraction studies that confirm the existence of a $(\sqrt{7}\,\mathrm{x}\,\sqrt{7})\mathbf{R}19°$ over-structure, as previously observed on the basal plane of graphite. Section 7.4 presents extensive HeSE studies which allow us to identify two distinct diffusional processes, separated by two orders of magnitude in diffusion rate. A fast Brownian/ballistic diffusion is found that suggests a substantial surface friction. The exact nature of the slow jump-like diffusion is unclear, but we can derive characteristic dimensions of the process and propose several possible mechanisms.

7.2 Adsorption and Desorption

7.2.1 Isothermal Adsorption

We have carried out isothermal adsorption measurements of at the HeSE spectrometer, as already described for the adsorption of H_2O in Chap. 5. We chose a correction factor of 4.3 for the ionization efficiency, as has been used before at the same instrument [186, 126], but this factor introduces another potential source of error in the calculation of the surface exposure.

Benzene wets the graphene surface and forms a commensurate $(\sqrt{7}\,\mathrm{x}\,\sqrt{7})\,\mathbf{R}19°$ structure in the sub-monolayer regime, as our adsorption and diffraction measurements confirm. We can therefore relate the monolayer coverage to a certain areal density, 1 ML = 1/7 molecules/uc = 0.0273 molecules/Å^2 (uc: graphene unit cell). This allows us to relate the surface coverage θ to the exposure E through kinetic theory of gases [14]:

$$\theta = \frac{E}{\sqrt{2\pi m k_B T_{gas}}} = \frac{\int P\,\mathrm{d}t}{\sqrt{2\pi m k_B T_{gas}}}, \tag{7.2}$$

with the gas temperature $T = 289.15$ K, the Boltzmann constant k_B, the mass of the benzene molecule $m = 78.11$ g/mol $= 12.971 \cdot 10^{-26}$ kg, and the pressure P. This means that an exposure of 1 L corresponds theoretically to a surface coverage of $1\,\mathrm{L} = 2.33 \cdot 10^{-2}\,\text{Å}^{-2} = 0.854$ ML, if we assume a sticking coefficient of unity.

We have performed a series of isothermal adsorption measurements in the temperature range 100 – 150 K while monitoring the specular reflected helium signal.

Adsorption in the range 100 – 120 K

The specular signal curves at temperatures below 120 K reveal a quite complex picture of benzene adsorption. Fig. 7.1 shows the observed intensities, which consist all of five regimes, named **A** – **E**. The rapid initial decay of the specular signal seen in **A** is characteristic for the adsorption of a non-interacting gas, as is expected in the very low coverage regime. If the decay exhibits an exponential behaviour $I/I_0 = exp(-\Sigma \cdot n \cdot \theta/\cos(\vartheta_i))$, as expected for random adsorption, or a power-law $I/I_0 = (1-\theta)^{\Sigma \cdot n \cdot / cos(\vartheta_i)}$, as for the case of lattice adsorption, can not be distinguished

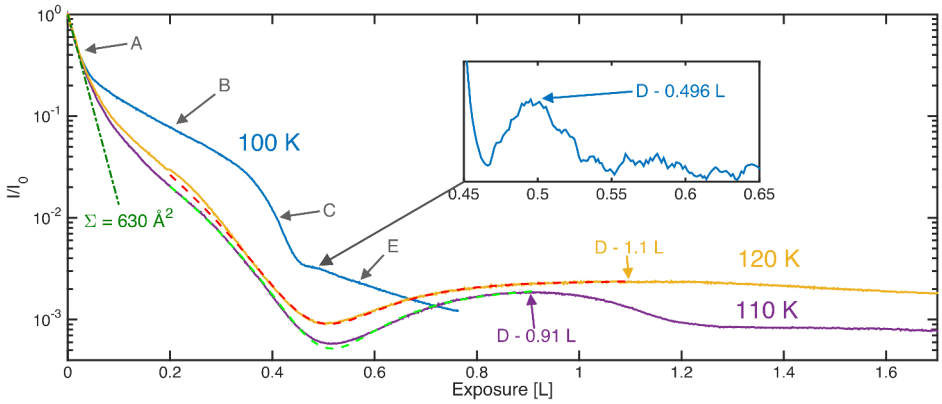

Figure 7.1: Specular reflected signal versus exposure during isothermal adsorption of benzene at 100 K, 110 K, and 120 K. Inset: close view of small peak of the 100 K curve after subtraction of linear baseline. Letters A through E: Adsorption regimes. Dark green dash-dotted line: Slope of the initial adsorption; Light green and red dashed lines: interference model for reflective adsorbates.

in this case, both models work equally well. Here, Σ is the helium scattering cross section, n the surface area that is occupied by a single molecule at monolayer coverage, and the term $\cos(\vartheta_i)$ corrects for an apparent change of the scattering cross section since scattering happens at an initial angle $\vartheta = 22.2°$ with respect to the surface normal. At this point, we can not yet establish values for the dimensions, since we lack a calibration of the surface coverage with exposure. This initial decay is followed by a substantial slowing of the decay rate in zone **B**. We interpret this to be a sign of island formation, in which case an additional adsorbed molecule does not accommodate a surface area that corresponds to its large scattering cross section, but rather one that corresponds to its molecular size. The origin of the additional fast decay of the specular signal in zone **C** is not entirely clear to us. The most probable case is that at high surface coverage, a substantial part of the arriving molecules adsorbs on top of the first layer, which is itself reflective. They would thus cause an attenuation of the monolayer reflections that corresponds to the adsorption of a free gas. The second possibility would be that, upon growing, islands saturate at a certain size, since the constant association rate of molecules to the island, which depends on the flux of incoming molecules, is matched by an equal dissociation rate of molecules from the island, which scales with the island's circumference. The saturated islands would then find themselves in equilibrium with a surrounding 2D gas, which causes again a large signal decay rate. Independently of this interpretation, the local maximum at point **D** can be interpreted as the completion of the first

layer. For the measurement at 100 K, the maximum is tiny, it is shown as an inset in Fig. 7.1 after subtraction of a baseline to enhance visibility. We now have the information to calibrate the surface coverage from exposure. If the sticking probability was constant and all molecules adsorbed in the first layer, then surface coverage would scale linearly from 0 to 1 ML at point **D**. However, since we expect a strong decrease in the adsorption rate to the first layer at high coverages, the exposure that corresponds to 1 ML, is lower. As a lower estimate for this value served the kink of the 100 K between **B** and **C**. The above described processes in zone **C** would presumably only happen at very high surface coverage. As an estimate of the exposure equivalent of 1 ML, we thus propose $E_{ML} = (0.43 \pm 0.09)$ L, with the centre of zone **C** as the proposed value and its width as an uncertainty. This allows us to determine the scattering cross section of the benzene molecule. Assuming an initial sticking coefficient close to unity (as also done by Zacharia et al. [163]), a helium scattering cross section of the benzene molecule of $\Sigma_{init} = (630 \pm 120)\,\text{Å}^2$ is obtained at 100 K. This is a remarkably large scattering cross section that we can only tentatively explain by the very large polarisability of the benzene molecule, which is six times larger in comparison with, e.g., CO [187, 188].

We have reproduced the high coverage development of the specular signal to a good match by applying a model developed by Comsa et al. [38]. In this model, reflective scattering from both the substrate and the adsorbate is taken into account, as well as interference between the two layers due to a height difference h. The total scattering amplitude is the sum of the two contributions $A = A_S + A_A e^{i\varphi}$, with a phase difference φ and the substrate and adsorbate scattering amplitudes A_S, and A_A, respectively. The specular reflected signal is the square of the total scattering amplitude A:

$$\frac{I}{I_0} = \left(\frac{A}{A_0}\right)^2 = [A_S^2 + 2A_S A_A \cos\varphi + A_A^2]/A_0^2, \tag{7.3}$$

where the interference term in the middle is determined by $\varphi = 2\pi \frac{2h\cos\gamma_i}{\lambda}$, with the angle γ_i of the incoming helium beam and the helium wavelength λ. We assumed different expressions for A_S and A_A, corresponding to no adparticle interaction, maximum attraction and maximum repulsion. The experimental data could only be rea-

sonably reproduced under the assumption of lattice gas adsorption,i.e.:

$$\frac{A_S}{A_0} = (1-\theta)^{\frac{\Sigma_A}{2} n_s} \tag{7.4}$$

$$\frac{A_A}{A_0} = (\theta)^{\frac{\Sigma_V}{2} n_s}, \tag{7.5}$$

with the scattering cross sections Σ_A and Σ_V for an adparticle and a vacancy, respectively. The resulting curves obtained by fitting the described model can be seen as the bright green and red dashed lines in Fig. 7.1. The assumption of a lattice adsorption is not reasonable in this high coverage range, especially not after the observation of island formation. Furthermore, we made an important assumption that is not straightforward to justify, namely that the surface coverage θ depends linearly on the exposure. It is thus important to note that the obtained results have to be interpreted with care, as their only justification lies in their ability to reproduce the line shape. The parameters that were obtained from the fitting are listed in Tab. 7.1. At

T [K]	Σ_{init} [Å^2]	A_S [%]	A_A [%]	Σ_A [Å^2]	Σ_V [Å^2]	h [Å]
100 K	630 ± 120	–	–	–	–	–
110 K	640 ± 130	33.56 ± 0.07	4.47 ± 0.02	199 ± 1	25 ± 2	3.387 ± 0.004
120 K	550 ± 110	43.0 ± 0.2	4.84 ± 0.01	275 ± 2	6.9 ± 0.5	3.380 ± 0.001

Table 7.1: Uptake isotherms of benzene on GR at different temperatures.

both temperatures, the specular reflectivity of the benzene monolayer A_A is about 4.5 % of the graphene reflectivity, which itself we have determined to 20 %. The apparent helium scattering cross section of the adsorbate, Σ_A, is three times smaller than the Σ_{init}, indicating a strong overlap of cross sections. The helium scattering cross section of a vacancy, Σ_V, is very low, since it reflects the additional area that is freed for specular scattering upon removal of a benzene molecule. The height difference, h, contributes to Eq. (7.3) in a periodic manner, producing the same results with a periodicity of 0.97 Å. We thus had first to make the assumption that the height difference corresponds rather closely to the adsorption height of a benzene molecule, and second, rely on DFT results on the adsorption height of a benzene molecule, which predict values from 3.2 to 3.4 Å [179, 180]. The obtained 3.38 Å are in good consistency with calculations and a difference of ± 0.97 Å to the next possible solution let this value seem to be the most reasonable one.

Adsorption above 120 K

At temperatures above, an equilibrium between adsorption and desorption was quickly reached. 150 K was the highest temperature, at which a significant change in reflectivity was barely observed at partial pressures up to 10^{-7} mbar, which is an upper limit for pressure that can be safely imposed on the UHV system of the instrument.

7.2.2 Thermal and Isothermal Desorption

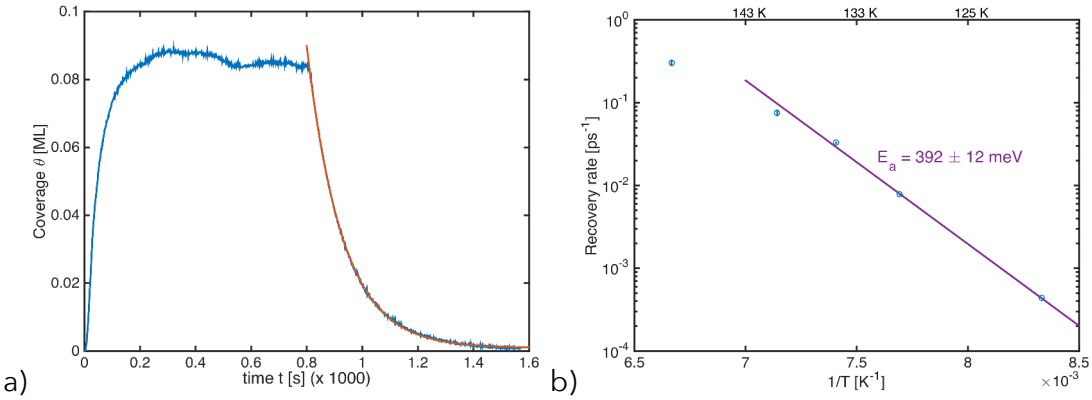

Figure 7.2: a) Exponential decay of surface coverage at 130 K after benzene exposure is stopped at $t = 800$ s. b) Arrhenius plot of exponential decay rate (errorbars are barely visible). The point at 150 K seems to deviate from the activated behaviour and has been excluded from the fitting.

For the isothermal desorption measurements, we exposed the graphene surface to $7 \cdot 10^{-9}$ mbar benzene overpressure and waited until the system was in equilibrium. We then turned off the exposure and monitored the specular signal recovery. From this we calculated the corresponding surface coverage as a function of time. An example is shown in Fig. 7.2 a), the surface coverage first rises during exposure and then decays exponentially after exposure has been interrupted after 800 s. We repeated this process for several temperatures in the range 120 – 150 K. The initial desorption rate, which is identical to exponential decay rate, exhibits an activated temperature dependence up to about 135 K. Fig. 7.2 b) shows an Arrhenius plot of the desorption rate. The slope of the Arrhenius law corresponds to an activation energy of desorption of (392 ± 12) meV. This is slightly lower than the value obtained by Zacharia et al. on graphite, employing thermal desorption measurements

((500 ± 80) meV) [163].

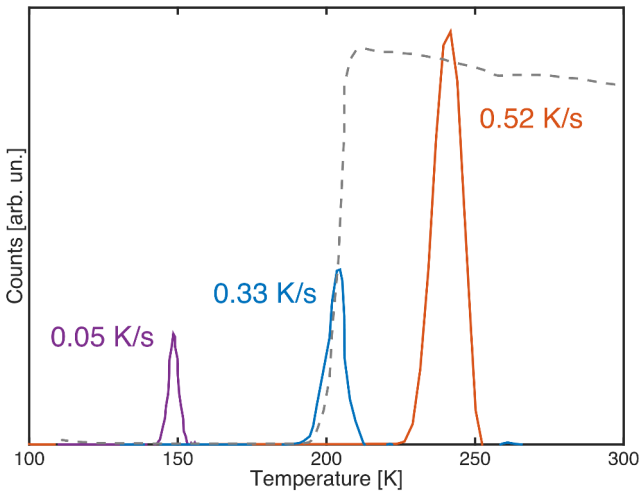

Figure 7.3: Thermal desorption at different heating rates. Solid lines: Derivative of specular signal during thermal desorption at constant heating rate. Dashed line: Specular signal during desorption at 0.33 K/s heating rate for comparison.

We monitored the specular signal while heating a benzene coverage in the monolayer range at a constant heating rate r. The specular signal exhibited a sharp rise at a certain temperature. The derivative of the specular signal with respect to temperature exhibits a sharp peak with its maximum at the temperature of highest desorption rate, in analogy to the commonly measured mass spectrometer signal in TDS. We applied the Redhead formula [16] (Eq. (3.6)) to calculate the activation energy for desorption, using an estimated attempt rate $\nu = 10^{12}\,\mathrm{s}^{-1}$, based on the result for a surface friction that we obtained from HeSE, studies, as will be discussed later in this chapter. Zacharia et al. have determined a much larger attempt rate $\nu = 5 \cdot 10^{15}\,\mathrm{s}^{-1}$ from isothermal desorption [163], however, this high value contradicts our findings on isothermal desorption and on surface friction. The results are listed in Tab. 7.2, where the uncertainty of the maximum desorption temperature T_{max} is based on the peak width. The results show large discrepancies and a general rise with heating rate. This lets us doubt if the Redhead formula is a justified approach to calculate the activation energy of desorption from our measurements.

r [K/s]	T_{max} [K]	E_a [meV]
0.05	148 ± 2	408 ± 7
0.33	204 ± 3	536 ± 11
0.52	241 ± 7	626 ± 15

Table 7.2: Activation energy of desorption calculated by the Redhead formula at different hating rates r.

7.3 Adsorbate Structure

We have performed diffraction scans along the inclination angle γ and the azimuthal angle α of a monolayer coverage of benzene on the graphene surface at 110 K. We observed a large number of well defined diffraction peaks. The positions of the diffraction peaks seem to confirm the existence of a $(\sqrt{7}\,\mathrm{x}\,\sqrt{7})\,\mathbf{R}19°$ commensurate overlayer, as observed on the basal plane of graphite. Fig. 7.4 shows the diffraction data together with the unit cell vectors of the overlayer. The diffraction pattern is consistent with LEED results obtained by Bardi [145]. The illustration shows well, how the seemingly complex diffraction is actually made up of two hexagonal repeating structures, that are rotated by +19° and -19°, respectively, with respect to the graphene surface. This coexistence of two diffraction patterns stems from the fact that the same $\pm 19°$ rotation is possible for the $(\sqrt{7}\,\mathrm{x}\,\sqrt{7})\,\mathbf{R}19°$ structure, and both types coexist. The radial component corresponds to a momentum exchange Δk in the range of 0 to about 4 $\mathrm{Å}^{-1}$. Comparison of the peak position with the neutron powder diffraction results discussed in Chap. 6 shows good agreement (compare with Fig. 6.3). The peak orders are numbered in both plots in the same manner to simplify identification.

7.4 Diffusion of Benzene on Graphene/Nickel(111)

7.4.1 Slow Jump Diffusion

We have performed HeSE measurements on three different surface coverages of benzene on the graphene surface at 110 K. Along the two principal axes of the hexagonal graphene surface, $\overline{\mathbf{\Gamma}\mathrm{K}}$ and $\overline{\mathbf{\Gamma}\mathrm{M}}$, measurements have been performed over a momentum transfer range from 0 to 3.2 $\mathrm{Å}^{-1}$. A first series of measurements

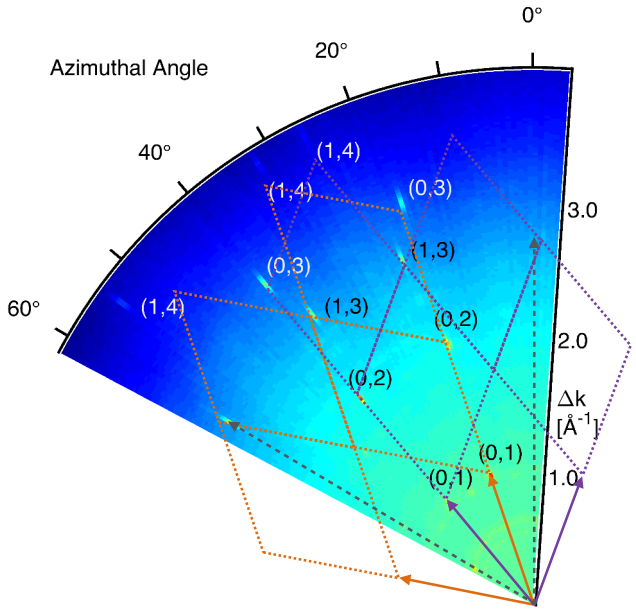

Figure 7.4: Polar colour-plot of helium diffraction signal from monolayer benzene on the surface of graphene/Ni(111) at 110 K with Δk along the radial coordinate and the azimuthal angle along the angular coordinate. Grey dashed arrows: Unit cell vectors of the reciprocal graphene lattice. Orange and purple arrows: Unit cell vectors of the reciprocal $(\sqrt{7}\,\mathrm{x}\,\sqrt{7})\,\mathbf{R}19°$ benzene overstructure, with selected repetitions indicated by dotted lines.

was obtained with the use of a power supply that delivers up to 10 A current, allowing us to access a Fourier time range from 0.6 to 600 ps. Measurements were then repeated under the same conditions with a different power supply that delivers up to 1 A current, but at higher precision, allowing us to focus on smaller Fourier times in the range from $5 \cdot 10^{-2}$ to 60 ps. The coverages at which measurements have been undertaken can be seen in Tab. 7.3.

I/I_0	θ [ML]
1/1.3	0.02
1/3	0.06
1/10	0.12

Table 7.3: Relative specular intensities I/I_0 and corresponding surface coverages θ, at which HeSE measurements have been performed.

Fig. 7.5 shows an example ISF in the form of the real polarization amplitude as a

function of the SE time. The solid red line shows the results from fitting the sum of an exponential decay and a constant term to the polarization amplitude:

$$I(\Delta k, t) = I_{qe}(\Delta k) \cdot \exp[-\alpha(\Delta k)t] + I_{el}(\Delta k), \tag{7.6}$$

with the elastic and quasi-elastic polarization amplitudes $I_{el}(\Delta k)$ and $I_{qe}(\Delta k)$, respectively, and the exponential decay rate $\alpha(\Delta k)$. In order to exclude the influence of a second, faster, exponential decay, data below a threshold in the range of 30 – 45 ps were excluded from the fitting since simultaneous fitting of a sum of exponential decays has turned out to be too unstable. The exact position of the threshold has been decided for each measurement based on the distribution of the residuals that are statistically spread around zero only if the influence of the faster decay is negligible.

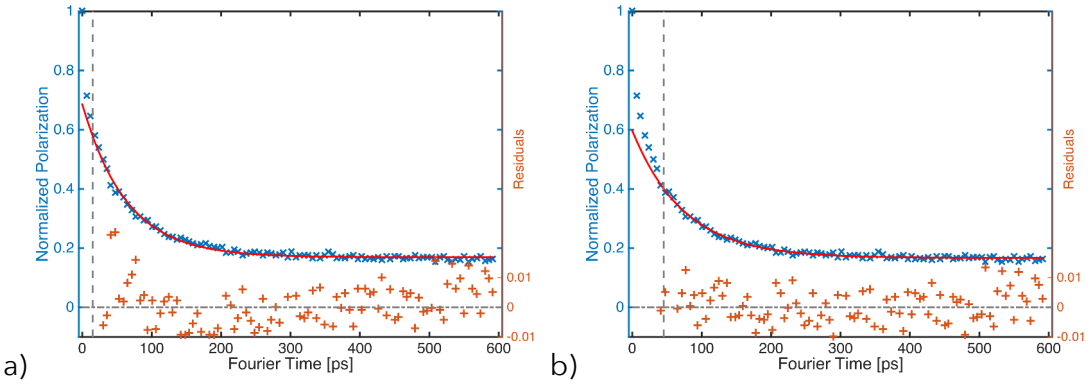

Figure 7.5: ISF at 110 K and $\theta = 0.06$ ML, $\Delta k = 0.22\,\text{Å}^{-1}$. A second, fast, exponential decay made it necessary to exclude data at low Fourier times. The red solid lines shows a least squares fit of Eq. 7.6. The orange crosses show the fitting residuals. If the lower threshold is chosen too low, the fast decay influences the fitting. Although hard to judge by the eye, this can be observed by observing statistical distribution of the residuals: a) The threshold has been chosen too low (15 ps), the residuals exhibit an asymmetrical behaviour. b) If a threshold is set to 45 ps, the influence of the fast decay becomes negligible, the residuals are homogeneously spread around zero.

Comparing the exponential decay rate at $\Delta k = 0.17\,\text{Å}^{-1}$ and $\Delta k = 0.33\,\text{Å}^{-1}$ at four different temperatures in the range 100 – 120 K reveals an activated dependence of the decay rate on temperature. Fig. 7.6 shows an Arrhenius plot of the decay rate. A linear fit to the logarithm of the decay rate versus the inverse temperature returns

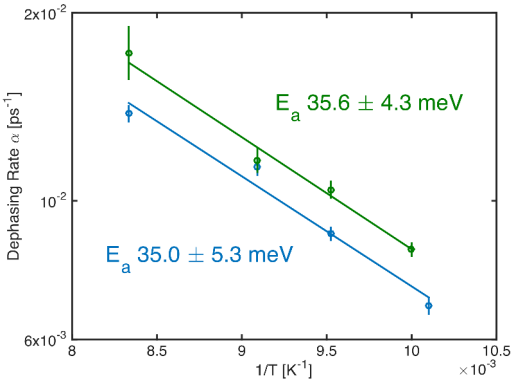

Figure 7.6: Arrhenius plot of the decay rate as a function of inverse temperature. Depicted in blue are data measured at $\Delta k = 0.17\,\text{Å}^{-1}$; depicted in green are data measured at $\Delta k = 0.33\,\text{Å}^{-1}$

an activation energy at both momentum transfers of about (35 ± 5) meV. Since these results stem from coherent scattering, but models of activated self-diffusion are in general based on the assumption of incoherent scattering, a systematic error might exist in this result, due to a possible structural change with temperature.

Fig. 7.7 a) shows the resulting relative elastic contribution $I_{el}(\Delta k)$. Multiplication with the absolute scattering amplitude $\tilde{I}(\Delta k, t = 0)$ yields the absolute elastic contribution $\tilde{I}_{el}(\Delta k)$ (Fig. 7.7 c)). In addition to the specular reflection and first order diffraction peaks, it also contains additional widespread peaks with a maximum at about 0.75 Å in both $\overline{\mathbf{\Gamma}\mathrm{M}}$ and $\overline{\mathbf{\Gamma}\mathrm{K}}$ direction. This might indicate an ordering of the benzene molecules with an average distance $d = 2\pi/0.75\,\text{Å}^{-1} = 8.4\,\text{Å}$. This is quite close to the inter-molecular distance in the commensurate $(\sqrt{7}\,\mathrm{x}\,\sqrt{7})\,\mathbf{R}19°$ over-structure ($2.46\,\text{Å} \cdot \sqrt{7} = 6.59\,\text{Å}$). Assuming ordering due to repulsive interaction scales the inter-molecular distance with the inverse of the square-root of surface coverage. This would result in a distance $d = 27.6\,\text{Å}$ at 0.06 ML coverage. If these additional features stem from surface ordering, it is thus plausible to assume that they are related to an attractive interaction and resulting island formation. The width of these peaks can be estimated from the relative elastic amplitude to about $0.3\,\text{Å}^{-1}$, which would correspond to an island diameter in the order of 20 Å, or three benzene molecules.

Fig. 7.7 b) and d) show the relative and absolute quasi-elastic contributions, respectively. As for the case of H_2O on graphene/Ni(111), the relative amplitude exhibits asymmetric peaks at the shoulders of the specular and first order diffraction peak,

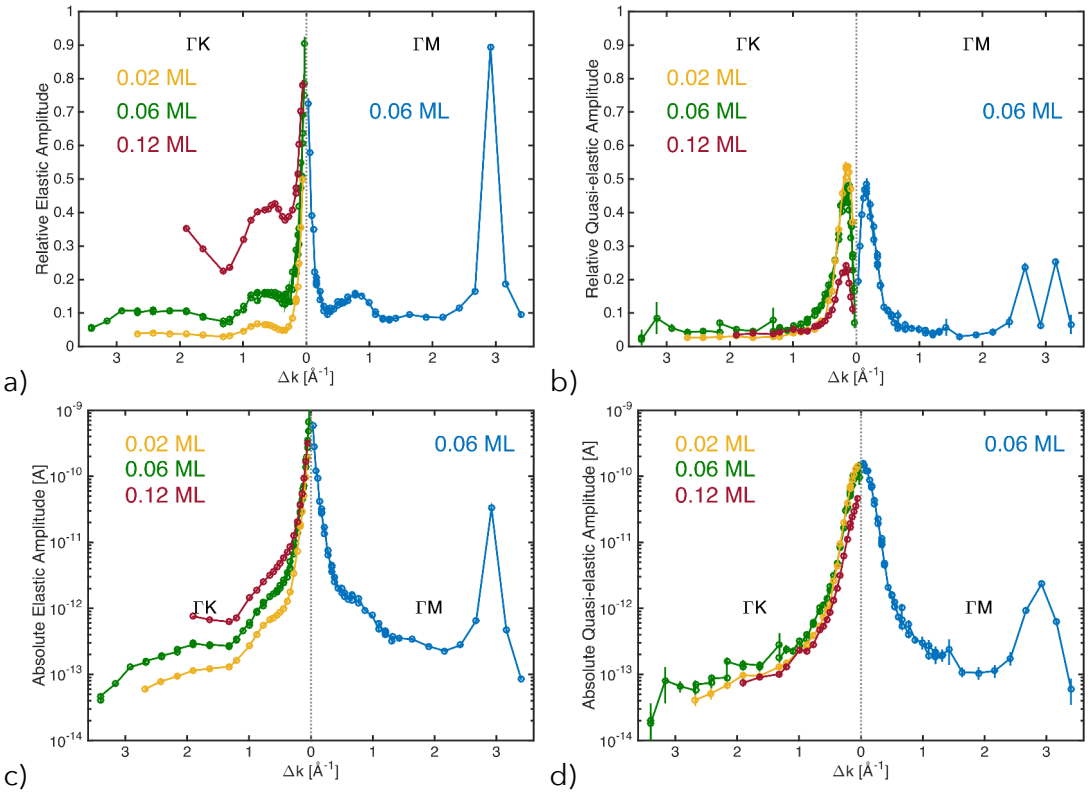

Figure 7.7: Quasi-elastic and elastic amplitudes of different surface coverages of benzene at 110 K. a) and c) Normalized and absolute elastic polarization amplitudes, $I_{el}(\Delta k)$ and $\tilde{I}_{el}(\Delta k)$, respectively b) and d) Normalized and absolute quasi-elastic polarization amplitudes, $I_{qe}(\Delta k)$ and $\tilde{I}_{qe}(\Delta k)$, respectively.

while the absolute amplitude, exhibits simply broadened diffraction peaks. The observed peaks in the relative amplitude are thus merely the relative difference between broad quasi-elastic and the narrow elastic peaks.

The observed exponential decay rates are shown in Fig. 7.8 a). They exhibit a steep initial rise. As discussed in Sec. 3.3.3, we suspect a link between the observed enhancement of the decay rate and de Gennes narrowing. In analogy to the procedure described in Sec. 5.4.1, we tentatively calculated the incoherent decay rates $\alpha_{inc}(\Delta k)$ by division by $I_{qe}(\Delta k)$ and subsequent rescaling such that $\alpha(\Delta k) = \alpha_{inc}(\Delta k)$ in regions where no diffraction is expected. The incoherent decay rates are shown in Fig. 7.8 b), they exhibit a sinusoidal behaviour as expected for jump diffusion.

The results from fitting the CE model with possible jumps to nearest, next-nearest

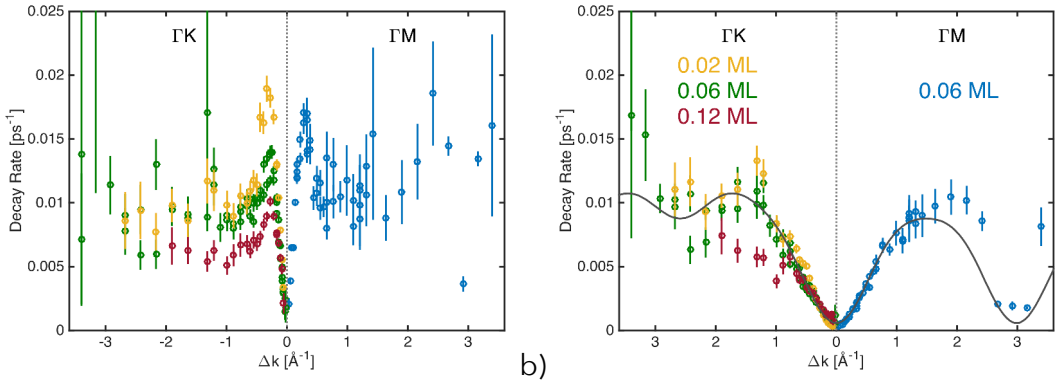

Figure 7.8: Decay rates versus Δk of different benzene surface coverages at 110 K. a) Coherent decay rate $\alpha(\Delta k)$. b) Incoherent decay rate $\alpha_{inc}(\Delta k)$. Grey solid line: CE model of jump diffusion.

and next-next-nearest neighbours are presented in Fig. 7.8 b). It seems to reproduce well the data at most momentum transfers, except for a discrepancy around 2 Å^{-1}. The parameters that were obtained by the fitting are: the jump rate $\eta = (14.1 \pm 0.4) \cdot 10^{-3}$ ps^{-1}, the offset $c = (0.6 \pm 0.1) \cdot 10^{-3}$ ps^{-1}, the probabilities for jumping to nearest, next-nearest and next-next-nearest neighbours, $p_n = (82 \pm 6)\,\%$, $p_{nn} = (2 \pm 10)\,\%$ and $p_{nnn} = (13 \pm 8)\,\%$, respectively, and the jump distance $l = (2.46 \pm 0.05)$ Å.

The CE model only applies to jump diffusion on a Bravais lattice, which would only be the case for jumps between **hollow** sites in the graphene/Ni(111) surface. Benzene molecules are in general expected to adsorb in a stacked configuration, as discussed earlier, i.e. on top of a C atom. We would therefore expect jump diffusion to occur between top sites, a process which would bear a different signature [35]. A non-degeneracy between the two different adsorption sites atop a carbon atom would introduce a second, faster exponential decay. The search for this faster decay is complicated by the fact, that in addition, we observe a very fast decay that stems from Brownian-type diffusion, as will be discussed later in this section. In general, we would expect a rather weak degeneracy between the two adsorption sites, since hydrogen atoms on the Ni(111) surface have exhibited a very low degeneracy [50] and since the additional symmetric graphene layer is not expected to increase the non-degeneracy between sites.

It seems reasonable to assume that the observed jump diffusion stems from jumps between **top** sites, but a more detailed analysis is necessary to come to a definite

conclusion. It might thus be of interest to investigate other options of motion to explain the above discussed data. One option would be a jump rotation model, where a molecule turns in discrete steps of 60° in a sudden motion, just as for translational jump diffusion. The fact that the distance between two neighbouring H atoms in a benzene molecule is 2.5 Å as well as the fact that Fouquet at al. have calculated the energy barrier for rotation of a molecule at the edge of a cluster to 35 meV, undermines this assumption [136]. However, rotational diffusion would result in a quasi-elastic amplitude that rises with Δk, which is not what we observe. Also we do not expect rotations of a benzene molecule to be visible by HeSE and molecules outside of a cluster would exhibit continuous rotations at much faster rates than what we observe here [32]. Another model would be that of a discrete, jump-like association or dissociation of a molecule to or from an island. These two additional approaches might explain the occurrence of the slow exponential decay, and need further investigations in the future.

As can been seen in Fig. 7.8 b), the incoherent decay rate seems not to change with surface coverage for $\theta = 0.02$ ML and $\theta = 0.06$ ML coverage. At $\theta = 0.012$ ML, a certain divergence can be observed, however, it is difficult to judge if this corresponds to a change in the diffusion rate.

7.4.2 Fast Brownian-Type Diffusion

Further measurements at $\theta = 0.02$ ML and $\theta = 0.06$ ML coverage at 110 K have been undertaken, focussing on smaller Fourier times in the range $5 \cdot 10^{-2}$ to 60 ps. In this range, both exponential decays are well resolved. We have calculated a map of the DSF $S(\gamma, \Delta E)$ along the off-specular angle γ and the energy transfer ΔE by Fourier transformation of ISFs at different angles γ. A Hann window function [124] was used for the Fourier transformation, which was carried out by a standard FFT algorithm. A colour-map of the DSF is shown in Fig. 7.9. To increase visibility of faint features, the colour scaling is logarithmic and the elastic line has been cut off above a certain intensity. The Rayleigh phonon mode is faintly visible, but largely suppressed (grey dashed line in Fig. 7.9). An intense quasi-elastic broadening is visible, indicating that the observed fast exponential decay stems from a surface diffusion process, rather than from phonon decay.

We fitted a model function to the data that consists of the sum of two exponentially

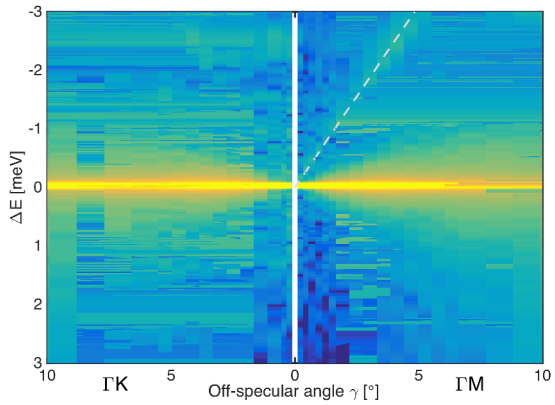

Figure 7.9: Colour map of $S(\gamma, \Delta E)$ at 0.06 ML coverage and 110 K; colouring on a logarithmic scale. Grey dashed line: Initial slope of the Rayleigh phonon mode.

decaying quasi-elastic contributions, as well as an elastic contribution:

$$I(\Delta k, t) = I_{fqe}(\Delta k) \cdot \exp[-\alpha_f(\Delta k)|t|] + I_{sqe}(\Delta k) \cdot \exp[-\alpha_s(\Delta k)|t|] + I_{el}(\Delta k), \quad (7.7)$$

where $I_{fqe}(\Delta k)$ and $\alpha_f(\Delta k)$ are the amplitude and the exponential decay rate of the fast contribution, respectively, and $I_{sqe}(\Delta k)$ and $\alpha_s(\Delta k)$ are the amplitude and the exponential decay rate of the slow contribution, respectively. Here, absolute values of the Fourier time t have been used, since the measurements have been undertaken for positive and negative Fourier times. Surface diffusion processes bear a symmetric behaviour with respect to t, while surface phonons and adsorbate vibrations would introduce asymmetrical contributions. An example ISF together with the different contributions from the fitting procedure can be seen in Fig. 7.10.

The relative amplitudes of the elastic and the slow quasi-elastic contribution $I_{el}(\Delta k)$ and $I_{sqe}(\Delta k)$ are shown in Fig. 7.11 a) and b), respectively. They are plotted as coloured points with error-bars, the corresponding results from the preceding measurement over large Fourier times are drawn as grey lines. The elastic contribution coincides well between the two measurements, the quasi-elastic contribution exhibits broader and more intense asymmetrical peaks at the shoulders of the specular and first order diffraction peak in the second measurement. This difference might either stem from a change in surface coverage between the two measurements, or from a second decay as for the case of non-degenerate jump diffusion.

The relative and absolute amplitudes of the fast exponential decay $I_{fqe}(\Delta k)$ and

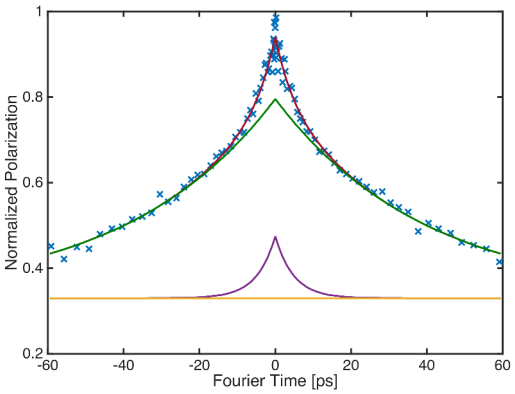

Figure 7.10: ISF at 110 K and $\theta = 0.06$ ML, $\Delta k = 0.17\,\text{Å}^{-1}$, direction $\overline{\Gamma M}$. The measured data are indicated by blue crosses. Yellow line: elastic contribution; green line: sum of elastic contribution and slow quasi-elastic contribution; Purple line: sum of elastic and fast quasi-elastic contribution; red line: sum of all three contributions.

$\tilde{I}_{fqe}(\Delta k)$ are depicted in Fig. 7.12 a) and b), respectively. A very broad contribution is seen with a much broadened specular peak, and a suppressed diffraction peak.

The coherent decay rate $\alpha_f(\Delta k)$ of the fast quasi-elastic contribution is shown in Fig. 7.13 a). Calculating the incoherent decay rate $\alpha_{f,inc}(\Delta k)$, as discussed in Sec. 3.3.3 and earlier in this section, yields the results shown in Fig. 7.13 b), a quadratic dependence on Δk, as the case for Brownian-type diffusion is clearly visible. Fitting $\alpha_f(\Delta k) = D \cdot (\Delta k)^2$ in the range 0 – 1.0 Å^{-1} in both crystal directions gives as a result a diffusion constant $D = (1.8 \pm 0.2)\,\text{Å}^2/\text{ps}$, where an uncertainty of about 10 % from the calculation of the incoherent decay rate has been assumed. This gives a friction $\eta = \frac{k_B T}{mD} = (0.65 \pm 0.07)\,\text{ps}^{-1}$. The fact that the same diffusion rate is observed at 0.12 ML surface coverage indicates that, at these low coverages, it stems entirely from surface friction, i.e. energy dissipation via surface phonons. The RHD model predicts a collisional friction $\eta = 0.13\,\text{ps}^{-1}$ at 0.06 ML and $\eta = 0.26\,\text{ps}^{-1}$ at 0.12 ML. Such an increase in friction with coverage should thus be observable, but the difference is not far above the experimental uncertainty. What can be concluded, is that the observed friction is significantly lower than what has been observed on HOPG, where a surface friction of $(1.7 \pm 0.2)\,\text{ps}^{-1}$ has been obtained [4], but slightly higher than results found on exfoliated graphite, $\eta = (0.3 \pm 1)\,\text{ps}^{-1}$ [32].

In the $\overline{\Gamma K}$ direction, a clear deviation from the parabolic dependence is visible and instead a linear rise in the decay rate can be observed in the range 1.0 – 2.5 Å^{-1}, as

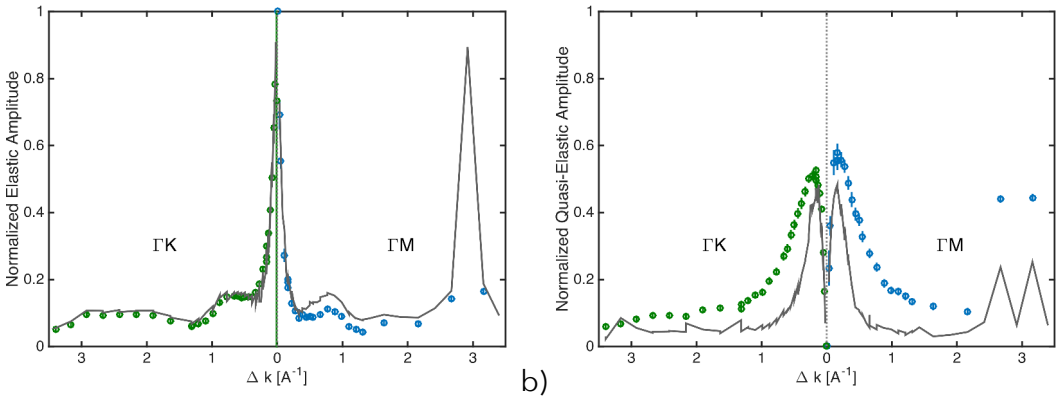

Figure 7.11: Comparison of relative quasi-elastic and elastic contributions at 110 K between measurements. Blue and green: 0.06 ML coverage in $\overline{\Gamma M}$ and $\overline{\Gamma K}$ direction, respectively. a) Elastic contribution from short-time measurements in colours; grey dashed line: elastic contribution from long-time measurement. b) Quasi-elastic contribution from short-time measurements in colours; grey dashed line: elastic contribution from long-time measurement.

indicated by an orange straight line. We interpret this as an onset of ballistic diffusion, in which a molecule follows a straight line at a length scale where the probability of encountering another molecule is negligible. The slope corresponds to the root of the mean square velocity of the ballistically diffusing molecules, from the observed data we obtain a slope of (1.6 ± 0.2) Å/s. By making use of the Boltzmann law, we obtain a root mean square velocity for a 2D gas $\sqrt{\langle v^2 \rangle}$, and relate it to the observed slope via $\sqrt{\langle v^2 \rangle} = \sqrt{2 \ln 2 \frac{2k_B T}{m}} = 1.8$ Å/s [27]. The results are just in agreement within the uncertainty. It has to be mentioned that the ISFs in this range have been fitted by a single exponential decay, while in the case of ballistic diffusion, a Gaussian time-dependence is expected. Additional fits indicate a general trend to such a time-dependence in this region, but due to what might be slight contributions from surface phonons at very short times, such a detailed analysis of the exact shape of the decay is rather involved and would extend beyond this PhD work.

The two blue arrow indicate the momentum transfers that correspond to the distance d between two adjacent molecules on the $(\sqrt{7} \times \sqrt{7})\mathbf{R}19°$ commensurate over structure, projected in the two crystal directions ($\overline{\Gamma M}$: $d = 6.19$ Å; $\overline{\Gamma K}$: $d = 6.44$ Å). It serves as an indicator for the mean free path of a molecule in an island. For higher momentum transfers, i.e. shorter distances, a molecule will statistically not encounter another molecule and follow a straight flight path. The purple arrow indicates the size

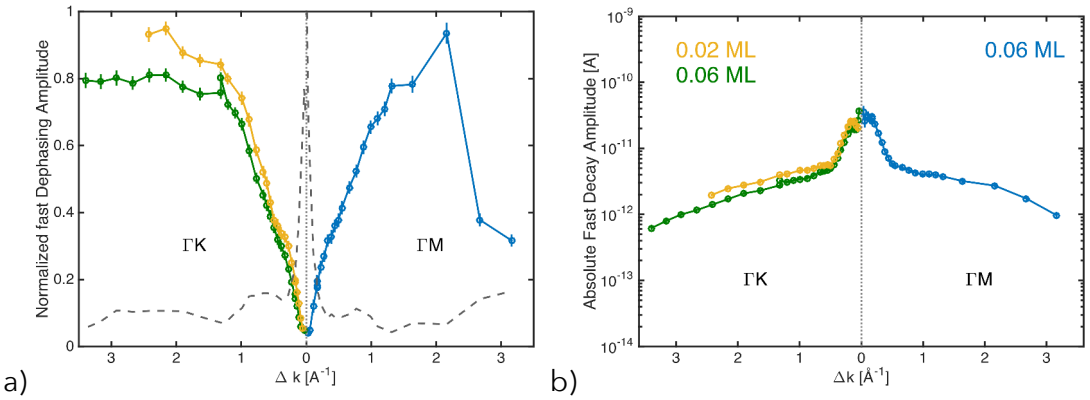

Figure 7.12: Amplitudes of the fast quasi-elastic contribution at 110 K. a) Relative amplitude $I_{fqe}(\Delta k)$, grey dashed line: relative elastic contribution at 0.06 ML. b) Absolute amplitude $\tilde{I}_{fqe}(\Delta k)$.

of the unit cell of graphene/Ni(111), $d = 2.49$ Å. Within this range, a molecule needs to overcome the walls of the PES. In the $\overline{\Gamma M}$-direction, a ballistic flight seems not to occur. We interpret this as an indication that surface friction is asymmetrical. Fouquet et al. found from Forcefield MD simulations, that a diffusing benzene molecule experiences a very flat PES when moving along the $\overline{\Gamma K}$-direction, while potential energy barriers in the order of several meV have to be overcome when moving along the $\overline{\Gamma M}$-direction [136]. Finally, two data points close to the first order diffraction peak show a dramatically decreased decay rate. However, the calculation of the incoherent decay rate is not correct in the close vicinity of diffraction peaks (Sec. 3.3.3), and thus these data points (as well as those very close to $\Delta k = 0$) should not be taken into account. The purple arrow indicates the momentum transfer that corresponds to the size of the graphene unit cell, i.e. the distance between to adjacent hollow adsorption sites. The abrupt ending of the ballistic "regime" at this point, raises the idea that the potential barriers, even if very small, might influence diffusion at length scales below the unit cell size.

7.5 Conclusions

We have studied the adsorption, structure and dynamics of sub-monolayer benzene adsorbed on a graphene/Ni(111) surface.

Specular ^{3}He reflection measurements of the adsorption of benzene on the graphene surface revealed an initial adsorption with low interaction between molecules

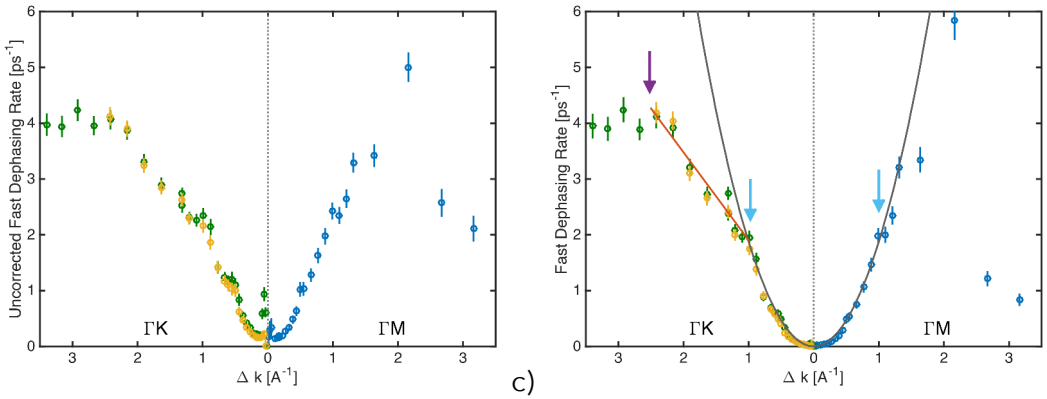

a) c)

Figure 7.13: Fast decay rate versus Δk at 110 K. Blue and green: 0.06 ML coverage in $\overline{\Gamma M}$ and $\overline{\Gamma K}$ direction, respectively; Yellow: 0.12 ML coverage in $\overline{\Gamma K}$ direction. a) Fast coherent decay rate $\alpha_f(\Delta k)$ as obtained from the measurements. b) Fast incoherent decay rate $\alpha_{f,inc}(\Delta k)$. Grey solid line: Brownian-type diffusion. Orange line: ballistic diffusion in $\overline{\Gamma K}$ direction in the range 1.0 – 2.5 Å^{-1}. Blue arrows: momentum transfers that correspond to the distance between two adjacent molecules on the $(\sqrt{7}\,x\,\sqrt{7})\,\mathbf{R}19°$ over-structure, projected in the two crystal directions. Purple arrow: momentum transfer that corresponds to the size of the graphene unit cell.

that allowed us to determine a helium scattering cross section for benzene of $\Sigma = (630 \pm 120)$ Å^2. The initial adsorption is then followed by a condensation of molecules into 2D islands up to monolayer completion. The clustered benzene molecules exhibit a reflectivity of 5 % of the reflectivity of the graphene surface and a height difference between the adsorbed layer and the graphene surface of (3.38 ± 0.02) Å. No second layer formation is observed, we expect the formation of 3D islands above the monolayer.

Isothermal desorption measurements of sub-monolayer coverages exhibit an exponentially decaying surface coverage. The initial desorption rate obeys an activated temperature dependence with an activation energy of desorption of (293 ± 12) meV. TDS measurements revealed the existence of a single desorption peak. Analysis of the dependence of desorption temperature with heating rate via the Redhead formula yield inconsistent activation energies of desorption between 400 and 600 meV.

We have performed helium diffraction measurements of a benzene monolayer at 110 K that confirmed the existence of a commensurate $(\sqrt{7}\,x\,\sqrt{7})\,\mathbf{R}19°$ over-layer. The

visible diffraction peaks could be identified by comparison with LEED and neutron scattering data.

HeSE measurements at 110 K and at three different coverages in the range 0.06 – 0.12 ML revealed the coexistence of three different types of molecular diffusion. A slow activated diffusion was observed, whose nature is not clear. We found good agreement with a translational jump diffusion model at a hopping rate $\eta = (14.1 \pm 0.4) \cdot 10^{-3}\,\mathrm{ps}^{-1}$ at 110 K, but rotational jump diffusion or a jump-like configurational change of islands might be possible explanations as well. A fast diffusion which consists of regimes of Brownian-type diffusion and of ballistic diffusion has been found. The ballistic part seems to exhibit an asymmetrical behaviour which can be linked to the PES. The Brownian-type diffusion is governed by static friction from interaction with the substrate, the measured friction is $\eta = (0.65 \pm 0.07)\,\mathrm{ps}^{-1}$.

8 H_2 on Exfoliated Graphite and on Highly Porous Carbon

8.1 Introduction

The role of hydrogen as a potential energy carrier is being more and more recognized, however its storage still suffers difficulties, especially with regard to the search for a lightweight mobile storage medium on board of vehicles. Due to their very large specific surface area and low specific weight, porous carbons and carbon nano-structures are being considered as serious candidates for hydrogen storage and a large number of investigations has been conducted on these materials in recent years [189, 190, 191]. Various specific carbon systems have been studied experimentally, such as nanofibers [192], nanotubes [193, 189, 194], nanohorns [195], porous carbons [196], and carbon aerogels [197]. The ability of a material to adsorb gases depends on its total pore volume and on its specific surface area, but also on the pore size distribution, i. e. the differential pore volume as a function of the pore diameter. It is commonly measured by isothermal adsorption of a light gas, where the gas pressure is gradually increased at constant temperature while monitoring the adsorbed volume until saturation.

The structure of an adsorbed layer of molecular hydrogen on the basal plane of graphite exhibits at temperatures below 22 K a commensurate $(\sqrt{3} \times \sqrt{3})\mathbf{R}30°$ structure for coverages up to a full monolayer and an incommensurate dense layer at higher coverages as evidenced by early diffraction measurements [198, 199]. Further neutron scattering studies showed a more complex picture, revealing several intermediate structural phases for H_2 and D_2 [200, 201, 202].

Diffusion of hydrogen in carbon materials has been studied intensely by means of quasi-elastic neutron scattering in recent years. The investigated carbon systems have been varied, including graphite [203], single wall carbon nanotubes (SWNT)

[204], carbon nanohorns [205], porous carbons [206, 207, 208], potassium intercalated graphite [209, 210], and platinum containing porous carbon [211]. Nguyen *et al.* observed different diffusion rates for H_2 and D_2 at low temperatures in a carbon molecular sieve (CMS) [212].

Two diffusion models were assumed in the interpretation of most of the above data: jump diffusion models of a discrete geometry [207, 210] and jump diffusion models over a continuous distribution of jump distances, as for liquids [205, 204, 203, 206, 208, 211].

To our knowledge, Brownian-type diffusion of adsorbed molecular hydrogen has not been observed yet by neutron scattering at large momentum transfers (at low momentum transfers, all types of translational diffusion approach Brownian-type diffusion).

The goal of the work presented in this chapter was to study and compare the adsorption and the diffusional dynamics of molecular hydrogen adsorbed on the surfaces of a novel highly porous carbon (from now on referred to as D-96-7) and on exfoliated graphite Papyex [158, 159]. We have observed a combination of Brownian-type and jump diffusion over a large temperature and momentum transfer range in both systems.

This chapter is organised as follows: In section 8.2 we give a brief overview of the synthesis of D-96-7 and we describe the experimental methods of the conducted diffraction and spectroscopy measurements. In section 8.3 we present and discuss the experimental results. We first show results from adsorption measurements on D-96-7 (sec. 8.2.1). We then discuss neutron and X-ray scattering results and their implications on the structure of the material (sec. 8.3.1). We finally present our findings on the diffusion rates and activation energies and their implications on static and kinetic friction of hydrogen in both materials and compare them to results from other carbon materials.

8.2 Experimental

8.2.1 Sample Characterization

The synthesis and characterisation of D-96-7 have been entirely conducted by L. Hoyos and will be published in the future. Because of their relevance to the interpretation of the experimental data, they are nevertheless briefly described here: The D-96-7 has been synthesised via direct route assembly using pluronic F-127 as surfactant and with tetraethyl-orthosilicate (TEOS), aniline served as a carbon source. It exhibits a micro- and mesoporous structure and a very high specific surface area. Due to the carbonization temperature and the source of carbon used, the material contains both short range ordered graphitic regions as well as regions of amorphous carbon.

Initially, a reaction mixture was prepared by dissolving 1.05 mol aniline in a 5 % F-127 (Sigma) solution. Then, 1 mol TEOS were added and the pH was adjusted to 5.0 with 1M HCl. The clear solution was heated to 95 °C for 96 h. The material was carbonized in inert atmosphere (60 ml/min N_2), at 750 °C. The final material was put in contact with 40 % HF to dissolve the silica and obtain a pure carbon.

Nitrogen adsorption/desorption isotherms of D-96-7 were measured in a Micromeritics ASAP 2020 instrument at 77 K. Prior to the measurement, the samples had been activated under vacuum at 250 °C for 12 h. The percentage of residual nitrogen in D-96-7 was determined using elemental analysis (CHN LECO, Truspec Micro).

The N_2 sorption isotherm of D-96-7 is shown in Fig. 8.1 a). The pore size distribution has been calculated by using the software of the instrument (Micromeritics Data Master V 4.03). The microporous, mesoporous and total area were determined using the t-plot model [213] at a relative pressure (P/P_0) from 0.1 to 0.6, the Barrett-Joyner-Halenda (BJH) model [214] at P/P_0 from 0.3 to 1.0 and the BET model [215] at P/P_0 from 0.05 to 0.3, respectively.

A concave isotherm curve is obtained for D-96-7. The presence of a hysteresis at high relative pressure has been associated with a type IV isotherm. The change in slope at high pressures indicates a multilayer pore filling mechanism, which is typical for mesoporous materials and for a strong interaction between the adsorbate and the pore walls. The presence of a type H3 hysteresis loop has been associated with

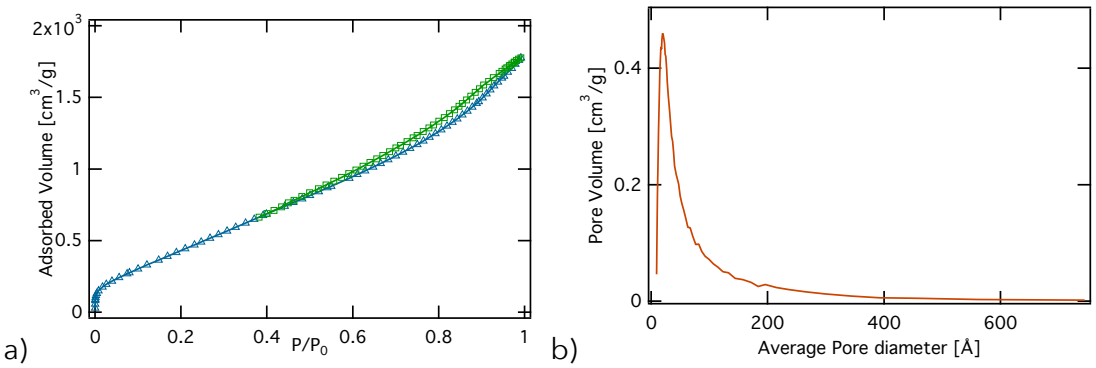

Figure 8.1: a) Nitrogen adsorption/desorption isotherms of D-96-7 measured at 77 K. Increasing pressure is indicated by blue triangles, decreasing pressure by green squares. b) Pore size distribution of D-96-7 obtained from the 77 K N_2 adsorption measurements.

micro- and mesopores with a slit shape pore morphology. The microporous, mesoporous, and total pore volume and size were determined using the Horvath-Kawazoe (HK) model [216], the BJH model [214], and the BET model [215], respectively. The resulting pore size distribution is shown in Fig. 8.1 b). A range of parameters deduced from the adsorption/desorption measurements are summarised in Tab. 8.1. D-96-7 has a high specific area surface of 1712 m^2/g, and pore volume of 2.75 cm^3/g with primary contribution of the mesopore volume and with relatively low microporosity.

	t-plot/HK		BET			BJH	
	V_{micro} [cm^3/g]	D_{micro} [A]	V_{meso} [cm^3/g]	D_{meso} [A]	S_{BET} [m^2/g]	V_{total} [cm^3/g]	S_{BJH} [m^2/g]
N_2	2.75	19	2.34	167	1711.88	2.75	1971.24

V_{micro}: microporous pore volume; D_{micro}: microporous pore size; V_{meso}: mesoporous pore volume; D_{meso}: mesoporous pore size; S_{BET}: specific surface area from the BET model; V_{total}: total pore volume; S_{BJH}: specific surface area from the BJH model.

Table 8.1: Characteristic parameters of adsorption and morphology of D-96-7 from N_2, CO_2 and H_2 vapour adsorption measurements.

Papyex is an exfoliated and re-compressed graphite that consists mainly of (0001) basal graphite planes with an average size of several hundred Å [158]. These planes are partially oriented with about 75 % exhibiting orientation around a plane with a HWHM of its mosaic spread of 15°, and about 25 % being completely randomly oriented, the basal planes are stacked in about 30 % as α graphite and in about 70 %

as β graphite [217, 218]. BET analysis reveals a Type II sorption isotherm, indicating that Papyex contains a negligible amount of micropores and has a total surface area of about 20 m^2/g. SANS experiments employing contrast variation show that the voids in Papyex are connected and fillable [158].

8.2.2 Neutron Small-Angle Scattering Measurements

To examine the structure of our Papyex sample, SANS measurements have been performed on the D22 diffractometer at ILL [20] at a neutron wavelength $\lambda = 6$ Å and at detector distances 11.2 m and 2 m (with a rectangular collimation of length of 11.2 m and 21.8 m, respectively). These set-ups cover a total Q-range of $0.004 \leq Q \leq 0.45$ Å^{-1}. The beam size at sample position was 7 x 10 mm^2 and the sample thickness was 1 mm. Measurement time at each set-up was 120 s. Prior to the measurement, a 6 x 10 mm^2 chip of Papyex with a thickness of 1 mm had been out-gassed under vacuum at a temperature of 1000 K over 24 h and filled into a standard Quartz SANS sample holder under argon atmosphere.

The structure of D-96-7 has been studied by SANS on the PAXY diffractometer at LLB, Saclay, France at three set-ups of neutron wavelength λ and detector distance l: $\lambda = 4$ Å, $l = 1.245$ m; $\lambda = 10$ Å, $l = 3.194$ m; $\lambda = 12$ Å, $l = 6.807$ m. Combining these set-ups covers a total Q-range of $0.004 \leq Q \leq 0.47$ Å^{-1}. Prior to the measurement, the fine powder of D-96-7 was filled into pockets of aluminium foil of approximately 10 x 20 mm^2 width and 1 mm thickness.

8.2.3 Neutron Time-of-Flight Measurements

Neutron TOF spectroscopy measurements were performed on the IN6 spectrometer at ILL [21] using a set-up of three composite pyrolytic graphite monochromators at a neutron wavelength $\lambda = 5.12$ Å. The scattering functions from neutron TOF spectroscopy, $S(Q, \omega)$, covered a momentum transfer range of $0.1 \leq Q \leq 2.0$ Å^{-1} and an energy transfer range of $-6 \leq \hbar\omega \leq 2$ meV. The data were grouped into windows of $\Delta Q = 0.1$ Å^{-1} and $\Delta(\hbar\omega) = 50\,\mu$eV in momentum transfer and energy transfer, respectively. All data were treated using the LAMP software package [219]. Prior to the measurement, D-96-7 was crushed to a fine powder and filled into a hollow, cylindrical aluminium sample holder with an annular width of 1 mm. The sample was

heated in vacuum at 350 °C for 20 h to remove volatile contaminants from the surface. The Papyex sample was cut into disks of 18 mm diameter. About 30 disks were then stacked flat-lying in a cylindrical aluminium sample holder of 2 cm diameter. The temperature was controlled using a standard liquid helium cryostat ("orange" cryostat [161]). Both samples were cooled to 1.5 K and the quantity corresponding to 0.5 monolayer (ML) of hydrogen gas was dosed through a stainless steel capillary that was connected to a pressure control monitor. Throughout the entire experiment, connection to a 500 cm^3 reservoir at room temperature was maintained for security reasons. In our set-up any desorbed hydrogen rises to the reservoir, where the desorbed quantity can be deduced through pressure monitoring. A listing of the relative coverages obtained at sample temperatures between 5 and 80 K is given in Tab. 8.2. For the neutron scattering experiments, an elastic scattering resolution measurement was performed at 1.5 K. Spectra were then measured at temperatures between 5 K and 80 K.

Sample temperature [K]	Relative coverage D-96-7 [ML]	Relative coverage Papyex [ML]
5	0.5	0.5
8	0.5	–
10	–	0.5
12	0.5	–
17	0.46	0.5
22	0.39	0.5
30	0.33	–
40	0.29	0.48
50	0.26	–
60	0.22	0.39
80	–	0.27

Table 8.2: Relative coverages in fractions of a monolayer (ML) used in the experiment at sample temperatures between 5 and 80 K. The values are deduced from the hydrogen pressure in a security reservoir connected to the sample.

8.3 Data Analysis and Results

8.3.1 Neutron Scattering – Structure

Fig. 8.2 shows the energy-integrated scattered intensities $S(Q)$ of the TOF measurements of D-96-7 and Papyex at different temperatures, as well as the measured SANS and diffraction response. Both substrates exhibit a strong small angle scattering that is commonly found for materials with a hierarchical structure. The Papyex substrate exhibits a bright peak at about 1.8 $Å^{-1}$, D-96-7 shows no diffraction signal at high Q.

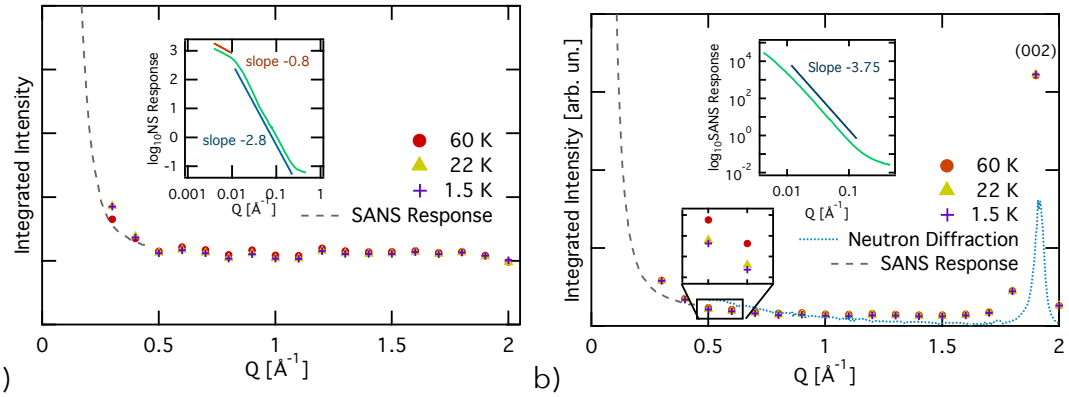

Figure 8.2: Energy-integrated intensities S(Q) obtained at IN6 for D-96-7 and Papyex after hydrogen adsorption at 1.5 K (crosses), 22 K (triangles) and 60 K (circles). The data are compared to SANS measurements (solid and dashed lines) and to neutron diffraction measurements (dotted line). a) D-96-7 b) Papyex. The (002) Bragg reflection at 1.87 $Å^{-1}$ is clearly visible for the Papyex sample. Insets: log-log plot of SANS response.

Over a range of about 0.1 – 0.01 $Å^{-1}$, the SANS response of the Papyex substrate follows a power law scaling, $I \propto Q^{-\alpha}$ with $\alpha = (3.751 \pm 0.006)$. This is in the range of the value found by Gilbert et al., $\alpha \approx 3.5$ [158] (see Inset of Fig. 8.2). Although this might be interpreted in terms of a generalised Porod type scaling, $I(Q) \propto Q^{-(6-d)}$, which would yield a fractal dimension $d = 2.25$, this is not easily justified (as has been discussed in detail by Gilbert [158]). The SANS response of D-96-7 follows a power law scaling as well, over a range of about 0.2 – 0.02 $Å^{-1}$. Here, we find an exponent $\alpha = (2.81 \pm 0.02)$. In terms of interpretation of this exponent as a fractal dimension, this would yield an unreasonable result of $d = 3.2$. An in-depth analysis of the SANS data is unfortunately beyond the scope of this work.

Now looking at the structure factor $S(Q)$, obtained by energy integration of the spectra from the TOF measurements (Fig. 8.2), we find that the signal is mostly flat for both substrates. Papyex however, exhibits a strong peak at about 1.8 $Å^{-1}$ in both the IN6 and the D20 data, which stems from the (002) Bragg reflection from the basal planes of graphite. No Bragg peak of the Basal plane is found for the D-96-7 substrate within the Q range of the present experiments. This is interpreted in terms of an absence of long-range order. For both samples, the scattering signal rises with temperature at most values of Q (see inset of Fig. 8.2 b)). This is due to a higher amount of the ortho-hydrogen spin state at higher temperatures (see Chap. 9), which yields a much higher neutron scattering cross section than the para-state. It is interesting to notice that this effect is stronger than the concurring loss in signal that stems from a desorption of hydrogen with increasing temperature (see Tab. 8.2).

8.3.2 Neutron Spectroscopy – Dynamics

We will now discuss the dynamic scattering functions, $S(Q,\omega)$, which were extracted from the IN6 neutron time-of-flight spectra. An example of a scattering function at a momentum transfer of $Q = 1.0\,Å^{-1}$ is shown in Fig. 8.3. To extract the dynamic information, the TOF spectra for a given momentum transfer were fitted to a test function using a least-square algorithm. For both activated diffusion processes and Brownian-type diffusion, we generally expect a broadening of the elastic line, the QENS broadening around $\omega = 0$, that obeys a Lorentzian shape [19]. Hence, we used a convolution of the resolution function, $R(Q,\omega)$ (that was obtained from the clean substrate at 1.5 K), with a delta function (elastic scattering) and a single Lorentzian distribution that represents the quasi-elastic broadening, as well as a constant background, C:

$$S(Q,\omega) = \left[I_{el} \cdot \delta(\omega) + I_{inel} \cdot \frac{\hbar}{\pi} \frac{\Gamma}{\omega^2 + \Gamma^2} \right] * R(Q,\omega) + C, \tag{8.1}$$

where Γ is the HWHM of the Lorentzian distribution.

We used the reduced χ^2 as a representation of the goodness-of-fit. It showed no improvement upon adding a flat or sloped background. Also, no sign of a second Lorentzian broadening was found within the energy range and resolution of the instrument. Furthermore, we did not find a deviation from the Lorentzian shape, such

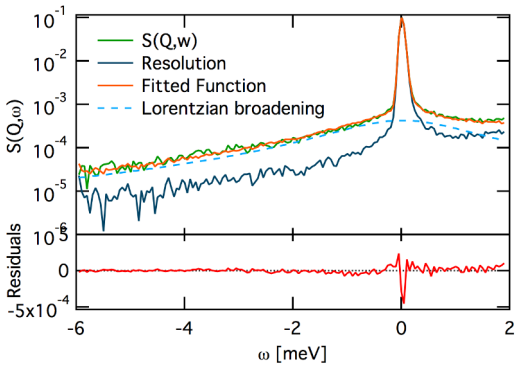

Figure 8.3: A representative slice of the scattering function $S(Q,\omega)$ at a momentum transfer of $Q = 1.0\,\text{Å}^{-1}$ and a temperature of 40 K of the Papyex sample. The green line shows the data of the hydrogen containing sample at 40 K. The dark blue line shows the measured data points of the Papyex sample at a temperature of 1.5 K (resolution function). The green solid line is the fitted model function and the light blue dashed line is the Lorentzian distribution that was extracted by the fit. The lower panel shows the residuals of the fit function.

as a Gaussian or a Voigt shape of the quasi-elastic broadening. The residuals of the fits show no systematic errors and only an increase in absolute statistical error is observed in close vicinity of the elastic peak at $\omega = 0$ (Fig. 8.3).

The fitting parameters I_{el} and I_{inel} in equation (8.1) correspond to the elastic and inelastic scattering contributions of the entire sample *relative* to the signal of the empty sample at a temperature of 1.5 K. The elastic and inelastic intensities $S_{el}(Q)$ and $S_{inel}(Q)$, respectively, were obtained by multiplication of I_{el} and I_{inel} with $S(Q)$. The Q-dependence of $S_{el}(Q)$ and $S_{inel}(Q)$ is shown for both substrates in Fig. 8.4. For further analysis, we have omitted the region above $Q = 1.75\,\text{Å}^{-1}$ (indicated in Fig. 8.4 by a grey dashed line) to avoid contributions from a graphite Bragg peak, even though for the D-96-7 sample, there seems to be no sign of it.

$S_{el}(Q)$ is for both samples almost identical to the integrated intensity (upper panels in Fig. 8.4). This is due to the fact that the carbon sample itself is a much stronger neutron scatterer than the relatively small amount of adsorbed hydrogen.

$S_{inel}(Q)$ exhibits no substantial Q-dependence for either system. We have averaged $S_{inel}(Q)$ over Q in order to analyse the temperature dependence (Fig. 8.5). It decreases with temperature, reflecting an activation barrier. We find activation energies of $E_A = (9.19 \pm 0.05)\,\text{meV}$ for the Papyex substrate and $E_A = (7.67 \pm 0.09)\,\text{meV}$

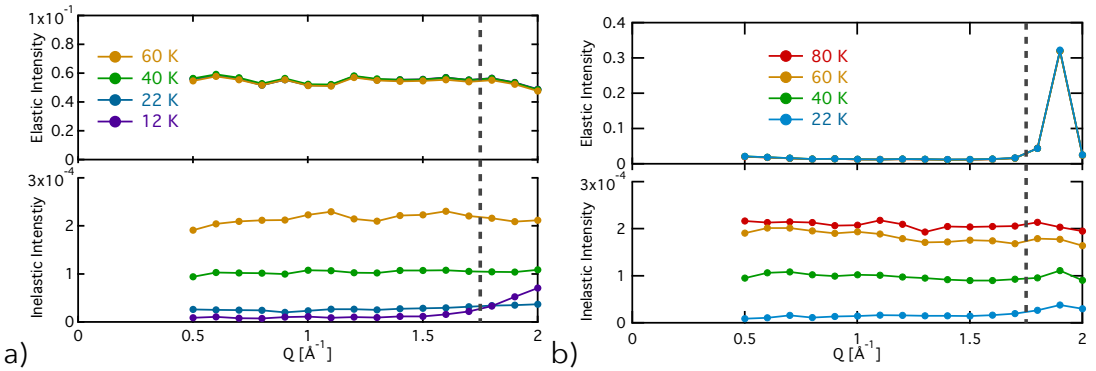

Figure 8.4: Elastic and inelastic intensities as a function of momentum transfer, Q at different temperatures. Values to the right of the dashed grey line have not been taken into account for analysis of the quasi-elastic broadening. a) Results for the D-96-7 substrate. b) Results for the Papyex substrate.

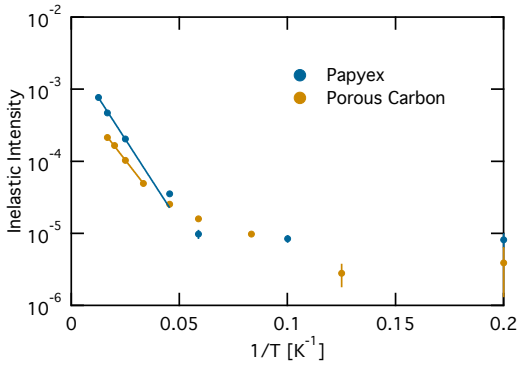

Figure 8.5: Inelastic intensity as a function of temperature.

for D-96-7 (Fig. 8.5). At temperatures below 20 K, the inelastic signal becomes too weak to be distinguished from instrumental background. We interpret this drop of signal as a freezing of the hydrogen diffusive dynamics, in consistency with neutron diffraction measurements of hydrogen on graphite that discovered a transition between an ordered commensurate layer below 22 K and a liquid state above this temperature [200, 202].

The QENS broadening $\Gamma(Q)$ exhibits a strong temperature dependence and rises in general with increasing Q (Fig. 8.6). We found that $\Gamma(Q)$ consists of the sum of a parabolic part and a sinusoidal part:

$$\Gamma(Q) = \hbar\eta_{JD}\frac{\int\left[1 - J_0(Q \cdot l \sin\theta)\right] f(\theta)\mathrm{d}\,\theta}{\int f(\theta)\mathrm{d}\,\theta} + \hbar D_{BR} Q^2, \tag{8.2}$$

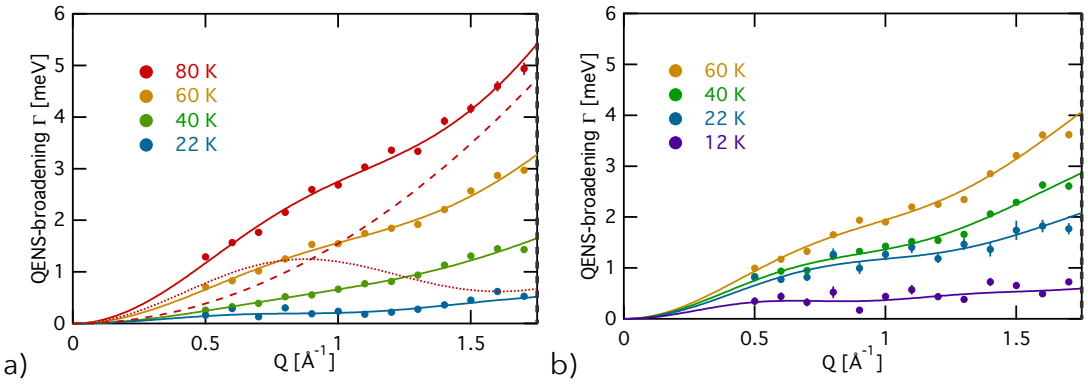

Figure 8.6: The quasi-elastic line broadening Γ as a function of momentum transfer, Q, for a range of sample temperatures. The error bars are too small to be visible for most data points. The continuous lines show the results from fitting Eq. (8.2) to the broadening. Both contributions to the broadening have been shown separately for the 80 K data: the dashed red line shows the contribution from collisional diffusion and the dotted red line show the contribution from jump diffusion.

where the first part of the right hand side corresponds to jump diffusion from hopping between adsorption sites on a Bravais lattice, and the second part of the right hand side corresponds to Brownian-type diffusion. Here, $\hbar$ denotes the reduced Planck constant. η_{JD} and l are the hopping rate and distance, respectively, of jump diffusion. J_0 denotes the 0th order cylindrical Bessel function and $f(\theta)$ describes the angular distribution of planes in the substrate along the angle of inclination θ with respect to the normal of the scattering plane. D_{BR} denotes the diffusion constant of the Brownian part.

The CE model of jump diffusion has been discussed in Sec. 3.2.5. For the case of two dimensional diffusion on a surface in a multi-crystalline system, the jump vectors l, connecting initial and final adsorption site of a jump, need to be averaged isotropically [220]. This produces a zeroth order Bessel function J_0. The distribution $f(\theta)$ of inclination angles θ is different for both systems. While D-96-7 is completely 3-D isotropic, Papyex consists of planes with an inclination that is normally distributed around $\theta = 90°$ with a HWHM of about 15° [218]. This has been taken into account by numerical integration of Eq. (8.2). It has to be noted that the isotropic averaging is only an approximation that omits the fact that the correct isotropic averaging of Eq. (8.1) produces in general a non-Lorentzian QENS broadening. This matter is discussed in detail in Sec. 9.3, where the correct averaging is applied, which necessitates a rather involved global fitting of the entire spectrum. Here, the approximate

solution produces very good results, and we will therefore rely on it. An exemplary result of fitting Eq. (8.2) can be seen in Fig. 8.6. In a), both contributions of the equation have been plotted separately for the result from 80 K. The dotted red line shows the contribution from jump diffusion and the dashed red line the contribution from Brownian-type diffusion.

The second term of Eq. (8.2), $\hbar D_{BR} Q^2$, stems from continuous Brownian motion, the origin of which is in general twofold. It may stem on the one hand from interaction with the surface, which is expressed by a surface friction η_{sur}. On the other hand, it may also stem from a collisional friction η_{coll}, which arises from collisions between particles. The diffusion constant D_{BR} is related to the collisional and surface friction via $D_{BR} = \langle v^2 \rangle / (\eta_{sur} + \eta_{coll})$, where $\langle v^2 \rangle = \frac{2}{m} k_B T$ is the thermally averaged velocity of the diffusing molecule. The collisional friction has been observed by us for diffusion of benzene molecules on a graphite surface, where we successfully calculated the collisional friction by a RHD model. This parameter-free model takes into account the exchange between angular and rotational momentum between colliding molecules, as well as collision probabilities based on the distribution of molecules on the surface [32]. The collisional friction is calculated by:

$$\eta_{coll}(\theta, T) = \frac{\kappa}{\kappa + 1} \left(\frac{3}{2} + \frac{1}{\kappa} \right) \frac{d g_d(d+)}{A_{uc}} \sqrt{2\pi} \theta \sqrt{\frac{k_B T}{\mu}}, \tag{8.3}$$

where $\mu = m/2 = 1.008\,\text{g/mol}$ is the reduced mass of the colliding molecules, $d = 3.6\,\text{Å}$ is the collision distance. $g_d(d+) = 1.75$ is the value of the radial distribution function at the distance of collision d, i.e. at its first maximum. We extracted these values from path-integral calculations for liquid hydrogen, as can be seen in Fig. 8.7 [221]. The value of the collision distance d agrees well with the intermolecular distance at the completion of an incommensurate monolayer $d = 3.53\,\text{Å}$, as measured by neutron scattering [200]. $\kappa = 2I/\mu d^2 = 0.044$ is the moment of inertia of the molecule, normalised by $2\,\mu d^2$. For the hydrogen molecule, κ is very small since the mass is situated very close to the centre of mass of the molecule. This means that the exchange between angular and rotational momentum between colliding molecules is negligible in this case. $A_{uc} = 15.7\,\text{Å}^2$ is the surface area that is covered by a single molecule at full monolayer coverage i.e. the unit cell size of a $(\sqrt{3} \times \sqrt{3})\mathbf{R}30°$ over-structure. θ is the relative surface coverage in ML, it depends on the sample temperature and has been calculated from the hydrogen pressure in the reservoir; the exact values can be found in Tab. 8.2. k_B is the Boltzmann constant

and T the sample temperature.

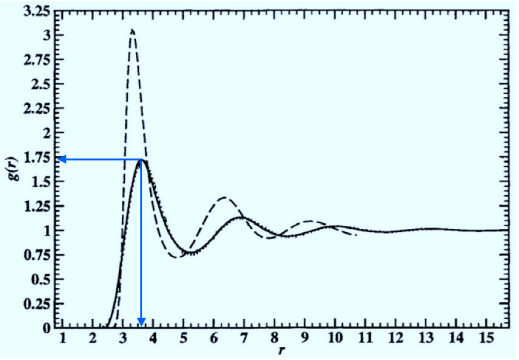

Figure 8.7: Radial distribution function $g(r)$ of liquid para-hydrogen versus distance r, calculated by path integral simulations, from [221] (Solid line). Blue arrows: values for g(d) and d of the first maximum, which we used to calculate the collisional friction. The dashed line is of no importance for this work.

T [K]	l [Å]	η [ps^{-1}]	D_{JD} [m^2/s] $\times 10^{-8}$	D_{BR} [m^2/s] $\times 10^{-8}$	η_{coll} [ps^{-1}]	η_{sur} [ps^{-1}]
5–17	–	–	–	–	–	–
22	6.1 ± 0.6	0.13 ± 0.03	1.2 ± 0.4	0.20 ± 0.02	2.19	42 ± 4
40	4.7 ± 0.1	0.19 ± 0.01	1.0 ± 0.1	0.77 ± 0.01	2.83	18.7 ± 0.2
60	4.49 ± 0.07	0.70 ± 0.02	3.5 ± 0.1	1.44 ± 0.02	2.82	14.3 ± 0.2
80	4.38 ± 0.07	1.35 ± 0.03	6.5 ± 0.3	2.36 ± 0.04	2.25	11.8 ± 0.2

Table 8.3: Papyex substrate: diffusion parameters extracted from fitting equation (8.2) to the experimental data. T: surface temperature; l: jump distance, η: jump rate; D_{JD} diffusion constant of jump diffusion; D_{BR} diffusion constant of Brownian-type diffusion; η_{coll}: collisional friction from the RHD model; η_{sur}: surface friction. In the range from 5 – 17 K, statistical error of the experimental data was too large and the data have been omitted.

The results from the RHD model are compared to the fitted parameters in Tab. 8.4 for D-96-7 and in Tab. 8.3 for Papyex. The obtained jump length l is in the order of 6 Å for the D-96-7 substrate, in good agreement with results from other systems, such as on carbon-aerogel (Chap. 9), or other porous carbon materials [207]. For the Papyex substrate, the distance is rather of the order of 4.5 Å at most temperatures. This corresponds to the inter-molecular distance within the commensurate structure $a = 4.26$ Å, but assuming repulsive interaction, the distance should scale inversely with the root of the surface coverage, i.e. at 0.5 ML, $a = 6.03$ Å. The calculated distance might be slightly influenced by the approximate isotropic av-

T [K]	l [Å]	η [ps^{-1}]	D_{JD} [m^2/s] $\times 10^{-8}$	D_{BR} [m^2/s] $\times 10^{-8}$	η_{coll} [ps^{-1}]	η_{sur} [ps^{-1}]
5–12	–	–	–	–	–	–
17	7.3 ± 0.6	0.02 ± 0.01	9 ± 3	0.36 ± 0.05	1.77	18 ± 3
22	5.8 ± 0.5	1.18 ± 0.01	10 ± 2	0.66 ± 0.07	1.70	12 ± 1
30	6.0 ± 0.3	1.14 ± 0.06	10 ± 1	0.90 ± 0.05	1.68	12.1 ± 0.6
40	6.4 ± 0.2	1.13 ± 0.03	10.2 ± 0.8	1.02 ± 0.03	1.71	14.4 ± 0.4
50	6.0 ± 0.1	1.29 ± 0.03	11.6 ± 0.5	1.34 ± 0.02	1.71	13.6 ± 0.2
60	5.8 ± 0.1	1.47 ± 0.03	13.2 ± 0.6	1.53 ± 0.03	1.59	14.6 ± 0.3

Table 8.4: D-96-7 substrate: diffusion parameters extracted from fitting equation (8.2) to the experimental data. T: surface temperature; l: jump distance, η: jump rate; D_{JD} diffusion constant of jump diffusion; D_{BR} diffusion constant of Brownian-type diffusion; η_{coll}: collisional friction from RHD model. In the range from 5 – 12 K, statistical error of the experimental data was too large and the data have been omitted.

eraging of $\Gamma(Q)$, but further analysis would be necessary to investigate this issue. From the jump rate η_{JD}, a diffusion constant D_{JD} has been calculated by the relation $D_{JD} = \eta_{LD}\frac{l^2}{4}$ for each measurement [207]. For both substrates, the diffusion constants are shown in an Arrhenius plot in Fig. 8.8. Above about 20 K, D_{JD} exhibits an activated behaviour (blue dots and lines). D_{BR} follows approximately a $\sqrt{T}$-dependence, the experimental data are shown as red dots. By matching the theoretical diffusion constant $D_{BR} = \frac{2k_BT}{m}/(\eta_{sur} + \eta_{coll})$ to the experimental results, we obtain a value for η_{sur}. For the D-96-7 substrate, η_{sur} seems not to change with temperature and we thus assume a constant averaged value $\eta_{sur} = (13.9 \pm 0.1)\,\text{ps}^{-1}$. For the Papyex substrate, a temperature dependence seems to exist, with an increasing surface friction for lower temperatures. Up to this point, we have not understood the reason for this change in surface friction in detail. Averaging over all temperatures gives $\eta_{sur} = (14.7 \pm 0.1)\,\text{ps}^{-1}$, which is close to the findings on D-96-7. The calculated surface friction is immense in comparison to e.g. values below $1\,\text{ps}^{-1}$ for the case of benzene on graphite and graphene [32]. The slope of D_{JD} in the Arrhenius plot shown in Fig. 8.8 produces for the Papyex substrate an activation energy of jump diffusion $E_a = (12.6 \pm 0.1)\,\text{meV}$ and a pre-exponential factor $D_{0,JD} = (4.1 \pm 0.1) \cdot 10^{-7}\,\text{m}^2/\text{s}$. For the D-96-7 substrate we find $E_a = (2.7 \pm 0.6)\,\text{meV}$ and $D_{0,JD} = (2.2 \pm 0.3) \cdot 10^{-7}\,\text{m}^2/\text{s}$. In Fig. 8.9, we compare D_{JD} to results from studies on similar carbon systems. Our finding for the Papyex substrate are very close to what has been found before on the same substrate at lower temperatures [203], on a highly porous commercial carbon black XC-72 [206, 208], and on single walled nanotubes [204]. It is very surprising that D-96-7 exhibits an activation energy that

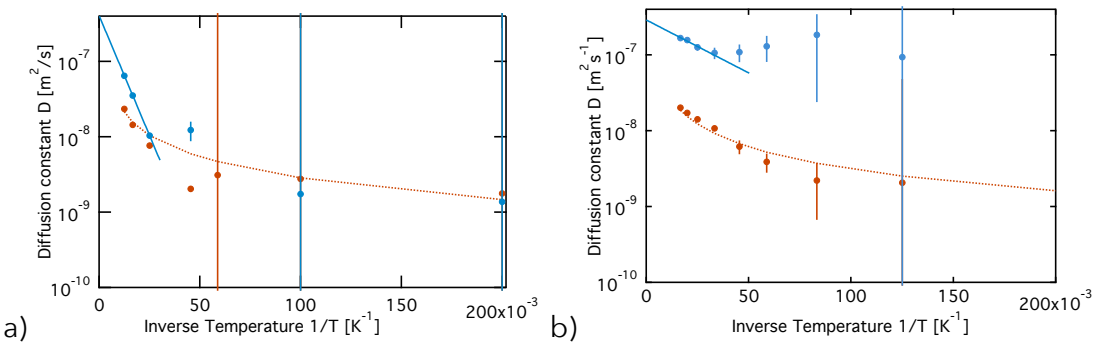

Figure 8.8: Arrhenius plots of the logarithm of the diffusion constant D versus inverse temperature. Blue dots: Experimental jump diffusion constant; blue line: Linear Fit to high temperature data; orange dots: Experimental Brownian-type diffusion constant; orange line: Theoretical Brownian-type diffusion of combined surface and collisional friction. a) Results for Papyex substrate. b) Results for D-96-7 substrate.

is significantly lower than what has been found on all carbon materials that we are aware of. It is by almost a factor 5 lower than the activation energy on Papyex, and even lower than in liquid hydrogen (3.9 ± 0.1) meV [222]. The results are, however, corroborated by the fact that the same experimental and analytical procedure has been applied to both systems and by the fact that the results for Papyex are in line with prior studies by Bienfait et al. [203]. Furthermore, the diffusion constant of D-96-7 seems to level off at low temperatures. This might be a sign of diffusion via quantum-tunneling, but a better general understanding of the observed diffusion processes and further investigations are necessary, to test this rather unlikely hypothesis.

The fact that only one single Lorentzian contribution has been observed which exhibits a broadening that is the sum of these two processes, is very intriguing. It indicates that both processes occur to the same molecule, but in a uncorrelated manner. If molecules would exhibit either one process, or the other, depending, e.g. on the local structure and hydrogen density, then a sum of the two Lorentzian contributions would be observed in $S(Q, \omega)$. The fact that the sum is found in the width of the Lorentzian broadening, suggests that $S(Q, \omega)$ contains the convolution of two Lorentzian functions, which means that its Fourier transformed in time and space, the Van Hoove correlation function $G(R, t)$, is constituted of the product of two exponential decays, as it does arise for two uncorrelated processes, exhibited by *the same* molecule. This suggests that, in the accessible time range of about 13 ps, that

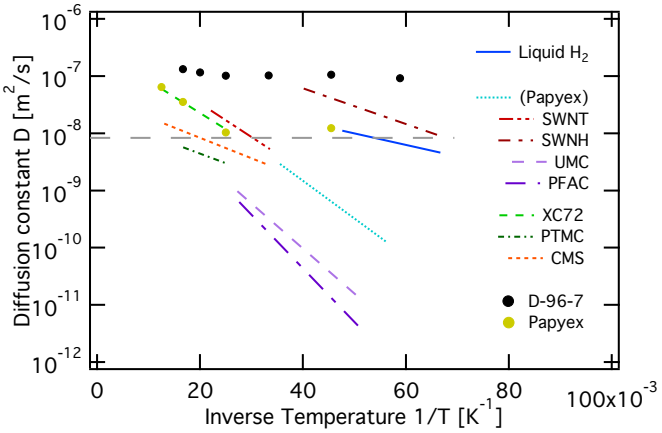

Figure 8.9: Comparison of the diffusion constants obtained here with the results from earlier measurements on liquid hydrogen [222] and on a variety of carbon systems: Papyex [203] (in brackets for distinction), single-walled nanotubes (SWNT) [204], single-walled nanohorns (SWNH) [205], commercial ultra-microporous carbon (UMC) [207], polyfurfuryl alcohol-derived activated carbon (PFAC) [207], carbon black XC-72 (XC72) [206, 208], Pt-containing microporous carbon (PTMC) [211], carbon molecular sieve (CMS) [212]. The results from this work are depicted by black (D-96-7) and yellow (Papyex) dots.

is given by the instrumental resolution, a molecule would undergo both diffusion processes, in contrast to the picture that, depending on the local environment, it exhibits only one of the two processes.

8.4 Conclusions

In this chapter, we have presented neutron TOF studies of molecular hydrogen diffusion in a novel highly porous carbon D-96-7 and on exfoliated graphite Papyex.

Structural studies by SANS and neutron diffraction show that both materials exhibit a small angle response that obeys a power-law behaviour over a large range. At higher momentum transfers, no diffraction was observed for D-96-7, and only the (002) graphite Bragg peak at 1.8 $Å^{-1}$ for Papyex. The scattered intensity of adsorbed hydrogen is much weaker than the carbon substrate and rises with temperature due to conversion of the hydrogen spin states.

The neutron spectroscopy measurements exhibit a Lorentzian QENS broadening

that reveals two diffusion processes: 1. An activated jump diffusion mechanism with jump lengths that are of the order of 4 - 6 Å has been discovered, with an activation energy of diffusion $E_a = (2.7 \pm 0.6)$ meV for hydrogen on D-96-7 and $E_a = (12.6 \pm 0.1)$ meV for hydrogen on Papyex. 2. A Brownian type diffusion that is caused by contributions of collisional and of surface friction, was identified. The collisional friction stems from inter-molecular collisions, which we have described by a RHD model, while the surface friction stems from interaction with the substrate. We could deduce an averaged surface friction $\eta_{sur} = (13.9 \pm 0.1)\,\mathrm{ps}^{-1}$ for hydrogen on D-96-7 and $\eta_{sur} = (14.7 \pm 0.2)\,\mathrm{ps}^{-1}$ for hydrogen on Papyex. Furthermore, both diffusion processes seem to occur to the same molecule, but in an uncorrelated manner.

9 H_2 on Carbon Aerogel

9.1 State of Current Research and Interest

The reasoning for diffusion studies of H_2 in porous carbon materials has already been laid out in Chap. 8. In this chapter, we present a study of the adsorption, dynamics and ortho-para conversion of hydrogen in a carbon aerogel (CG) [223]. CGs have high specific surface area and their three-dimensional structure and electric properties can be tuned, e.g. by addition of dopants [197]. The CG used in the present study serves us as a "standard" aerogel, which we aim to tune in future studies for different pore geometries and surface chemistry. We have recently submitted the results of this study to Carbon journal [224].

The role of carbon substrates in the conversion from ortho- to para-hydrogen has been the subject of numerous studies. An exhaustive review of research on the ortho-para conversion has been published by Ilisca in 1992 [225]. The review focused on the different conversion channels that had been discussed theoretically, the main ones being paramagnetic and ferromagnetic interaction, as well as chemical dissociation at a metal surface. First measurements on the conversion were performed in 1929 [226]. In these first experiments, already, activated carbon helped to obtain a rapid ortho-para conversion. A systematic investigation of the activity of different substrates was performed in 1932 [227], where it was shown that the conversion mechanism on carbon, in contrast to metal substrates, involves a bimolecular interaction. Neutron scattering on ortho- and para-hydrogen has been investigated theoretically [228, 229] and experimentally [230, 231, 232, 233]. NMR measurements of the conversion have been performed on solid hydrogen [234] and in the confined geometry of a zeolite adsorbate [235]. The latter study also showed a change in conversion rates. The conversion has been measured also in activated nanoporous carbon [207] and carbon nanotubes [236]. While in both cases a rapid

conversion was observed, Contescu *et al.* observed an incompleteness of the conversion that was suggested to be due to hindered rotations caused by narrow confinement in ultra-micropores [207]. This assumption was corroborated by calculations of the dynamics of H_2 in single walled carbon nanotubes (SWNT) [237].

This chapter is organised as follows: In sec. 9.2 we give a brief overview of the synthesis of this carbon aerogel and we describe the experimental methods. In sec. 9.3 we present and discuss the experimental results. We first show results from adsorption measurements on the carbon aerogel (sec. 9.3.1). We then discuss neutron and X-ray scattering results and their implications on the structure of the material (sec. 9.3.2). We finally present our findings on the ortho-para conversion of the hydrogen spin states (sec. 9.3.3) and on the diffusion of hydrogen in the material (sec. 9.3.4). The chapter finishes with a concluding section that summarises the major results of the study.

9.2 Experimental

The CG sample preparation and characterisation was conducted by K. László and B. Nagy from the Budapest University of Technology and Economics and a detailed description of the preparation of the carbon aerogel has been published [223]. Here, a brief description will be given because of its relevance for the study.

9.2.1 Synthesis of the Carbon Aerogel

For the synthesis of the CG, Resorcinol (R)-formaldehyde (F) hydrogel, with an R/catalyst ratio of 50 was prepared in a first step. After one week of curing the gels were supercritically dried according to the method described in [238]. The dry aerogel rods were converted into carbon aerogel by heat treatment in a high purity nitrogen atmosphere (99.996 %, Linde) in a rotary quartz reactor at a temperature of 1173 K for 1 h in a 25 ml/min nitrogen flow.

9.2.2 Sample Characterisation

Nitrogen adsorption/desorption isotherms were measured at 77 K with a Nova 2000e (Quantachrome) computer controlled surface area and pore size analyser.

The apparent surface area, S_{BET}, was calculated using the BET model [215]. The total pore volume, $V_{0.95}$, was derived from the amount of vapour adsorbed at relative pressure 0.95, assuming that the pores are then filled with liquid adsorbate. The micropore volume, W_{0-DR}, and the adsorption energy, E_{DR}, were derived from the Dubinin–Radushkevich plot [239]. The pore size distribution in the micro- and mesopore regions was calculated using density functional theory [240]. Carbon dioxide and hydrogen adsorption/desorption isotherms were measured at 273 K with an Autosorb-1 surface area and pore size analyser and at 77 K with an Autosorb-1C (both from Quantachrome), respectively. Transformation of the primary adsorption data was performed by the Quantachrome software ASiQwin version 3.0.

The submicroscopic structure of the carbon aerogel was explored by small and wide angle X-ray scattering (SAXS/WAXS) on the BM02-D2AM beamline at the European Synchrotron Radiation Facility (ESRF), Grenoble, France at 19.8 keV. The powdered sample was placed in a glass capillary tube of diameter 1.5 mm. The scattered intensity was collected in the wave vector transfer range $0.006 < q < 10\,\text{Å}^{-1}$. Intensities were normalised with respect to a standard sample (lupolen).

The elemental analyses of C, H, O, N and S were carried out in a LECO Truspec Micro CHNS microanalysis apparatus with a LECO Truspec Micro O accessory for O analysis. The amounts of C, H, S and N were determined from the amounts of CO_2, H_2O and NO_2 produced in the combustion of a portion of the sample (1 mg of sample was used for each assay, with two repetitions). The oxygen fraction was determined from the amounts of CO and CO_2 released in a pyrolysis at very high temperature, in a different portion of sample.

X-ray photoelectron spectroscopy (XPS) measurements were made on a powdered sample in a SPECS spectrometer with a Phoibos 100 hemispherical analyser. The base pressure in the UHV chamber was about $1.0 \cdot 10^{-7}$ Pa. The X-ray radiation source delivered non-monochromatic Mg Kα (1253.6 eV) at 100 W X-ray power and an anode voltage of 11.81 kV. The photo-excited electrons were analysed in constant pass energy mode, using a pass energy of 50 eV for the survey spectra and 10 or 30 eV for the high resolution core level spectra, respectively. Spectra were recorded at a take-off angle of 90°. No binding energy correction was done because the sample did not exhibit any charging effects. CasaXPS software was used for data processing.

9.2.3 Neutron Scattering

Neutron TOF spectroscopy was performed on the backscattering spectrometer OSIRIS at the ISIS neutron source, UK, [22] using a pyrolytic graphite (002) analyser set-up. The scattering functions from neutron TOF spectroscopy, $S(Q,\omega)$, where $Q = |k_i - k_f|$ is the momentum transfer and $\hbar\omega = E_i - E_f$ is the energy transfer, covered a momentum transfer range of $0.2 \leq Q \leq 1.8\,\text{Å}^{-1}$ and an energy transfer range of -0.2 $\leq \omega \leq$ 1.0 meV. The data were grouped into windows with widths of $\Delta Q = 0.2\,\text{Å}^{-1}$ and $\Delta\omega = 5\,\mu$eV in momentum transfer and energy transfer, respectively. All OSIRIS data were extracted using the Mantid software package [241]. The instrument resolution function was measured with a vanadium sample and with the sample itself at the base temperature of the cryostat. The latter resolution function was used for the data interpretation to exclude the introduction of systematic errors caused by minor discrepancies between the scattering geometry of the vanadium and the sample. We note also that the elastic line of OSIRIS is not symmetric in energy and cannot be approximated easily by a smooth standard function.

The powdered carbon aerogel was filled into a hollow, cylindrical aluminium sample holder with an annular width of 1 mm. Prior to the neutron scattering measurements, the sample was out-gassed for 60 hours in vacuum at a temperature of 393 K to remove volatile contaminants from the surface. The temperature was controlled using a standard liquid helium cryostat ("orange" cryostat [161]). For the neutron scattering experiments the sample was first cooled to 1.7 K in order to obtain an elastic scattering resolution measurement of the clean carbon sample. Afterwards, the sample was heated to 20 K and the quantity corresponding to 0.5 ML of hydrogen gas was dosed through a stainless steel capillary that was connected to a pressure control monitor. The hydrogen coverage was calculated from the amount of injected hydrogen molecules, the BET specific surface area of the sample and the surface area of a single hydrogen molecule of 15.6 Å^2 [198]. Throughout the entire experiment, connection to a 500 cm^3 reservoir at room temperature was maintained for security reasons. In our set-up any desorbed hydrogen rises to the reservoir, where the desorbed quantity can be deduced through pressure monitoring. A listing of the relative coverages obtained at sample temperatures between 10 and 80 K is given in Tab. 9.1. The sample temperature was equilibrated for at least 30 min prior to all neutron measurements.

The polarisation analysis (PA) measurements were performed on the IN11 NSE spec-

Sample temperature [K]	Relative coverage [ML]
10	0.5
20	0.5
40	0.49
50	0.46
60	0.38
80	0.24

Table 9.1: Relative coverages in fractions of a monolayer (ML) used in the experiment at sample temperatures between 10 and 80 K.

trometer at ILL [20], using polarised neutrons with a wavelength of 5.5 Å.

9.3 Results and Discussion

The pore structure and the surface area of the final carbon gel depend not only on the initial conditions of synthesis but also on the drying and carbonizing techniques. From among the three kinds of drying techniques (ambient drying, freeze-drying and supercritical drying) the last one proved to be the most advantageous for carbons with high surface area and controlled pore structure [223, 238]. The SEM and TEM images (Fig. 9.1) show the loose interconnected and complex porosity of the CG. The high resolution TEM image reveals that the nanostructure of the carbon matrix is made of disordered graphene layers occasionally showing a certain graphite- and onion-like assembly. The extension of these microcrystalline regions however does not exceed tens of nanometers.

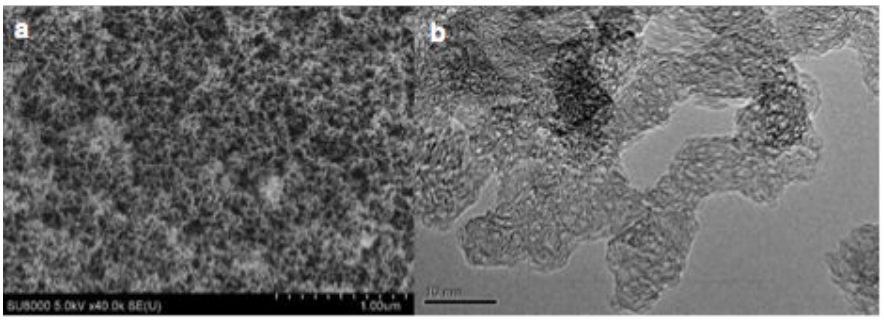

Figure 9.1: SEM a) and TEM b) image of the CG used in the experiment.

9.3.1 Isothermal Adsorption Measurements

	T K	S_{BET} m^2/g	S_{DR} m^2/g	W_{0-DR} cm^3/g	E_{DR} kJ/mol	$V_{0.95}$ cm^3/g
N_2	77	808	915	0.326	17.9	0.952
CO_2	273	–	232	0.077	26.6	–
H_2	77	–	323	0.012	9.6	–

T: Temperature of the adsorption measurement; S_{BET}: specific surface area; S_{DR}: surface area from the DR model; W_{0-DR}: micropore volume from the DR model; E_{DR}: adsorption energy from the DR model; $V_{0.95}$: pore volume from the N_2 adsorption isotherm at $p/p_0 = 0.95$.

Table 9.2: Characteristic parameters of adsorption and morphology of the CG from N_2, CO_2 and H_2 vapour adsorption measurements.

The texture of the CG was explored by adsorption of N_2, CO_2 and H_2, respectively. The low temperature (77 K) N_2 adsorption/desorption isotherm is of type IV [242] (Fig. 9.2 a)). The hysteresis loop of the N_2 data reveals a slit-shape pore morphology in the mesopore range [242]. On the contrary, the 77 K hydrogen adsorption/desorption isotherm (Fig. 9.2 b)) reveals the reversible nature of hydrogen adsorption under the examined conditions. The BET specific surface area of the CG is of the order of 800 m^2/g. In agreement with the electron microscope images above the sample has a well developed porosity with a pore volume of 0.952 cm^3/g at a relative pressure $p/p_0 = 0.95$. The steep uptake above this p/p_0 is a sign of wide mesopores – narrow macropores. A range of parameters deduced from the adsorption/desorption measurements are summarised in Tab. 9.2.

The results of complementary adsorption isotherm measurements of CO_2 on the CG sample are shown in Fig. 9.3. Comparison of the different adsorption isotherms demonstrates the role of the size as well as the kinetic energy of the probe molecules in sorption processes [242]. The combination of pore size distributions based on CO_2 and N_2 isotherm measurements reveals the co-existence of mesopores and ultra-micropores in the CG. Pore size distribution functions were derived by quenched solid density function theory (QSDFT) for N_2 and non-local DFT (NLDFT) for CO_2, respectively, with slit/cylinder geometry.

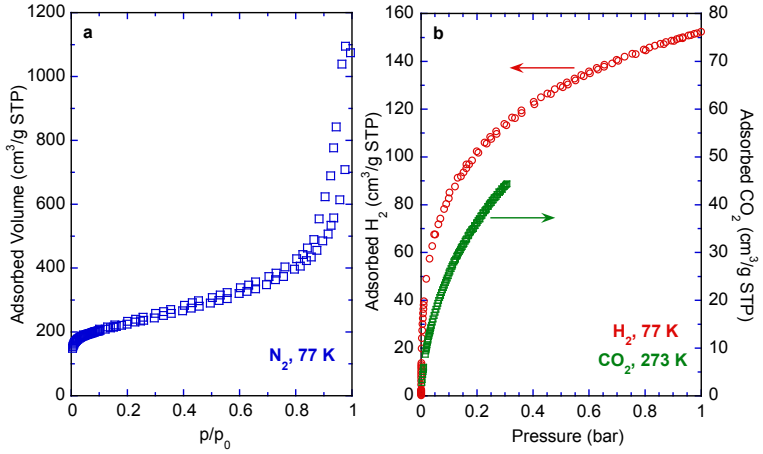

Figure 9.2: Nitrogen a) carbon dioxide (green squares) and hydrogen (red circles) b) adsorption/desorption isotherms of the carbon aerogel.

9.3.2 Neutron and X-ray Scattering - Structural Information

Fig. 9.4 displays structural data of the CG that were obtained from neutron TOF and NSE spectroscopy as well as from X-ray scattering. The neutron data for the clean CG are compared to the data from the hydrogen loaded sample at different temperatures. Neutron and X-ray scattering show both a strong small angle signal of the CG, a feature that is commonly found for materials with a hierarchical structure. The neutron data do not reach a sufficiently small angle to allow for an in-depth analysis. The surface area derived from small angle X-ray scattering (SAXS) results (1630 m^2/g) also confirms the presence of ultra-micropores, as was revealed by the adsorption measurements. The radius of the spherical elementary beads units was found to be 60 Å, similar to earlier findings [243]. No graphite Bragg peak is found in the neutron and X-ray data within the Q-range of the present experiments. This indicates an absence of long-range order in the carbon network, although it does not exclude graphitic short range order as seen in the electron microscope images.

The scattering signal from the hydrogen filled sample is higher than the signal from the empty sample, as expected. However, raising the temperature to 80 K leads to a loss of scattered signal. This loss can be attributed to the gradual desorption of the adsorbed hydrogen, which is also indicated by a rise of pressure in the expansion volume linked to the sample (Tab. 9.1).

At $Q > 0.5\,Å^{-1}$ the X-ray scattering signal decays by several orders of magnitude,

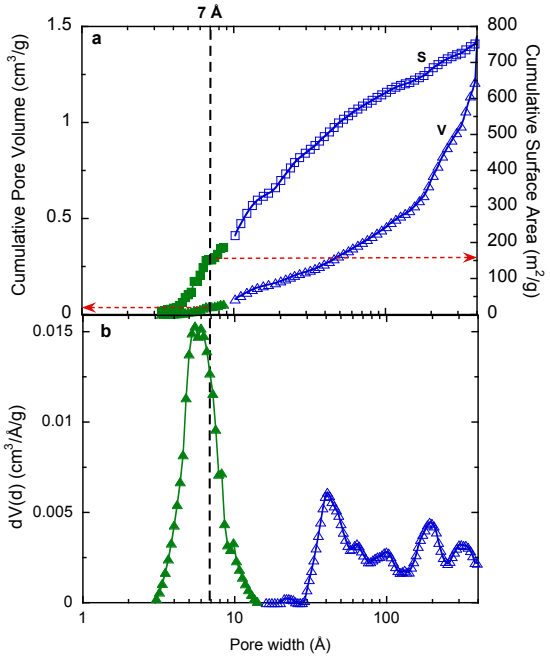

Figure 9.3: a) Cumulative pore size distribution (triangles) and surface area (squares) and b) incremental pore size distribution of the carbon aerogel obtained from the 77 K N_2 (blue open symbols) and room temperature CO_2 (green closed symbols) adsorption measurements derived by QSDFT (N_2) and NLDFT (CO_2) models, respectively, with slit/cylinder geometry. Arrows indicate the pore volume, V, and surface area, S, of pores with pore width $w < 7$ Å.

whereas the neutron spectrometers observe a constant signal that is typical for incoherent scattering. The origin of the constant neutron scattering signal at high Q was validated by PA measurements on the neutron spin-echo spectrometer IN11 [162]. Neutron PA measurements exploit neutron spin flips to differentiate the scattering processes: coherent scattering leaves the neutron spin unchanged upon sample interaction, whereas incoherent scattering leads to spin flips that result in a net final beam polarisation of 1/3 and a 180° turn of the polarisation. The PA data from a 1 ML hydrogen/CG sample is shown in the lower panel of Fig. 9.4. It shows predominant coherent scattering in the small angle regime but reveals also substantial incoherent scattering in the higher Q-range. The incoherent scattering is mainly caused by scattering from the hydrogen molecules, because hydrogen has a large incoherent scattering cross section compared to other elements and in comparison to carbon in particular [244].

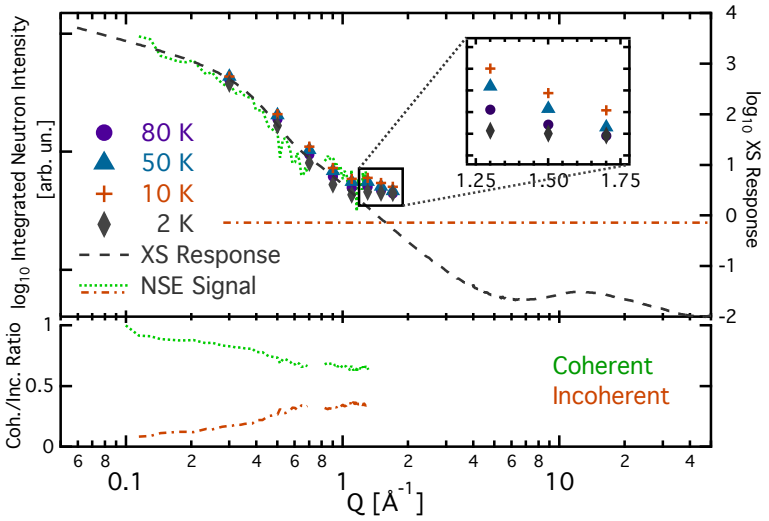

Figure 9.4: (upper panel) Energy-integrated neutron spectroscopy signal $S(Q)$ obtained at OSIRIS for the CG before hydrogen adsorption at 1.7 K (rhombi) and for the hydrogen loaded CG at 10 K (crosses), 50 K (triangles) and 80 K (circles), respectively. The data are compared to SAXS/WAXS measurements (dashed line) and the integrated intensity obtained on the neutron spin-echo spectrometer IN11 (dotted green line: coherent signal, dash-dotted red line: incoherent signal). The dash-dotted line shows the (constant) signal that stems from incoherent neutron scattering. The inset shows a magnification of the OSIRIS signal. (lower panel) Relative incoherent and coherent scattering contribution to the neutron spin-echo signal as function of momentum transfer Q.

9.3.3 Ortho-Para Conversion

The neutron structural data of the hydrogen filled sample that are shown in Fig. 9.4 were collected several hours after preparation of the sample. During these measurements the signal was stable. In the period immediately after dosing of hydrogen, however, we observed a strong decrease of the neutron scattering intensity (Fig. 9.5), which we attribute to the conversion from ortho- to para-hydrogen, since no desorption of hydrogen was observed. At a neutron wavelength of 6.6 Å, as used in the present TOF experiments, the ratio between the scattering cross sections of ortho- and para-hydrogen can be safely assumed to be at least 50:1 (Tab. 9.3) [229, 245]. This allows us to convert the integrated scattered intensity directly to the relative abundance of ortho- and para-hydrogen. We note that the wavelength dependence of the ratio of the scattering cross sections does not influence our results significantly, because almost all detected signal stems from elastic scattering.

scatterer	scattering cross section [10^{-28} m^2/atom]	absorption cross section [10^{-28} m^2/atom]
para-H_2	< 0.9	1.2
ortho-H_2	80	1.2
C	5.55	0.01

Table 9.3: Total neutron scattering cross sections and absorption cross sections for hydrogen and carbon at a neutron wavelength of about 6.6 Å and 5 Å for hydrogen and carbon, respectively. The data are taken from refs. [244, 245].

Furthermore, we do not expect any significant conversion induced by the impinging neutrons because the sample contains of the order of 10^{20} hydrogen molecules, whereas the neutron flux is of the order of 10^8 s^{-1}. The initial percentage of ortho-

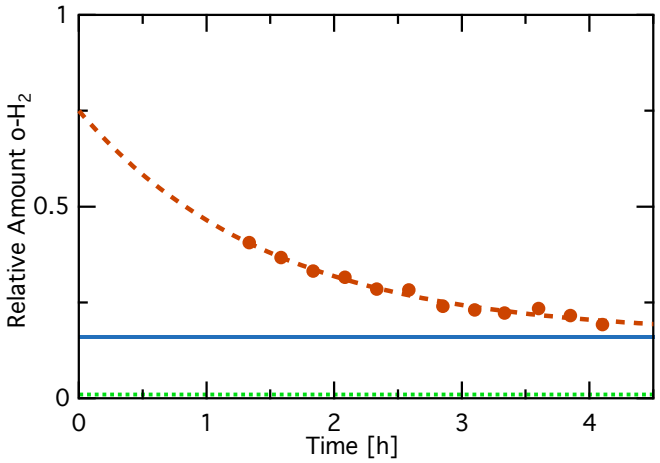

Figure 9.5: Fraction of ortho-hydrogen obtained from the integrated neutron scattering intensity of 0.5 ML hydrogen in CG at 20 K versus time after hydrogen dosing (red circles). A decay in signal due to ortho-para conversion is clearly visible. Dashed red line: fit of an exponential decay. Blue solid line: asymptotic value of the exponential fit; green dotted line: expected final ortho-hydrogen fraction in liquid hydrogen at 20 K: 1 % [246].

hydrogen in a gas at room temperature is 75 %. Upon cooling pure hydrogen to 20 K this percentage decreases to 1 % (liquid hydrogen) with a very slow conversion rate of 0.7 % per hour [246]. Different catalysts can speed up this process and the first observation of such a catalytic activation was, indeed, made on activated carbon [226]. Fig. 9.5 shows a very fast decay for the CG sample with a half-time of (80 ± 18) minutes in comparison to about 100 hours for liquid hydrogen.

Two main routes are considered for the accelerated conversion in carbon systems: the first one proceeds through molecular dissociation and recombination in a different spin state [227]. The second possibility is through interaction with a local magnetic field gradient [236]. The latter conversion channel has been preferred recently for activated carbon since the mobility at low temperature is suggested to be relatively small. In this model, the ortho-para conversion is mediated by the paramagnetism of unpaired electrons, which exist either at the edge of graphitic planes or at chemisorbed oxygen atoms that are part of surface functional end groups [236]. As discussed above, our SAXS/WAXS measurements also show that the CG has an amorphous structure at atomic length scales (Fig. 9.4), which means that the overall structure of the CG is heavily distorted compared to, e.g., graphite. Moreover, XPS measurements of the bulk CG revealed the presence of about 5 wt % oxygen. XPS also showed that 60 % of the remaining carbon is in sp^2 form. Similar O content and about 0.5 wt % hydrogen were detected in the bulk carbon by CHNS microanalysis showing the homogeneity of the sample. The presence of oxygen atoms as well as the large quantity of unpaired electrons at the edges and defect-points will help to accelerate the ortho-para conversion as observed here.

The data in Fig. 9.5 are well represented by an exponential decay fit, which is converging at an ortho-hydrogen abundance of about 18 % (resulting in 25 % scattering intensity). This asymptotic value is much higher than the 1 % that are observed as equilibrium value in liquid hydrogen at 20 K [246], which indicates that the conversion mechanism is fast, but hindered. Such a hindered decay has been observed before for other nanoporous carbon materials [207]. Calculations suggest that a strong confinement in ultramicropores can lead to hindered rotations of the hydrogen molecule, inhibiting the conversion of the spin state [207, 235, 247, 237]. Contescu et al. proposed that the percentage of unconverted ortho-hydrogen reflects the fraction of hydrogen that is adsorbed in pores with $w < 7$ Å, although their study found no direct proportionality between the amount of unconverted ortho-hydrogen and the volume of ultramicropores: Studying two types of activated carbons, they found 26 % and 8 % of remaining neutron scattering signal, respectively, and a corresponding fraction of 25 % and 19 % of pore volume in a range of $w < 7$ Å. In our CG system the CO_2 vapour adsorption measurement revealed only a small ultramicropore volume (Fig. 9.3): the volume of pores with $w < 7$ Å is 0.04 cm^3/g, equivalent to 4 % of the total pore volume ($V_{0.95}$), whereas we have observed a much higher ratio of remaining ortho-hydrogen. However, if we consider that the adsorption takes place on the surface, it is more reasonable to employ the fraction of the

available surface area in the ultramicropore regime rather than the ultramicropore volume. As can be seen in Fig. 9.3 a), the cumulative surface area of the pores with $w < 7\,\text{Å}$ is about $155\,\text{m}^2/\text{g}$, which represents 20 % of the total accessible surface, which is in good agreement with the observed remaining signal at the neutron scattering measurements. Thus, we propose that the relative surface area in ultramicropores is linked to the hindered ortho-para conversion.

9.3.4 Neutron Spectroscopy - Dynamics

Now we will discuss the dynamic scattering functions, $S(Q,\omega)$, which were extracted from the OSIRIS neutron TOF spectra. In a first treatment step, the data were normalised by a standard vanadium sample and then grouped into 8 Q groups. Fig. 9.6 a) shows $S(Q,\omega)$ for the hydrogen filled CG sample at 80 K. A cut of the scattering function at a momentum transfer of $Q = 1.5\,\text{Å}^{-1}$ is shown in Fig. 9.7. The spectrum shows a strong elastic peak around $\omega = 0\,\text{meV}$ and a weak, but clearly discernible quasi-elastic broadening, which appears at the base of the elastic peak. In our dynamic range we found no additional inelastic features caused by vibrations or rotons (see Fig. 9.6 a)). Fig. 9.6 b) demonstrates, that the quasi-elastic signal is caused by the adsorbed hydrogen and not by the carbon gel substrate itself, since no substantial quasi-elastic broadening is observed without adsorbed hydrogen.

The dynamic information in the TOF spectra for a given momentum transfer was extracted by fitting test functions using a least-square algorithm. For each spectrum, the QENS broadening of the elastic line resembled closely a Lorentzian shape, as in the case of activated jump diffusion on a Bravais lattice [19]. In this case, the Q-dependence of the HWHM of the Lorentzian broadening, $\Gamma(Q)$, is of the form:

$$\Gamma(Q) = \frac{1}{N\tau}\sum_{j=1}^{N}\left[1 - \exp(\mathrm{i}Q\cdot l_j)\right], \tag{9.1}$$

where τ is the residence time of the hydrogen molecule between two jumps ($1/\tau$ is the jump rate) and l_j is the j-th jump vector. Although the sample is highly disordered, the TEM pictures (Fig. 9.1) show that a short range graphitic order still exists and a strong sp^2 contribution can be seen in the XPS spectra. For this reason and since at a fairly high density of 0.5 ML as in the case studied here, hydrogen molecules on a surface would arrange in a close-packed pattern, a planar hexagonal

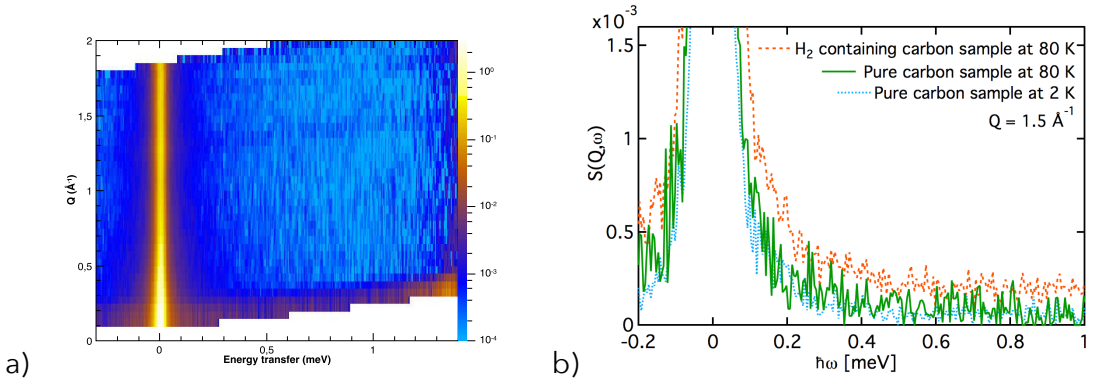

Figure 9.6: a) 2D colour map of the TOF spectra of the hydrogen containing sample at a temperature of 80 K. The spectral window shows a strong elastic peak with a quasi-elastic broadening and a signature of frame overlap at maximum energy transfer. No inelastic features are found in the spectral window. b) Temperature dependence of the normalised scattering functions, $S(Q,\omega)$, of the empty carbon gel sample. Blue dotted line: clean sample at 2 K; green solid line: clean sample at 80 K; orange dashed line: hydrogen containing sample at 80 K.

geometry of $N = 6$ jump vectors seems to be the most likely structure. The sample is isotropically orientated, therefore the quasi-elastic scattering function $S_{QENS}(Q,\omega)$ (QENS signifies quasi-elastic neutron scattering) needs to be averaged spherically [248]:

$$S_{QENS}(Q,\omega) = \frac{1}{4\pi}\int \frac{1}{\pi}\frac{\Gamma(Q)}{\omega^2+\Gamma(Q)^2}\mathrm{d}\,\Omega, \tag{9.2}$$

where $\mathrm{d}\,\Omega$ is the infinitesimal solid angle in the direction of Q. We have performed this integration numerically by summing over $N = 400$ Lorentzian distributions with isotropically randomised orientations. For the fitting we used a test function, which is a convolution of the resolution function $R(Q,\omega)$ (which was obtained from the clean CG substrate at 1.7 K) with a delta function $\delta(\omega)$ (elastic scattering) and $S_{QENS}(Q,\omega)$ that represents the quasi-elastic broadening, as well as a constant background, C:

$$\begin{aligned} S(Q,\omega) = [(1 + I_{el}\cdot \mathrm{e}^{-\frac{1}{3}Q^2<u^2>})\cdot\delta(\omega) \\ + I_{inel}\cdot\sum_{n=1}^{N}\frac{1}{N\pi}\frac{\Gamma(Q)_n}{\omega^2+\Gamma(Q)_n^2}] * R(Q,\omega) + C, \end{aligned} \tag{9.3}$$

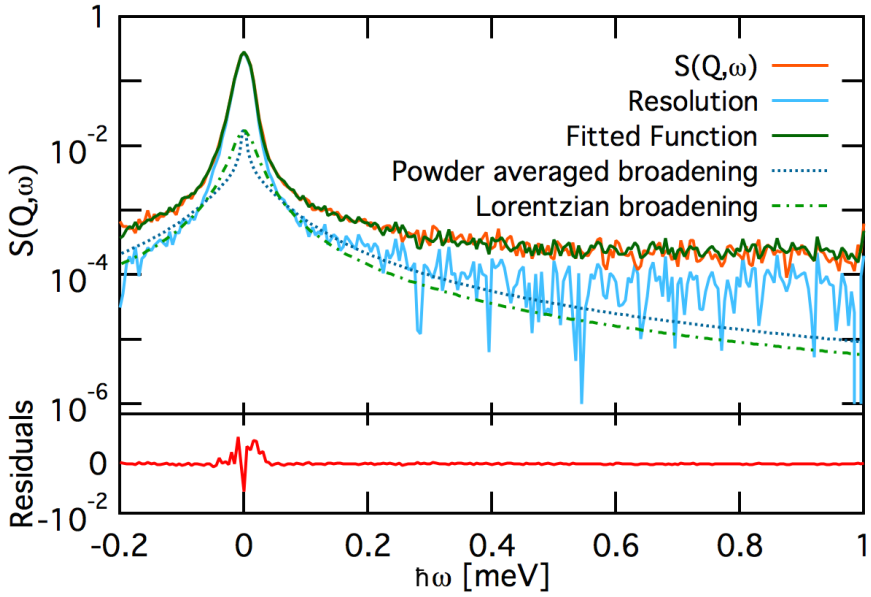

Figure 9.7: A representative slice of the normalised scattering function $S(Q,\omega)$ at a momentum transfer of Q = 1.5 Å^{-1} and a temperature of 80 K. The orange solid line shows the experimental data of the hydrogen containing sample at 80 K. The blue solid line shows the data of the clean CG sample at a temperature of 1.7 K (resolution function). The green solid line is the fitted function and the grey dotted line is the quasi-elastic broadening that was extracted by the fit. The green dash-dotted line represents the equivalent broadening that would be created using a single Lorentzian function without spatial integration. The lower panel shows the residuals of the fit function.

where $\Gamma(Q)_n$ is the HWHM of the n-th Lorentzian distribution and $< u^2 >$ is the mean square atom displacement in the Debye-Waller factor $-\frac{1}{3}Q^2 < u^2 >$. The fitting parameters I_{el} and I_{inel} in equation (9.3) correspond to the elastic and inelastic scattering contributions of the entire sample *relative* to the signal of the empty sample at a temperature of 1.7 K.

For each temperature, all spectra were fitted at once. For the fitting, $I_{inel}(Q)$ and $C(Q)$ are described by a linear polynomial in Q and the powder averaged summation of Lorentzian distributions is a function of τ and I. Thus, in total eight degrees of freedom were fitted to the measured data.

We used the reduced χ^2 as a representation of the goodness-of-fit. χ^2 showed no improvement upon adding a sloped background in addition to a flat background. Furthermore, no additional Lorentzian broadening was found within the energy range

and resolution of the OSIRIS spectrometer. We also tested deviations of the quasi-elastic broadening from the Lorentzian shape, such as a Gaussian or a Voigt shape, but the alternative shapes did not lead to an improvement of the fit. The residuals of the fits show no systematic errors and only an increase in absolute statistical error is observed in the vicinity of the elastic peak at $\omega = 0$ (Fig. 9.7). Hence, we conclude that we only observe a single diffusion process in the resolution window of the OSIRIS spectrometer. On the other hand, we observe a temperature dependence of the background, which indicates the existence of a fast diffusion process that cannot be resolved with the OSIRIS spectrometer.

The Q-dependence of the elastic and inelastic intensities, $S_{H,el}(Q)$ and $S_{H,inel}(Q)$, is shown in Fig. 9.8. These have been obtained by multiplication of I_{el} and I_{inel} with the integrated scattering intensity $R(Q)$ of the resolution measurement.

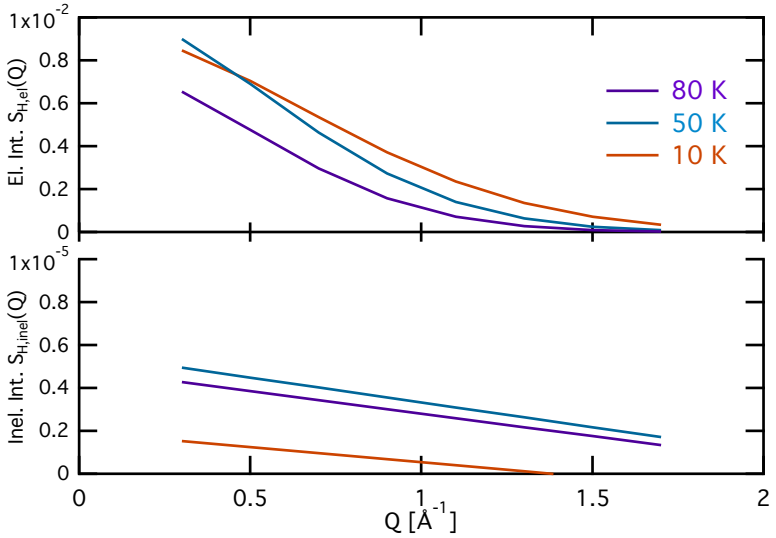

Figure 9.8: Elastic and inelastic intensities as a function of momentum transfer, Q. The data were obtained for a hydrogen coverage of the equivalent of 0.25 – 0.5 ML on CG (Tab. 9.1).

The inelastic intensity $S_{H,inel}(Q)$ remains fairly constant in the temperature range from 40 to 80 K, but exhibits a substantial decrease at temperatures below 20 K (Fig. 9.8). We attribute this sudden loss of the quasi-elastic contribution to a freezing of the hydrogen diffusive dynamics, in consistence with neutron diffraction measurements of hydrogen on graphite that discovered a transition between an ordered commensurate layer below 22 K and a liquid state above this temperature [202]. Furthermore, at all temperatures the inelastic intensity drops monotonically with Q. The

latter finding might be an indication for a rotational diffusive contribution that could not be resolved in the present study as it falls outside of the spectral window of the OSIRIS instrument. In addition, the constant background shows an increase with Q and with temperature. This hints strongly towards a fast rotational diffusion that is so broad, as to appear in form of a constant contribution.

The elastic intensity $S_{H,el}(Q)$ obeyed the Debye-Waller law, when each spectrum was fitted independently with a single Lorentzian contribution. In the global fitting procedure, we therefore assumed a Debye-Waller behaviour. The results of the global fitting are shown in Tab. 9.4 and Fig. 9.8. The mean square atom displacement is of the order of $(2.3\,\text{Å})^2$ and rises slightly with temperature, which is too high for rotations or molecular vibrations. Therefore, we tentatively attribute these dynamics to confined motion of hydrogen molecules in the ultra-micropores.

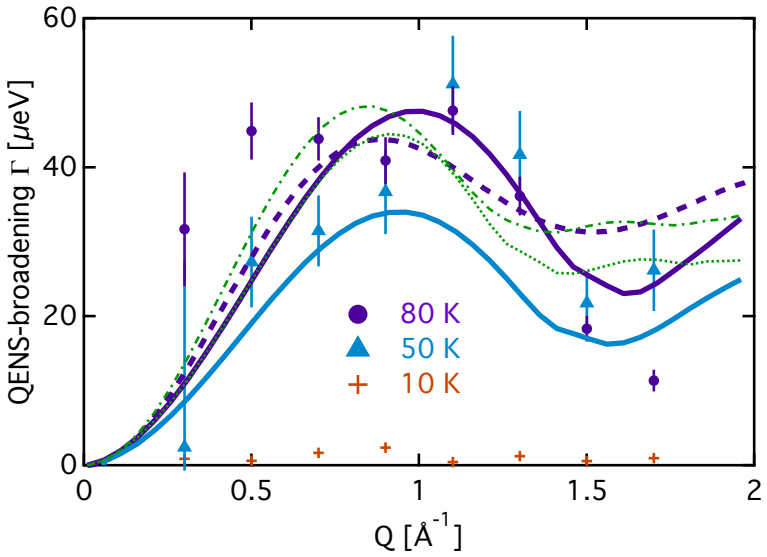

Figure 9.9: QENS broadening Γ versus Q, for a range of sample temperatures. The symbols show the HWHM obtained from fitting a single Lorentzian function as inelastic contribution to each spectrum independently. The dashed line shows the least-squares fit of an isotropically averaged broadening. The continuous lines show an approximation to the results from a global, powder averaged, approach, where the Lorentzian distribution is isotropically averaged. In the latter approach, a single Lorentzian was fitted to the powder averaged distribution of Lorentzians at each Q. The green lines show fits corresponding to the dynamics on non-hexagonal lattices. The green dotted line corresponds to a quadratic two-dimensional lattice and the green dash-dotted line corresponds to a three-dimensional cubic arrangement.

Fig. 9.9 displays the quasi-elastic broadenings that were obtained for sample temperatures of 10, 50 and 80 K, respectively. No significant broadening was observed for the sample at 10 K and 20 K, which agrees with a picture of a frozen hydrogen layer [202]. The data between 40 and 80 K were fitted with a powder averaged Chudley-Elliott (CE) jump diffusion model [19, 33].

T [K]	$\sqrt{< u^2 >}$ [Å]	d [Å]	I_{el} [arb. u.]	$I_{inel}(\times 10^{-3})$ [arb. u.]
10	1.85 ± 0.01	4.48 ± 0.06	9.4 ± 0.2	-
20	2.15 ± 0.02	5.19 ± 0.07	10.3 ± 0.3	-
40	2.26 ± 0.02	5.44 ± 0.08	10.5 ± 0.3	5.7 ± 0.4
50	2.23 ± 0.02	5.37 ± 0.08	10.8 ± 0.3	5.7 ± 0.3
60	2.31 ± 0.02	5.57 ± 0.08	9.6 ± 0.2	6.3 ± 0.2
80	2.39 ± 0.02	5.87 ± 0.08	7.0 ± 0.1	4.6 ± 0.1

T [K]	l [Å]	η [ps^{-1}]	$D\,(\times 10^{-10})$ [m^2/s]
40	5.15 ± 0.02	0.026 ± 0.001	11.6 ± 0.6
50	4.96 ± 0.03	0.046 ± 0.002	18.9 ± 0.9
60	5.02 ± 0.02	0.058 ± 0.002	24.2 ± 0.8
80	4.98 ± 0.04	0.064 ± 0.002	26.3 ± 0.8

Table 9.4: Fit parameters extracted from fitting equation (9.3) to the experimental spectra. $\sqrt{< u^2 >}$ is the square-root of the mean-square atom displacement from the Debye-Waller factor, d is the sphere diameter of a confined diffusion model, I_{el} is the absolute elastic intensity at $Q = 0$, I_{inel} is the absolute inelastic intensity at $Q = 0$, l the jump distance, η is the hopping rate and D is the diffusion constant.

The procedure for the powder averaging has been discussed in detail by Jobic [248]: He demonstrates, that a simple angular averaging of the broadening (Eq. (9.1)), as suggested by Chudley and Elliott for the case of a liquid [33], is in general insufficient, since deviations of the line-shape from a Lorentzian distribution are not taken into account. In the case of two-dimensional diffusion, angular averaging leads to a singularity for $Q \perp l$, that needs to be avoided by convolving with a finite resolution [220]. As Jobic points out, a more intricate but also more accurate analysis of the line-shape consists in averaging $S_{QENS}(Q, \omega)$ over the entire angular space, leading in general to a non-Lorentzian line-shape as shown in Fig. 9.7. In our analysis, we have applied both methods for comparison, a 3D isotropic averaging of $\Gamma(Q)$ and a 3D isotropic averaging of $S_{QENS}(Q, \omega)$. The results are shown in Fig. 9.9: the symbols represent the HWHM of a single Lorentzian broadening for each spectrum, while the dashed line gives the least-squares fit of the isotropically averaged broadening and

the solid lines represent the result from the application of the angular averaging of $S_{QENS}(Q,\omega)$. In the latter averaging, a single residence time τ and jump distance l define the shape of the quasi-elastic scattering function $S_{QENS}(Q,\omega)$ and the integrated broadening is in general non-Lorentzian (Fig. 9.7). Up to about 0.8 Å^{-1}, the line shape is close to a Lorentzian distribution. For larger values of Q however, significant deviations arise that produce an apparent "narrowing" of the single Lorentzian broadening (points in Fig. 9.9). 3D isotropic averaging of $\Gamma(Q)$ is obviously not able to reproduce this (dashed line in Fig. 9.9). A residual analysis of the spectral fits with the powder averaged $S_{QENS}(Q,\omega)$ validated this approach over the whole Q-range. Fig. 9.10 shows the temperature dependence of the diffusion constant D

Material	E_a [meV]	D_0 [m^2/s]($\times 10^{-8}$)
PFAC	18.9	28.5
UMC	15.4	12.6
(Papyex)	31 ± 2	64 ± 7
SWNT	11.6 ± 0.4	52 ± 7
Liquid	3.9 ± 0.2	9 ± 1
SWNH	6.18	–
PTMC	6.6 ± 0.8	2.1 ± 0.3
XC72	9.6 ± 0.4	35 ± 9
CMS	6.4 ± 0.9 (estimated)	3.5 ± 0.5 (estimated)
Papyex	12.6 ± 0.1	41 ± 1
D-96-7	2.7 ± 0.6	22 ± 3
CG	7.5 ± 0.6	1.6 ± 0.2

Table 9.5: Tabular comparison of the diffusion activation energies, E_a, and the prefactors, D_0, obtained here with the results from earlier measurements on liquid hydrogen [222] and on a variety of carbon systems: Grafoil [203], single-walled nanotubes (SWNT) [204], single-walled nanohorns (SWNH) [205], commercial ultra-microporous carbon (UMC) [207], polyfurfuryl alcohol-derived activated carbon (PFAC) [207], carbon black XC-72 (XC72) [206, 208], Pt-containing microporous carbon (PTMC) [211], carbon molecular sieve (CMS) [212]. Errors are indicated when they were provided by the authors. The data for CMS were not explicitly given the authors of the original study, but extracted by us from a graph.

in an Arrhenius plot. In this representation, i.e., $\ln(D)$ vs. $1/T$, an activated diffusion appears as a straight line, since it is described by the equation $D = D_0 \exp[-E_A/k_B T]$, where E_A is an activation barrier and k_B is the Boltzmann constant. For the CG system we obtain a pre-exponential diffusion constant $D_0 = (1.6 \pm 0.2) \cdot 10^{-8}$ m^2/s and an activation energy $E_A = (7.5 \pm 0.6)$ meV. In Fig. 9.10 we display the diffusion con-

stants of hydrogen that were recently obtained by other authors on carbon systems [203, 204, 205, 206, 207, 211, 212], as well as the diffusion of liquid hydrogen [222]. Tab. 9.5 shows a comparison of the extracted pre-exponential factors and activation energies of the materials in Fig. 9.10. The comparison shows that the activation energies differ only weakly between most of the carbon materials. The prefactor of our CG sample, however, is an order of magnitude lower than prefactors observed on the studied activated carbon materials [206, 207, 208]. The prefactor obtained here is similar to the prefactors observed for a carbon molecular sieve [212] and for a Pt-containing microporous carbon [211].

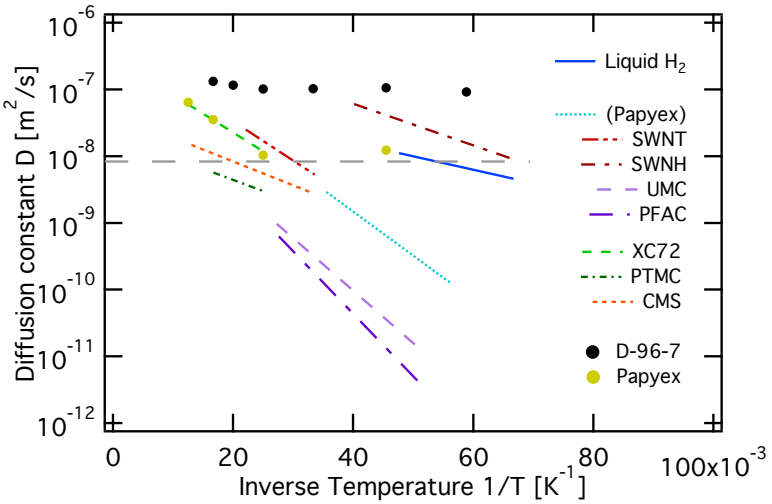

Figure 9.10: Comparison of the diffusion constants obtained here with the results from earlier measurements on liquid hydrogen [222] and on a variety of carbon systems: Grafoil [203], single-walled nanotubes (SWNT) [204], single-walled nanohorns (SWNH) [205], commercial ultra-microporous carbon (UMC) [207], polyfurfuryl alcohol-derived activated carbon (PFAC) [207], carbon black XC-72 (XC72) [206, 208], Pt-containing microporous carbon (PTMC) [211], carbon molecular sieve (CMS) [212].

9.4 Conclusions

In this chapter, we have presented hydrogen diffusion studies in a standard carbon aerogel. Neutron and X-ray scattering analyses show no graphitic ordering in the material, but a hierarchical structure above the nanometre length scale.

We have observed a highly accelerated ortho-para conversion of the spin isomer states of the hydrogen molecule, which can be explained by the large number of available electron donors at the CG surface. We have also observed a partial hindrance of the conversion that we link to hindered rotations due to the narrow confinement in ultramicropores with a pore diameter of less than 7 Å. The percentage of non-converted hydrogen agrees well with the relative available surface area in these ultramicropores.

Hydrogen desorbs from the CG at much higher temperatures than for some other recently studied porous carbons, such as polyfurfuryl alcohol-derived activated carbon or ultramicroporous carbon [207], which allowed us to follow the diffusion up to 80 K. The neutron spectroscopy data showed an activated jump diffusion mechanism with jump lengths that are of the order of the inter-molecular distance in the $(\sqrt{3}\,x\,\sqrt{3})\mathbf{R}30°$ hydrogen monolayer structure. The rather common approach of assuming a single Lorentzian quasi-elastic broadening of the scattering signal showed to be insufficient to describe our data in the high Q-range. An isotropic angular averaging of the quasi-elastic line was needed to obtain satisfactory results.

The hopping rate is in the ps range, like in other porous carbons. The obtained diffusion constants are similar to recent data from Pt-containing microporous carbon.

10 Discussion and Outlook

The aim of this PhD work was to study molecular diffusion on the surfaces of carbon materials by neutron and helium spectroscopy. For this purpose, we investigated a series of systems: water and benzene adsorbed on the surface of graphene/Ni(111), as well as molecular hydrogen adsorbed on the surfaces of exfoliated graphite, on a novel highly porous carbon, and on carbon aerogel. All these systems have in common, that relatively small molecules undergo weak physisorption on the (in most cases) hexagonal carbon surface. A detailed comprehension of these systems has both a fundamental interest, regarding an understanding of surface friction and potential energy surfaces, as well as a large technological interest, be it a molecular doping of graphene or the search for energy storage materials.

The questions regarding these systems were in general threefold: they aimed at an understanding of the adsorption/desorption process, the growth and structure of the adsorbate layer, and the type of surface diffusion. A point of emphasis was also the characterisation of the studied carbon materials, in terms of small and large scale structure, as well as surface chemistry.

Graphene Growth on a Ni(111) Surface

We started by a characterisation of the graphene/Ni(111) surface and discussed the growth procedure by chemical vapour deposition. Helium diffraction showed a first order diffraction peak of the graphene layer that is by two orders of magnitude larger compared to that of the Ni(111) surface, but found at the same position, indicating the creation of a commensurate (1 x 1) structure. From diffraction peak intensities we calculated an electron density corrugation with a peak to peak height of 0.06 Å upon scattering of ^{3}He at a beam energy of 8 meV. Inelastic scattering revealed the persistence of the two low energy surface phonons of the pristine Ni(111) surface, the Rayleigh mode and the longitudinal resonance, which indicates a strong electron-phonon coupling of the graphene-nickel system. These findings

confirm that graphene/Ni(111) can be created with very high quality and forms an ideal support system for the study of interactions between metals, carbon and eventually adsorbate atoms.

Water on the Graphene/Ni(111) Surface

We then discussed the behaviour of adsorbed water on the graphene/Ni(111) surface. Adsorption studies revealed an initial low-coverage adsorption regime with weak interaction between the water molecules. We deduced a helium scattering cross section of the H_2O molecule of (144 ± 1) Å^2. An amorphous ice layer forms at temperatures of up to 105 K, while at higher temperatures and at a coverage of about 0.25 ML, condensation sets in, resulting in island formation. From 125 K onwards, we observed water desorption. Thermal and isothermal desorption revealed two desorption processes with activation energies of 450 and 510 meV, respectively, which we attribute to desorption from the edges and the surfaces of islands. Spin-echo studies revealed a slow jump diffusion between presumably hollow adsorption sites with an activation energy of diffusion of (51 ± 12) meV. At short Fourier times, the persistence of the two graphene surface phonons and a fast diffusion process were observed which we assume to stem from uni-axial rotational diffusion of water molecules on the graphene surface.

To our knowledge, this is the first detailed observation of water diffusion on a graphene surface. Surface diffusion being in itself a highly interesting and technologically important feature, it also serves as a very precise measure of the interaction energies between the substrate and the adsorbate. If the fast diffusion proves to stem from rotating H_2O molecules, then a rotational friction can be established from the experimental results. From the combined results of the two diffusion processes, a detailed picture of the potential energy surface can be established. The question then arises, how the electronic structure of the graphene surface influences the diffusion of H_2O molecules, especially since H_2O is regarded as a potential graphene dopant. Therefore, it would be highly interesting to perform a systematic comparison of this system with an HOPG surface with a weakly interacting graphene/metal system that is lattice-matched (e.g. Cu(111)) and with a strongly interacting, but lattice mismatched graphene/metal system (e.g. Ru(0001)).

Benzene on the Graphene/Ni(111) and on a Graphite Surface

We then moved on to the adsorption of benzene on graphite and graphene. Neutron scattering studies allowed us to confirm the $(\sqrt{7}\,x\,\sqrt{7})\,\mathbf{R}19°$ structure in the sub-monolayer range, except for very low coverage, where no structural ordering was observed. Above the monolayer, we proved experimentally that benzene forms 3D islands of crystalline benzene rather than a second flat layer.

On the surface of graphene, we could also observe the $(\sqrt{7}\,x\,\sqrt{7})\,\mathbf{R}19°$ structure at coverages of up to 1 monolayer by helium scattering. Adsorption studies revealed a very large helium scattering cross section of $(630 \pm 120)\,\text{Å}^2$. At very low coverage, adsorption with weak interaction between adsorbates was observed, with a formation of islands at about 0.25 ML. At high sub-monolayer coverage, an adsorption regime was observed, which we attribute either to adsorption on top of the benzene layer, or to a saturation of island growth. Monolayer completion was observed, but no growth of a second layer, in accordance with the results from neutron diffraction on graphite. Above 120 K, desorption sets in with an activation barrier of (392 ± 12) meV. At 110 K, we observed two diffusion processes: a slow activated diffusion might be attributed, whose nature is yet unclear, with possible explanations being: jumps between adsorption sites, discrete jump rotations, or a jump-like association/dissociation to and from islands, respectively. Simultaneously, a fast Brownian diffusion exists, which is dominated by a surface friction of $(0.65 \pm 0.07)\,\text{ps}^{-1}$. At length scales shorter than the inter-molecular distance in the commensurate structure, ballistic diffusion is found in only one of the two principal crystal directions, which we link to the asymmetry of the potential energy surface, resulting in directions of high and low surface friction.

Our observations appear to match with those from earlier studies on similar systems [4, 136, 32]. A comparison with a weakly interacting graphene/metal system would be highly interesting with regard to the question about the influence of the electronic graphene structure. Furthermore, the observed asymmetrical ballistic diffusion might be linked to the super-lubricity of graphene that has been observed using scanning force microscopy [175, 176, 75]. A systematic study of polycyclic aromatic hydrocarbons of increasing size (e.g., coronene) on the graphene surfaces could bridge the gap between the two cases.

Molecular Hydrogen in Porous Carbons

We studied molecular hydrogen adsorbed on the surfaces of a porous carbon and a carbon aerogel, as well as on exfoliated graphite. The question was, how the porous structure influences hydrogen diffusion.

For this purpose, we performed neutron TOF scattering on three systems: The first is exfoliated graphite Papyex, a material that consists of graphitic islands with structural coherence length of several hundred $Å^2$. It can be regarded as a substitute for graphite. The two porous structures, a carbon aerogel and a highly porous carbon called D-96-7, contain a high amount of ultra-micropores, which we expect to cause confinement of hydrogen molecules. In fact, we observed an incomplete conversion of the hydrogen spin states in the carbon-aerogel, which we linked to a rotational confinement in ultra-micropores. In all three systems we observed jump diffusion of a comparable length scale, but with large differences in the activation energy and in the pre-exponential factor of the diffusion constant. While Papyex and carbon aerogel compare well with other carbon systems, D-96-7 exhibits an extremely low activation energy. In addition, Brownian surface diffusion was observed on Papyex and on D-96-7, which we estimate to stem from a small contribution of collisional friction and a large contribution of surface friction.

We are not aware of any previous findings of Brownian hydrogen diffusion on carbon surfaces and we do not yet understand the reason for a coexistence of two diffusion processes in this system, nor for the existence of the immensely high observed surface friction. Further neutron time-of-flight studies of the discussed systems at additional surface coverages would allow to test the applicability of the RHD model as a description of the kinetic friction. Numerical calculations could also provide an estimate for surface friction. Furthermore, the carbon aerogel can be tuned in terms of surface chemistry and porosity. Systematic neutron studies of hydrogen in different versions of the carbon aerogel are planned. Last, but not least, characterisation of the porous carbons as potential hydrogen storage materials would be of great interest and might even provide a link between sorption properties under technological conditions and our observations on the surface diffusion. A technological use of our studies, especially in such an extremely important field as energy storage, would be a great outcome of this research.

11 Discussion et Perspectives en Français

L'objectif de cette recherche doctorale était l'investigation de la diffusion moléculaire sur des surfaces de matériaux carbonés par spectroscopie neutronique et d'hélium. Dans ce but, nous avons étudié une série de systèmes: de l'eau et du benzène adsorbés à la surface de graphène/Ni(111), ainsi que de l'hydrogène moléculaire aux surfaces de graphite exfolié, d'un nouveau carbone poreux et d'un aérogel de carbone. Tous ces systèmes ont en commun, que des molécules relativement petits subissent une physisorption faible à la surface hexagonale de carbone. Une étude détaillée de ces systèmes est d'un intérêt fondamental en ce qui concerne une compréhension du frottement et des surfaces d'énergie potentielle, ainsi que d'un intérêt technologique, qu'il s'agisse du dopage moléculaire de graphène ou de la quête pour des matériaux de stockage d'énergie.

La question concernant ces systèmes comportait en général trois volets: elle visait à une compréhension du processus d'adsorption/désorption, de la croissance et de la structure du couche d'adsorbat et du type de diffusion à la surface. Un accent était aussi mis sur la caractérisation des matériaux de carbone étudiés, en termes des structures à petite et à grande échelle, ainsi que sur la chimie de surface.

La Croissance de Graphène à la Surface (111) de Nickel

Nous avons commencé avec une caractérisation de la surface graphène/Ni(111) et discuté la procédure de croissance par déposition chimique en phase vapeur. Diffraction d'hélium a montré un pic de diffraction de premier ordre, lequel est par deux ordres de grandeur plus intense, comparé au pic de diffraction de la surface Ni(111). Par contre, il et situé à la même position, ce qui nous indique la création d'une structure proportionnelle (1 x 1). Nous avons calculé une hauteur de l'ondulation en densité électronique de 0.06 Å à partir des intensités des pics de diffraction d'hélium avec une énergie du faisceau de 8 meV. Par diffusion inélastique nous avons montré que deux phonons de surface de la surface vierge

Ni(111), notamment le mode Rayleigh et la résonance longitudinale, persistent après la croissance du couche de graphène à cause d'un couplage fort du système graphène-nickel. Ces observations confirment que du graphène/Ni(111) de très haute qualité peut être créé et qu'il constitue un système idéal pour l'étude de l'interaction entre des métaux, du carbone et éventuellement des atomes et molécules d'adsorbat.

L'eau à la Surface de Graphène/Ni(111)

Nous avons ensuite discuté le comportement d'eau adsorbée à la surface de graphène/Ni(111). Des études d'adsorption ont montré un régime d'adsorption initiale à basse couverture avec une faible interaction entre les molécules d'eau. Ceci nous a permit de déduire une section efficace de diffusion d'hélium pour le molécule H_2O de (144 ± 1) Å^2. Une couche de glace amorphe se forme durant adsorption à des températures au dessous de 105 K, alors qu'au dessus la condensation commence à une couverture d'environ 0.15 ML, ce qui aboutit à la formation d'îlots. A partir de 125 K, nous avons observé la désorption d'eau. Des études de désorption thermique et isothermique ont révélé deux processus de désorption avec des énergies d'activation de 450 et de 510 meV, respectivement, lesquels nous attribuons à la désorption à partir des bords et des surfaces d'îlots. Par des études de diffusion à écho de spin nous avons découvert une diffusion par sauts entre des sites d'adsorption creux avec une énergie d'activation de (51 ± 12) meV. A des temps de Fourier courts, les deux phonons de surface et un processus de diffusion rapide ont été observé, le dernier nous assumons de résulter d'une diffusion rotationnelle uniaxiale des molécules d'eau à la surface de graphène.

A notre connaissance, celle-ci est la première observation détaillée de diffusion d'eau à la surface de graphène. La diffusion de surface elle-même étant un aspect très intéressant et technologiquement important, elle constitue aussi une mesure très précise des énergies d'interaction entre le substrat et l'adsorbat. Si le processus rapide se confirme de provenir d'une diffusion rotationnelle, un frottement rotationnel pourra être établi a partir des résultat expérimentales. Avec les résultats combinés de ces différents processus de diffusion, un image détaillé de la surface d'énergie potentielle peut être formé. La question se lève, comment la diffusion des molécules d'H_2Oest influencée par la structure électronique de la surface de graphène, spécialement puisque H_2O est vue comme un dopant potentiel de

graphène. Il serait donc très intéressant d'effectuer une comparaison systématique de ce surface avec une surface HOPG, avec un système graphène/métal à interaction faible et avec la même constante de réseau (par exemple Cu(111)) et avec un système graphène/métal à interaction forte, mais avec une décalage en constante de réseau (par exemple Ru(0001)).

Benzène aux Surfaces de Graphène/Ni(111) et de Graphite

Nous avons ensuite discuté l'adsorption de benzène à la surface de graphite et de graphène/Ni(111). Des études de diffusion neutronique nous ont permit de confirmer la structure proportionnelle $(\sqrt{7}\,\mathrm{x}\,\sqrt{7})\,\mathbf{R}19°$ au régime sous-monocouche, sauf à très basse couverture, auquel cas aucun ordre structurale a été observé. Au-dessus de la monocouche, nous avons montré expérimentalement que le benzène forme des îlots cristallines trois-dimensionnelles plutôt qu'une deuxième couche.

Pour le cas de benzène à la surface de graphène, nous avons aussi observé la structure $(\sqrt{7}\,\mathrm{x}\,\sqrt{7})\,\mathbf{R}19°$ à des couvertures sous-monocouche par diffusion d'hélium. Des études d'adsorption ont révélé une très grande section efficace de diffusion d'hélium de $(630 \pm 120)\,\text{Å}^2$. Une adsorption à interaction faible a été observé à des couvertures très basses, ainsi que la formation d'îlots à partir d'une couverture de 0.25 ML. A grande couverture sous-monocouche, un régime particulier d'adsorption a été observé, lequel nous attribuons soit à une adsorption au dessus du monocouche, soit à une saturation de la croissance d'îlots. Une complétion du monocouche a été observé, mais aucun croissance d'une deuxième couche, conformément aux résultats de la diffraction neutronique sur graphite. Au-dessus de 120 K, la désorption commence avec une énergie d'activation de (392 ± 12) meV. A 110 K, nous avons observé deux processus dynamiques: une diffusion lente et activée avec des explications possibles étant des sauts entre des sites d'adsorption, des rotations par sauts ou des associations discrets à un îlot; le deuxième processus observé est une diffusion Brownienne rapide, laquelle est dominée par un frottement de la surface de $(0.65 \pm 0.07)\,\text{ps}^{-1}$. A des échelles de longueur plus petites que la distance inter-moléculaire dans la structure proportionnelle, la diffusion balistique a été observé dans seulement un des deux directions principales. Nous relions cette observation à la symétrie de la surface d'énergie potentielle, ce qui résulte dans une direction de frottement fort et une direction de frottement faible.

Nos observations semblent de concorder avec ceux des études antérieurs sur des systèmes similaires [4, 136, 32]. Une comparaison avec un système graphène/métal à interaction faible serait très intéressant en ce qui concerne la question sur l'influence de la structure électronique de graphène. En outre, la diffusion balistique asymétrique que nous avons observé pourrait être liée avec la super-lubricité de graphène, laquelle a été observé en utilisant de la microscopie à effet de force [175, 176, 75]. Une étude systématique des hydrocarbures aromatiques polycycliques de tailles différentes (par exemple coronène) à la surface de graphène pourrait combler l'écart entre les deux cas.

Hydrogène Moléculaire dans des Carbones Poreux

Nous avons étudié l'hydrogène moléculaire adsorbé aux surfaces d'un carbone poreux et d'un aérogel de carbone, ainsi que du graphite exfolié. L'objectif était d'étudier l'influence de la structure poreuse sur la diffusion d'hydrogène. Dans ce but, nous avons effectué des expériences de diffusion neutronique en temps-de-vol sur ces trois systèmes: le premier est un graphite exfolié nommé Papyex, un matériel qui consiste d'îlots de graphite avec une longueur de cohérence structurale de plusieurs centaines d'Å^2. Il peut être considéré comme substitut pour le graphite. Les deux structures poreux, un aérogel de carbone et un carbone poreux nommé D-96-7, contiennent une grande quantité de micropores, lesquels nous assumons de causer un confinement des molécules d'hydrogène. Nous avons observé une conversion incomplète d'états de spin d'hydrogène dans l'aérogel de carbone, lequel nous lions à un confinement rotationnel dans les ultra-micropores. Dans les trois systèmes, nous avons observé une diffusion par sauts d'une échelle de longueur comparable, mais avec des grands différences dans l'énergie d'activation et dans le facteur pré-exponentiel de la constante de diffusion. Pendant que Papyex et l'aérogel de carbone se comparent bien avec des autres systèmes de carbone, D-96-7 montre une énergie d'activation extrêmement basse. En outre, une diffusion Brownienne a été observé sur Papyex et sur D-96-7, ce qui nous estimons de provenir d'une forte contribution de frottement de la surface.

Nous ne sommes pas conscients des observations antérieurs de diffusion Brownienne d'hydrogène sur des surfaces de carbone et nous ne comprendrons pas encore toute a fait la raison pour la coexistence de deux processus de diffusion dans ce

système, ni pour l'existence du frottement fort de la surface observé. Des études additionnels de diffusion neutronique en temps-de-vol sur les systèmes discutés à des couvertures additionnels nous permettraient de tester l'applicabilité du modèle RHD comme description pour le frottement cinétique. Des calculs numériques pourraient aussi fournir une estimation pour le frottement de la surface. En outre, l'aérogel de carbone peut être ajusté en termes de chimie de surface et porosité. Des études systématiques de diffusion neutronique sur l'hydrogène dans des versions différents d'aérogel de carbone sont déjà prévu. Finalement, une caractérisation des carbones poreux comme matériels potentiels pour le stockage d'hydrogène serait d'un grand intérêt et pourrait même fournir un lien entre des propriétés de sorption sous des conditions technologiques et nos observations sur la diffusion de surface. Un usage technologique de nos études serait, spécialement dans une domaine d'une telle importance comme le stockage d'énergie, un résultat favorable de cette recherche.

Bibliography

[1] D. Hollenbach and E. E. Salpeter, Astrophys. J. **163**, 155 (1971).

[2] L. Schlapbach and A. Züttel, Nature **414**, 353 (2001).

[3] R. Guerra, U. Tartaglino, A. Vanossi, and E. Tosatti, Nat Mater. **9**, 634 (2010).

[4] H. Hedgeland *et al.*, Nature Phys. **5**, 561 (2009).

[5] N. Stetson, *2014 Annual Progress Report* (U S Department of Energy, Washington, 2014), pp. IV–3–IV–10.

[6] A. Churchard *et al.*, Phys. Chem. Chem. Phys. **13**, 16955 (2011).

[7] Y. Xia, Z. Yang, and Y. Zhu, J. Mater. Chem. A **1**, 9365 (2013).

[8] A. K. Geim and K. S. Novoselov, Nat Mater. **6**, 183 (2007).

[9] F. Schedin *et al.*, Nat Mater. **6**, 652 (2007).

[10] T. O. Wehling *et al.*, Nano Letters **8**, 173 (2008).

[11] K. S. Novoselov, A. K. Geim, S. V. Morozov, and D. Jiang, Science **306**, 666 (2004).

[12] X. Dong *et al.*, Small **5**, 1422 (2009).

[13] A. P. Jardine, S. Dworski, P. Fouquet, and G. Alexandrowicz, Science **304**, 1790 (2004).

[14] G. Attard and C. Barnes, *Surfaces*, *Oxford Chemistry Primers* (Oxford University Press, Oxford, 1998).

[15] H. Ulbricht, R. Zacharia, N. Cindir, and T. Hertel, Carbon **44**, 2931 (2006).

[16] P. A. Redhead, Vacuum **12**, 203 (1962).

[17] G. L. Squires, *Introduction to the Theory of Thermal Neutron Scattering* (Cambridge University Press, Cambridge, 2012).

[18] H. Schober, J. Neutron Res. **17**, 109 (2014).

[19] M. Bée, *Quasielastic neutron scattering* (Adam Hilger, Bristol, 1988).

[20] ILL, *The Yellow Book 2008* (Institut Laue Langevin, Grenoble, 2008).

[21] Y. Blanc, *Le Spectrometre a temps de vol IN6* (Institut Laue Langevin, Grenoble, 1983).

[22] M. T. F. Telling and K. H. Andersen, Phys. Chem. Chem. Phys. **7**, 1255 (2005).

[23] F. Mezei, in *Neutron Spin Echo*, Vol. 128 of *Lecture Notes in Physics*, edited by F. Mezei (Springer, Berlin, 1980).

[24] A. Einstein, Ann. Phys. **4**, 549 (1905).

[25] J. P. Bouchaud and A. Georges, Phys. Rep. **195**, 127 (1990).

[26] R. Kubo, M. Toda, and N. Hashitsume, Statistical Physics II: Nonequilibrium Statistical Mechanics, Springer, Heidelberg (2012).

[27] S. Miret-Artés and E. Pollak, J. Phys. Cond. Mat. **17**, S4133 (2005).

[28] R. Martínez-Casado, J. L. Vega, A. S. Sanz, and S. Miret-Artés, J. Phys. Cond. Mat. **19**, 176006 (2007).

[29] D. Chandler, J. Chem. Phys. **60**, 3500 (1974).

[30] D. Chandler, J. Chem. Phys. **60**, 3508 (1974).

[31] D. Chandler, J. Chem. Phys. **62**, 1358 (1975).

[32] I. Calvo-Almazán *et al.*, Carbon **79**, 183 (2014).

[33] C. T. Chudley and R. J. Elliott, Proc. Phys. Soc. **77**, 353 (1961).

[34] J. M. Rowe, J. J. Rush, L. A. De Graaf, and G. A. Ferguson, Phys. Rev. Lett. **29**, 1250 (1974).

[35] F. E. Tuddenham *et al.*, Surf. Sci. **604**, 1459 (2010).

[36] K. Sköld and G. Nelin, J. Phys. Chem. Solids **28**, 2369 (1967).

[37] A. P. Jardine *et al.*, Prog. Surf. Sci. **84**, 323 (2009).

[38] G. Comsa and B. Poelsema, *Scattering of Thermal Energy Atoms from Disordered Surfaces*, Vol. 115 of *Springer Tracts in Modern Physics* (Springer, Heidelberg, 1989).

[39] N. Esbjerg and J. K. Nørskov, Phys. Rev. Lett. **45**, 807 (1980).

[40] J. L. Beeby and L. Dobrzynski, J. Phys. C. **4**, 1269 (1971).

[41] D. Farias and K. H. Rieder, Rep. Prog. Phys. **61**, 1575 (1998).

[42] J. P. Toennies, Appl. Phys. Lett. **3**, 91 (1974).

[43] R. E. Stickney, *The Structure and Chemistry of Solid Surfaces, ed. by GA Somorjai* (John Wiley, New York, 1969).

[44] P. Debye, Ann. Phys. **348**, 49 (1913).

[45] F. E. Tuddenham, Ph.D. thesis, University of Cambridge, Cambridge, 2011.

[46] J. Ellis and A. P. Graham, Surf. Sci. **377–379**, 833 (1997).

[47] P. Fouquet *et al.*, Rev. Sci. Instrum. **76**, 053109 (2005).

[48] A. P. Jardine *et al.*, Phys. Chem. Chem. Phys. **11**, 3355 (2009).

[49] A. R. Alderwick, A. P. Jardine, and H. Hedgeland, Rev. Sci. Instrum. **79**, 123301 (2008).

[50] J. Zhu, Ph.D. thesis, University of Cambridge, 2015.

[51] P. G. De Gennes, Physica **25**, 825 (1959).

[52] P. N. Pusey, J. Phys. A **8**, 1433 (1975).

[53] A. M. Lahee, J. R. Manson, J. P. Toennies, and C. Wöll, J. Chem. Phys. **86**, 7194 (1987).

[54] S. Böttcher, M. Weser, Y. S. Dedkov, and K. Horn, Nanoscale Res Lett **6**, 1 (2011).

[55] S. Böttcher, Ph.D. thesis, Freie Universität, Berlin, 2014.

[56] A. Dahal and M. Batzill, Nanoscale **6**, 2548 (2014).

[57] R. Rosei, M. De Crescenzi, F. Sette, and C. Quaresima, Phys. Rev. B **28**, 1161 (1983).

[58] Y. Gamo, A. Nagashima, M. Wakabayashi, and M. Terai, Surf. Sci. **374**, 61 (1997).

[59] A. Allard and L. Wirtz, Nano Letters **10**, 4335 (2010).

[60] H. Shichibe *et al.*, Phys. Rev. B **91**, 155403 (2015).

[61] D. Maccariello, D. Campi, A. Al Taleb, and G. Benedek, Carbon **93**, 1 (2015).

[62] L. L. Patera *et al.*, ACS Nano **7**, 7901 (2013).

[63] J. Wintterlin and M. L. Bocquet, Surf. Sci. **603**, 1841 (2009).

[64] F. Bianchini *et al.*, J. Phys. Chem. Lett. **5**, 467 (2014).

[65] W. B. Zhang, C. Chen, and P. Y. Tang, J. Chem. Phys. **141**, 044708 (2014).

[66] D. E. Parreiras, E. A. Soares, G. Abreu, and T. Bueno, Phys. Rev. B **90**, 155454 (2014).

[67] A. Politano, B. Borca, M. Minniti, and J. J. Hinarejos, Phys. Rev. B **84**, 035450 (2011).

[68] M. Mayrhofer-Reinhartshuber, P. Kraus, and A. Tamtögl, Phys. Rev. B **88**, 205425 (2013).

[69] G. Boato, P. Cantini, and R. Tatarek, Phys. Rev. Lett. **40**, 887 (1978).

[70] B. Borca *et al.*, New J. Phys. **12**, 093018 (2010).

[71] K. D. Gibson and S. J. Sibener, J. Phys. Chem. C **118**, 29077−29083 (2014).

[72] P. R. Kole, A. P. Jardine, and H. Hedgeland, J. Phys. Conf. Ser. **22**, 304018 (2010).

[73] G. Benedek, G. Brusdeylins, C. Heimlich, and J. P. Toennies, Surf. Sci. **178**, 545 (1986).

[74] C. Oshima, T. Aizawa, R. Souda, and Y. Ishizawa, Sol. Sta. Comm. **65**, 1601 (1988).

[75] J. A. Yan, W. Y. Ruan, and M. Y. Chou, Phys. Rev. B **77**, 125401 (2008).

[76] K. H. Michel and B. Verberck, Phys. Rev. B **78**, 085424 (2008).

[77] A. M. Shikin, D. Farıas, V. K. Adamchuk, and K. H. Rieder, Surf. Sci. **424**, 155 (1999).

[78] T. Aizawa *et al.*, Surf. Sci. **237**, 194 (1990).

[79] F. de Juan, A. Politano, G. Chiarello, and H. A. Fertig, Carbon **85**, 225 (2015).

[80] H. Yanagisawa, T. Tanaka, and Y. Ishida, Surf. Interf. Anal. **37**, 133 (2005).

[81] A. Politano, A. R. Marino, and G. Chiarello, J. Phys. Conf. Ser. **24**, 104025 (2012).

[82] A. Politano *et al.*, Carbon **50**, 4903 (2012).

[83] W. Menezes, P. Knipp, G. Tisdale, and S. J. Sibener, Phys. Rev. B **41**, 5648 (1990).

[84] P. D. Ditlevsen and J. K. Nørskov, Surf. Sci. **254**, 261 (1991).

[85] F. Mazzola *et al.*, Phys. Rev. **11**, 216806 (2013).

[86] A. Tamtögl, P. Kraus, and M. Mayrhofer-Reinhartshuber, Phys. Rev. B **87**, 035410 (2013).

[87] P. Kraus, A. Tamtögl, and M. Mayrhofer-Reinhartshuber, Phys. Rev. B **87**, 245433 (2013).

[88] A. Politano, A. R. Marino, V. Formoso, and G. Chiarello, Carbon **49**, 5180 (2011).

[89] G. A. Kimmel *et al.*, J. Am. Chem. Soc. **131**, 12838 (2009).

[90] O. Leenaerts, B. Partoens, and F. M. Peeters, Phys. Rev. B **79**, 235440 (2009).

[91] X. Xiao, Y. T. Cheng, and B. W. Sheldon, J. Neutron Res. **23**, 2174 (2008).

[92] F. Yavari *et al.*, Small **6**, 2535 (2010).

[93] N. N. Avgul, A. V. Kiselev, and P. L. Walker, Jr, *Chemistry and Physics of Carbon* (Dekker, New York, 1970), Vol. 6.

[94] D. V. Chakarov, L. Österlund, and B. Kasemo, Vacuum **46**, 1109 (1995).

[95] D. V. Chakarov, L. Oesterlund, and B. Kasemo, Langmuir **11**, 1201 (1995).

[96] A. S. Bolina, A. J. Wolff, and W. A. Brown, J. Phys. Chem. B. **109**, 16836 (2005).

[97] R. B. Phelps, L. L. Kesmodel, and R. J. Kelley, Surf. Sci. **340**, 134 (1995).

[98] X. Feng, S. Maier, and M. Salmeron, J. Am. Chem. Soc. **134**, 5662 (2012).

[99] J. A. McMillan and S. C. Los, Nature **206**, 806 (1965).

[100] P. Jenniskens, S. F. Banham, D. F. Blake, and M. R. S. McCoustra, J. Chem. Phys. **107**, 1232 (1997).

[101] P. Löfgren, P. Ahlström, D. V. Chakarov, and J. Lausmaa, Surf. Sci. **367**, L19 (1996).

[102] P. Löfgren, P. Ahlström, J. Lausma, and B. Kasemo, Langmuir **19**, 265 (2003).

[103] M. T. Suter, P. U. Andersson, and J. B. C. Pettersson, J. Chem. Phys. **125**, 174704 (2006).

[104] P. U. Andersson, M. T. Suter, N. Marković, and J. B. C. Pettersson, J. Phys. Chem. C **111**, 15258 (2007).

[105] A. Glebov *et al.*, J. Chem. Phys. **112**, 11011 (2000).

[106] E. N. Voloshina *et al.*, Phys. Chem. Chem. Phys. **13**, 12041 (2011).

[107] M. Dion, H. Rydberg, E. Schröder, and D. C. Langreth, Phys. Rev. **92**, 246401 (2004).

[108] M. C. Gordillo and J. Martí, Phys. Rev. B **78**, 075432 (2008).

[109] B. S. Gonzalez, J. Hernandez-Rojas, J. Breton, and J. M. GomezLlorente, J. Phys. Chem. C **111**, 14862 (2007).

[110] T. O. Wehling, A. I. Lichtenstein, and M. I. Katsnelson, Appl. Phys. Lett. **93**, 202110 (2008).

[111] G. R. Jenness, O. Karalti, and K. D. Jordan, Phys. Chem. Chem. Phys. **12**, 6375 (2010).

[112] O. Leenaerts, B. Partoens, and F. M. Peeters, Phys. Rev. B **77**, 125416 (2008).

[113] A. Ambrosetti and P. L. Silvestrelli, J. Phys. Chem. C **115**, 3695 (2011).

[114] M. Rubeš, P. Nachtigall, J. Vondrášek, and O. Bludský, J. Phys. Chem. C **113**, 8412 (2009).

[115] J. Ma *et al.*, Phys. Rev. B **84**, 033402 (2011).

[116] G. R. Jenness and K. D. Jordan, J. Phys. Chem. C **113**, 10242 (2009).

[117] X. Li *et al.*, Phys. Rev. B **85**, 085425 (2012).

[118] G. Tocci, L. Joly, and A. Michaelides, Nano Letters **14**, 6872 (2014).

[119] J. H. Park and N. R. Aluru, J. Phys. Chem. C **114**, 2595 (2010).

[120] D. J. Ward, Ph.D. thesis, University of Cambridge, Cambridge, 2013.

[121] R. L. Summers, *Nasa technical note tn d-5285* (National Aeronautics and Space Administration, WASHINGTON, D. C., 1969).

[122] E. M. McIntosh, Ph.D. thesis, University of Cambridge, Cambridge, 2013.

[123] A. L. Glebov, A. P. Graham, and A. Menzel, Surf. Sci. **427-428**, 22 (1999).

[124] F. J. Harris, Proc. IEEE **66**, 51 (1978).

[125] A. J. Dianoux, F. Volino, and H. Hervet, Mol. Phys. **30**, 1181 (1975).

[126] H. Hedgeland, Ph.D. thesis, University of Cambridge, Cambridge, 2006.

[127] E. Bahn *et al.*, Phys. Chem. Chem. Phys. **16**, 22116 (2014).

[128] S. Gokhale *et al.*, J. Chem. Phys. **108**, 5554 (1998).

[129] W. Liu *et al.*, New J. Phys. **15**, 053046 (2013).

[130] B. Boddenberg and J. A. Moreno, Z. Naturfor. A **31 a**, 854 (1976).

[131] R. Stockmeyer and H. Stortnik, Surf. Sci. **81**, L315 (1979).

[132] P. Meehan *et al.*, J. Chem. Soc., Faraday Trans. 1 **76**, 2011 (1980).

[133] M. Monkenbusch and R. Stockmeyer, Ber. Bunsenges. Phys. Chem. **84**, 808 (1980).

[134] P. Jakob and D. Menzel, Surf. Sci. **220**, 70 (1989).

[135] H. Hedgeland *et al.*, Phys. Rev. B **80**, 125426 (2009).

[136] P. Fouquet *et al.*, Carbon **47**, 2627 (2009).

[137] D. C. Glass, C. N. Gray, and G. G. Adams, Toxicology and Industrial Health **17**, 113 (2001).

[138] M. T. Smith, Ann. Rev. Publ. Health **31**, 133 (2010).

[139] W. R. Browne and B. L. Feringa, Nature Nanotech **1**, 25 (2006).

[140] E. G. Cox, Rev. Mod. Phys. **30**, 159 (1958).

[141] C. J. Craven, P. D. Hatton, C. J. Howard, and G. S. Pawley, J. Chem. Phys. **98**, 8236 (1993).

[142] G. A. Jeffrey, J. R. Ruble, R. K. McMullan, and J. A. Pople, Proc. Roy. Soc. A **414**, 47 (1987).

[143] T. F. Headen *et al.*, J. Am. Chem. Soc. **132**, 5735 (2010).

[144] B. Boddenberg and J. A. Moreno, J. Phys. Colloq. **38**, C4 (1977).

[145] U. Bardi, S. Magnanelli, and G. Rovida, Surf. Sci. Lett. **165**, L7 (1986).

[146] U. Bardi, S. Magnanelli, and G. Rovida, Langmuir **3**, 159 (1987).

[147] I. Gameson and T. Payment, Chem. Phys. Lett. **123**, 150 (1986).

[148] B. Boddenberg and R. Grosse, Z. Naturfor. A **41 a**, 1361 (1986).

[149] R. Grosse and B. Boddenberg, Z. Phys. Chem. **152**, 1 (1987).

[150] C. Bondi and G. Taddei, Surf. Sci. **203**, 587 (1988).

[151] A. Vernov and W. A. Steele, Langmuir **7**, 3110 (1991).

[152] A. Vernov and W. A. Steele, Langmuir **7**, 2817 (1991).

[153] R. Hentschke and B. L. Schürmann, Surf. Sci. **262**, 180 (1992).

[154] M. A. Matties and R. Hentschke, Langmuir **12**, 2495 (1996).

[155] M. A. Matties and R. Hentschke, Langmuir **12**, 2501 (1996).

[156] N. Klomkliang *et al.*, Chem. Eng. Sci. **69**, 472 (2012).

[157] S. D. Chakarova-Käck, E. Schröder, B. I. Lundqvist, and D. C. Langreth, Phys. Rev. Lett. **96**, 1 (2006).

[158] E. P. Gilbert, P. A. Reynolds, and J. W. White, J. Chem. Soc., Faraday Trans. 1 **94**, 1861 (1998).

[159] C. Bockel, J. P. Coulomb, and N. Dupont-Pavlovsky, Surf. Sci. **116**, 369 (1982).

[160] T. C. Hansen, P. F. Henry, and H. E. Fischer, Meas. Sci. Technol. **19**, 034001 (2008).

[161] D. Brochier, Technical Report No. 77/74, Institut Laue-Langevin, Grenoble (unpublished).

[162] B. Farago, Physica B **241-243**, 113 (1997).

[163] R. Zacharia, H. Ulbricht, and T. Hertel, Phys. Rev. B **69**, 155406 (2004).

[164] B. E. Warren, Phys. Rev. **59**, 693 (1941).

[165] T. Arnold *et al.*, Phys. Rev. B **74**, 085421 (2006).

[166] A. Y. Brewer *et al.*, Mol. Phys. **111**, 73 (2012).

[167] S. Ergun and M. Berman, Acta Crystall. Sec. A **29**, 12 (1973).

[168] K. W. Herwig, J. C. Newton, and H. Taub, Phys. Rev. B **50**, 15287 (1994).

[169] T. Arnold *et al.*, Phys. Chem. Chem. Phys. **4**, 345 (2002).

[170] D. D. Do, D. Nicholson, and H. D. Do, J Colloid Interface Sci **325**, 7 (2008).

[171] J. Krim, Adv. Phys. **61**, 155 (2012).

[172] Y.-z. Hu, T.-b. Ma, and H. Wang, Friction **1**, 24 (2013).

[173] T. W. Scharf and S. V. Prasad, J Mater Sci **48**, 511 (2012).

[174] Y. Mo, K. T. Turner, and I. Szlufarska, Nature **457**, 1116 (2009).

[175] M. Dienwiebel *et al.*, Phys. Rev. Lett. **92**, 126101 (2004).

[176] G. S. Verhoeven, M. Dienwiebel, and J. W. M. Frenken, Phys. Rev. B **70**, 165418 (2004).

[177] Y.-H. Zhang *et al.*, Nanotechnology **21**, 065201 (2010).

[178] A. Z. AlZahrani, Appl. Surf. Sci. **257**, 807 (2010).

[179] Y. Hsun Su, Y. Kai Wu, S.-L. Tu, and S.-J. Chang, Appl. Phys. Lett. **99**, 163102 (2011).

[180] S. M. Kozlov, F. Viñes, and A. Görling, Carbon **50**, 2482 (2012).

[181] V. Krasnenko, J. Kikas, and M. G. Brik, Physica B **407**, 4557 (2012).

[182] K. Berland and P. Hyldgaard, Phys. Rev. B **87**, 205421 (2013).

[183] B. Das, R. Voggu, C. S. Rout, and C. N. R. Rao, Chem. Commun. **41**, 5155 (2008).

[184] R. Kubo, Rep. Prog. Phys. **29**, 255 (1966).

[185] R. Zwanzig and M. Bixon, Phys. Rev. A **2**, 2005 (1970).

[186] K. A. Stoerzinger, Ph.D. thesis, University of Cambridge, Cambridge, 2011.

[187] P. Lazzeretti, M. Malagoli, and R. Zanasi, Chem. Phys. Lett. **167**, 101 (1990).

[188] G. Maroulis, J. Phys. Chem. B. **100**, 13466 (1996).

[189] A. Züttel *et al.*, Int. J. Hydrogen Energy **27**, 203 (2002).

[190] A. Züttel, Naturwissenschaften **91**, 157 (2004).

[191] S. L. Candelaria *et al.*, Nano Energy **1**, 195 (2012).

[192] A. Chambers, C. Park, R. T. K. Baker, and N. M. Rodriguez, J. Phys. Chem. B. **102**, 4253 (1998).

[193] A. C. Dillon *et al.*, Nature **386**, 377 (1997).

[194] P. Chen, X. Wu, J. Lin, and K. L. Tan, Science **285**, 91 (1999).

[195] H. Tanaka *et al.*, J. Phys. Chem. B. **108**, 17457 (2004).

[196] L. Wang and R. T. Yang, Carbon **50**, 3134 (2012).

[197] H. Kabbour *et al.*, Chem. Mater. **18**, 6085 (2006).

[198] M. Nielsen, J. P. McTague, and W. Ellenson, J. Phys. Colloq. **38**, C4 (1977).

[199] L. W. Bruch, M. W. Cole, and E. Zaremba, *Physical Adsorption: Forces and Phenomena*, Vol. 6 of *International series of monographs on chemistry* (Clarendon Press, Oxford, 1997).

[200] H. Freimuth, H. Wiechert, and H. J. Lauter, Surf. Sci. **189/190**, 548 (1987).

[201] H. Freimuth, H. Wiechert, H. P. Schildberg, and H. J. Lauter, Phys. Rev. B **42**, 587 (1990).

[202] H. Wiechert, Physica B **169**, 144 (1991).

[203] M. Bienfait *et al.*, Phys. Rev. B **60**, 11773 (1999).

[204] D. Narehood *et al.*, Phys. Rev. B **67**, 1 (2003).

[205] F. Fernandez-Alonso *et al.*, Phys. Rev. Lett. **98**, 1 (2007).

[206] O.-E. Haas *et al.*, J. Phys. Chem. C **112**, 3121 (2008).

[207] C. I. Contescu *et al.*, Carbon **50**, 1071 (2012).

[208] O.-E. Haas, J. M. Simon, and S. Kjelstrup, J. Phys. Chem. C **113**, 20281 (2013).

[209] J. Purewal *et al.*, Phys. Rev. B **79**, 1 (2009).

[210] J. Purewal *et al.*, J. Chem. Phys. **137**, 224704 (2012).

[211] Y. Yang *et al.*, Carbon **49**, 1305 (2011).

[212] T. X. Nguyen, H. Jobic, and S. K. Bhatia, Phys. Rev. Lett. **105**, 1 (2010).

[213] B. C. Lippens and J. H. De Boer, Journal of Catalysis **4**, 319 (1965).

[214] E. P. Barrett, L. G. Joyner, and P. P. Halenda, J. Am. Chem. Soc. **73**, 373 (1951).

[215] S. Brunauer, P. H. Emmett, and E. Teller, J. Am. Chem. Soc. **60**, 309 (1938).

[216] G. Horváth and K. Kawazoe, J. Chem. Eng. Japan **16**, 470 (1983).

[217] Y. Finkelstein, D. Nemirovsky, and R. Moreh, Physica B **291**, 213 (2000).

[218] J. P. Coulomb and M. Bienfait, J. Physique **42**, 293 (1981).

[219] D. Richard, M. Ferrand, G. J. Kearley, and A. D. Bradley, *The Lamp Book* (Institut Laue Langevin, Grenoble, 2010).

[220] R. E. Lechner, Solid State Ionics **77**, 280 (1995).

[221] K. A. Gernoth, M. J. Harrison, and M. L. Ristig, Int. J. Mod. Phys. B **20**, 5057 (2006).

[222] D. E. O'Reilly and E. M. Peterson, J. Chem. Phys. **66**, 934 (1977).

[223] O. Czakkel, K. Marthi, E. Geissler, and K. Laszló, Micropor. Mesopor. Mat. **86**, 124 (2005).

[224] E. Bahn *et al.*, Carbon (2016).

[225] E. Ilisca, Prog. Surf. Sci. **41**, 217 (1992).

[226] K. F. Bonhoeffer and P. Harteck, Z. Elktrochem. Angew. P. **35**, 621 (1929).

[227] H. S. Taylor and A. Sherman, Trans. Faraday Soc. **28**, 247 (1932).

[228] J. Schwinger and E. Teller, Phys. Rev. **52**, 286 (1937).

[229] J. A. Young and J. U. Koppel, Phys. Rev. **135**, A603 (1964).

[230] F. G. Brickwedde, J. R. Dunning, H. J. Hoge, and J. H. Manley, Phys. Rev. **54**, 266 (1938).

[231] R. B. Sutton *et al.*, Phys. Rev. **72**, 1147 (1947).

[232] M. Hamermesh and J. Schwinger, Phys. Rev. **71**, 678 (1947).

[233] G. L. Squires and A. T. Stewart, Proc. Roy. Soc. A **230**, 19 (1955).

[234] F. Schmidt, Phys. Rev. B **10**, 4480 (1974).

[235] M. Rall, J. Brison, and N. Sullivan, Phys. Rev. B **44**, 9932 (1991).

[236] P. A. Georgiev *et al.*, Carbon **43**, 895 (2005).

[237] T. Lu, E. M. Goldfield, and S. K. Gray, J. Phys. Chem. B. **110**, 1742 (2006).

[238] O. Czakkel *et al.*, Micropor. Mesopor. Mat. **148**, 34 (2012).

[239] M. M. Dubinin and L. V. Radushkevich, Chem. Zentr. **1**, 875 (1947).

[240] J. Landers, G. Y. Gor, and A. V. Neimark, Colloids Surf. A **437**, 3 (2013).

[241] O. Arnold, J. C. Bilheux, J. M. Borreguero, and A. Buts, Nucl. Instr. Meth. Phys. Res. A **764**, 156 (2014).

[242] F. Rouquerol *et al.*, *Adsorption by Powders and Porous Solids* (Academic Press, Oxford, 2014).

[243] B. Nagy *et al.*, Carbon **66**, 210 (2014).

[244] V. F. Sears, Neutron News **3**, 26 (1992).

[245] K. B. Grammer *et al.*, Phys. Rev. B **91**, 1 (2015).

[246] P. A. Egelstaff, B. C. Haywood, and F. J. Webb, Proc. Phys. Soc. **90**, 681 (1967).

[247] R. A. Trasca, M. K. Kostov, and M. W. Cole, Phys. Rev. B **67**, 1 (2003).

[248] H. Jobic, J. Physique **10**, Pr1 (2000).